CRANFIELD UNIVERSITY

Anthony Roy McAndrew

Modelling of Ti-6Al-4V Linear Friction Welds

School of Aerospace, Transport and Manufacturing

PhD Thesis

Academic Year 2014 - 2015

Supervisors: Dr Paul Colegrove and Professor Stewart Williams

This thesis is submitted in partial fulfilment of the requirements for the degree of Doctorate of Philosophy

This thesis is dedicated to my father, Ian Robert McAndrew.

“It is the glory of God to conceal a matter; to search out a matter is the glory of kings.” (Proverbs 25:2 New International Version)

Abstract

Linear friction welding (LFW) is a solid-state joining process that is finding increasing industrial interest for the fabrication of Ti-6Al-4V preforms. The fundamental science behind the process needs to be better understood to aid further process implementation. In practice, many aspects of the process are difficult to measure experimentally. Consequently, many researchers use computational models to provide an insight to the process behaviour, such as the thermal cycles and flash formation. Despite these recent research efforts, the effects of the workpiece geometry and process inputs on Ti-6Al-4V linear friction welds are still not fully understood. This thesis focuses on the development and validation of computational models to address this issue.

Two and three-dimensional (2D/3D) computational models were developed using the finite element analysis software DEFORM. The models were validated with a systematically designed set of experimental welds. The validated models and experimental data were used to characterise the effects of the process inputs and workpiece geometry on the: thermal fields, material flow, flash morphology, interface contaminant removal, microstructure, energy usage, welding forces, coefficients of friction and welding times. The results showed that there is a benefit to using larger pressures and oscillating the workpieces along the shorter of the two interface-contact dimensions when producing Ti-6Al-4V welds. This is because the burn-off required to remove the interface contaminants is reduced. Hence for the same burn-off, the factor of safety on contaminant removal is greater. Furthermore, these conditions can also reduce the interface temperature and refine the weld microstructure, which may offer additional benefits, such as reduced residual stresses and improved mechanical properties.

In conclusion, the thesis aim was successfully addressed, therefore increasing understanding of the LFW process. The work showed that although the 3D models captured the full multi-directional flow behaviour, 2D models were better suited to parametric and geometric studies.

Acknowledgements

To my friends and colleagues at the Welding Engineering and Laser Processing Centre (WELPC), thank you for your support, guidance and educational insights. In particular, great appreciation goes to my academic supervisor Dr Paul Colegrove for his invaluable supervision and guidance; it has been a pleasure to learn from you. I must also give a special mention to Mr Adrian Addison for his insightful conversations and enthusiasm to help me learn.

To my friends and colleagues at The Welding Institute (TWI) and The Boeing Company, especially Dr Michael Russell, Mr Bertrand Flipo and Mr David Bolser, thank you for the invaluable opportunities and support. Furthermore, I am also grateful to both companies, along with the Engineering and Physical Sciences Research Council (EPSRC), for funding the research presented in this thesis.

The advice on finite element modelling provided by Mr James Farrar of Wilde Analysis and Dr Richard Turner of the University of Birmingham was greatly appreciated.

To my family and friends, thank you so much for your never-ending love and support. I truly appreciate everything you do for me. In particular, I must thank my father for encouraging me to start my doctorate.

To Emma, my wonderful fiancée, thank you so much for your daily reassurances, support and love.

To God, thank you for giving me the strength and wisdom to complete this important chapter of my life.

Declaration

Many of the chapters in this thesis are based on articles that have been, or are intended to be, published elsewhere. A list of these is given below. For each of these articles, the author of this thesis (Anthony R. McAndrew) contributed principally to all aspects of the work described therein.

1. McAndrew, A. R., Colegrove, P. A., Flipo, B. C. D. & Russell, M. J. Modelling of flash formation and defect removal in Ti-6Al-4V linear friction welds. in *1st international joint symposium on joining and welding,* Osaka, Japan, 6-8 November 2013, (Fujii, H.) 291–298 (Woodhead publishing, 2013).***Note**

2. McAndrew, A. R., Colegrove, P. A., Addison, A. C., Flipo, B. C. D. & Russell, M. J. Energy and force analysis of Ti-6Al-4V linear friction welds for computational modeling input and validation data. *Metallurgical and Materials Transactions A* **45,** 6118-6128 (2014).

3. McAndrew, A. R., Colegrove, P. A., Addison, A. C., Flipo, B. C. D. & Russell, M. J. Modelling the influence of the process inputs on the removal of surface contaminants from Ti-6Al-4V linear friction welds. *Materials & Design* **66,** 183-195 (2015).

4. McAndrew, A. R., Colegrove, P. A., Addison, A. C., Flipo, B. C. D., Russell, M. J. & Lee, L. A. Modelling of the workpiece geometry effects on Ti-6Al-4V linear friction welds. *Materials & Design* **87,** 1087-1099 (2015).

5. McAndrew, A. R., Colegrove, P. A., Addison, A. C., Flipo, B. C. D. & Russell, M. J. 3D modelling of Ti-6Al-4V linear friction welds. (*To be submitted*).

***Note**: This conference article was peer-reviewed and won the award for the best paper presented at the 1st International Joint Symposium on Joining and Welding. The event, held in Osaka, Japan, in November 2013, attracted an international attendance and included over 50 papers from the field of welding and joining.

This thesis is submitted on the conditions contained in the regulations, and has not been submitted for any other academic or professional award. All of the work described was carried out as part of the course of study at Cranfield University and not previously or subsequently.

Candidate (A. R. McAndrew) Date:

Supervisor (P. A. Colegrove) Date:

Supervisor (S. W. Williams) Date:

Table of Contents

List of Figures

The figures displayed in this thesis, along with the page number they appear on, are listed below:

List of Tables

The tables displayed in this thesis, along with the page number they appear on, are listed below:

List of Equations

The equations described or used in this thesis, along with the page number they appear on, are listed below:

List of Abbreviations

The abbreviations used in this thesis are listed below:

Abbreviation	***Definition***
2D	Two-Dimensional
3D	Three-Dimensional
ALE	Arbitrary Lagrangian Eulerian
ANOVA	Analysis of Variance
BCC	Body-Centred-Cubic
DOE	Design of Experiments
DRX	Dynamic Recrystallisation
EDS /EDX	Energy-Dispersive X-ray Spectroscopy
EXP	Experiment
FEA	Finite Element Analysis
FEM	Finite Element Method
FSW	Friction Stir Welding
FSSW	Friction Stir Spot Welding
HAZ	Heat Affected Zone
HCF	High Cycle Fatigue
HCP	Hexagonal Close Packed
Hv	Vicker’s Hardness

Abbreviation	*Definition*
LCF	Low Cycle Fatigue
LFW	Linear Friction Welding
MD	Molecular Dynamics
MMC	Metal Matrix Composite
OFW	Orbital Friction Welding
PWHT	Post-Weld Heat Treatment
RFW	Rotary Friction Welding
SEM	Scanning Electron Microscope
TMAZ	Thermo-Mechanically Affected Zone
TWI	The Welding Institute
U. K.	United Kingdom
U.S.S.R	Union of Soviet Socialist Republics
WCZ	Weld Centre Zone

List of Nomenclatures

The nomenclatures used in this thesis are listed below:

Symbol	*Definition*	*Units*
A	Amplitude	mm
A_s	Surface area	mm^2
A_1	Johnson-Cook constant	MPa
a	Acceleration	$mm \cdot s^{-2}$
B	Johnson-Cook constant	MPa
b_o	Burn-off	mm
C	Johnson-Cook constant	MPa
C_p	Specific heat capacity	$J \cdot kg^{-1} \cdot K$
E_x	Total energy input	J
F_a	Applied force (Normal force)	N
F_f	Friction force	N
F_{in}	In-plane force	N
F_{int}	Interface force	N
F_n	Normal force (Applied force)	N
F_{pa}	Phase average force	N
f	Frequency	Hz
H	Specific enthalpy	$J \cdot kg^{-1}$

Symbol	*Definition*	*Units*
h	Convective heat transfer coefficient	$W \cdot m^{-2} \cdot K^{-1}$
k	Thermal conductivity	$W \cdot m^{-1} \cdot K^{-1}$
M	Mass	kg
m	Johnson-Cook constant	Dimensionless
n	Johnson-Cook constant	Dimensionless
P_n	Normal pressure (Applied pressure)	MPa
Q	One-dimensional heat flow	W
q	Power input	W
q'	Power input per unit area	$W \cdot m^{-2}$
q''	Power input per unit volume	$W \cdot m^{-3}$
T	Temperature	$^{\circ}$C or K
T_0	Initial material temperature	$^{\circ}$C or K
T_{flash}	Flash/interface temperature	$^{\circ}$C or K
T_{HAZ}	HAZ temperature	$^{\circ}$C or K
T^*	Homologous temperature	$^{\circ}$C or K
t	Time	s
t_t	Total time	s
v	Velocity	$mm \cdot s^{-1}$
v_r	Rubbing velocity / Average rubbing velocity	$mm \cdot s^{-1}$

Symbol	*Definition*	*Units*
v_{ss}	Steady-state burn-off rate	mm · s^{-1}
x	Distance	mm
x_1	Displacement	mm
x_0	Displacement point prior to x_1	mm
x_2	Displacement point subsequent to x_1	mm
x_{HAZ}	Thickness of the HAZ	mm
α	Alpha phase OR Thermal diffusivity	None or $m^2 \cdot s^{-1}$
β	Beta phase	None
ε	Equivalent plastic strain	Dimensionless
$\dot{\varepsilon}^*$	Ratio of test strain rate to a reference strain rate	Dimensionless
ρ	Density	kg · m^{-3}
σ_{JC}	Johnson-Cook flow stress	MPa
ω	Angular frequency	Hz

Chapter 1: Introduction

1.1 Introduction and Context

This chapter presents the thesis background, motivation, sponsors, aim and objectives, and structure.

1.2 Background and Motivation

Linear friction welding (LFW) is a solid-state joining process that works by oscillating one workpiece relative to another whilst under a large compressive force, see Figure 1.1(a). Friction between the oscillating surfaces produces heat which causes the interface material to plasticise. The plasticised material is then expelled from the interface causing the workpieces to shorten (burn-off) in the direction of the compressive force[1–4]. During the burn-off the interface contaminants, such as oxides and foreign particles, which can affect the properties[5,6] and possibly the service life of a weld[7], are expelled from the weld into the flash[8]. Once free from contaminants, pure metal to metal contact occurs resulting in an integral bond[8–12]. Figure 1.1(b) shows an example of a completed weld.

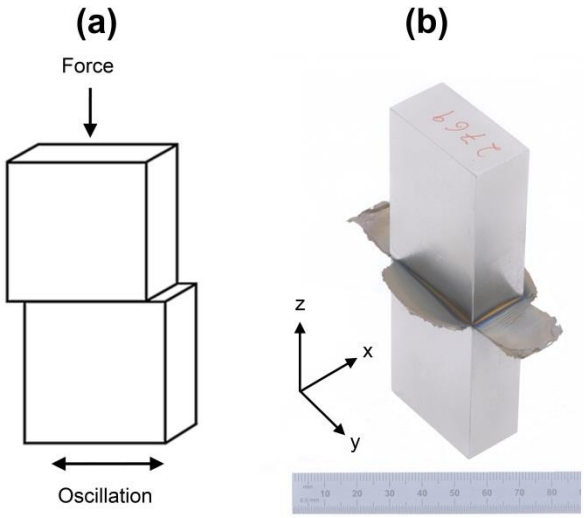

Figure 1.1: (a) LFW process schematic and (b) a completed Ti-6Al-4V weldment showing the expelled interface material (flash), where oscillation occurred in the 'y' direction.

Components machined from a solid block are expensive due to the proportionally large amount of material that is purchased compared to the amount that remains after machining. This is particularly true for materials like titanium and nickel-based alloys. LFW reduces the material required to make a component by joining smaller workpieces to produce a preform, which is subsequently machined to the desired dimensions, as shown in Figure 1.2. This significantly reduces manufacturing costs[1,2,8]. In addition to the economic benefits, the process also offers many advantages over traditional fusion welding methods[1,2], including: excellent mechanical properties; avoidance of melting, allowing for a range of dissimilar materials to be joined[13–17]; and very low defect rates. Currently, LFW is an established technology for the manufacture of titanium alloy integrated bladed disks (blisks) for aero-engines[2,8,18–20]. However, due to the many benefits the process offers it is finding increasing interest from other industrial sectors – particularly for the joining of Ti-6Al-4V.

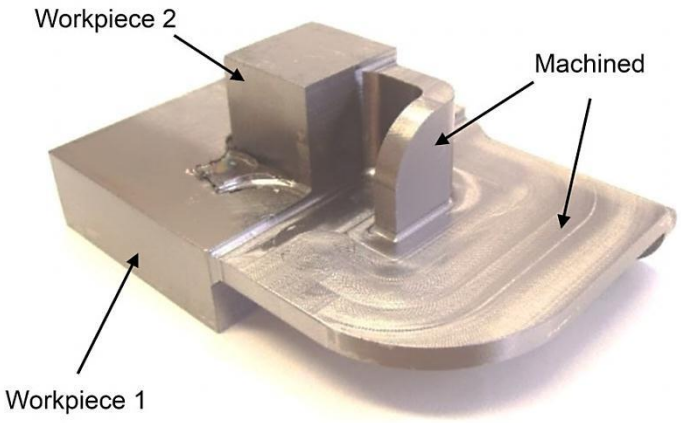

Figure 1.2: Fabrication of a titanium alloy (Ti-6Al-4V) preform using the LFW process. The as-welded structure can be seen on the left side of the figure and the final machined component on the right. (Courtesy of TWI)[1].

Despite this interest, the process has experienced limited additional industrial implementation[4,21]. This is partly due to a lack of fundamental scientific understanding of LFW[21]. When compared to other friction welding processes, where there is numerous published publically available work, relatively little investigation has taken place into the LFW process[1,3,10]. The rapid nature of the

process and the fact that the interface of the workpieces cannot be observed during welding means that using physical experiments alone may fail to provide adequate insight into the LFW process. Computational modelling offers a pragmatic method for understanding what is happening during the rapidly evolving process, allowing for increased fundamental scientific understanding[7,22–24]. An increased understanding will aid further industrial development, optimisation and implementation of LFW.

Both The Welding Institute (TWI) and The Boeing Company have identified a need to use computational models to provide a greater insight into the LFW process. Consequently, both companies, along with the Engineering and Physical Sciences Research Council (EPSRC), provided funding for the current project: "*Modelling of Ti-6Al-4V Linear Friction Welds".*

1.3 Aim and Objectives

The aim of this thesis is to use computational modelling to increase the fundamental scientific understanding of the LFW process for the joining of Ti-6Al-4V.

The primary objectives are as follows:

- Conduct a systematic series of experimental welds to provide input and validation data for the computational modelling work.
- Use the finite element analysis (FEA) software DEFORM to develop 2D models that predict the effects of the process inputs and workpiece geometry on the thermal fields, material flow and interface contaminant removal.
- Use DEFORM to develop 3D models to compare with the 2D modelling approach and to investigate the "keystone" weld, which has multiple surfaces that must be joined concurrently.

1.4 Thesis Structure

In total, this thesis consists of 8 chapters and 8 appendices. The remaining chapters are as follows:

Chapter 2 presents a comprehensive literature review. Emphasis was placed on the LFW process, the titanium alloy Ti-6Al-4V and computational modelling techniques. The primary purpose of the review was to identify “gaps” in the knowledge of the subject of LFW so that a novel, focused and industrially relevant research project could be formulated. The conclusions from the literature review led to the thesis aim and objectives detailed in section 1.3 being identified.

Chapters 3 to 6 detail the research that was completed to achieve the thesis aim.

- Chapter 3 focuses on the design and analysis of experimental Ti-6Al-4V linear friction welds to determine input and validation data for the computational modelling work. A simple 2D thermal model is also presented to investigate the initial heating of the weld.

- Chapter 4 focuses on the development and validation of 2D thermo-mechanical models to characterise the effects of the LFW process inputs on Ti-6Al-4V linear friction welds.

- Chapter 5 uses the modelling approach developed in the previous chapter to characterise the effects of the workpiece geometry on Ti-6Al-4V linear friction welds.

- Chapter 6 focuses on the development and validation of 3D thermo-mechanical models. This is to make comparisons with the 2D modelling approach used in chapters 4 and 5 and to investigate the “keystone” weld.

Chapter 7 presents a general discussion of the thesis research outcomes. The thesis research outcomes are discussed in a “global” context and are then compared to the LFW literature. Finally, practical implications of the research outcomes are presented.

Chapter 8 presents a summary of the thesis and recommendations for further research.

Many of the chapters described above (chapters 3-6) are based on articles that have been, or are intended to be, published elsewhere, as discussed in the “Declaration” section. A reference to the relevant article(s) is given at the start of each chapter.

The 8 appendices detail the data sets, technical drawing, assumptions, justifications, photos, and equipment associated with the research described in the above chapters.

Chapter 2: Literature Review

2.1 Introduction and Context

This chapter provides a review of the state-of-the-art of the LFW process so that the primary "gaps" in knowledge for the subject area could be identified. Emphasis was placed on the LFW process, the titanium alloy Ti-6Al-4V and computational modelling techniques. The conclusions from the review provided a foundation on which a novel, focused and industrially relevant research project was based, as detailed in section 1.3.

2.2 Friction

Friction is the force resisting motion between two or more interacting surfaces. Friction causes the kinetic energy of the moving surfaces to be converted into heat[3,10,25–28]. In reality an apparently smooth surface consists of many microscopic projections, which are known as asperities. When one surface moves relative to another these asperities interact, as shown in Figure 2.1(a). The interaction of these asperities via elastic and plastic yielding is responsible for the friction[26,27,29].

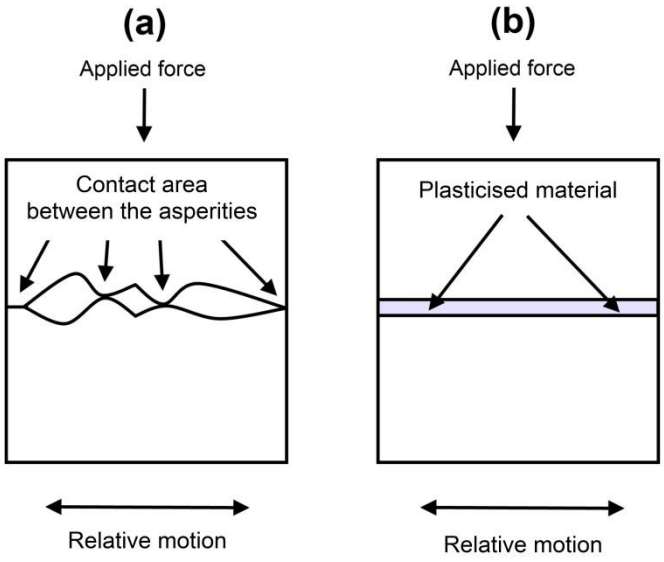

Figure 2.1: An illustration of different friction conditions: (a) asperity interaction (sliding friction) and (b) viscous flow (sticking friction).

Friction due to asperity interaction is often termed as “dry” or “sliding” friction. Leonardo da Vinci (1452 – 1519) is generally noted as being the first person to develop the basic concepts of dry friction, which were expanded on by Guillaume Amontons (1663 – 1705) and Charles Augustin Coulomb (1736 – 1806)[25,26,30]. The “classic” laws of dry friction are as follows[26,31]:

- The friction force is directly proportional to the normal (applied) force (Amontons’ 1st law).
- The friction force is independent of the apparent contact area (Amontons’ 2nd Law).
- The friction force is independent of the velocity of relative motion (Coulomb’s law).

These three observations were summarised as[28,31,32]:

$$F_f = \mu \cdot F_n \qquad \textbf{2.1}$$

Where μ is the coefficient of friction, F_f is the friction force, and F_n is the normal force. Equation 2.1, is often referred to as “Coulomb(ic) friction”[10,33–35].

Recently, many of the long established laws regarding the friction force, and hence the coefficient of friction, have been shown to be invalid[25,31]. Despite this, equation 2.1, assuming a constant coefficient of friction, still gives a good representation of the friction force at “low” normal forces[10,31,33]. Problems typically arise at more “extreme” conditions where significant plastic deformation of the asperities occurs[10,31,33]. For example, if the applied force is large enough the asperities significantly deform so that the true cross-sectional area approximately equals the apparent cross-sectional area, as shown in Figure 2.1(b). When this happens the apparent friction stress equals the material yield stress (τ_y) causing full plastic flow of the interface[10,33]. This is referred to as “sticking” friction and cannot be suitably described by coulombic friction[10,33]. Consequently, the friction between the interface of the contacting surfaces is often considered as a function of the normal pressure, as shown in Figure 2.2. If

the normal pressure is low, Coulombic friction occurs; if the normal pressure is large sticking friction occurs and takes on a value of the material yield stress independent of the normal pressure. Furthermore, sticking friction occurs more readily as the temperature of the contacting surfaces is increased[10]

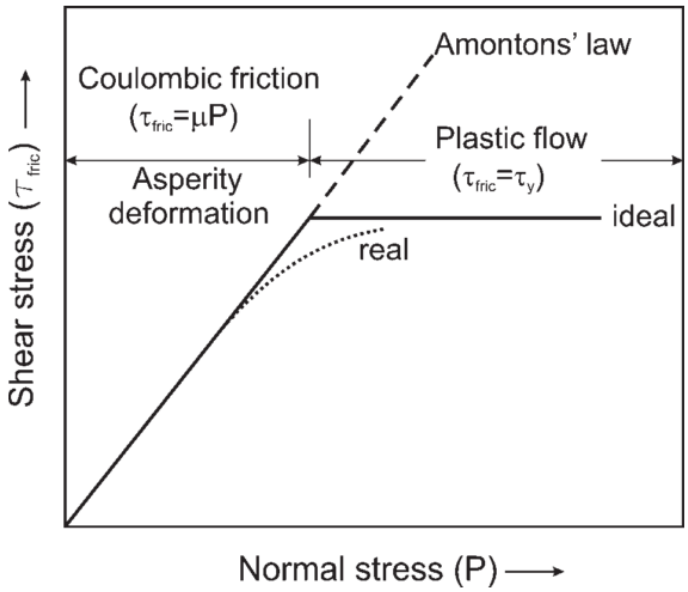

Figure 2.2: Characterisation of the friction stress as a function of the normal pressure[33].

2.3 Friction Welding

Friction welding is a solid-state joining process that utilises the heat generated during friction[3,10,11]. The heat causes the interface of the workpieces to be joined to soften, plasticise and mechanically mix together, allowing for a bond to be formed[9–11,36,37].

2.3.1 Advantages

Friction welding offers many advantages to the manufacturing sector, for example:

- The weld remains in the solid-state, avoiding many of the defects associated with the melting and solidification during fusion welding[11,23,38–

[43], such as pores and solidification cracks. The distortion of the welded component is also reduced[10,44–48].

- The process has lower peak temperatures than fusion welding, reducing intermetallic formation and allowing for a range of dissimilar materials to be joined[14,17,49].
- The process does not need a filler metal, flux and shielding gas[10].
- The process is easily automated, making the process highly repeatable and not dependant on human influence[1,2,50].
- When used to fabricate preforms the material usage and manufacturing costs are reduced when compared to subtractive techniques (e.g. CNC machining)[1,2,8,51].

2.3.2 Processes

There are several friction welding processes, which are summarised below:

Friction Stir Welding (FSW)

Friction stir welding is a friction based process developed at The Welding Institute (TWI), Cambridge, U.K. in 1991. The process works by using a non-consumable tool, which is rotated and plunged into the interface between two workpieces. The tool is then moved through the interface and the heat causes the material to become hot and viscous. The rotating tool then mechanically mixes the softened material of the two workpieces[4,52–54], as shown in Figure 2.3.

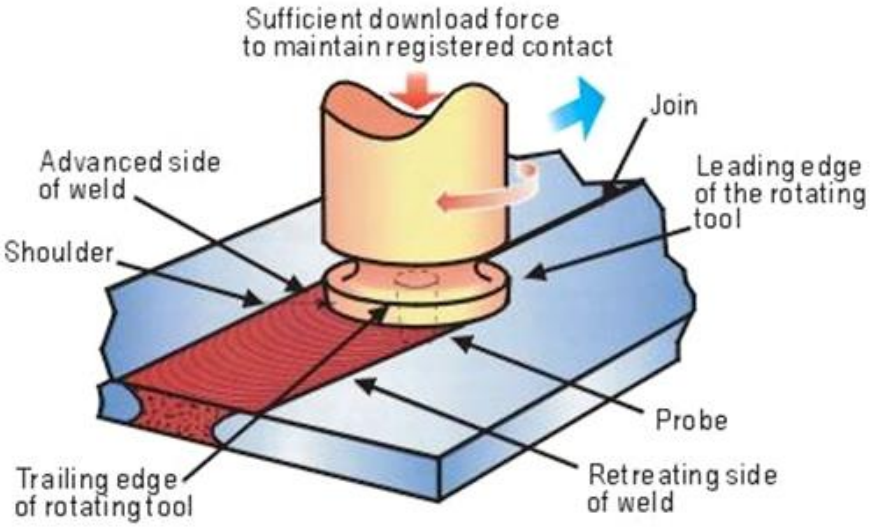

Figure 2.3: Friction stir welding[55].

Friction Stir Spot Welding (FSSW)

Friction stir spot welding is a derivative of friction stir welding and was co-developed by the Mazda Motor Corporation and Kawasaki Heavy Industries. FSSW differs from FSW in that no traverse motion of the non-consumable tool occurs[56,57]. The tool is rotated and plunged into the workpieces to produce a lap joint, as shown in Figure 2.4.

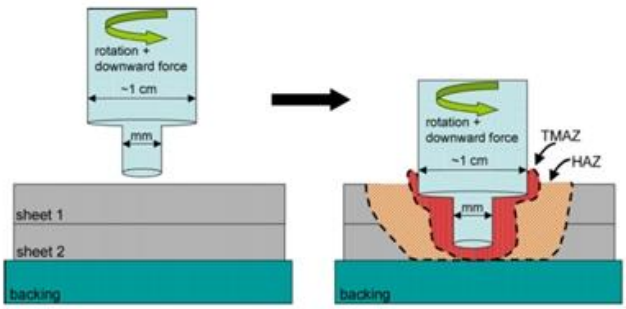

Figure 2.4: Illustration of the friction stir spot welding process[56].

Rotary Friction Welding (RFW)

Rotary friction welding has been used heavily in industry since the 1940s. The process works by rotating one cylindrical workpiece about its axis whilst under a large normal force relative to another cylindrical workpiece[4,10,11,33], as shown in

Figure 2.5. The interface material plasticises and is expelled from the joint, resulting in the workpieces shortening along the direction of the normal force. Once free from contaminants, pure metal to metal mixing occurs resulting in a bond. The process can only be used for joining rotationally symmetrical workpieces[3].

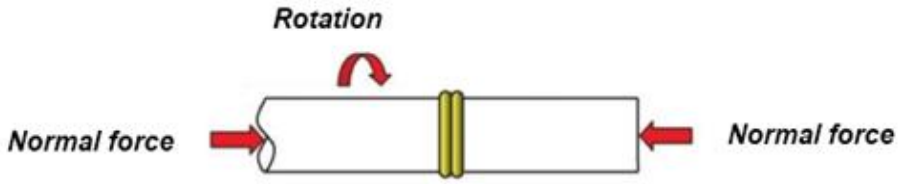

Figure 2.5: Rotary friction welding[10].

Orbital Friction Welding (OFW)

Orbital friction welding was developed in the 1970s[33]. Orbital friction welding overcame the limitations of rotary friction welding by allowing non circular workpieces to be joined[3]. The process works in a similar manner to RFW, however, orbital motion is used instead of rotary. The process is illustrated in Figure 2.6.

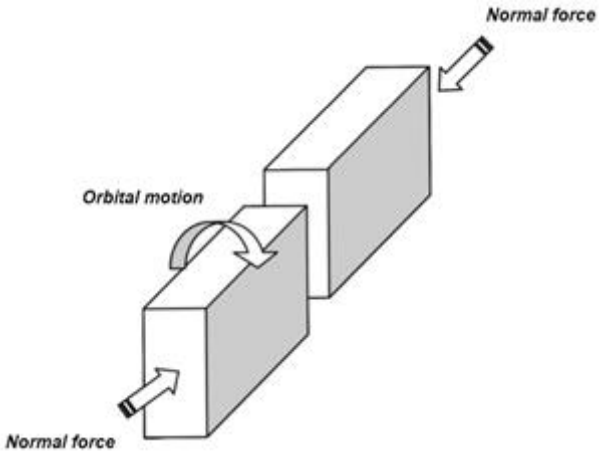

Figure 2.6: Orbital friction welding[10].

2.4 Linear Friction Welding (LFW)

2.4.1 Background

The linear friction welding process was first patented in the late 1920s[8], however there was very little detail recorded on its use. A discussion of the concept was then recorded in the U.S.S.R. in the 1960s[58], but the process was described as being “very doubtful” for a manufacturing technique[8,58]. This was due to the difficulty in generating reciprocating linear motion[58]. Even today there is no official definition of the process and there is no universal patent; although there are many unique specific application patents[8,59]. The first real structured research into the process took place at TWI, Cambridge in the 1980s[2].

When compared to other friction welding processes, where there are numerous published works, there is relatively little information available about LFW until recently[1,3,10].

2.4.2 Process Phases

As described in section 1.2, linear friction welding is a solid-state joining process that works by linearly oscillating one workpiece relative to another whilst under a large compressive force. Although one continuous process, LFW is said to occur over four[3,22,60] phases:

Phase I: Initial Phase

Contact exists between the asperities on the two surfaces to be joined and heat is generated due to friction, see Figure 2.1(a). The asperities soften and deform, increasing the true area of contact between the workpieces. As shown in Figure 2.7, the shear force can remain fairly constant throughout this phase due to the increasing contact area being offset by the decrease in yield strength of the asperities. Negligible axial shortening (burn-off) perpendicular to the direction of oscillation is observed.

Phase II: Transition Phase

The material plasticises and becomes highly viscous causing the true area of contact to increase to 100 percent of the cross-sectional area, see Figure 2.1(b). As shown in Figure 2.7, the shear force increases to overcome the material yield stress of the plasticised layer[3]. The heat conducts back from the interface plasticising more material and the burn-off begins to occur due to the expulsion of the viscous material.

Phase III: Equilibrium Phase

The interface force, thermal profile and burn-off rate reach a quasi-steady-state condition and significant burn-off occurs through the rapid expulsion of the viscous material from the interface. As shown in Figure 2.7, the steady-state burn-off occurs in a relatively constant manner.

Phase IV: Deceleration and Forging Phase

Once the desired burn off is reached, the relative motion is ceased and the workpieces are aligned. In some applications an additional forging force may be applied to aid consolidation.

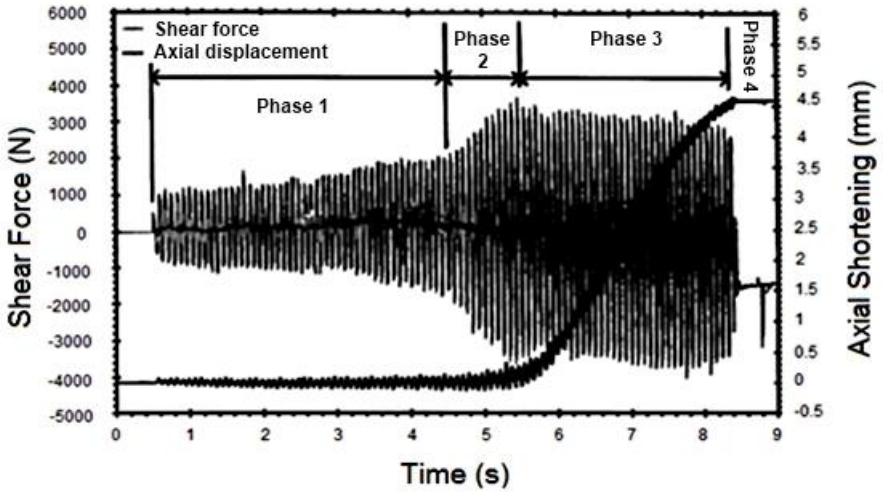

Figure 2.7: Shear force and displacement history of a Ti-6Al-4V linear friction weld (amplitude of oscillation: 3mm, frequency of oscillation: 12 HZ, friction pressure: 42.9MPa)[3].

2.4.3 Process Inputs

There are eight process inputs used during linear friction welding[1–3,6–8,13,17,39,46,61–68], these are:

- **Linear oscillation frequency**: The number of completed oscillatory cycles per second. Typical values used are between 20 Hz and 75 Hz.

- **Linear oscillation amplitude**: The maximum displacement of the oscillating workpiece from its datum point. Typical values used are between 1 mm and 5 mm.

- **Applied / Normal force**: The normal force applied to the workpieces during the oscillatory motion. The applied force is usually defined after the workpiece dimensions are known. This is so that a pressure may be defined. Forces are often defined to give pressures between 40 MPa and 120 MPa.

- **Ramp-up time**: The time taken to ramp-up the oscillation amplitude to the desired value. This typically takes less than a second.

- **Burn-off**: This can be measured in two ways:

    - **Burn-off to distance**: The distance the workpieces shorten before the oscillatory motion is decayed to a stop.

    - **Burn-off to time**: The time taken before the oscillatory motion is decayed to a stop. The burn-off achieved is then dependent on the combination of the other process inputs used.

  The burn-off distances recorded in the literature are typically between 1 mm and 6 mm.

- **Linear oscillation decay time**: Time taken to decay the amplitude and frequency from the processing value to zero. The process typically takes

between 0.1 seconds and 2 seconds, with the former being more common.

- **Forging force**: The force used to help consolidate the workpieces once the oscillatory motion is ceased. As with the applied force, the value is usually defined after the workpiece dimensions are known. Typical values used generate a pressure between 40 MPa and 240 MPa.

- **Forging time**: The time the forging force is applied. Typical values used are between 1 seconds and 10 seconds.

Many authors appear to consider the frequency, amplitude, applied force and burn-off to be the process inputs of primary importance[2,3,6,24,50,69,70]. Furthermore, there are several important factors worthy of note that are dependent on the process inputs[1,8,50]:

- **Total upset**: This is the combination of the burn off distance plus any extra shortening achieved during the forging phase.

- **Shear / friction / interface force**: The force at the interface of the workpieces parallel to the oscillatory motion.

- **Burn-off rate**: The rate that the burn-off occurs during phase 3.

- **Welding time**: The time taken to complete the process.

- **Average rubbing velocity**: The average absolute velocity generated over a cycle of oscillation, which is determined from the amplitude, A, and frequency, f, of oscillation[1]:

$$v_r = 4 \cdot A \cdot f \qquad \textbf{2.2}$$

2.4.4 Weld Features

The macrostructures of linear friction welds are similar in appearance in that they have several distinct zones – a weld centre zone (WCZ), a thermo-

mechanically affected zone (TMAZ) and a heat affected zone (HAZ) – and are surrounded by the flash[2,5,8,13,16,24,41–46,61,62,66,71–79]. A typical example of a weld is shown in Figure 2.8. Technically the WCZ and the TMAZ are both "thermo-mechanically affected zones" but due to the vastly different microstructures they possess they are often considered separately[2,6,8,45,61]. The WCZ experiences *significant* dynamic recrystallisation (DRX), the TMAZ does not. The material in HAZ is not deformed mechanically but is affected by the heat. The remainder of the weld is the parent material.

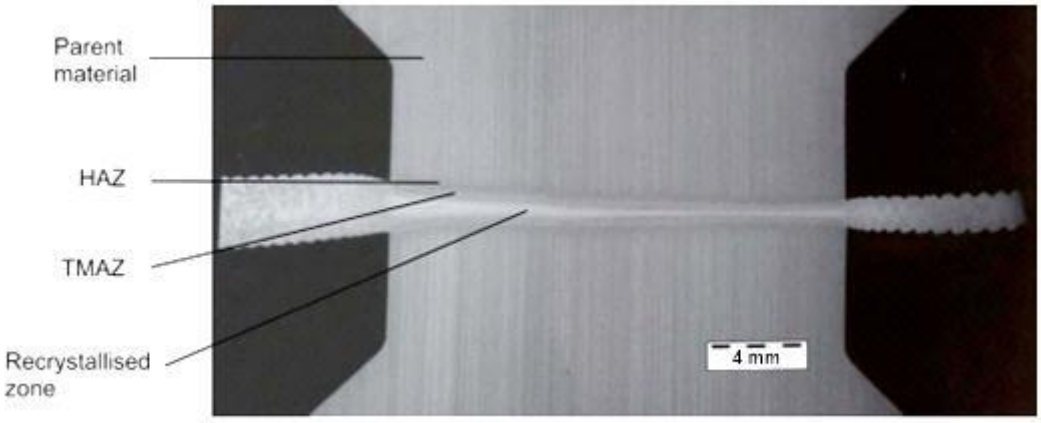

Figure 2.8: Metallographic section of a titanium alloy (Ti-6Al-4V) to illustrate typical features of a LFW (Courtesy of TWI)[2].

The extent of the WCZ, TMAZ and HAZ appear to be dependent on the processing conditions. For example, an increase of the applied force can reduce the extent of the WCZ and TMAZ[2,61,80,81]. A reduction in the size of the workpiece geometry can also reduce these values[19]. An increase of the rubbing velocity can reduce the extent of the HAZ[7,82].

The weld region is surrounded by the flash in the direction of and perpendicular to the direction of oscillation. The material and processing conditions have a big influence on the flash morphology[1,2,5–7,61,63,81]. The flash can appear as a single entity or have a bifurcated appearance, as shown in Figure 2.9(a) and (b) respectively. In many situations where the flash is expelled as a single entity, the flash in the direction of oscillation is not uniform in thickness, but has a series of observable "ripples"[3,6,41,50,60,62,66,73], as shown in Figure 2.8. The flash

morphology generally displays a more noticeable rippling effect when the amplitude of oscillation is increased[7,34,81].

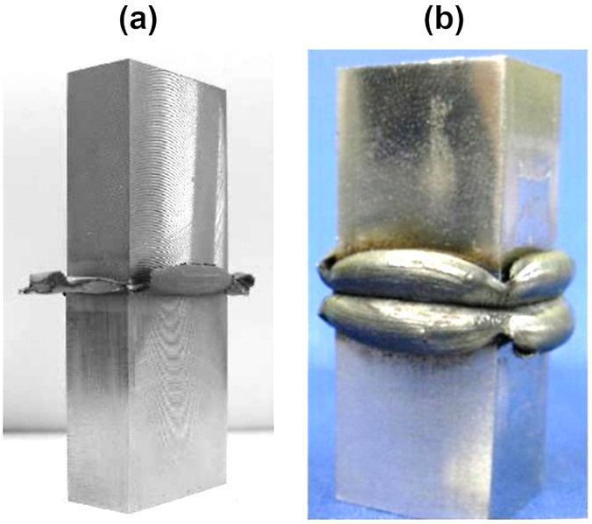

Figure 2.9: Flash morphology for: (a) Titanium alloy[6] (Ti-6Al-4V) and (b) a Nickel based super alloy (waspaloy)[5].

According to Ofem et al.[50], the ripples in the flash may be a symptom of a "ploughing effect". When the oscillation amplitude is at maximum displacement the in-contact surface area is decreased. This causes a pressure increase, resulting in the cooler material being plunged further into the highly viscous material. As the workpieces are brought back together the cooler material "ploughs" the hot viscous material from the interface, generating a noticeable ripple in the flash, as illustrated in Figure 2.10.

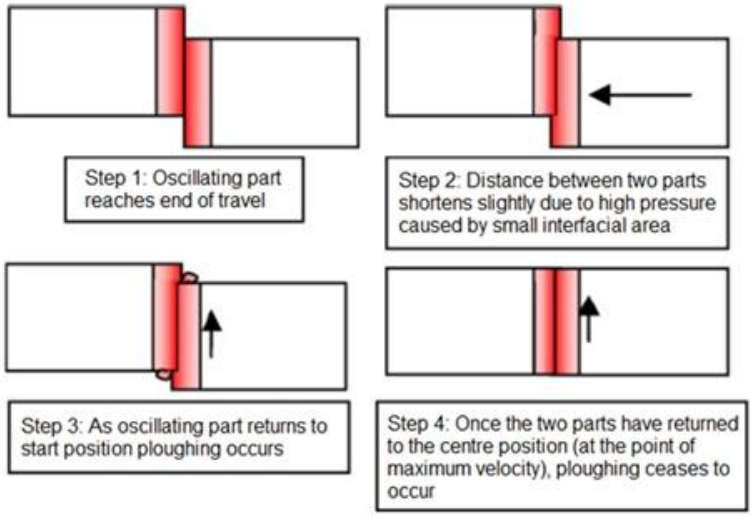

Figure 2.10: Suggested ploughing mechanism[50].

2.4.5 Weld Defects

Interface contaminants, such as oxides and foreign particles, affect the properties[5,6] and possibly the service life of a weld[7] and are therefore a primary cause for a linear friction weld being defective[5,6,8,10,11,27,63,65,75]. Oxides are generated during phase 1 when the hot interface material reacts with the atmosphere[30]. It is also possible that some oxides may remain at the interface due to insufficient pre-weld cleaning. The foreign particles may constitute oil or grease from workpiece machining which were also not removed during pre-weld cleaning. At the start of phase 2 the oxides and foreign particles become trapped at the interface during the merging of the viscous material. The majority of the contaminants, however, often appear to be oxides, as confirmed by energy-dispersive X-ray spectroscopy (EDS /EDX)[5,48,63,83]. According to Bhamji et al.[8], it is important that the contaminants are expelled from the interface into the flash as this allows for full metal to metal mixing and a bond being formed.

The interface contaminants are believed to be increasingly expelled toward the extremities of the weld as more burn-off occurs[7], as shown in Figure 2.11(b). Many authors suggest that a weld is likely to be free from contaminants if all of the initial contacting interface material is expelled into the flash[5,8,27,50]. Wanjara and Jahazi[6] have shown that for the same burn-off, contaminants were present

at the interface if lower values of frequency and amplitude were used, whereas if higher values were used the interface was typically free from contaminants. Therefore interface contaminant removal appears to be critically dependent on the combination of process inputs used. However, the reasons why the process inputs affect interface contaminant removal are not understood. Also, there has been no investigation into the effects of the workpiece geometry on contaminant removal. According to Grujicic et al.[84], excessive burn-off to facilitate the removal of the interface contaminants leads to a loss of material and productivity, which ultimately increases industrial costs. Therefore there is an industrial need to understand the mechanisms behind interface contaminant removal to increase safety and reduce costs.

In rare circumstances, voids due to porosity have been observed at the interface of titanium alloy linear friction welds[6,66,68], as shown in Figure 2.11(c). This often occurs when comparatively low values of burn-off are used. Lang et al.[66] noticed that the voids were located toward the edges of the weld interface. This suggests that the porosity was due to an initial foreign particle (probably trapped surface gasses) which had not been expelled into the flash due to an inadequate amount of burn-off. This is believed because defects typically associated with fusion welding processes, such as porosity, are typically avoided during solid-state joining process. This is primarily due to the avoidance of the melting and solidifying of the material[11,23,38–44].

In addition to being required for contaminant removal, a suitable burn-off must be applied to allow for sufficient mechanical mixing of the interface layer[9,10]. Insufficient bonding at the interface results in welds having poorer mechanical properties[2,5,46]. Addison[2] suggested that Bifurcated flash, as shown in Figure 2.9(b), can be an indication that there is unsuitable bonding. Addison[1,2] also noticed that fine features of workpieces, such as the corners, regularly contain a small unbonded region, as shown in Figure 2.11(d). These unbonded regions can be eliminated by optimising the process inputs or machining the unbonded area off[1]. Addison[1,2], however, did not state what the optimum process inputs were.

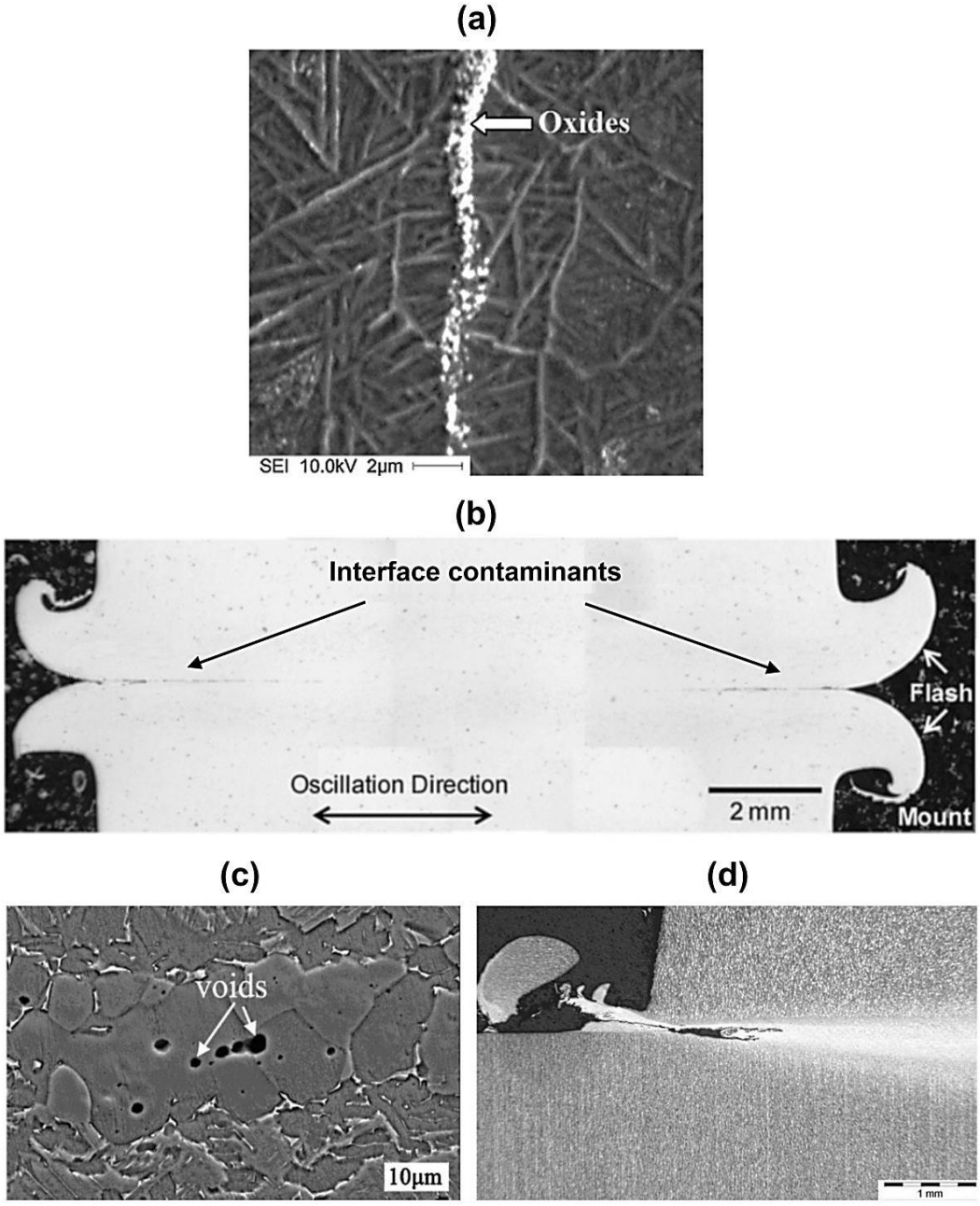

Figure 2.11: Linear friction weld defects: (a) oxides at the interface of a Ti-6Al-4V weld[6], (b) interface contaminants located at the interface extremities of linear friction welded waspaloy[5], (c) voids observed in titanium alloy linear friction welds[68], and (d) an unbonded region located at a "fine feature" in a Ti-6Al-4V weld (Courtesy of TWI)[1].

2.4.6 Energy Usage

Several authors[3,6,22,24,41,60] have investigated the effects of the process inputs on the power density input using equation 2.3 or equation 2.4:

$$q' = \mu \cdot P_n \cdot v_r \quad \textbf{2.3}$$

Where q' is the power density, v_r is rubbing velocity, P_n is normal pressure, and μ is coefficient of friction.

$$q' = \frac{A \cdot f \cdot P_n}{2 \cdot \pi \cdot A_s} \quad \textbf{2.4}$$

Where q' is the power density, A is the amplitude of oscillation, f is the frequency of oscillation, P_n is the normal pressure and A_s is the cross sectional surface area.

Analysis of the units in equation 2.4 indicate that the parameters on the right do not give the correct units for power per unit area. This may be due to a poorly named variable; the pressure term should have been force. Also, the coefficient of friction is not considered.

Regardless of the equation used, many of these authors used average values for the rubbing velocity, coefficient of friction and pressure, thus only giving an approximation of the power input. In addition, they did not investigate the effects of the process inputs on the overall energy required to make a weld, which is of economic and environmental concern[50].

Ofem et al.[50], addressed this by demonstrating that the output data from a LFW machine can be used to calculate the instantaneous power input, q in the form of [50]:

$$q = F_{int} \cdot v \quad \textbf{2.5}$$

Where F_{int} is the interface force of the workpieces and v is the instantaneous velocity. By integrating equation 2.5 as a function of time, the overall energy used to make a linear friction weld can be estimated:

$$E_x = \int_0^{t_t} F_{int} \cdot v \, dt \qquad \textbf{2.6}$$

Where, E_x is the total energy inputted to a weld; and t_t is the total time to make the weld.

This method of calculating the power and energy includes the effects of the changing velocity and friction coefficient over each cycle of oscillation. Ofem et al.[50] showed that an increase of the rubbing velocity increased the power input but reduced the overall welding time. Consequently, the overall energy required to produce a weld was fairly constant over the rubbing velocity range investigated. The shortfall in this work was that the effects of the applied force and burn-off distance were not investigated. Also, the analysis was only conducted for steel workpieces.

2.4.7 Residual Stress

Significant residual stresses are present in a linear friction weld after processing[61,74]. The residual stresses are generated via two mechanisms. The first is due the plastic deformation experienced by the workpieces at elevated temperatures[38,85]. The second is due to the thermally induced strain[70,86], which results from the difference in thermal expansion and contraction of the material during heating and cooling. The primary mechanism is due to the thermally induced strain that occurs during the post-oscillatory motion cooling[70]. Understanding residual stress formation is important because it negatively influences weld performance and life[8,70,85].

Residual stresses have been investigated for linear friction welds using:

- Non-destructive testing, such as synchrotron x-ray diffraction[61,64,70,74,87] and neutron diffraction[38,64,85]. Both of these methods involve calculating the strains and stresses from changes in the crystal lattice spacing.

- Destructive testing, such as the contour method[74,85]. The contour method is far cheaper than the non-destructive methods but the residual stresses are only measured in the plane of the sectioning, i.e. the contour.

- Numerical models[70,87]. Provided suitable input data is used, models can be used to predict the origin of residual stresses.

Regardless of the material, process input combination and direction of oscillatory motion used, there is a broad agreement[38,61,70,74,85] that the residual stresses are generally largest in the direction of the longest contacting surface dimension ('y' in Figure 2.12). Followed by the shortest contacting surface dimension ('x' in Figure 2.12), and lowest in the direction normal to the weld plane ('z' in Figure 2.12). The residual stresses at the weld interface tend to be tensile. A sharp drop in the stresses either side of the weld line is often observed, becoming compressive until they eventually approach zero[38,61,70,74]. Romero et al.[61] and Bhamji et al.[8] claimed that since the weld plane is longer in the 'y' direction than in the 'x' direction it is likely that there is a larger thermal gradient in the 'y' direction, hence the increased residual stress. Bhamji et al.[8] also claimed that the residual stresses were lowest in the 'z' direction due to the forging force causing sufficient plasticity to compensate for any thermal mismatch.

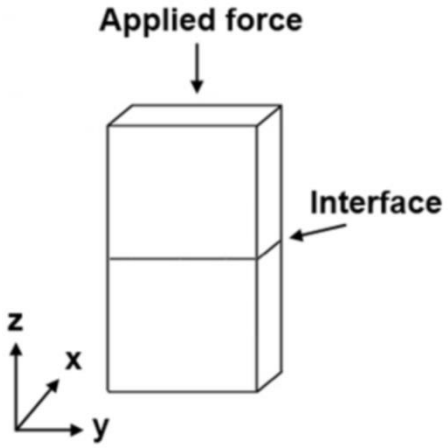

Figure 2.12: Residual stress formation with respect to the workpiece dimensions. Note that 'y' is larger than 'x'.

Post-weld heat treatment (PWHT) has been shown to significantly reduce the residual stresses in linear friction welds[74], even by as much as 90%[8]. According to a review by Bhamji et al. [8] the residual stress relief is dependent on the size of the workpiece geometry. For example, in a comparatively smaller welded sample negligible residual stress remained after PWHT, whereas in a larger welded sample significant stresses remained after an identical PWHT. Both welds displayed similar residual stress profiles prior to PWHT. In addition to residual stress relief, PWHT is also used to homogenize the microstructure[88] and improve the mechanical properties[5,18,42,68,80,89] (tensile, microhardness and toughness) of linear friction welds.

Romero et al.[61] and Turner et al.[70] have shown that residual stress formation can be minimised by appropriate selection of the process inputs; with higher applied pressures reducing the stress levels. This phenomenon was attributed to the higher pressures increasing the rate of material expulsion from the weld interface causing more heat rejection[61,80]. This resulted in a cooler weld and a lower thermal mismatch, which reduced the residual stress intensity[61]. This result demonstrates that stresses can be minimised by appropriate selection of the process inputs. This finding is particularly important if residual stress relief by a subsequent PWHT is difficult to obtain (e.g. dissimilar welds)[8].

2.4.8 Machines

On a basic level LFW machines work by oscillating one workpiece relative to another whilst under a large compressive force. According to Bhamji[90] , the force application is always generated by a hydraulic ram, whilst the oscillatory motion can be generated mechanically or hydraulically.

Mechanically operated systems often use a motor to rotate a crankshaft. Attached to the crankshaft are two cranks that can be phase shifted. A whipple beam is attached to the cranks. When the cranks are 180° out of phase the beam rotates around its centre point causing the centre to remain stationary, which effectively gives an oscillation amplitude of zero. To achieve oscillation amplitudes between zero and the maximum, the phase shift is altered between 0° and 180° [2,90]. The frequency is dependent on the revolutions per minute of the motor[2]. This process is illustrated in Figure 2.13(a).

Hydraulic operating systems work by pumping high pressure fluid into a stack of accumulators. A servo valve then allows the high pressure fluid from the accumulators to be alternated between each end of a cylinder. This oscillates a piston at a desired amplitude and frequency. The tooling that holds the workpiece to be welded is attached to the end of the piston. This is illustrated in Figure 2.13(b).

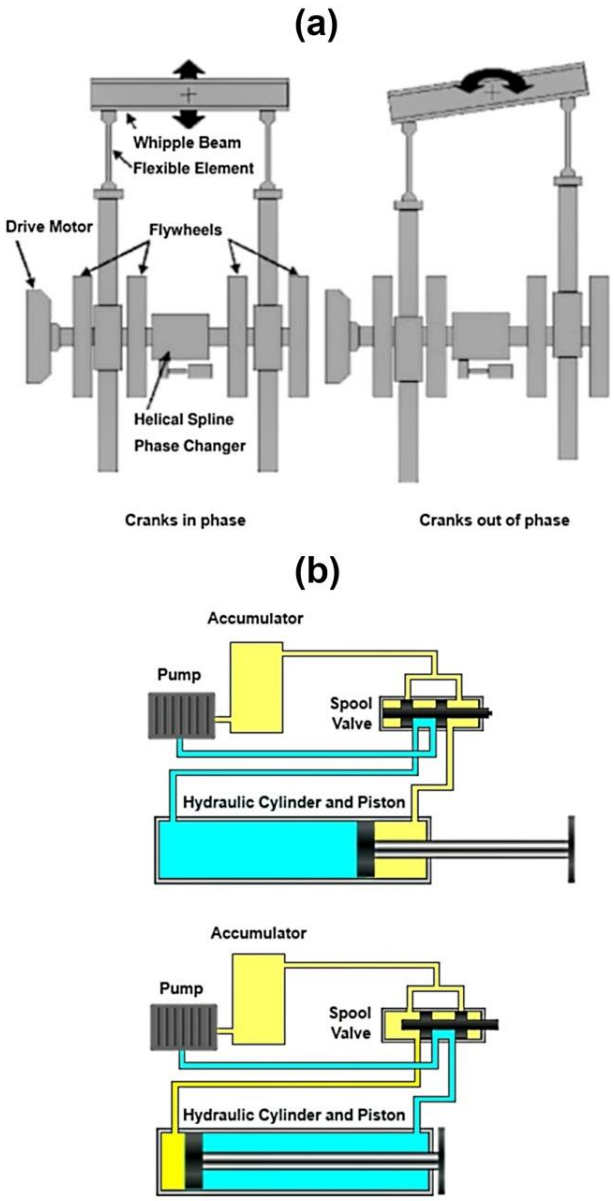

Figure 2.13: Schematic of (a) mechanically operated motion[91] and (b) hydraulically operated motion[90].

As far as the author can tell, there are five major LFW machine manufacturers: ACB (France), APCI (Indiana, U.S.A.), KUKA Systems, (Germany), MTI (Indiana, U.S.A.), and Thompson Friction Welding (England, U.K.).

2.4.9 Industrial Applications

In general, the LFW process is considered to be an “exotic” technology for the manufacture of high-value aerospace components[1,2]. This is primarily due to the

expensive cost of the first generation equipment and the fact that most industrial LFW machines are owned by aerospace manufacturers[2].

To date, the process is commercially established as a technology for the fabrication of titanium alloy integrated bladed disks (blisks) in aero-engines[2,8,18–20,90]. Titanium blisks are used in low temperature sections of aero-engines. Typically[4,92], Ti-6Al-4V (Ti-64) is used for applications up to 300 °C and Ti-6Al-2Sn-4Zr-2Mo-0.15Si (Ti-6242) for applications up to 480 °C. Figure 2.14(a) shows an example of a blisk manufactured using the LFW process. Rolls Royce, MTU Aero Engines and Pratt & Whitney all use the LFW process to commercially produce titanium alloy blisks[93].

LFW offers many advantages when manufacturing blisks, for example conventionally manufactured bladed disks assemblies are reliant on mechanical fixings and dovetail joints to join the blade to the disk, as shown in Figure 2.14(b). LFW allows for the blade to be integrally joined to the disk which significantly reduces the weight of the component[4,70,94], even up to 30%[4,70]. In addition to the weight savings, the lack of a mechanical interface between the blades and the disks eliminates common sources for fatigue crack initiation[4,92], which is often the life limiting feature[4]. This can result in extended inspection intervals[92]. Furthermore, linear friction welded blisks also have improved performance (e.g. better aerodynamics), which reduces the operating costs for the end user[7,19,45,62,68,74].

Another alternative to using mechanical fixings is to machine the blisk from a solid block[4,71,95]. When compared to the LFW process this is a costly exercise due to the amount of waste material generated – particularly for larger blisks[7,92]. In addition, blisks machined from a solid block must comprise of a single material[4,71]. Linear friction welding has the advantage of joining disks and blades of different materials[4,71].

Linear friction welded blisks, however, do have some disadvantages, such as the exhaustive quality control that is required to ensure reliable performance[4].

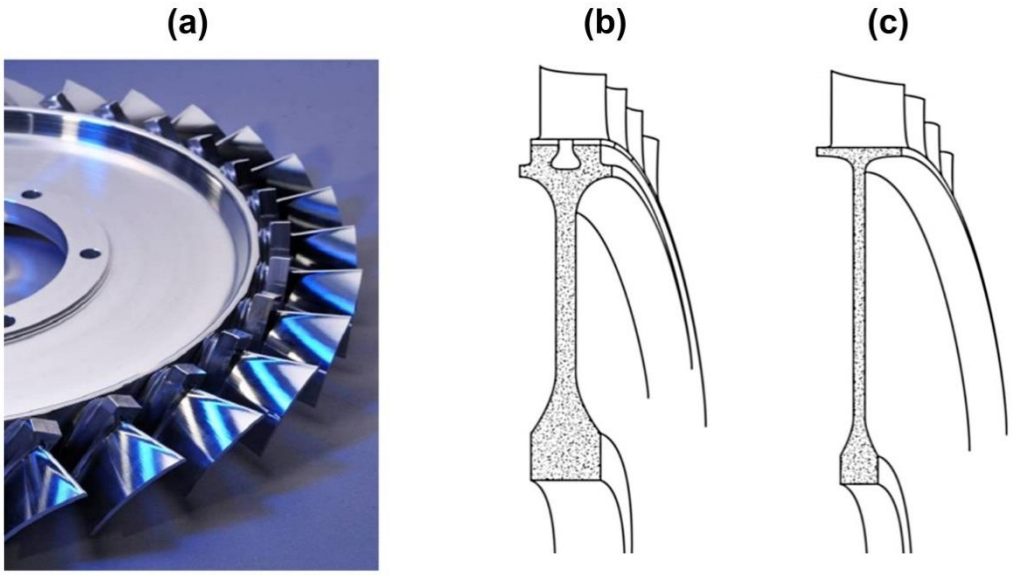

Figure 2.14: (a) an integrated bladed disk (blisk) manufactured at TWI (courtesy of TWI), (b) a conventional bladed disk assembly[7] and (c) a linear friction welded blisk[7].

The Boeing Company and TWI are interested in expanding the application of the LFW process to additively manufacture a wide range of aerospace preforms[51,59,96,97]. This is primarily due to the significant cost savings that can be achieved. For example, when compared to machining from block, savings of between 14% and 49%, with a typical average of 38%, can be achieved using LFW[51].

In addition to joining workpieces with a single surface of contact, as shown for the components in Figure 1.1(b), Figure 1.2 and Figure 2.14(a), The Boeing Company and TWI are also interested in joining “keystone” workpieces (trapezoid shaped). “Keystone” workpieces allow for the fabrication of structurally complex aerospace components[51,59,96,97].

The “keystone” weld involves the joining of a keystone workpiece to two flanges and a base plate, as shown in Figure 2.15. The flanges are welded to the base plate first (stage 1 weld) and the generated flash removed and the surfaces re-cleaned. The stage 1 welds are straight forward as only one surface is required to be joined to the base plate. However, production of the “keystone” weld

(stage 2 weld) can be problematic as there are three surfaces that need to be welded concurrently. The corners where the base plate, stage one and stage two welds meet – colloquially known as the “triple point” – are the areas of most concern[97].

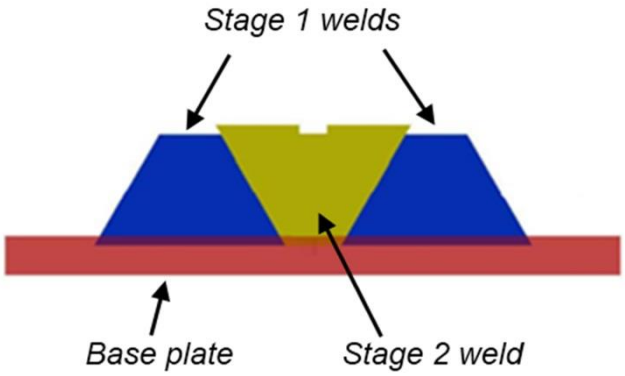

Figure 2.15: Manufacturing process of the keystone weld (Courtesy of TWI and The Boeing Company)[96].

TWI are encouraging industrial sectors outside of aerospace to consider the LFW process to mass manufacture lower-value preforms[1] – particularly for the joining of Ti-6Al-4V. Despite the increased industrial interest, the process has experienced limited additional industrial implementation[4,21], which is partly due to a lack of fundamental scientific understanding of LFW[21].

2.4.10 Materials Used

The LFW process is typically used for joining metals, however, it has been used to join plastics[98,99] and wood[100,101]. LFW is particularly effective for joining metals that have good high-temperature properties, i.e. compressive yield and shear strength, and low thermal conductivities[1,8]. This allows for the generated heat to remain at the interface causing the interface to rapidly heat and plasticise. This makes titanium alloys particularly suitable for the process, however many similar and dissimilar material combinations have also been investigated with varying degrees of success, as detailed in the following paragraphs.

Titanium Alloys

Titanium alloys have received the most attention with respect to the LFW process[1–3,6–9,19–24,38,39,41–43,45,60–62,66–70,72,74,80,81,85,89,95,102–115]. This is primarily due to them being very expensive to buy and machine[92,94], making them appealing for the manufacture of preforms. Of all the Titanium alloys, Ti-6Al-4V has received the most attention[1–3,6–8,19,23,38,39,41,45,60–62,67–70,74,81,85,105–108,111,114,115]. As the linear friction welding of Ti-6Al-4V is of increasing industrial interest (particularly for the sponsors of this project) its microstructure, mechanical properties and constitutive data will be reviewed further in section 2.5.

Nickel-Based Superalloys

The relatively poor oxidation behaviour of titanium alloys at high temperatures – particularly the beta phase – make them undesirable[4,92] due to embrittlement[92] for use in hot sections of aero-engines. As such, mechanical bladed disk assemblies and blisks used in hot sections are manufactured using nickel-based super alloys[4,75,92,116]. LFW is finding industrial interest for manufacture of nickel-based superalloy blisks for the same reasons detailed in section 2.4.9[5,117]. Currently, LFW of nickel-based superalloy blisks is in the research and development stages[8,117].

Various grades of polycrystalline[5,48,63,79,88,116,118,119] and single-crystal[75,83,117] nickel-based superalloys have been linear friction welded. The primary focus of many of these studies was on the weld microstructure, i.e. the grain size and allotropic phases etc. A particular issue with the welding of these alloys is the formation of an oxide layer at the interface[48,63,83,117]. In the study by Chamanfar et al.[48] these oxides were observed at the extremities of the weld and failure during tensile testing was initiated at these sites. This suggests there may have been insufficient burn-off to completely remove the oxide layer generated during phase 1, as discussed in section 2.4.5. Amegadzie et al.[83] showed that the oxide layer could be eliminated by using higher compressive forces.

Melting was also noticed to have occurred in some of the trials[75,83], which, as detailed in section 2.3.1, is not typical of the LFW process. Although melting did not occur in all cases it was noted that the interface temperature reached between 90% and 97% of the melting temperature in many of the trials[5,79,119].

Karadge et al.[117] studied welds between a polycrystalline nickel-based superalloy and a single crystal alloy. It was shown that the weldability was highly dependent on the orientation of the single crystal slip system. The weldability increased when the primary slip system was orientated to give a high Schmid factor[8]. The Schmid factor is a product of the "*cosine of the angle between the applied load and the slip plane*" and the "*cosine of the angle between the applied load and the slip direction*". Higher Schmid factors result in a greater shear stress being required in the slip direction to initiate slip.

Despite the difficulties in joining these materials, Chamanfar et al.[5,48] managed to successfully join polycrystalline waspaloy. The weld was free from oxides[48] and exhibited a yield strength and ultimate tensile strength slightly higher than the parent material[5] . Successful joining occurred when high pressures and burn-off values were used[5,48]. Moreover, when compared to the as-welded condition, the microhardness values were shown to be superior after PWHT[5].

Aluminium Alloys and Aluminium Based Metal Matrix Composites

LFW of aluminium alloys and metal matrix composites (MMCs) is finding increasing industrial interest for the fabrication of aerospace and automotive components[44,65].

Linear friction welded AL-Fe-V-Si 8009[37] and AA7075-T651[2] aluminium alloys were shown to have weld line tensile properties lower than that of their respective parent materials. In contrast, Addison[2] successfully joined the AA5083-0 alloy, which had weld line tensile properties equal to the parent material. Other aluminium alloys have also been joined, such as AA2024[87] and AA6082-T6[120], however, with the exception of a small discussion on the

microhardness values, which were lower than the parent material, there was no discussion on the mechanical properties.

Rotundo et al.[44,65] investigated the joining of AA2124/25 Vol.%SiC_p metal matrix composite (MMC) workpieces to each other[65] and to an aluminium alloy (AA2024) workpiece[44]. In both studies, the welds were said to have “good” tensile and fatigue properties.

Steels

Various different grades of steel have been investigated[1,2,46,50,76,78,81,84,121]. In general good mechanical properties are obtained and the weld strength often surpasses that of the parent material.

Dissimilar Materials

Although the LFW process is often said to be advantageous for joining dissimilar materials[13,17,117,122] (welds between different material classes e.g. titanium to steel, as opposed to slightly different grades of the same material, e.g. Ti-64 to Ti-6242) there has been few investigations into the area.

Several authors have investigated the joining of commercially pure copper to commercially pure aluminium[13] and to the aluminium alloy 6063[14,15]. Although intermetallics could be found at the weld interface of these combinations[13–15], Bhamji et al.[13] demonstrated that the tensile properties of the weld line can surpass those of the aluminium parent material. This is because the tensile tests failed in the aluminium parent material.

Bhamji et al.[17] investigated the joining of an Aluminium alloy (6082-T6) to a Magnesium alloy (AZ31). The results showed that when the welds were produced with higher applied forces the intermetallic formation reduced. The weld line tensile properties were slightly less than both parent materials.

Bhandari[16] investigated the joining of a titanium alloy (Ti-6Al-4V) to steel (SS304L). There was evidence of intermetallic formation at the weld line. When tensile tested the welds failed at the weld line. There was a slight increase in

the tensile value when the applied force was increased, although it was still weaker than both parent materials.

2.5 Titanium Alloy (Ti-6Al-4V)

Titanium alloys have two allotropic forms[92,94], alpha (α) and beta (β). The α phase is a hexagonal close packed (HCP) structure and the β phase is body centred cubic (BCC) structure[86,92,94], see Figure 2.16(a) and (b) for illustrations of the structures. The α and β phases are the basis for the classification of titanium alloys. There are three *major* classification types which are predominantly distinguished by their phase volume whilst at room temperature[92,94]:

- α-alloys. These comprise of commercially pure titanium and titanium alloys alloyed with α-stabilising and/or neutral elements. All α phase alloys, however, do contain a small percentage of β phase (<5%).
- α+β alloys. These alloys have a β volume fraction ranging between 5% and 40%. If only a small amount of β-stabilizing elements are added so that the β volume fraction is less than 10% then the alloy is sometimes referred to as a near-α alloy[94].
- β alloys (metastable β alloys). There are no commercially sold single β phase alloys. All of the titanium alloys referred to as “β alloys” are actually metastable β alloys as they are located in the α+β phase region (see Figure 2.16). The characteristic feature of the metastable β phase alloys is that they do not transform into martensite upon fast cooling from the β phase field to room temperature. It should be noted that these alloys can still exhibit an α phase volume fraction of more than 50% at equilibrium.

In general[92,94], α alloys have better creep, corrosion and oxidation resistance but are relatively insensitive to heat treatment. α+β alloys have an excellent combination of strength and ductility. β alloys can be hardened to reach high

strength levels, have good formability, but are not as easy to weld due to their affinity to oxidise.

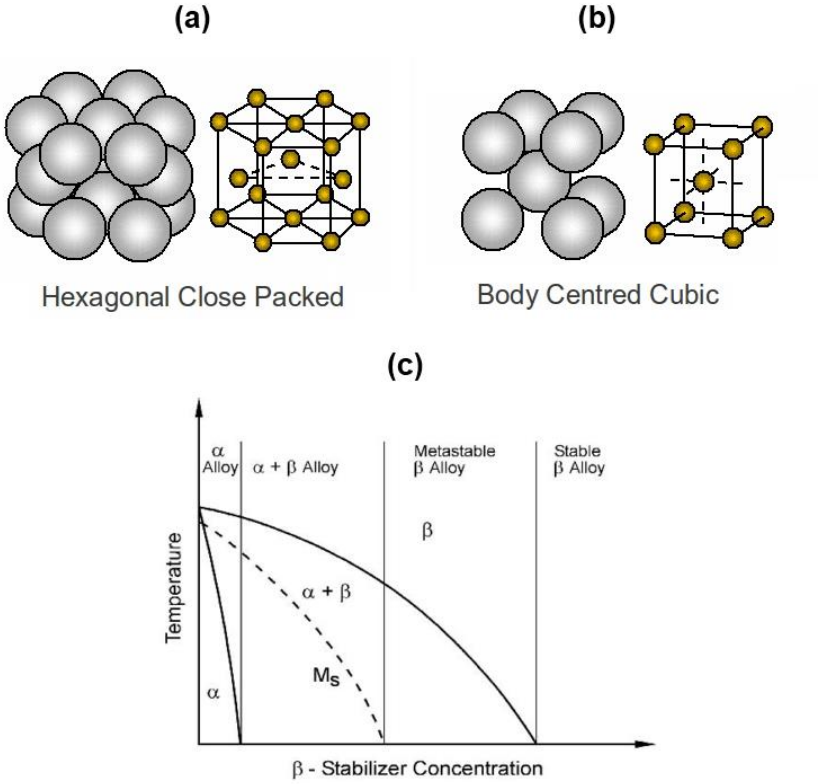

Figure 2.16 Allotropic phases of titanium alloys showing: (a) the HCP structure of the α phase[123], (b) the BCC structure of the β phase[123], and (c) the influence of the β-stabilising alloying elements on Ti-alloy phase diagrams (schematically)[94].

Ti-6Al-4V is an α+β alloy that was developed in the 1950s at the Illinois Institute of Technology, USA[92]. The alloy is known for its excellent strength to weight ratio. It is the most commonly used titanium alloy - approximately 50% of all titanium alloys used are of this composition[45,92].

2.5.1 Wrought Microstructure and Mechanical Properties

Microstructure

The Ti-6Al-4V alloy consists of approximately 6% aluminium, which stabilises the α phase, and 4% Vanadium, which stabilises the β phase[124,125]. The β phase constitutes ten percent by volume fraction at room temperature[126]. When viewed under a standard microscope the α and β phase often appear white and

black, respectively - under a scanning electron microscope (SEM) this feature is reversed.

Ti-6Al-4V, as with all α+β alloys, is commercially produced to have one of three types of microstructure[94]. These are fully lamellar, fully equiaxed and bi-modal. The microstructure obtained depends on the thermo-mechanical deformation process and the rate of cooling used[94]. Figure 2.17, shows an example of the three different microstructures. The three types of microstructures, and their processing histories, have a great effect on the mechanical properties they exhibit. Finer microstructures, which result from faster cooling rates, increase the strength and reduce crack nucleation. Whilst coarser microstructures exhibit increased resistance to creep and fatigue crack growth. Equiaxed structures tend to have greater ductility and fatigue strength. Lamellar microstructures have higher fracture toughness and exhibit greater resistance to creep. Bi-modal microstructures can be considered as a combination of the other two microstructures and possess a good mix of the superior properties exhibited by both[92,94].

It should be noted that the wrought Ti-6Al-4V typically used in the literature for the linear friction welding process, where reported, tends to be of the bi-modal microstructure[6,41,43,45,61,62,67,68,71,74,85].

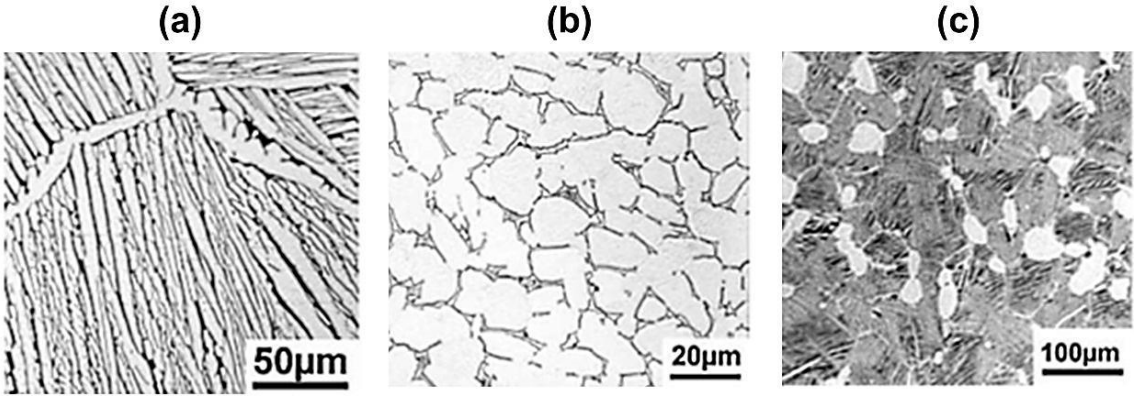

Figure 2.17: α+β titanium alloy microstructures: (a) Fully lamellar, (b) Fully equiaxed and (c) Bi-modal[94].

Mechanical Properties

At room temperature, commercial Ti-6Al-4V typically tends to have properties close to the following values shown in Table 2.1.

Table 2.1: Ti-6Al-4V room temperature properties.

Property	*Value (Units)*	*References*
Density	*4420 – 4430 (Kg·m^{-3})*	24,45,127
Melting Point	*1660 (^{o}C)*	7,24,94,127
Young's Modulus	*110 – 140 (GPa)*	92
Yield Strength	*800 – 1100 (MPa)*	92
Ultimate Strength	*900 - 1200 (MPa)*	86,92
Poisson's Ratio	*0.34 (-)*	45,70,111,112
Microhardness (Hv)	*300 – 400 (kg·mm^{-2})*	92
Toughness (Charpy Impact)	*17.8 (j)*	3

2.5.2 Microstructure and Mechanical Properties after LFW

Microstructure

As described in section 2.4.4, linear friction welds contain four distinct zones, the weld centre zone (WCZ), thermo-mechanically affected zone (TMAZ), heat affected zone (HAZ) and the parent material. Due to the structural stability of Ti-6Al-4V below temperatures of 800 °C [76,128] it is often difficult to detect a purely heat affected zone in Ti-6Al-4V[6,41,61].

The region of material that experiences the most significant change during the LFW process is the WCZ. The temperature at the interface surpasses that of the β-transus temperature[6,7,23,45,66] – 980 °C to 1010 °C depending on the quantities of the interstitial elements[6,22,61,62,74,128,129] – transforming the α grains into β grains. Significant DRX of the grains occurs in the single β-phase region. The fully β transformed microstructure cools rapidly after the frictional phase of the process, preventing β grain coarsening, resulting in a Widmanstätten[6,8,19,43,61] or Martensitic[6,19,61] microstructure, as shown in Figure 2.18(a) and (b) respectively. The difference, according to Ahmed and Rack[130],

is due to the rate of cooling from the single β-phase. If the weld cools at a rate faster than 410 $^{\circ}C \cdot s^{-1}$ a diffusionless transformation occurs resulting in Martensite; according to Karadge et al.[19] some metastable β-phase may also remain. If the weld cools at rate slower than 410 $^{\circ}C \cdot s^{-1}$ then a diffusional transformation occurs resulting in a Widmanstätten morphology.

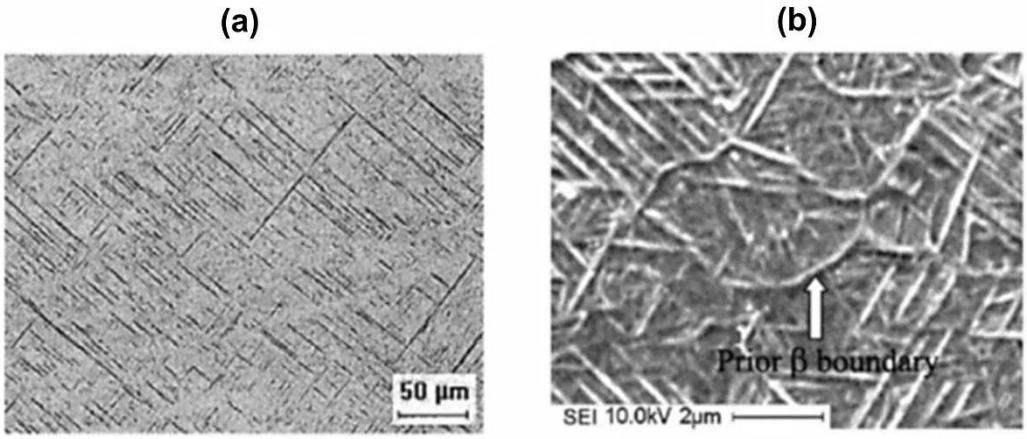

Figure 2.18: Ti-6Al-4V microstructures observed at the weld interface: (a) Martensite[106] and (b) Widmanstätten[6].

The majority of researchers suggest that the microstructure of the TMAZ does not reach the β-transus as fragments of the α grains from the parent material are still present[6,19,23,45,62]. These grains tend to be deformed, elongated and re-orientated in the direction of oscillation[2,6,23,39,41,61,62,68,74], see Figure 2.19. Uniquely, Frankel et al.[74] suggested that the TMAZ closest to the weld interface can reach the β-transus temperature and experience some small "pockets" of recrystallisation. The conditions that generate enough heat to allow the TMAZ to exceed the transus temperature are likely to depend on the processing conditions used.

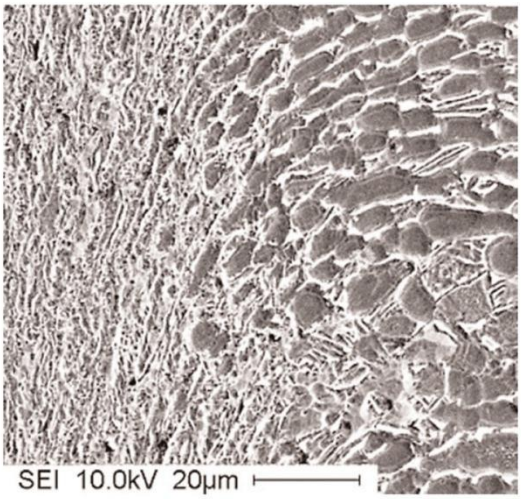

Figure 2.19: TMAZ section of linear friction welded bi-modal Ti-6Al-4V displaying the deformed and re-orientated grains[6].

Mechanical Properties

Mechanical testing has shown that the hardness, using the Vickers' hardness test, in the recrystallised weld interface (422+/-11 [41], 425+/-10 [61] and 398+/-3 [6]) is higher than that of the parent material (302+/- 20 [41], 328+/- 20 [61] and 317 to 352 [6]). The increased hardness at the weld interface is due to the refined microstructure[39,41,62]. However, there appears to be some conflicting results when it comes to the hardness in the TMAZ. Some researchers suggest that the hardness in the TMAZ is between that of the weld interface and the parent material[41,45], as shown in Figure 2.20(a); whilst other researchers suggest that the hardness in the TMAZ can be lower than that of the parent material[6,61], as shown in Figure 2.20(b). According to Grujicic et al.[45] a coarsening of the β grains in the TMAZ was responsible for the inferior hardness values. Romero et al.[61] stated that the conditions that cause inferior TMAZ properties are likely to be process input dependent. The researchers who achieved welds with superior TMAZ properties used higher amplitudes of oscillation.

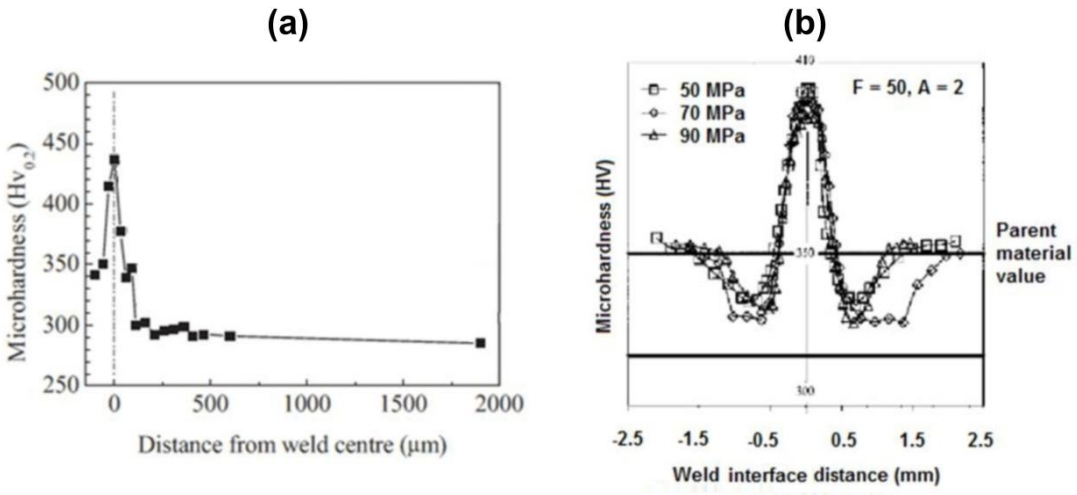

Figure 2.20: TMAZ hardness: (a) higher than parent[41] and (b) lower than parent[6].

Assuming a Ti-6Al-4V linear friction weld is free from interface contaminants, the weldment will typically fail in the parent material when tensile tested[2,6,8,68], as shown in Figure 2.21(a). If interface contaminants are present the weldment will fail at the weld line, as shown in Figure 2.21(b). Interestingly, Wanjara and Jahazi[6] demonstrated that a weldment can fail in the TMAZ when tensile tested if it was produced with a low power input. This was possibly due to grain growth occurring in the TMAZ, resulting in softening.

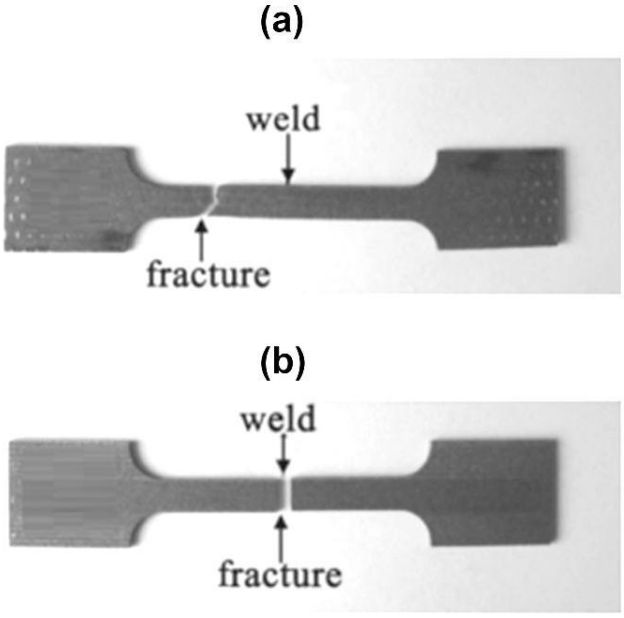

Figure 2.21: Tensile fracture location in (a) an integral weld and (b) a non-integral weld[68].

Linear friction welded Ti–6Al–4V has been investigated at various stress amplitudes ranging from the high cycle fatigue (HCF) to the low cycle fatigue (LCF) regime[107,108,114]. For all cases the fatigue failure occurred in the parent material. According to Wen et al.[107,108] the fatigue cracks initiated from the surface or near-surface defects of the parent material.

The impact toughness of titanium alloy linear friction welds is much harder to predict because the microstructure is very heterogeneous[3,24,62]. However, the value at the interface of a Ti-6Al-4V linear friction weld surpasses that of the parent material[3,62].

A repair weld involves the joining of a new workpiece onto the “stub” of a previously broken weldment. The mechanical properties and macroscopic appearance of a repaired Ti-6Al-4V weld were that same as the initial weld[1]. This is an important feature as it will allow for the repair of high-cost components, such as blisks.

2.5.3 Flow stress

The flow stress is the stress required to deform a material at a particular temperature, strain and strain rate[128,131,132]. Obtaining flow stress data at low strains and strain rates is relatively easy as the data can be recorded using compression and tensile tests[128,131]. High strain rate flow stress data is obtained using Split-Hopkinson bar tests[105].

Due to Ti-6Al-4V being a commonly used alloy there is much published data[7,105,128,131–134] on its flow stress characteristics for temperatures between 25 $^{\circ}$C and 1500 $^{\circ}$C, strains between 0 and 4 and strain rates between 0.0003 s^{-1} and 2000 s^{-1}. It should be noted that no single source covers the entire range detailed. Also, the initial microstructure, as discussed in section 2.5.1, was not detailed in all of the sources[7,105,132]. Some authors[7,128,131] present their flow stress data purely as experimental values, i.e. experiments were completed for a wide range of temperatures, strains and strain rates and the obtained data plotted in graphs. Whilst other authors completed a select few experiments to

determine constants to be put into flow stress models[105,132–136], such as the Johnson-Cook, Zerilli-Armstrong and Zener-Hollomon. The flow stress data is then presented as a function of the material model. The Johnson-Cook flow stress model is one of the most widely used material models. The model calculates the Von-Mises stress as a function of the strain hardening, strain rate sensitivity and temperature, and is described as follows:

$$\sigma_{JC} = [A_1 + B \cdot (\varepsilon^n)] \cdot [1 + C \ln(\dot{\varepsilon}^*)] \cdot [1 - (T^{*m})] \quad \textbf{2.7}$$

Where ε is the strain; $\dot{\varepsilon}^*$ is the ratio of strain rate to a reference strain rate, T^* is the homologous temperature (Kelvin), and A_1, B, n, C, and m are material constants determined by the regression-analysis procedure.

Figure 2.22 shows a comparison of Ti-6Al-4V flow stress data between different data sources. This includes the data reported by Turner et al.[7], Seshacharyulu et al.[128], Lee and Lin[105], and the finite element analysis software DEFORM's library.

All of the sources[7,105,128] show that the flow stress decreases as the temperature is increased. This is due to the thermal energy provided by the increasing temperature reducing the required mechanical energy to achieve the activation energy for slip (material flow) to occur. The rate of flow stress decrease with increasing temperature is different between the sources.

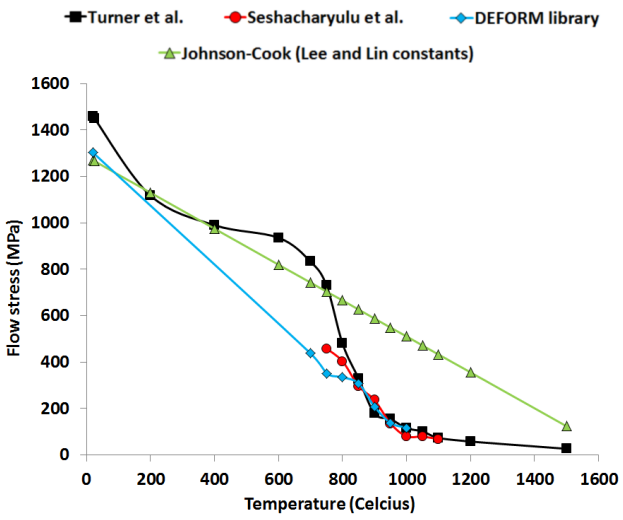

Figure 2.22: A comparison of flow stress data at a strain of 0.5 and a strain rate of 10 s^{-1} taken from different sources[7,105,128].

Lee and Lin[105] carried out experiments at 25 °C and between 700 °C and 1100 °C at intervals of 100 °C for strains between 0 to 0.25 at a strain rate of 2000 s^{-1} to determine constants (A_1, B, n, C, and m) to be put into the Johnson-Cook flow stress model. This model was used to plot the data in Figure 2.22. The Johnson-Cook model shows a linear decrease over the temperature range of interest, this is in contrast to the other sources. Furthermore, the flow stress values are much higher than the other sources at higher temperatures.

With the exception of the Lee and Lin[105] data, there is a good agreement between the flow stress values of the other sources for temperatures between 800 °C and 1100 °C. The differences between the sources arise at temperatures below 750 °C. First of all, this is because Seshacharyulu et al.[128] did not report values below 750 °C. The deviation between the data reported by DEFORM and Turner et al.[7] is probably due to the number of experimental points investigated. The data reported by Turner et al. [7], which was sourced from JMatPro[137], experimentally recorded the flow stress values at regular temperature intervals between 25 °C and 700 °C. This allowed for the true flow behaviour to be captured. The data reported by DEFORM investigated the flow stress behaviour at a temperature of 25 °C and 700 °C. The flow behaviour

between these two points was then interpolated, resulting in a linear decrease with increasing temperature.

The data reported by Turner et al.[7] is believed by the author to be the most representative of the Ti-6Al-4V flow stress, because it was obtained over the largest range of temperatures, strains and strain rates. Therefore, this source's[7] flow stress characteristics will be discussed in more detail. As shown in Figure 2.23, the rate of flow stress decrease with increasing temperature changes significantly over the temperature regime investigated.

At lower temperatures the Ti-6Al-4V microstructure[92,94,132] consists of the HCP α+β phase. The HCP structure has less slip systems, which also require a greater activation energy[132,134], than the β phase BCC structure[86]. Although there are several different slip systems in the HCP structure, only a few are responsible for dislocation movement at low temperatures[138]. This causes a relatively slow rate of flow stress decrease with increasing temperature.

When the temperature reaches 800 °C the beta phase volume fraction increases exponentially[92,128], as shown in Figure 2.24. Also, more of the alpha-phase HCP slip systems are readily activated as the temperature increases[86,132], causing increased plasticity and reduced anisotropy[139]. All of this results in a sharp drop in the flow stress around this temperature, as shown in Figure 2.23.

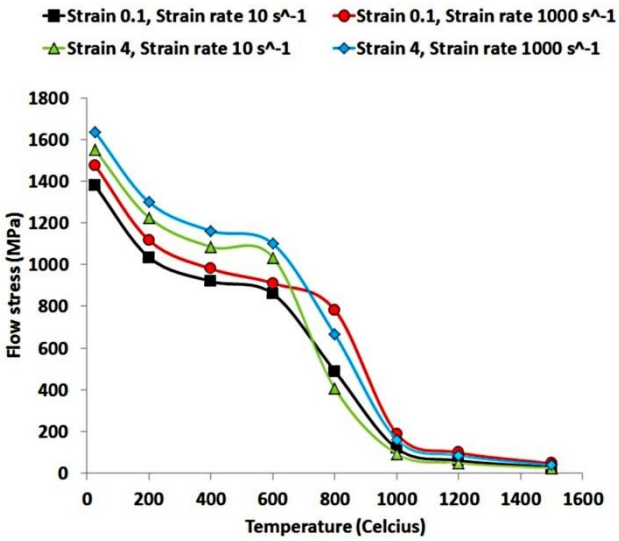

Figure 2.23: Flow stress vs. temperature at different strains and strain rates[7].

Once the alloy experiences the beta-transus temperature the material becomes very viscous and much less sensitive to the temperature[106,134], as shown in Figure 2.23. Therefore there is little change in the flow stress from 1000 °C up to the melting temperature.

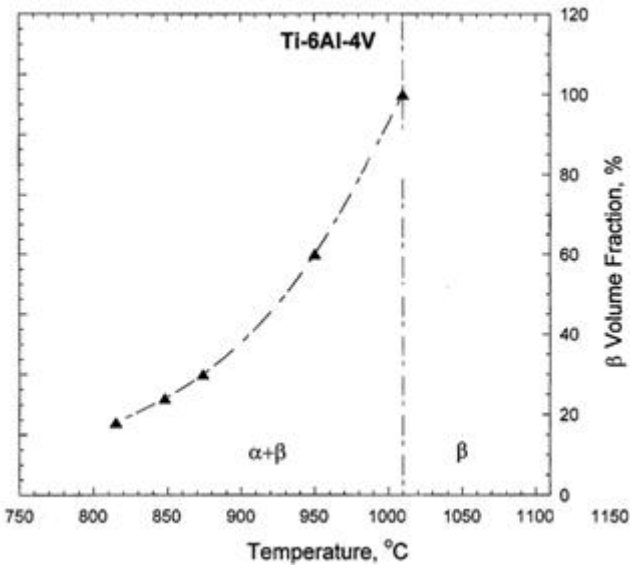

Figure 2.24: Variation of Ti-6Al-4V beta volume fraction with increasing temperature[128].

Although the temperature has the biggest effect on the Ti-6Al-4V flow stress behaviour, the strain and strain rate also have an influence, as shown in Figure

2.23. At lower temperatures an increase in the strain results in an increase of the flow stress. This is due to the low temperatures not allowing dynamic recovery and recrystallisation, allowing an increase in dislocation density as the strain is increased[132], i.e. strain hardening occurs. At higher temperatures, for a comparable strain rate, an increase of the strain causes more recovery and dynamic recrystallization (DRX)[140,141], which results in material softening causing the required flow stress to reduce, as shown in Figure 2.23.

For a comparable strain and temperature, an increase of the strain rate results in an increase of the required flow stress. At lower temperatures this is due to a faster rate of dislocation generation[105], i.e. increased rate of strain hardening. At higher temperatures DRX increases with the strain rate for titanium alloys[132,140]. The average size of the recrystallised grains decrease as the strain rate is increased[128,131,141–143]. Smaller grains require a greater stress to cause flow[86,92,128,131,138]. In addition, the strain rate sensitivity is reduced at higher temperatures, as shown in Figure 2.23.

2.5.4 Thermal Properties

Heat transfer plays an important role in welding. Heat is transferred via conduction, convection and radiation[6,7,35,40,116], with conduction being the primary transfer mechanism[144]. The purpose of this section is to detail the Ti-6Al-4V properties that affect the heat transfer.

The specific heat capacity, C_p, is the amount of thermal energy required to raise the temperature of a unit of material. Several sources for the Ti-6Al-4V heat capacity are shown in Figure 2.25(a). There is a noticeable difference between the sources for values above 900 K. As suggested by Boivineau et al.[129], this is due to the accuracy of the values being highly dependent on the method of measurement.

The thermal conductivity, *k*, is the ability of a material to transfer heat from one part of the material to another. Titanium alloys have a relatively low thermal conductivity when compared to other metals[2,92,94]. Figure 2.25(b) shows a

comparison of Ti-6Al-4V thermal conductivity values between several data sources. In general, the values are in broad agreement and show that the thermal conductivity increases with the temperature.

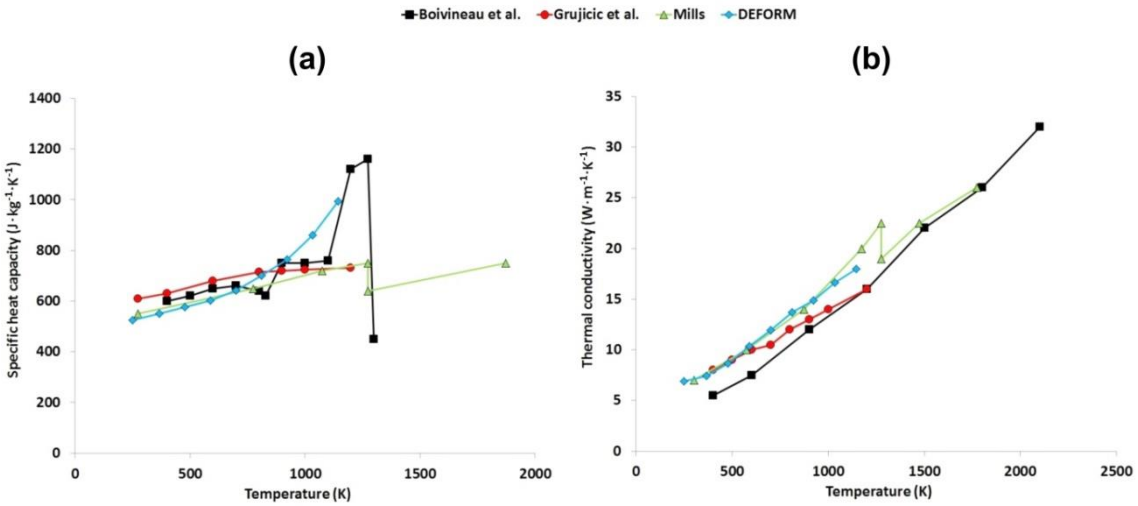

Figure 2.25: A comparison of Ti-6Al-4V thermal property data from different sources (Boivineau et al.[129], Grujicic et al.[45], Mills[145], and DEFORM's standard library) for: (a) heat capacity and (b) thermal conductivity.

In heat transfer analysis it is also important to consider the thermal diffusivity, α, which measures the relative ability of a material to conduct and store thermal energy. The thermal diffusivity is expressed as follows:

$$\alpha = \frac{k}{\rho \cdot C_p} \qquad 2.8$$

Where k is the thermal conductivity, ρ is the material density, and C_p is the specific heat capacity.

The emissivity is the relative ability of a material's surface to emit energy by radiation. The emissivity of Ti-6Al-4V, as investigated by Yang et al.[146], is displayed in Figure 2.26. The emissivity increases with temperature. Research by Boivineau et al.[129] suggests that the emissivity rapidly decreases once the liquid state is reached and maintains a constant value of about 0.4.

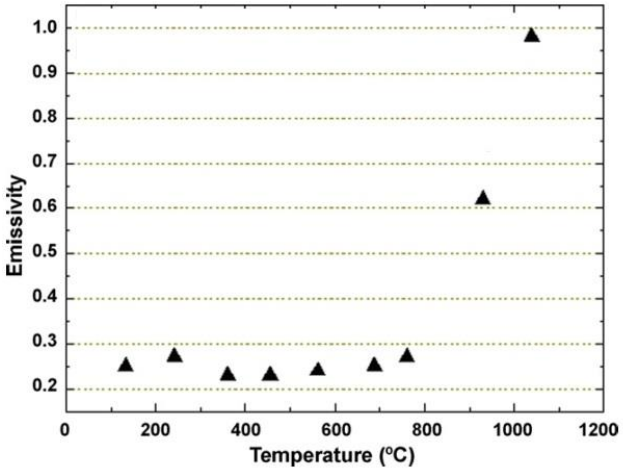

Figure 2.26: Emissivity vs. temperature for Ti-6Al-4V[146].

2.6 Modelling

In practice, many aspects of the LFW process are difficult to measure experimentally, particularly the phenomena associated with the weld interface, such as the temperature and deformation history. This is primarily due to the rapid nature of the process and the fact that the interface of the workpieces cannot be observed during welding. Computational modelling offers a pragmatic way to investigate the weld cycle history, allowing for an insight into the rapidly evolving process[7,24,27,70]. Weld modelling may be divided into two categories: analytical and numerical.

2.6.1 Analytical

Analytical models use equations to predict the outputs from the process[147]. The models often involve many simplifications, such as constant material properties[7,22,69] and one-dimensional heat flow[22], however a good match with experimental results can still be attained[7,22,69,147]. From a practical point of view, analytical modelling of heat flow has the advantage of being easier to setup[148] and can have quicker computational times than numerical models[147].

The literature on LFW analytical models is relatively sparse, when compared to experimental and numerical investigations, and is primarily concerned with the

heat flow and temperature distribution[7,22,69,73,112,149–151]. Some of the primary findings are reported below.

LFW Process Phase 1 Thermal Modelling

Vairis and Frost[22] were the first researchers to analytically model the LFW process. They developed a thermal model to predict the heating of Ti-6Al-4V workpieces during phase 1 of the process. Vairis and Frost[22] assumed the following:

- the heat flow was one dimensional.
- there was no heat loss to the surrounding environment.
- the co-efficient of friction linearly increased with the time from 0.25 to 0.55.
- the true area of contact increased linearly with time from 0% to 100%.
- the model was static, i.e. there was no transverse movement of the workpieces.

The thermal model was based on the "*heat flux being applied to a solid bounded by two parallel planes*" approach described by Carslaw and Jaeger[152]. One of the parallel planes was assumed to be the rubbing interface. This allowed for the temperature at any distance from the interface as a function of time to be determined.

The model was investigated with linear (constant) and non-linear (changed with temperature) material properties. The results were compared to thermocouple recordings. As can be seen in Figure 2.27, the modelled temperature rise deviates significantly from the experiment values after two seconds for the conditions that used constant material properties. The model that used non-linear material properties provided a better prediction of the experimental temperature.

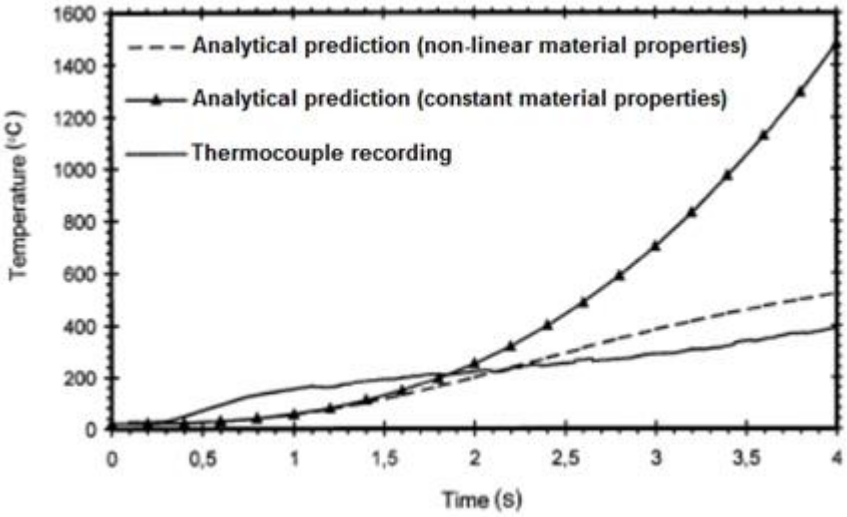

Figure 2.27: Comparison between the analytical models and experimental thermocouple data at 1.6 mm back from the interface during phase 1[22].

Similar to Vairis and Frost[22], Li et al.[73] used a one-dimensional transient heat flow equation to investigate the heating of Ti-5Al-2Sn-2Zr-4Mo-4Cr workpieces during phase 1 of the LFW process. This allowed the temperature, T, at a distance from the interface, x, as a function of time, t, to be determined. The equation was as follows:

$$T = T_0 + \frac{2\mathrm{q}'\sqrt{\frac{\alpha t}{\pi}}}{k}\exp\left(-\frac{x^2}{4\alpha t}\right) - \frac{\mathrm{q}'\mathrm{x}}{k}\left(1 - erf\left(\frac{x}{2\sqrt{\alpha t}}\right)\right) \qquad \textbf{2.9}$$

Where T_0 is the initial temperature of the material, q' is the power density, α is the thermal diffusivity, k is the thermal conductivity, and the term $erf\left(\frac{x}{2\sqrt{at}}\right)$ is the error function.

Using equation 2.9, with the assumption that there was no heat loss to the environment, Li et al.[73] demonstrated that the weld interface rapidly heats from room temperature to 1000 °C in approximately 0.3 seconds.

Although suitable for modelling the thermal fields during phase 1 of the LFW process, the above analytical models do not take into account the burn-off, which helps to cool the weld interface. The burn-off during phase 3 allows for a

steady-state condition to be achieved, i.e. the heat expelled during the burn-off approximately equals the heat generated from the viscous plastic deformation. Consequently, without the inclusion of the burn-off, the temperature throughout the analytically modelled workpieces keeps rising and never reaches a steady-state condition.

LFW Process Phase 3 (Steady-State) Thermal Modelling

Turner et al.[7] proposed a one-dimensional heat flow model for estimating the thermal profiles during the phase 3 of the LFW process:

$$T = T_0 + [T_{flash} - T_0] \cdot \exp\{-\frac{v_{ss} \cdot \mathrm{x}}{\alpha}\} \quad \textbf{2.10}$$

Where T is the temperature at any point, x, back from the interface; T_0, is the initial temperature of the material; T_{flash} is the temperature of the flash/interface region; v_{ss} is the steady-state burn-off rate; and α is the thermal diffusivity (which was assumed to be temperature independent). Prior knowledge of the steady-state burn-off rate,v_{ss}, and the interface temperature, T_{flash}, are required for the analysis, meaning the model has to be used retrospectively.

Turner et al.[7] compared the thermal profiles generated from their analytical model to those from numerical models. In general, good comparisons were made for Ti-6Al-4V welds.

Schroeder et al.[69] manipulated equation 2.10 to estimate the thickness of the heat affected zone during phase 3 of the process for Ti-6Al-4V workpieces. The equation was as follows:

$$x_{HAZ} = \alpha \cdot log\,[(T_{flash} - T_0)/(T_{HAZ} - T_0)] \cdot A_s \cdot \rho \cdot H \cdot (T_{flash}) \cdot q^{-1} \quad \textbf{2.11}$$

Where x_{HAZ} is the thickness of the HAZ, α is the diffusivity, T_{flash} is the temperature of the flash, T_0 is initial temperature of the material, T_{HAZ} is the temperature of the HAZ furthest away from the interface (assumed to be 900 $^{\circ}$C), A_s is the area of the mating surfaces, ρ is the density, H is the specific

enthalpy, and q is the power input. With the exception of the power input, all of the parameters were assumed to be constant.

For power inputs greater than 5 kW the model predicted the HAZ thickness well, as confirmed by experimental values, see in Figure 2.28

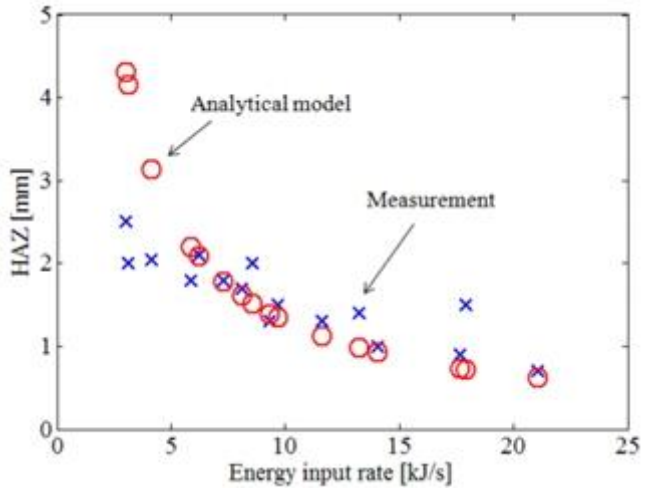

Figure 2.28: A comparison between analytical modelled and experimental heat affected zones[69].

2.6.2 Numerical

Analytical models often employ many simplifications, such as constant material properties[7,22,69] and one-dimensional heat flow[22]. This limits their ability to provide accurate information in complex process situations[10,35]. Therefore, for welding simulations, computational numerical modelling is often employed to discretise a problem into more manageable sub-problems. The solutions to these problems are then approximated at finite time steps[82,147,153].

Finite Element Analysis (FEA)

To the author's best knowledge, excluding one atomic scale investigation using molecular dynamics (MD)[154], all computational numerical investigations into the LFW process used finite element analysis (FEA)[7,21–24,40,45,69,70,74,78,84,87,95,101,110–112,121,155–159], which is also referred to as the finite element method/modelling (FEM).

FEA is a numerical technique used to find approximate solutions to boundary value problems for differential equations. According to Kobayashi et al.[160], FEA discretises (meshes) a continuum domain of a function into a series of more easily manageable sub-domains, i.e. finite elements. An element represents a portion of material in the domain and the intersecting lines between the elements, which are called nodes, represent a discrete point in space. The values of the function and its derivatives, when appropriate, are specified at the nodal points. The function is numerically approximated within each element by continuous functions that are individually described by the nodal point values associated with the element of interest[160]. The finite elements connected together on their boundaries are then assembled together to represent the entire domain. The path to a solution using FEA can be broken down into five steps[160]:

1. Identify the problem, i.e. the domain and boundary conditions.
2. Discretise the domain into finite elements.
3. Setup the individual element stiffness equations.
4. Assemble the individual element stiffness equations into a global stiffness matrix.
5. Approximate the solutions using numerical analysis techniques.

Several FEA packages have been used to model the LFW process, such as Abaqus[21,24,45,74,87,155–157], Elfen[22], Ansys[24,45,87,95,156–158], Forge[7,70] and DEFORM[40,69,78,159]. DEFORM is increasingly being used for the simulation of friction welding based processes[33,35,40,53,54,57,69,78,159,161,162] due to the software having greater capabilities than other codes with respect to metallurgical manufacturing processes[163]. For example, the software is better at handling large deformations, strain rates and re-meshing.

Reference Frames and Meshing

The term used to discretise a domain into finite elements is known as meshing. There are two basic variants of reference frames that can be used when meshing a domain: Eulerian and Lagrangian[153].

The Eulerian approach works on the principle that the flow properties are written as functions of space and time. The flow behaviour is determined by analysing the functions. The Lagrangian approach works on the principle that the pieces of the flow are “tagged”. The flow properties are determined by tracking the “tagged” points as they move in time. To put this in context – consider the flow of water in a river. The Eulerian approach would be to attach a thermometer to a fixed point on the river bank with the thermometer dipped into the water. This allows the temperature at the specific point in the river to be recorded as a function of time. The Lagrangian approach would be to throw a thermometer into the river so that the temperature at the “tagged” point can be recorded as it moves in time. In a finite element analysis model the thermometer would be represented by a node.

The “Arbitrary Lagrangian Eulerian” (ALE) approach was developed for solving problems that could not be suitably described by the Eulerian or Lagrangian approach[147]. The ALE approach, as the name suggests, is a hybrid of the two previously discussed methods. The ALE approach allows a mesh to function in the traditional Lagrangian fashion until the mesh becomes too highly distorted. During a re-mesh the most distorted regions of the mesh are then repositioned to a pre-defined Eulerian mesh density. The ALE approach appears to be the dominant method used when finite element modelling the LFW process[24,45,84,121,156,157].

Commonly used mesh element shapes in 3D FEA are tetrahedrons (triangles in 2D) or hexahedrons (quadrilaterals in 2D)[45,54,82,153,161,164], see Figure 2.29. Hexahedrons/quadrilaterals tend to improve the accuracy[165,166] and solution times[166] of the results. Tetrahedrons, however, can be more convenient to use for 3D analysis. This is due to the tetrahedral re-meshing being highly

automated, whereas 3D hexahedral meshing typically requires user intervention and is labour intensive[148,166].

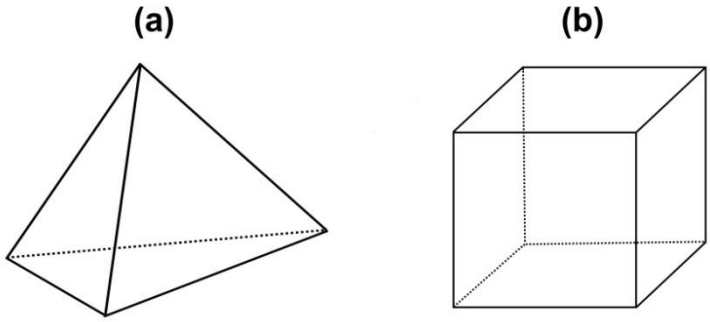

Figure 2.29: Mesh element types: (a) tetrahedron and (b) hexahedron.

The meshing of a model should be tailored to the outputs of interest. For example, a model that is required to predict plastic deformation will require a finer mesh than a purely thermal analysis[82]. A decrease of the average mesh element size increases the accuracy of the results but results in more elements being required, increasing the computational time[7].

As the plastic deformation primarily occurs at the interface during LFW, many authors use a mesh that is finer at the interface and coarser farther back[7,22–24,70,87,121,157,158]. Typical interface mesh element lengths used for LFW process models are between 1 mm and 0.08 mm[7,22–24,70,87,111,121,155–158]. 2D modelling values tend to be closer to the latter end of the scale, with values below 0.25 mm being optimal for capturing the flash morphology[7,69,82]. 3D LFW process models require substantially more time than 2D models to complete a simulation due to the increased element count, and terms included in the heat and mass flow equations. Consequently, authors often trade some of the accuracy of the results to decrease the simulation time. This is achieved by using larger elements at the interface region (0.5 mm – 1 mm)[111,121,155,156]. This approach is also used in other 3D friction based process models. For example, when using DEFORM to 3D model the friction stir[53,54,161] and friction stir spot[57] welding processes the plastic deformation zone was meshed with elements of between 0.8 mm and 0.5 mm in length – values considerable larger than 0.25 mm.

LFW Modelling Approaches

Various authors have developed two[7,21,22,24,40,69,70,82,87,110,112,156,157] and three[23,45,78,84,101,111,121,155,156,158,159] dimensional (2D/3D) computational LFW process models. Although 2D models are unable to replicate the flash in the direction perpendicular to the direction of oscillation they still give a good insight to the process without requiring long computational times.

According to the reviewed literature, there are three basic approaches that may be taken when finite element modelling the LFW process[7,21–24,34,40,45,69,70,78,84,87,101,110–112,121,155–159]. The first approach[23,40,45,78,84,87,101,112,158] involves modelling the two workpieces as individual objects, as shown in Figure 2.30(a). This allows the entire process to be modelled. However, the problem with this approach is that the coefficients of friction need to be known so that the thermal aspects of the model during phase 1 can be predicted accurately. Also, models of this type show that the two workpieces never truly merge during phases 2 and 3 – as happens in reality for many materials[2,6,66] – meaning it is impossible to model the flow behaviour after the workpieces merge (see Figure 2.1(b)).

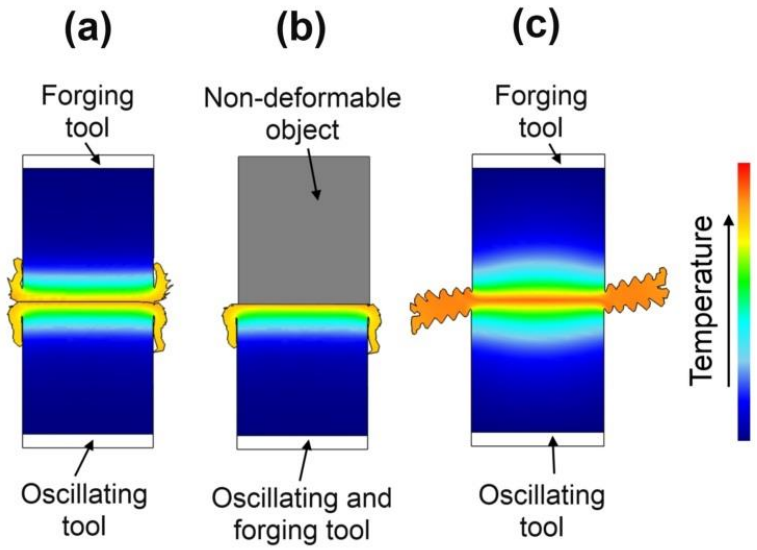

Figure 2.30: Modelling approaches: (a) two workpieces (b) one workpiece and (c) a single-body representing two workpieces.

The second approach[21,22,24,110,121,155–157,159] is to model only one workpiece, which is oscillated against a non-deformable surface, as shown in Figure 2.30(b). This approach allows for quicker computational times as only half of the geometry is modelled. Many of the problems with this approach are the same as the first. The third approach[7,34,69,70,111], as shown in Figure 2.30(c), was developed by Turner et al.[7], who noticed that prior to the workpieces merging there is negligible macroscopic plastic deformation, at least for the titanium alloy Ti-6Al-4V. Once merged the process may be modelled as a single-body due to there being full contact between the workpieces. A temperature profile needs to be mapped onto the single-body model to account for the heat generated prior to merging of the workpieces. This is vital, as the temperature profile will result in a low flow-strength for the material at the centre, which enables it to deform in preference to the surrounding material, allowing the single-body to represent two individual workpieces. Due to the merging of the interface material being modelled, this approach considers the true interface flow behaviour and produces much better replications of the flash morphology for Ti-6Al-4V workpieces[7,34,69]. The limitation of this approach is that the stages prior to workpiece merging are not modelled.

Regardless of the modelling approach used, various data are required to account for the heating of the workpieces during phase 1. For example, accurate knowledge of the coefficient of friction and/or shear force data must be known. As stated by Bhamji et al.[8] there is very little data of this sort publically available.

If modelling approach 3 is to be used, a thermal profile is required to account for the heating during phase 1. Turner et al.[7] showed that regardless of the assumed thermal profile, a steady-state condition is achieved within a few cycles of oscillation, i.e., phase 3 of the LFW process has occurred. The problem with this approach, however, is that the thermal history of the model prior to the process entering phase 3 is not necessarily being modelled correctly. Turner et al.[7] also assumed the thermal profile to be one-dimensional across the workpieces in the direction of oscillation. This is in contrast to many

other authors who, for a range of materials and conditions, have shown the thermal profiles prior to phase 3 to be cooler at the edges and hotter in the centre[22,24,40,45,69], or cooler at the centre and hotter at the edges[69,110,112].

In addition to the geometry setup, the user has the ability to decide on the type of analysis the model will provide: purely thermal, elasto-plastic or plastic. The thermal analysis neglects the elastic and plastic effects, and requires very little computational time. The elasto-plastic analysis allows for the inclusion of the elastic and plastic effects, therefore providing greater accuracy and insight, however considerable computational time is added. Purely plastic models neglect the elastic effects and assume incompressible flow, which is generally considered to be a "reasonable" assumption when significant plastic deformation occurs[147]. Consequently, plastic models require less computational time than the elasto-plastic analysis. Turner et al.[7,70] demonstrated that a purely plastic analysis during the oscillatory phases of the LFW process is sufficient to accurately capture the experimental trends. However, the elasto-plastic analysis must be used during the post-oscillatory motion cool down period if the residual stress formation is to be modelled[70].

Coupled Analysis and Process Efficiency

Welding simulations generally comprise a thermal analysis and a mechanical analysis. These can be run simultaneously (coupled) or independently (decoupled). A decoupled analysis works on the principle that the thermal analysis is run first and is used to form the basis of the subsequent mechanical analysis, i.e. no heat is generated during the mechanical analysis. The analysis must be coupled if the mechanical aspects are going to have an impact on the thermal fields. Due to a substantial amount of heat being generated via plastic deformation of the interface material during LFW, LFW process models must use the coupled analysis[82].

During friction welding simulations, the amount of mechanical energy estimated to be converted to heat when plastically deforming a material varies. Typical values used are: 90%[23,24,35,54], 95%[34,45,57,84] and 100%[7]. The remainder of the

energy is assumed to be associated with the phase transformations, changes in the grain boundary generation and migration, dislocation density and evolution, and stored in the form of crystalline defects[54,84]. The DEFORM user's manual suggests using 90% for all simulations[167].

Constitutive Data

Two different approaches have been used to account for the material constitutive data. This includes using a tabular format[7,22,23,70] (flow stress values at different strains, strain rates and temperatures, as shown in section 2.5.3) or equation based models[7,24,45,87,157], such as the Johnson-Cook model (see equation 2.7). According to Turner et al.[82], each approach has its own advantages. For example, the tabular approach generally appears to be much more robust and reliable - assuming the FEA code does not have to extrapolate too much outside the region where the data is available. However, this approach is less computationally efficient. In the author's opinion, extra care should be taken when using equation based models as they do not always accurately represent the true flow stress behaviour over the regime of interest, as shown in Figure 2.22. In addition, some of the models exclude or give poor representation of the fundamental behaviour. For example, the Johnson-Cook model gives poor flow stress estimates at low strain rates and the flow strength linearly reduces to zero with temperature, which rarely occurs in practice; and the Zener-Hollomon model excludes the strain effects[147].

Modelling Outputs

LFW process models have been used to obtain data on various weld responses, such as: residual stress formation[70,87], interface contaminant expulsion[7], strain rates[7], flash morphology[7,69], flash formation rates[7,23,24,40,69], thermal fields[7,22–24,40,45,69,70,78,157–159] and microstructural evolution[84]. The primary advantage of FEA is that it allows for the prediction of many outputs that are difficult to obtain experimentally. The following paragraphs discuss some of the key FEA findings in the literature.

Many authors have shown that the highest temperatures experienced during LFW are located at the weld interface and in the flash[7,22–24,40,45,69,78], as shown in Figure 2.31. The influence of the pressure on the peak interface temperature experienced during welding appears to be inconclusive. For example, Turner et al.[7,70] showed that the interface temperature decreased as the pressure was increased for Ti-6Al-4V workpieces, which is in good agreement with experimental observations for titanium alloys[61,80]. This is in contrast to Wu[158], who for a Ti-17 weld, showed that the interface temperature increased with the pressure. Fratini et al.[78] also noticed a temperature increase with pressure for ASTM A285 steel workpieces. Li et al.[121] for mild steel workpieces, showed that the pressure had a negligible effect on the interface temperature.

The influence of the frequency and amplitude of oscillation on the interface temperature is also unclear. Both Turner et al.[7] and Fratini et al.[78] have shown that an increase of these values can increase the interface temperature. Other researchers, however, showed that a change in the amplitude or frequency of oscillation has a minimal effect on the interface temperature[24,121].

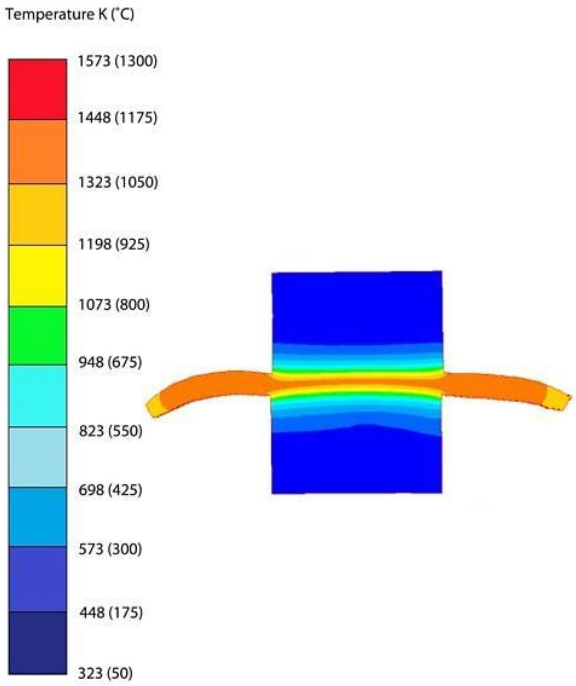

Figure 2.31: Temperature distribution in a 2D Ti-6Al-4V weld during phase 3[7].

Sorina-Müller et al.[23] compared the interface temperatures between a “prismatic” and a “blade-like” geometry for a titanium alloy – the larger prismatic geometry had a higher peak temperature. The reasons for this phenomenon were not discussed.

Ultimately, it is likely that the thermal fields during processing are dependent on the combination of process inputs, material and workpiece dimensions used. As stated by Bhamji et al.[8], more work is needed to identify the effects of the different processing conditions on the thermal fields, particularly as they are likely to influence the residual stress formation (see section 2.4.7.).

Li et al.[157], using a mild carbon steel; and Zhao et al.[110], using dissimilar titanium alloy workpieces demonstrated that once the weld cycle is complete, the heat stored in the flash can reflux back into the weld during when it cools. The reflux resulted in the edges of the weld and the flash cooling at a slower rate than the weld centre, see Figure 2.32. This phenomenon was noted to have an effect on the microstructure formation across the weld[157].

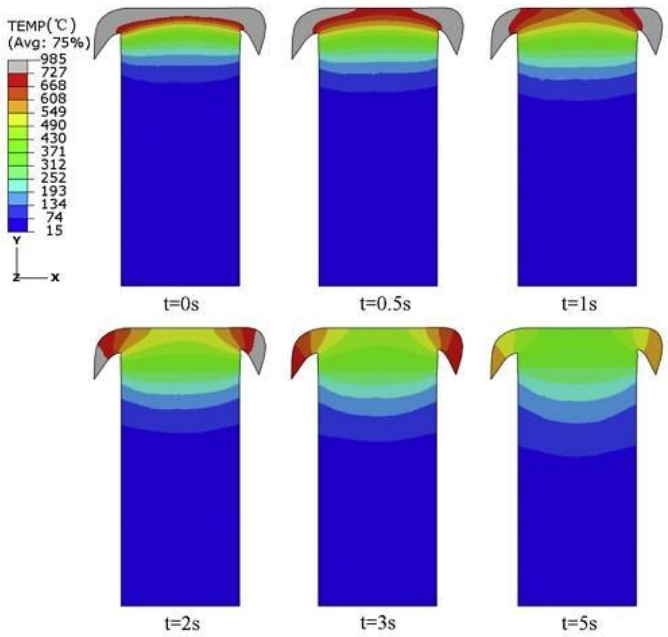

Figure 2.32: Temperature contours of a steel weld at different times during cooling. Note that t = 0 represents the beginning of the cooling phase[157].

Characterisation of the process inputs on the strain rate during LFW is of scientific importance[118]. This is because accurate knowledge of the strain rate aids in understanding of the interface grain size[118], which in itself can be used to predict mechanical properties[86,118].

Turner et al.[7,82] used models to show the dependence of the strain rate on the amplitude of oscillation for a titanium alloy, values between 500 s^{-1} and 2500 s^{-1} where reported. These values are in good agreement to those reported by Chamanfar et al.[118] (1520 s^{-1}) for nickel-based superalloys. The values reported by Turner et al.[7,82] and Chamanfar et al.[118] are much higher than the values reported by Jing et al.[115] (70 s^{-1}) and Vairis and Frost[3] (4.6 s^{-1}) for titanium alloys. Therefore, there is a level of uncertainty regarding the strain rates achieved during LFW[118].

Many authors have used FEA to investigate the burn-off rate (steady-state flash formation rate during phase 3). There is a general agreement that it increases with the frequency, amplitude or applied force[7,24,69,84,121].

Turner et al.[7] used a model to show the evolution of the interface nodal points from the weld line into the flash, as shown in Figure 2.33. They proposed that this approach could be used to investigate interface contaminant removal. Interestingly, they did not investigate the effects of the process inputs or workpiece geometry on the interface contaminant removal themselves. Based on section 2.4.5, it is likely that the burn-off required to remove the interface contaminants from the weld line into the flash is dependent on the processing conditions used.

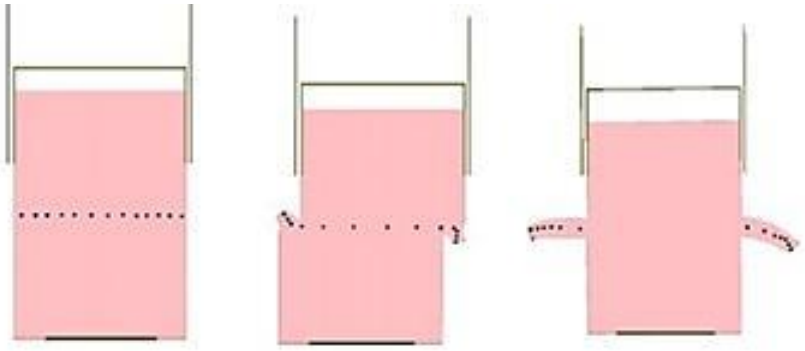

Figure 2.33: Selected nodes used to investigate the removal of interface contaminants from the weld interface into the flash[7].

Li et al.[111] noticed that experimental workpieces do not always oscillate parallel to each other, they can experience a “micro-swinging” phenomenon, as shown in Figure 2.34. This phenomenon is due to the workpieces moving in the chuck or movement of the chuck itself. A model was produced to investigate this effect for Ti-6Al-4V welds. The models showed that the burn-off rate increased with larger angles of micro-swing, which was due to one workpiece digging further into the other and extruding more material per cycle. According to Li et al.[111], the different micro-swinging angles had negligible effect on the interface temperature at the centre of the weld.

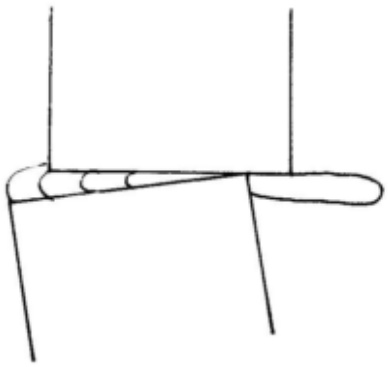

Figure 2.34: An illustration of the micro-swing effect[111].

Finally, recent work by Grujicic et al.[84] used FEA to investigate the microstructural evolution of a Carpenter Custom 465 precipitation-hardened martensitic stainless steel during LFW. The FEA was used to predict the spatial distribution and the mean radius of the grains at the interface region, as shown

in Figure 2.35(e). The models were in good agreement with the experimental findings in showing that the average grain size is largest at the centre of the weld interface.

2.6.3 Validation

A model's accuracy is highly dependent on the material properties, boundary conditions and assumptions used. The most important fact to remember is that a model is just an approximation of a real-life engineering problem. Agreeing with Reilly[147] and Turner et al.[7], models must be critically compared to experiments to test their validity. Successful validation for a range of outputs allows for the data predicted by the models that are non-amenable to experimental measurement to be trusted. In addition, without validation the results may be unreliable to form a basis for further investigation. To date, the following experimental responses have been used to validate LFW process models: burn-off histories[7,23,40,69,78,87,155,157], flash morphologies[7,69], thermal histories (using thermocouples)[7,22,69,157], residual stresses[70,87], shear forces[22], and the average microstructural grain radius and spatial distribution as shown in Figure 2.35. Figure 2.35 also shows that LFW process models frequently capture experimental trends, confirming that modelling does provide an insight into the process.

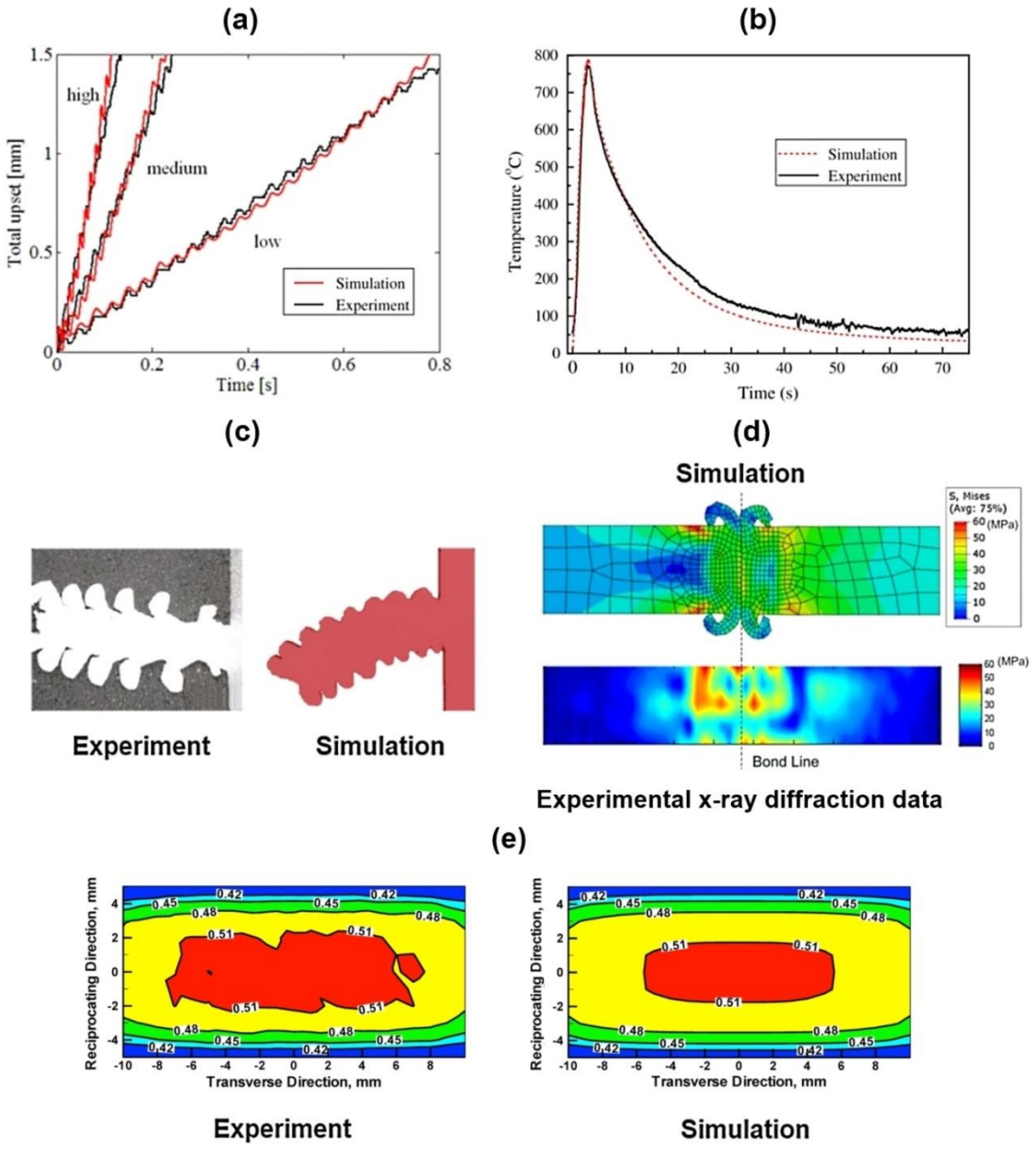

Figure 2.35: Modelling validation displaying: (a) burn-off histories for Ti-6Al-4V workpieces for high, medium and low energy inputs[69]; (b) thermal histories for a steel weld[157]; (c) flash morphology for a Ti-6Al-4V weld[7]; (d) residual stresses in an aluminium alloy weld[87]; and (e) the spatial distribution of the precipitate mean radius (in microns) over the mid-plane/contact surface of the LFW joint in Carpenter Custom 465, H1000[84].

2.7 Summary and Conclusions

2.7.1 Summary

A review of the published literature on linear friction welding, the titanium alloy Ti-6Al-4V, heat transfer and various modelling techniques was conducted. The key findings from the review are summarised below:

- Friction welding processes utilise the heat generated during friction to produce solid-state bonds. Several friction welding techniques have been developed, such as rotary, orbital, friction stir, friction stir spot and linear friction welding. When compared to other friction welding processes, where there are numerous publications, relatively little investigation has taken place into the LFW process. Although, there have been an increasing amount of LFW publications in the last four years.

- The LFW process works by oscillating one workpiece relative to another whilst under a large applied force. Although one continuous process, LFW occurs over four phases: initial, transition, equilibrium, and deceleration and forging. The process is controlled by eight inputs, but the oscillation amplitude, oscillation frequency, applied force and burn-off are believed to be the most influential.

- There is a desire from industry to reduce the material and costs associated with the manufacture of components. LFW provides a solution to this requirement by joining smaller workpieces to produce a preform.

- Much of the research into the LFW process is for single-surface-contacting workpieces. There is an interest from industry to investigate the LFW process on multi-surface contacting workpieces, such as the keystone geometry.

- LFW has experienced limited industrial implementation outside of blisk manufacture. One of the reasons for this is due to a lack of fundamental scientific understanding of LFW.

- Linear friction welds are similar in appearance to each other in that they have several distinct zones – a weld centre zone (WCZ), a thermo-mechanically affected zone (TMAZ), a heat affected zone (HAZ) and the parent material – and are surrounded by the expelled interface material (flash). For many materials the tensile, microhardness and impact properties are superior in the WCZ when compared to the other zones.

- The primary reason for a linear friction weld being defective is due to the inclusions of contaminants, such as oxides, in the WCZ. Contaminant removal appears to be critically dependent on the combination of process inputs used. The workpiece geometry may also have an effect on contaminant removal; however this hypothesis has not been tested.

- There has been little investigation into the effects of the process inputs on the power input and subsequent energy use. Many of the existing methods for calculating the power input make significant assumptions, like assuming the co-efficient of friction and the rubbing velocity are constant. A better way of assessing the power input and energy usage involves using the force and displacement history data from a LFW machine.

- Linear friction welds contain significant residual stresses. Turner et al.[70] showed they are primarily formed during the post-oscillatory motion cooling. The residual stresses can be reduced by appropriate selection of process inputs and post-weld heat treatments.

- Although LFW is suitable for joining a range of similar and dissimilar materials, the titanium alloy Ti-6Al-4V (particularly the bi-modal microstructure) is the material most frequently used.

- There are numerous data sources that describe the material properties of Ti-6Al-4V, including the flow stress, specific heat capacity, thermal conductivity and emissivity. These values could be used as input data for LFW process models.

- The rapid nature of the LFW process and the fact that the interface of the workpieces cannot be observed during welding means that using physical experiments alone may fail to provide adequate insight into the process fundamentals. Computational modelling offers a pragmatic method to understand what is happening throughout the rapidly evolving process, allowing for increased fundamental scientific understanding of LFW. FEA Modelling provides an insight into many responses that are difficult to obtain experimentally, e.g. the interface contaminant removal, thermal fields and material flow.

- LFW process models can be broken down into two categories: analytical and numerical. FEA is almost exclusively used for the numerical modelling of LFW. DEFORM is believed to be the software package that will yield the best results. This is because it has been specifically developed for processes where significant plastic deformation occurs and where a lot of re-meshing is required, as is the case with LFW. DEFORM uses the arbitrary lagrangian eulerian (ALE) approach.

- Experimental validation of models is important to ensure the accuracy of the results. Successful validation for a range of outputs allows the data predicted by the models that are non-amenable to experimental measurement to be trusted. Currently, there is limited publically available experimental data for a wide range of processing conditions that can be used for either modelling inputs or validation.

2.7.2 Conclusions

Linear friction welding is finding increasing industrial interest for the fabrication of Ti-6Al-4V preforms. This is primarily due to the significant cost savings that

can be achieved when compared to subtractive manufacturing techniques. Currently, a lack of fundamental scientific process understanding is preventing further industrial uptake of LFW. The “gaps” in the knowledge include:

- A clear understanding of the effects of the process inputs and workpiece geometry on the thermal fields, material flow and interface contaminant removal during the LFW of Ti-6Al-4V.
- An understanding of the mechanisms behind the material flow at the “triple point” in Ti-6Al-4V “keystone” welds.
- A lack of experimental data for a wide range of processing conditions that can be used to provide input and validation data for computational models.

Computational modelling offers a pragmatic method to address the first two “gaps”. It should be noted, however, that any model that assumes the interface contaminant evolution can be represented by a few selected interface nodes, as was the case in the work by Turner et al.[7], would have to be justified. For example, does the constitutive data of the physical contaminants affect the interface material flow behaviour? If so, does the assumption of a few selected nodes, with no differing constitutive data, really provide adequate insight into the contaminant removal? These questions were not addressed by Turner et al.[7]. However, it should be noted that contaminant removal was a minor consideration in the article[7] and the methodology appeared to be presented to provide a platform for future research. Moreover, although 2D models can provide an adequate insight into the LFW process for welds with a single-surface of contact, they cannot describe the “keystone” weld. This is due to the geometric effects of the “keystone” workpieces. As such, a 3D coupled thermo-mechanical model would be required to understand the material flow at the “triple point”.

A systematic series of experimental welds could be conducted and analysed to provide input and validation data for computational models, therefore addressing the third “gap”.

The conclusions from this review allowed for the thesis aim and objectives in section 1.3 to be identified.

Chapter 3: Analysis of Experimental Welds to Determine Input and Validation Data for Computational Models

This chapter is an edited version of the following article:

McAndrew, A. R., Colegrove, P. A., Addison, A. C., Flipo, B. C. D. & Russell, M. J. Energy and force analysis of Ti-6Al-4V linear friction welds for computational modeling input and validation data. Metallurgical and Materials Transactions A ***45****, 6118-6128 (2014).*

3.1 Introduction and Context

As shown in the previous chapter, there is a lack of publically available experimental data for a wide range of processing conditions that can be used to provide input and validation data for computational models[8]. Although several researchers have provided data, such as coefficients of friction[22,27,34] and shear stress[34], it is often limited in that it's only presented for a few conditions. Moreover, the presented data often neglect the effects of the different phases of a weld (see section 2.4.2 for phase definitions). Furthermore, the reason for the transition between phase 1 and phase 2 is unclear, it is important to understand the physics behind the phase transition as it may aid future modelling investigations[7].The research reported in this chapter addressed the above issues to provide input and validation data for the computational modelling work reported in this thesis, and to understand the reason for the transition between phase 1 to phase 2.

3.2 Methodology

3.2.1 Experimental

The experiments used workpieces with dimensions of 40 mm by 20 mm by 60 mm with oscillation taking place in the 40 mm length direction, as shown in Figure 3.1(a). See Appendix "A" for full details of the workpieces. The Ti-6Al-4V

parent material had a bimodal alpha-beta microstructure, as shown in Figure 3.1(b). Immediately prior to welding the faying surfaces of the workpieces were cleaned with acetone.

Design Expert V.7, a design of experiments (DOE) software package, was used to identify a range of experiments for a regression model. To keep the number of experiments low, the inputs that had the largest effect on the outputs were investigated[2,6]: oscillation amplitude, A; oscillation frequency, f; applied force, F_a; and the burn-off, b_o. Although the amplitude and frequency of oscillation were considered as two individual process inputs for the experimental design, it is worth pointing out that they are sometimes combined into a single input term called the average rubbing velocity, v_r, (see equation 2.2).

The experiments were completed using the FW34 LFW machine at TWI, Cambridge. The operating window for the combination of frequency, amplitude and applied force that can be used with this machine is illustrated in Figure 3.1(d). The final input, the burn-off, was adjusted between 1 mm and 3 mm because previous studies[2,6] indicated that this critically affected whether the interface contaminants, such as oxides, were removed. These input constraints were entered into the DOE software to generate a range of experimental conditions for a D-optimal regression analysis. D-optimal designs are often used when there are design input combination constraints[168,169], i.e. the experimental design region is irregular and can't be described using a factorial approach – as was the case with the FW34 LFW machine. The experimental design was specified to include enough experiments to account for a quadratic relationship between the inputs and outputs since this behaviour has been observed in the literature[1,6]. Some of the experiments were repeated to test the variance, giving 25 experimental conditions for the DOE analysis, which are listed (welds 1 – 25) in Table 3.1. For the experimental run the forging force in phase 4 remained the same as the applied force used during the earlier phases. The ramp up time, oscillation decay time and forging time were kept constant and had values of 0.1 seconds, 0.1 seconds and 10 seconds respectively. In addition to the DOE analysis, four experiments were completed using thermocouples (welds 26 –

29). To insert the k-type thermocouples several workpieces had four 1.2 mm diameter holes drilled through them perpendicularly to the oscillation direction and parallel to the direction of the applied force at the positions shown in Figure 3.1(c) (See Appendix A for full details). To position the thermocouples at distances of 0.3 mm, 1 mm, 2.5 mm and 4.5 mm from the weld interface a plug was placed into the holes at the interface end of the workpiece. The thermocouple wire was inserted through the opposite end until it made contact with the plug. The thermocouples where then fixed into position using an epoxy resin.

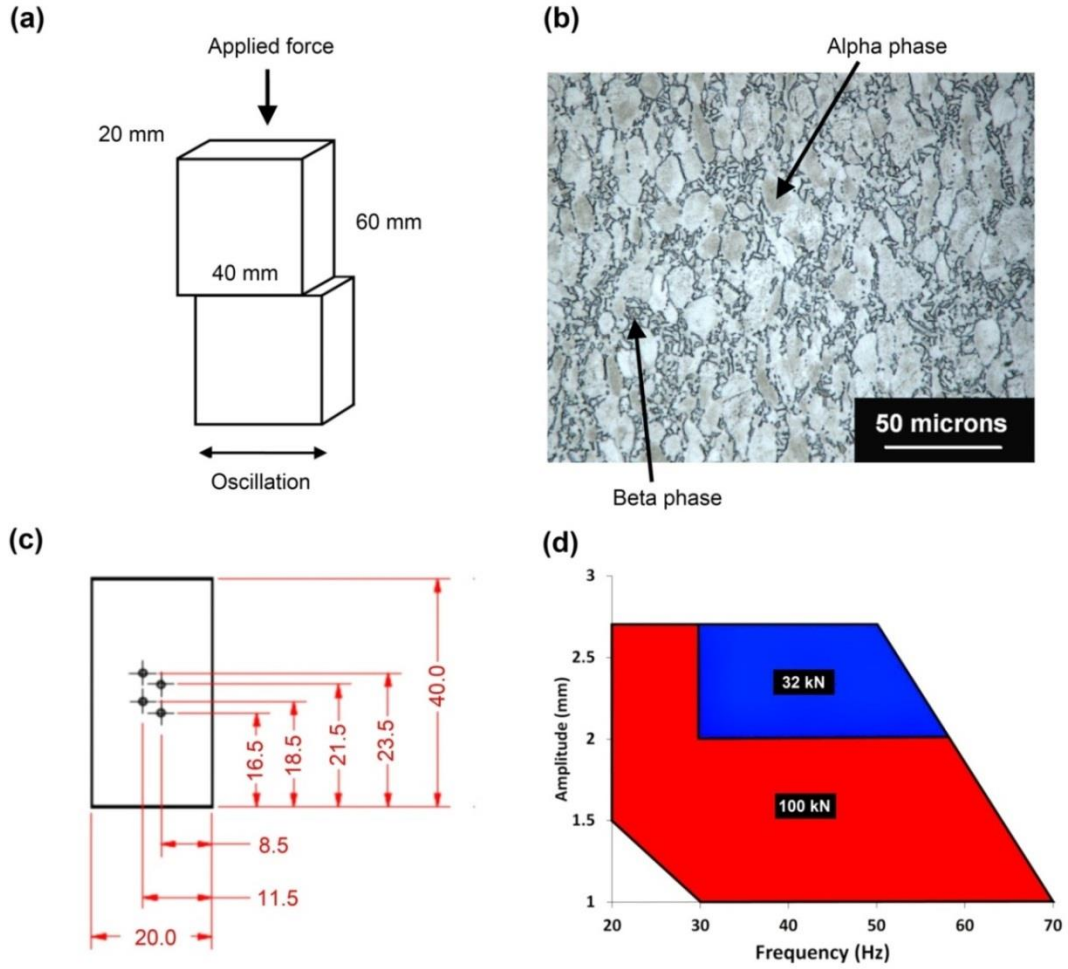

Figure 3.1: Experimental details showing: (a) workpiece dimensions and movement, (b) bimodal alpha-beta microstructure, (c) workpiece prepared for thermocouples (dimensions in millimetres), and (d) FW34 process input operating window.

Table 3.1: Experimental conditions.

Weld	*Oscillation frequency (Hz)*	*Oscillation amplitude (mm)*	*Average rubbing velocity ($mm \cdot s^{-1}$)*	*Applied force (kN)*	*Pressure (MPa)*	*Burn-off (mm)*	*Purpose*
1	*50*	*2.7*	*540*	*66*	*82.5*	*1*	*DOE*
2	*70*	*1*	*280*	*100*	*125*	*3*	*DOE*
3	*20*	*2.7*	*216*	*100*	*125*	*3*	*DOE*
4	*70*	*1*	*280*	*100*	*125*	*1*	*DOE*
5	*58.2*	*2*	*465.6*	*32*	*40*	*1*	*DOE*
6	*50*	*2.7*	*540*	*100*	*125*	*2*	*DOE*
7	*30*	*2.7*	*324*	*32*	*40*	*1*	*DOE*
8	*60*	*1.9*	*456*	*100*	*125*	*3*	*DOE*
9	*30*	*2*	*240*	*32*	*40*	*3*	*DOE*
10	*50*	*2.7*	*540*	*32*	*40*	*3*	*DOE*
11	*23.3*	*1.3*	*121.2*	*77.3*	*96.6*	*1*	*DOE*
12	*20*	*2.7*	*216*	*100*	*125*	*1*	*DOE*
13	*30*	*1*	*120*	*100*	*125*	*3*	*DOE*
14	*20*	*1.5*	*120*	*100*	*125*	*2*	*DOE*
15	*42.3*	*1.5*	*253.8*	*68.3*	*85.4*	*2*	*DOE*
16	*31.6*	*2.3*	*290.7*	*68.3*	*85.4*	*2.5*	*DOE*
17	*64.1*	*1.5*	*384.6*	*66*	*82.5*	*1*	*DOE*
18	*42.1*	*2.4*	*404.2*	*32*	*40*	*2*	*DOE*
19	*64.1*	*1.5*	*384.6*	*66*	*82.5*	*3*	*DOE*
20	*60*	*1.9*	*456*	*100*	*125*	*1*	*DOE*
21	*30*	*2*	*240*	*32*	*40*	*3*	*DOE*
22	*20*	*2.7*	*216*	*100*	*125*	*1*	*DOE*
23	*50*	*2.7*	*540*	*32*	*40*	*3*	*DOE*
24	*20*	*1.5*	*120*	*100*	*125*	*2*	*DOE*
25	*30*	*1*	*120*	*100*	*125*	*3*	*DOE*
26	*20*	*1.5*	*120*	*100*	*125*	*3*	*Thermocouple*
27	*50*	*2.7*	*540*	*100*	*125*	*3*	*Thermocouple*
28	*30*	*2*	*240*	*32*	*40*	*3*	*Thermocouple*
29	*50*	*2.7*	*540*	*32*	*40*	*3*	*Thermocouple*

Metallographic specimens were produced from the experiments (welds 1 – 25) in Table 3.1. The welds were sectioned 45 degrees to the direction of oscillation and parallel to the applied force. The sectioned samples were mounted and then ground using 240, 1200, 2500 and 4000 grit silicon carbide papers. After grinding, the sectioned samples were polished using colloidal silica on a micro-cloth and etched using a 3% hydrofluoric acid solution. The metallographic samples were viewed under a refractive microscope to determine the microstructure of the weld interface and to see if any interface contaminants could be observed.

3.2.2 Analysis of the Force and Displacement History

High-speed data acquisition systems were used to measure the oscillator position, x_1, in-plane force, F_{in}, axial position (the displacement perpendicular to the direction of oscillation) and the applied force, F_a – see schematic diagram in Figure 3.2 for definitions. The axial position was used to estimate the burn-off history.

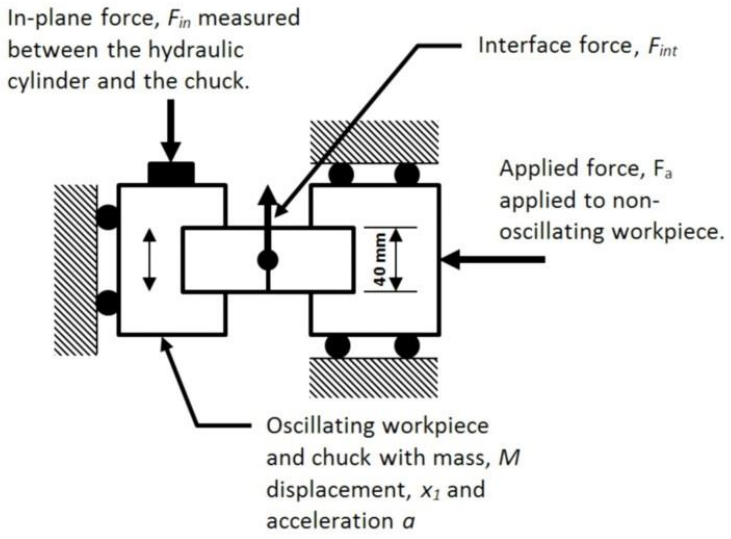

Figure 3.2: Schematic diagram showing the LFW process.

To determine the force at the interface of the two workpieces and the energy input, the data were analysed in a similar way to that described in Ofem et al.[50]. The analysis assumed that:

- The friction from the bearings on the oscillating tool was negligible.
- The movement of the samples in the tooling was negligible.

Based on the schematic diagram in Figure 3.2, the instrumentation between the oscillating chuck and hydraulic cylinder records the in-plane force, F_{in}. This does not represent the force at the weld interface, F_{int}, due to the effects of momentum acting on the workpiece and tooling. Summing the forces on the chuck in the vertical direction enables the weld interface force, F_{int}, to be determined:

$$F_{int} = F_{in} - M \cdot a \quad \textbf{3.1}$$

Where M is the mass of the chuck and workpiece (approximately 280 kg) and a is the acceleration. The force convention is shown in Figure 3.2. Note that while F_{in} is positive downwards, F_{int} is positive upwards.

The acceleration may be calculated using numerical differentiation or if sinusoidal displacement is assumed the acceleration may be calculated from:

$$a = \frac{d^2x}{dt^2} = -A \cdot \omega^2 \cdot \sin(\omega \cdot t)dt = -x_1 \cdot \omega^2 \ = -x_1 \cdot (2 \cdot \pi \cdot f)^2 \quad \textbf{3.2}$$

Where t is the time, ω is the angular frequency and $x_1$is the displacement. Equation 3.2 is less susceptible to noise[50] when compared to the numerical differentiation method. Since the motion of the workpieces in these experiments was sinusoidal, equation 3.2 was used for the analyses presented in this chapter.

The *average* interface force generated over a phase, F_{pa}, was divided by the applied force to determine the *average* dynamic friction coefficient, μ:

$$\mu = \frac{F_{pa}}{F_a} \quad \textbf{3.3}$$

The total energy inputted to the weld interface, E_x, may then be estimated by integrating the power with respect to time:

$$E_x = \int_0^{t_t} F_{int} \cdot v \, dt \quad \textbf{3.4}$$

Where t_t is the total duration of the weld and v is the velocity.

The velocity was determined using the “2 point central finite difference method” in the form of:

$$v = \frac{x_2 - x_0}{t_2 - t_0} \quad \textbf{3.5}$$

Where v is the velocity at point x_1; $x_0$is the displacement point prior to x_1; x_2 is the displacement point subsequent to x_1; and t_0 and t_2 are the times at x_0 and x_2, respectively.

To determine the *average* power input for one of the phases, the energy input for that phase was divided by the phase duration. Finally, the burn-off rate during phase 3 was determined by calculating the gradient of the line where the burn-off reached steady-state.

3.2.3 Regression Analysis

An "analysis of variance" (ANOVA) was conducted using Design Expert V.7. This identified which inputs and input interactions were statistically important for mathematically modelling the process outputs. The statistically insignificant factors were then removed from the regression models. Several statistical criteria were considered when reducing the factors. These are listed below, and the reader is referred to the cited texts for further explanation of their meanings and methods of calculation[169,170]:

- **R-Squared (R^2)**: The percentage of variation in the data explained by the regression model. Values greater than 90% are desirable.
- **Adjusted R-Squared (Adj R^2)**: As for R^2 but adjusted for the number of factors in the model. Values greater than 90% are desirable.
- **Predicted R-Squared (Prd R^2)**: A measure of the percentage of variation explained by the model for new data. The values should be within 20% of the Adj R^2 value.
- **Adequate Precision (Ad. Pr)**: This is the signal to noise ratio and compares the range of the predicted values at the design points to the average prediction error. Values greater than 4 are desirable.
- **P-Values (P-V)**: This helps the user determine which input factors are of significance. The smaller the value the better, with values equal to or

lower than 0.05 being statistically significant. The overall value for the equation describes how significant it is.

The raw data used for the statistical analysis is displayed in appendix “B”.

3.2.4 Thermal Model (Phase 1)

To understand the condition of the material at the transition between phase 1 and 2, a 2D thermal model of phase 1 was created using the DEFORM finite element analysis (FEA) software, which uses the ALE approach. Grujicic et al.[45] demonstrated that there is very little variation in the thermal profile in the through-thickness direction, allowing the process to be modelled with a 2D model oriented in the direction of oscillation. As shown in Figure 3.3, the tooling extended to within 5 mm of the interface as occurred in the experiments. Temperature dependent thermal conductivity, specific heat and emissivity data from the DEFORM software’s library were used. The convective heat transfer coefficient was assumed[7] to be 10 $W \cdot m^{-2} \cdot K^{-1}$. The conductive heat transfer coefficient with the tooling was assumed[7] to be of 10000 $W \cdot m^{-2} \cdot K^{-1}$. The temperature of the environment was assumed to be 20 $^{\circ}C$. A uniform mesh size of 0.5 mm was used across the 2D model. All models had a time step of 0.001 seconds.

A uniform heat flux (q') was applied across most of the workpiece interface which was linearly reduced to 50% of this value an amplitude (A) away from the edge as shown in Figure 3.3. The reduction at the edges was due to the sinusoidal movement of the workpieces – the point at the corner is only in contact with the other workpiece 50% of the time (See Appendix “E” for mathematical explanation). The heat flux was determined using two methods. Method 1 calculated the heat flux using the power input equation 3.4 in conjunction with the instantaneous in-contact surface area of the workpieces, i.e the energy inputted to the weld was calculated using the following equation:

$$E_x = \int_0^{t_t} \frac{F_{int} \cdot v}{\mathrm{A_s}}\, dt \qquad 3.6$$

Where t_t is the total duration of the weld, v is the velocity and $\mathrm{A_s}$ is the in-contact surface area of the workpieces.

Method 2 calculated the heat flux by dividing the *average* power input for phase 1 derived from the statistical analysis by the average in-contact area of the workpieces over a cycle of oscillation. The results were compared to thermocouple measurements.

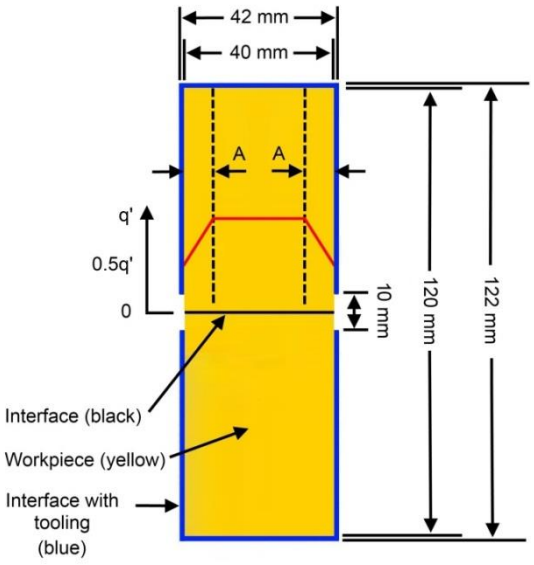

Figure 3.3: Developed 2D thermal model.

3.3 Results and Discussions

3.3.1 Weld Appearance and Microstructural Observations

Regardless of the process inputs used, the macrostructures of the Ti-6Al-4V linear friction welds were similar in appearance in the fact that they had several distinct zones – a weld centre zone (WCZ), a thermo-mechanically affected zone (TMAZ) and the parent material – and were surrounded by the expelled interface material (flash). Due to the structural stability of Ti-6Al-4V below temperatures of 800 °C [76,128] it was difficult to detect a purely heat affected

zone. These characteristics are typical of Ti-6Al-4V linear friction welds[2,6,8,45,61]. The different zones are displayed in Figure 3.4(a).

The weld centre zone, which many authors suggest experiences significant recrystallisation[6,8,45,61], was found to have either a Widmanstätten and/or Martensitic microstructure, as shown in Figure 3.4(b) and Figure 3.4(c), respectively. The weld centre zone was then followed by a thermo-mechanically affected zone (TMAZ). The material in this region had been deformed mechanically and affected by the heat from the welding process but did not appear to have undergone any significant recrystallisation due to the original grains of the parent material being present. The remainder of the workpieces consisted of the initial parent material, as previously shown in Figure 3.1(b). The welds that had only experienced a small amount of burn-off, i.e. approximately 1 mm, had contaminants along the weld interface, as shown in Figure 3.4(d).

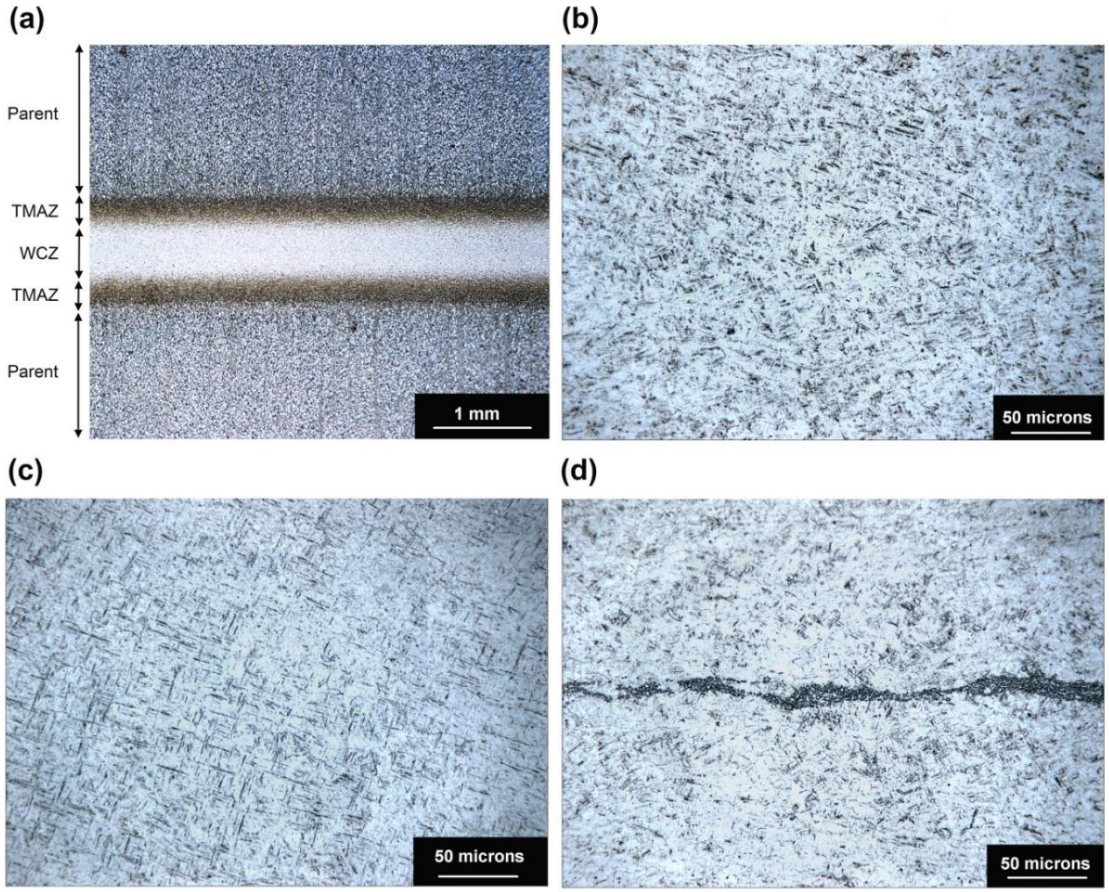

Figure 3.4: Weld microstructures: (a) generic appearance of a weld (weld 6), showing the weld centre zone (WCZ), the thermo-mechanically affected zone (TMAZ), and the parent material (Parent); (b) Widmanstätten (weld 8); (c) Martensite (weld 2); and (d) interface contaminants for a weld with a low burn-off (weld 11).

3.3.2 Force Histories

A plot of the force history for a typical weld is shown in Figure 3.5(a). Typically the in-plane force started out with a relatively low value during phase 1, before increasing to a maximum during phase 2 and then reducing a little and stabilising during phase 3. This is typical of most α+β titanium alloy linear friction welds[3,34,80]. For two of the welds the force histories were enlarged so that the force variation over a single cycle during phase 3 could be viewed, which is shown in Figure 3.5(b) for a low rubbing velocity weld and Figure 3.5(c) for a high rubbing velocity weld. The two responses are remarkably different.

Firstly the magnitude of the component caused by acceleration (*M.a*) is much greater for the high rubbing velocity weld due to the high accelerations. Secondly, the variation of the interface force over a cycle differed: for the low rubbing velocity weld the force reached a peak value shortly after the workpieces changed direction and was then relatively uniform until the workpieces changed direction again. This behaviour is similar to that reported by Ofem et al.[50] who noticed that when the workpieces were at the end of each stroke the higher pressure caused by the smaller interfacial area caused the cooler material to forge into the hotter material. This shortening then resulted in "ploughing" as the workpieces were brought back together, which generated the peak force just after the maximum amplitude. Once fully aligned the 'ploughing' ceased and the interface force decreased. The possible reasons for the slight differences between the force traces in this work and the ones observed by Ofem et al.[50] could be due to the effects of the different oscillation amplitudes, workpiece sizes and workpiece materials used. For the high rubbing velocity weld there was no initial peak – the interface force increased continuously until the workpiece changes in direction. It is unclear whether the 'ploughing' mechanism was active or not. There were fewer data points recorded over a cycle due to the higher frequency which made it more difficult to view the point to point variation. In addition, for high rubbing velocities the component of the force due to acceleration was a much larger proportion of the total force, which may have increased the error in the calculated interface force. These phenomena were independent of the applied force.

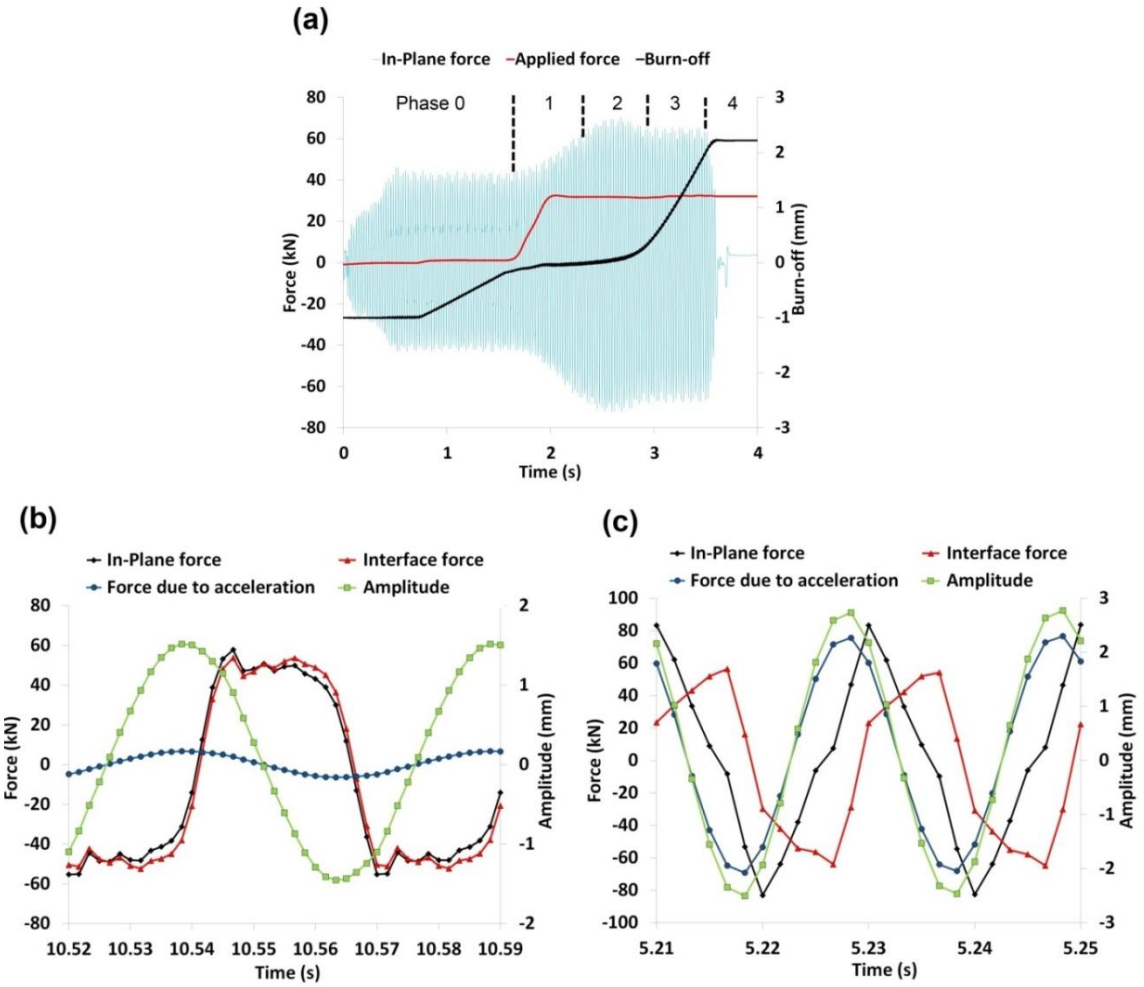

Figure 3.5: Force history displaying: (a) the phases, in-plane force, applied force and burn-off for weld 18 (Phase 0 is the time one of the workpieces was oscillated in free space prior to contact with the other); and the in-plane and interface forces as a function of time for welds produced with (b) a low rubbing velocity (120 mm/s) at 100 kN and (c) a high rubbing velocity (540 mm/s) at 100 kN.

3.3.3 Regression Analysis

The results from the statistical tests performed on the final regression models are displayed in Table 3.2. Much of the variability within the results is accounted for. The only exception was the welding time for phase 2, which was probably due to the effects of human error when calculating the short duration of this phase. The raw data obtained from the experiments which were used for the statistical analysis are displayed in appendix “B”. The relative error between the

experimental design point values and the regression models are shown in Table 3.3. Note that a positive relative error means that the experimental point value was lower than the predicted regression value. The relative error was calculated as follows:

$$Relative\ error\ (\%) = \frac{(Regression\ value - design\ point\ value) * 100}{design\ point\ value} \quad \textbf{3.7}$$

Table 3.2: Statistical tests performed on the final regression analysis models.

Process output Equation	*Equation Units*	*R^2 (%)*	*Adj. R^2 (%)*	*Prd. R^2 (%)*	*Ad. Pr.*	*P-V*
Burn-off rate	*[mm·s^{-1}]*	*93.4*	*91.7*	*88.4*	*23.4*	*<0.0001*
Welding time (Phase 1)	*[s]*	*98.0*	*97.3*	*95.8*	*32.3*	*<0.0001*
Welding time (Phase 2)	*[s]*	*73.5*	*69.8*	*63.6*	*12.6*	*<0.0001*
Welding time (Phase 3)	*[s]*	*98.9*	*98.1*	*96.6*	*41.9*	*<0.0001*
Av. power input (Phase 1)	*[kW]*	*99.8*	*99.7*	*99.5*	*102.2*	*<0.0001*
Av. power input (Phase 2)	*[kW]*	*99.6*	*99.4*	*99.0*	*70.7*	*<0.0001*
Av. power input (Phase 3)	*[kW]*	*99.6*	*99.5*	*99.2*	*89.6*	*<0.0001*
Av. interface force (Phase 1)	*[kN]*	*97.8*	*97.1*	*96.2*	*37.9*	*<0.0001*
Av. interface force (Phase 2)	*[kN]*	*88.6*	*84.9*	*77.4*	*16.3*	*<0.0001*
Av. interface force (Phase 3)	*[kN]*	*89.9*	*86.6*	*82.0*	*16.2*	*<0.0001*
Weld energy (Phases 1 – 4)	*[kJ]*	*99.1*	*98.7*	*97.8*	*51.3*	*<0.0001*

The regression models are listed below:

$$\boldsymbol{Burn-off\ rate}\ (\boldsymbol{Phase\ 3}) = 0.69581 - 0.042711 * f + 0.039751 * A - 6.79114 * 10^{-3} * F_a + 0.036051 * f * A + 4.66901 * 10^{-4} * f * F_a \quad \textbf{3.8}$$

$$\boldsymbol{Welding\ time}\ (\boldsymbol{Phase\ 1}) = 21.03498 - 0.44181 * f - 8.22664 * A - 5.58333 * 10^{-3} * F_a + 0.079203 * f * A + 2.70505 * 10^{-3} * f^2 + 0.90686 * A^2 \quad \textbf{3.9}$$

$$\boldsymbol{Welding\ time}\ (\boldsymbol{Phase\ 2}) = 1.60014 - 0.012349 * f - 0.25048 * A - 2.31191 * 10^{-3} * F_a \quad \textbf{3.10}$$

$$\boldsymbol{Welding\ time}\ (\boldsymbol{Phase\ 3}) = 2.91648 - 0.073095 * f - 1.88682 * A - 2.24770 * 10^{-3} * F_a + 1.36173 * b_o + 0.014157 * f * A - 0.010635 * f * b_o - 0.25621 * A * b_o + 5.94592 * 10^{-4} * f^2 + 0.37487 * A^2 \quad \textbf{3.11}$$

$$\boldsymbol{Average\ power\ input}\ (\boldsymbol{Phase\ 1}) = -18.26366 + 0.32678 * f + 9.27832 * A + 0.061476 * F_a + 0.087638 * f * A - 4.21790 * 10^{-4} * f * F_a - 2.33759 * 10^{-3} * f^2 - \quad \textbf{3.12}$$

$1.93524 * A^2$

$$\boldsymbol{Average\ power\ input}\ (\boldsymbol{Phase\ 2}) = -5.01193 + 0.24946 * f + 3.65772 * A - 0.084170 * F_a + 0.12852 * f * A + 0.020175 * A * F_a - 2.36684 * 10^{-3} * f^2 - 1.08098 * A^2 + 5.31310 * 10^{-4} * {F_a}^2 \quad \textbf{3.13}$$

$$\boldsymbol{Average\ power\ input}\ (\boldsymbol{Phase\ 3}) = 6.21627 - 0.083060 * f - 2.22581 * A - 0.057055 * F_a + 0.16352 * f * A + 6.46109 * 10^{-4} * f * F_a + 0.025004 * A * F_a \quad \textbf{3.14}$$

$$\boldsymbol{Average\ interface\ force}\ (\boldsymbol{Phase\ 1}) = 1.29038 + 0.35088 * f + 11.98137 * A + 0.22589 * F_a - 0.024402 * f * A - 2.88474 * 10^{-3} * f * F_a - 2.69876 * A^2 \quad \textbf{3.15}$$

$$\boldsymbol{Average\ interface\ force}\ (\boldsymbol{Phase\ 2}) = 64.54841 - 0.67552 * f - 9.63483 * A - 0.057582 * F_a + 0.14140 * f * A + 0.055478 * A * F_a + 4.88048 * 10^{-3} * f^2 \quad \textbf{3.16}$$

$$\boldsymbol{Average\ interface\ force}\ (\boldsymbol{Phase\ 3}) = 55.71070 - 0.63561 * f - 6.22698 * A - 0.016212 * F_a + 0.10859 * f * A + 0.032661 * A * F_a + 5.10434 * 10^{-3} * f^2 \quad \textbf{3.17}$$

$$\boldsymbol{Weld\ energy}\ (\boldsymbol{Phase\ 1-4}) = 87.35071 - 1.26541 * f - 29.40070 * A - 0.18032 * F_a + 3.89068 * b_o + 0.20616 * f * A + 7.43934 * 10^{-3} * f^2 + 4.09790 * A^2 + 7.58175 * 10^{-4} * {F_a}^2 \quad \textbf{3.18}$$

Where: A is the oscillation amplitude (mm), f the oscillation frequency (Hz), F_a the applied force (kN), and b_o the burn-off (mm).

Table 3.3: Relative error between the experimental design point values and the regression model values

Weld	*Eq.* **3.8** *(%)*	*Eq.* **3.9** *(%)*	*Eq.* **3.10** *(%)*	*Eq.* **3.11** *(%)*	*Eq.* **3.12** *(%)*	*Eq.* **3.13** *(%)*	*Eq.* **3.14** *(%)*	*Eq.* **3.15** *(%)*	*Eq.* **3.16** *(%)*	*Eq.* **3.17** *(%)*	*Eq.* **3.18** *(%)*
1	12.3	2.4	-30.0	80.0	1.6	-0.3	-0.7	2.6	4.7	5.0	-1.0
2	11.2	1.9	-23.0	0.1	1.7	-0.5	2.2	1.2	-0.9	1.3	-0.6
3	-14.7	-0.8	8.8	-3.7	-1.0	3.0	1.1	-0.3	1.1	0.3	-5.8
4	11.7	-10.5	10.4	21.9	-0.7	1.3	1.3	-0.7	4.0	0.4	2.0
5	20.8	42.9	-17.3	-19.6	-2.5	-1.1	-3.1	-0.9	-2.9	-3.4	-2.5
6	-3.4	-17.2	-62.5	9.4	-0.3	-1.3	0.7	-0.1	0.4	0.4	0.1
7	15.6	-4.4	-27.4	4.2	-1.1	-6.5	-5.4	1.4	-2.3	-1.7	2.9
8	-6.7	-18.7	364.3	-3.6	-0.5	2.1	0.9	-1.1	-1.5	-0.7	1.0
9	-9.2	-12.0	21.3	3.3	1.0	0.9	1.9	1.1	0.4	1.3	-2.6
10	-1.8	-3.1	10.5	-2.9	2.5	1.9	4.3	0.0	-1.8	-1.0	0.6
11	29.5	-11.2	-8.2	-3.5	-8.8	-8.4	6.1	-0.1	0.8	-0.9	-3.6
12	8.0	3.6	6.2	-8.9	-1.0	0.0	-0.9	-0.7	-1.5	-0.8	1.9
13	14.3	14.7	-33.8	-6.3	-3.8	-1.9	-4.9	-2.1	-2.5	-2.4	-1.2
14	4.8	6.6	3.6	-0.3	5.1	1.1	-0.7	1.4	-0.6	0.1	2.1
15	-19.5	3.4	90.3	8.1	3.8	3.5	-0.4	0.1	1.3	-0.1	2.3
16	-15.8	-15.5	103.5	15.9	-0.5	1.3	-0.6	-2.8	1.4	-0.5	1.8
17	-8.4	-7.4	55.6	-10.9	3.1	2.1	0.2	3.0	1.3	-0.4	-3.0
18	1.3	-14.7	4.5	-18.3	-0.6	-1.9	-1.5	-0.7	-0.8	0.8	-0.7
19	-16.8	21.6	21.7	4.9	-1.9	-2.4	0.2	-1.6	-2.0	1.9	3.0
20	3.9	-4.5	-17.5	-62.5	-1.1	-3.0	-3.4	-0.1	-2.3	-3.1	-4.3
21	-4.6	25.0	-22.0	0.2	1.0	2.9	3.0	-0.5	1.7	1.5	1.1
22	12.0	6.8	-0.9	-8.9	0.2	0.0	1.2	0.4	-1.2	-0.6	2.6
23	-0.4	6.9	9.5	-2.9	-1.2	2.9	1.0	-0.9	2.4	0.0	1.1
24	-2.6	0.0	24.3	7.9	6.2	2.9	1.1	1.8	1.8	1.4	2.9
25	6.5	-6.7	11.6	2.5	-2.1	1.6	-1.2	-0.1	0.0	1.7	0.2

All of the regression analysis plots from this point onward display the results as a function of the statistical equations (equations 3.8 - 3.18) as this allowed for a better understanding of the process relationships. Where possible, comparisons are made with the experimental design points from Table 3.1 (termed “design point” in the regression graphs). As will be shown in the regression graphs throughout this chapter and in Table 3.3, with several exceptions, the relative error between the statistical equations and the physical design points was typically less than 10%. This suggests that the equations captured the process behaviour well.

Although the frequency and amplitude of oscillation are two separate process inputs, the regression analysis demonstrated that it was acceptable to consider

them as a single input – an average rubbing velocity (see equation 2.2) – as varying either while keeping the average rubbing velocity constant had relatively little effect on the results (Although it should be emphasised that this result may only be applicable to Ti-6Al-4V for the process input range investigated). To illustrate this, the steady state burn-off rate is plotted as a function of the frequency and average rubbing velocity in Figure 3.6(a). Therefore all subsequent regression analysis plots are displayed as a function of the average rubbing velocity. Figure 3.6(b) shows how the burn-off rate was affected by the combination of rubbing velocity and applied force, it increased with both. The amount of burn-off had no effect on this value.

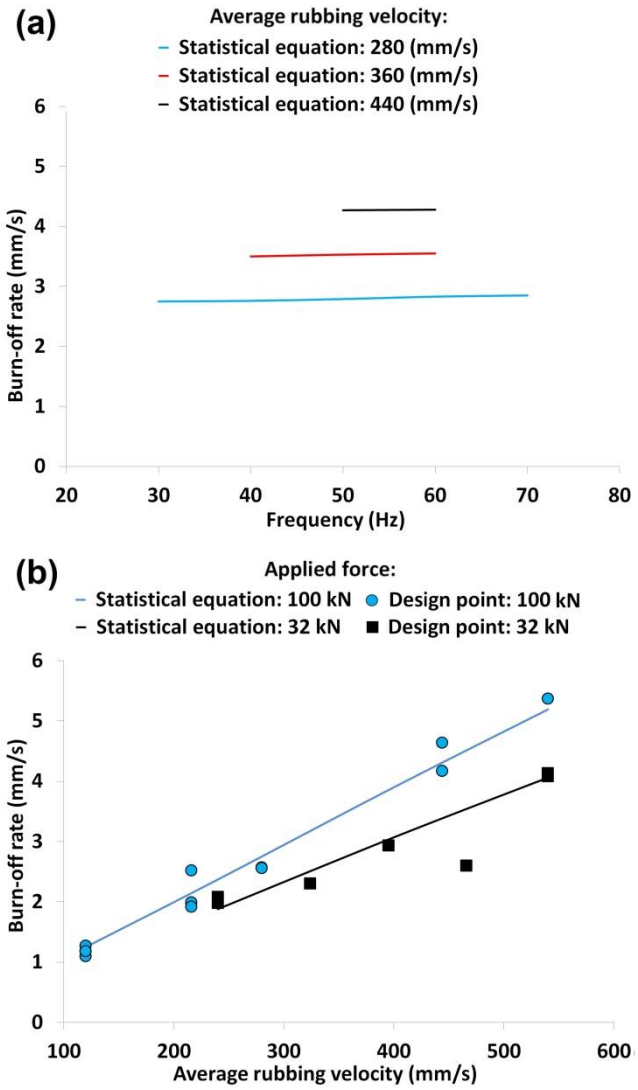

Figure 3.6: Regression analysis for the steady-state burn-off rate: (a) as a function of the oscillation frequency and average rubbing velocity for an applied force of 100 kN, and (b) as a function of the average rubbing velocity and applied force.

The results from the regression analysis for the average welding time, power, interface force, and coefficient of friction for the three main phases (phases 1, 2 and 3) are displayed in Figure 3.7. Due to Phase 4 being very short in duration, it was ignored in the analysis.

From Figure 3.7(a), the input parameter that had the greatest effect on the duration of each of the phases was the average rubbing velocity. The duration was inversely related to the rubbing velocity, power and burn-off rate. This is

because the higher rubbing velocities increased the rate of heat generation, enabling the material to heat and plasticise more rapidly (reducing the duration of phases 1 and 2). In addition, the higher rubbing velocities reduced the duration of phase 3 due to an increased rate of material expulsion, see Figure 3.6. Although not shown, the duration of phase 3 varied linearly with the amount of burn-off. In fact, with the exception of the duration of phase 3, the burn-off input had no influence on the results in Figure 3.7 and is therefore not included.

The results for the power in Figure 3.7(b) show that increasing the rubbing velocity increases the power input to the weld for all phases. The power input for phase 1 was generally the lowest of the three and was greatly affected by the applied force. The power input for phases 2 and 3 was greater and showed less dependence on the applied force.

The interface force was largely independent of the rubbing velocity, being mainly affected by the phase and applied force, as shown in Figure 3.7(c). This result was not anticipated or reported elsewhere. To understand why this may have occurred, this result is compared with the flow stress vs. temperature and strain-rate data for this alloy which is reproduced in Figure 3.8. As the rubbing velocity is increased so is the strain rate[7], which increases the required flow stress. The increased rubbing velocity also increases the heat input (see Figure 3.7(b)), which, due to the relatively low thermal conductivity of titanium, can increase the interface temperature[7], thus reducing the required flow stress. The net result appears to be a cancellation of the two effects, resulting in minimal change of the average interface force required to maintain oscillation.

The average interface force increases with the applied force, as shown in Figure 3.7(c). For phase 1 this is due to more of the asperities at the interface of the workpieces being “squashed” onto each other, increasing the true surface contact area, which increases the friction force[28,32]. For phases 2 and 3 this was probably due to the rate of expulsion of the viscous material from the interface. For a comparable rubbing velocity a decrease in the applied force decreases the rate of material expulsion, see Figure 3.6(b), causing less high temperature material to be removed from the joint. Consequently, the extra heat from the

remaining material is combined with the heat generated from the viscous plastic deformation during the next cycle of oscillation, resulting in a higher interface temperature. The higher temperature reduces the material flow strength and therefore the required interface force to maintain the oscillatory motion. This theory is supported by experimental investigations completed by Romero et al.[61] who compared the microstructures and residual stresses of Ti-6Al-4V linear friction welds and concluded that the interface temperature reduces considerably when welds are produced with higher applied forces. Ti-6Al-4V modelling work by Turner et al.[7,70] also supports this view.

The coefficient of friction is obviously strongly linked to the interface force. This parameter has been reported because of its common use in process models[22,45,159]. As shown in Figure 3.7(d), the average value was relatively insensitive to the rubbing velocity, however with the lower forces it ranged between about 0.8 and 1.3, depending on the phase; while at the higher forces it was consistently around 0.4. Due to the big difference in the results in phase 1 and the fact that a merging of the materials occurs in phases 2 and 3, it is highly unlikely that coulombic friction is occurring at any point during the LFW process. Therefore coulombic modelling – even during phase 1 – for the LFW process is highly questionable.

Finally there appears to be an advantage in using high rubbing velocities to minimise the overall energy input to a weld – see Figure 3.9. This is a consequence of the higher power input of these welds, which caused the interface material to heat and plasticise more rapidly during phase 1, then shorten much more rapidly during phases 2 and 3. This reduced the overall duration and hence energy wasted due to conduction etc.

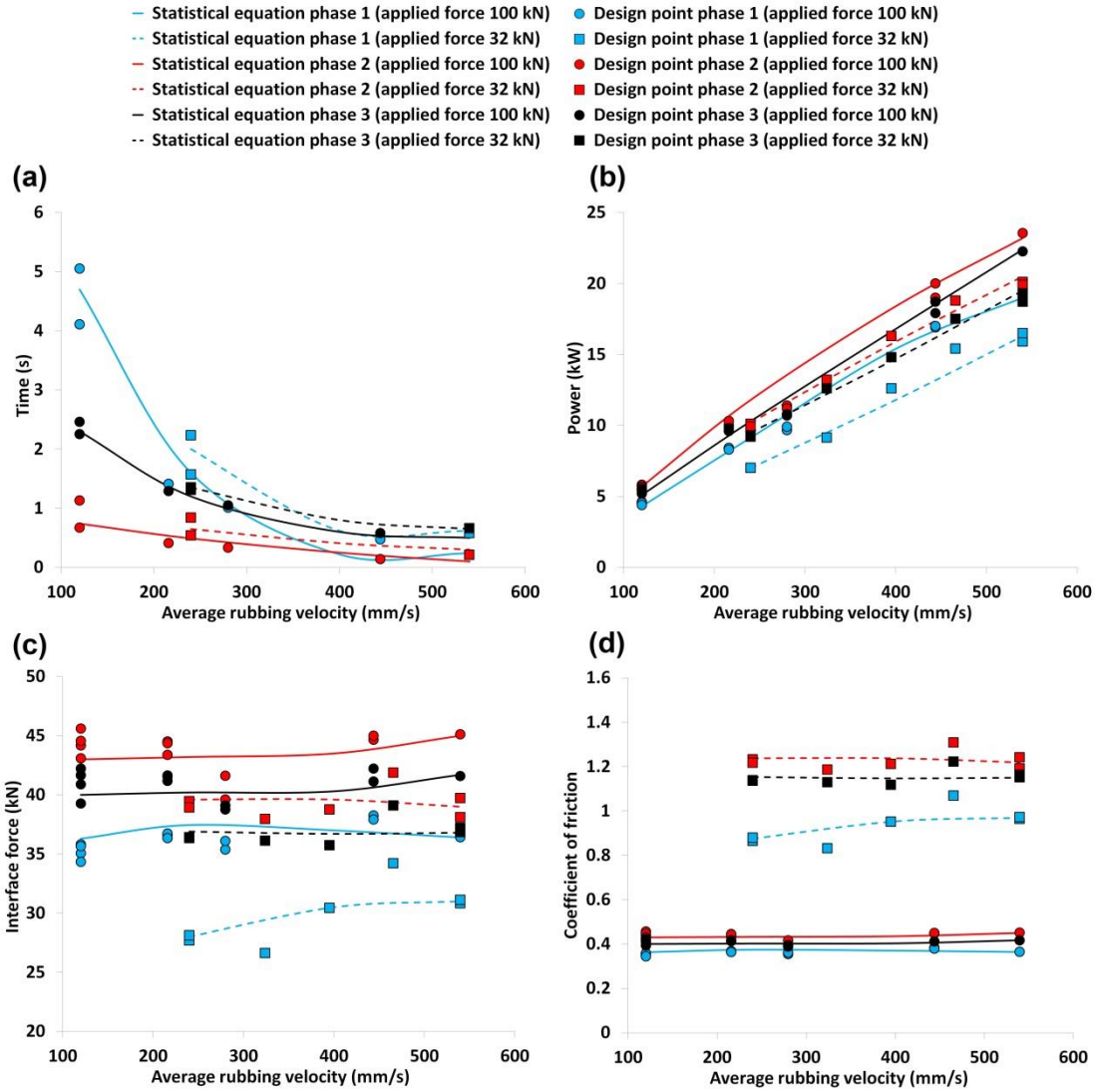

Figure 3.7: Regression analysis as a function of the average rubbing velocity, applied force and weld phase for: (a) welding time, (b) power, (c) interface force and (d) coefficient of friction. Note that the average welding time for phase 3 in (a) is for 3 mm of burn-off.

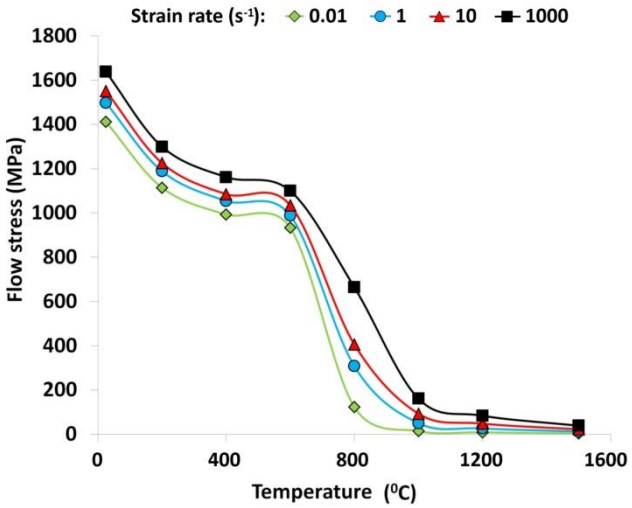

Figure 3.8: Ti-6Al-4V flow stress data as a function of temperature and strain rate at a strain of 4 (reproduced from Turner et al.[7]).

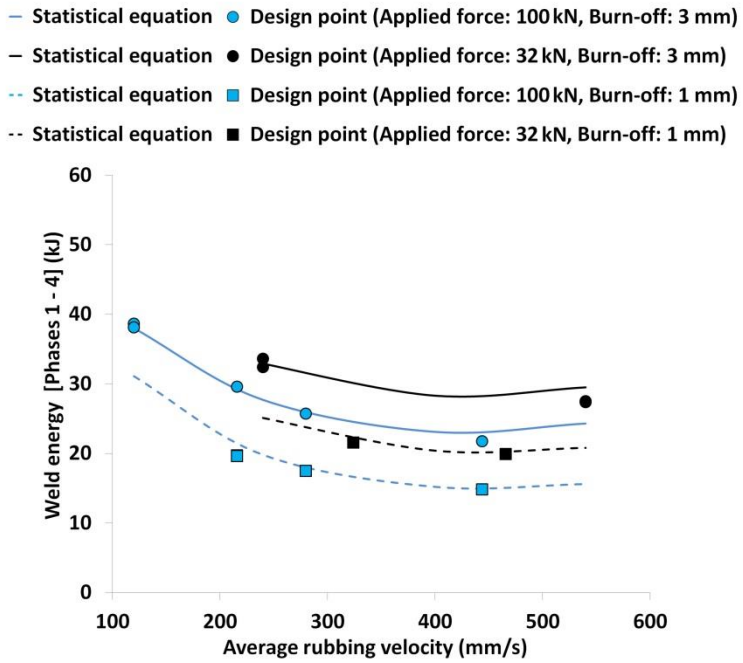

Figure 3.9: Regression analysis for the weld energy as a function of the average rubbing velocity for different applied forces and burn-off distances.

3.3.4 Thermal Profiles at the End of Phase 1

Figure 3.10 displays thermal profiles at the end of phase 1 for four different process input combinations. As stated earlier, the heat flux was determined from the force and displacement history (Method 1) and the statistical analysis

(Method 2). The temperatures recorded at the interface at the end of phase 1 typically ranged between 940 °C and 1100 °C, with an average of approximately 1030 °C across these processing conditions. It is well known that the beta-transus temperature for titanium is around 1000 °C [6,61] and, as seen in Figure 3.8, there is a significant reduction in the flow stress at this temperature. This lower flow stress likely allows for adhesion between the two materials and facilitates extrusion of the hot metal from the weld region. This may explain why the transition from phase 1 to phase 2 is approximately associated with the beta-transus temperature.

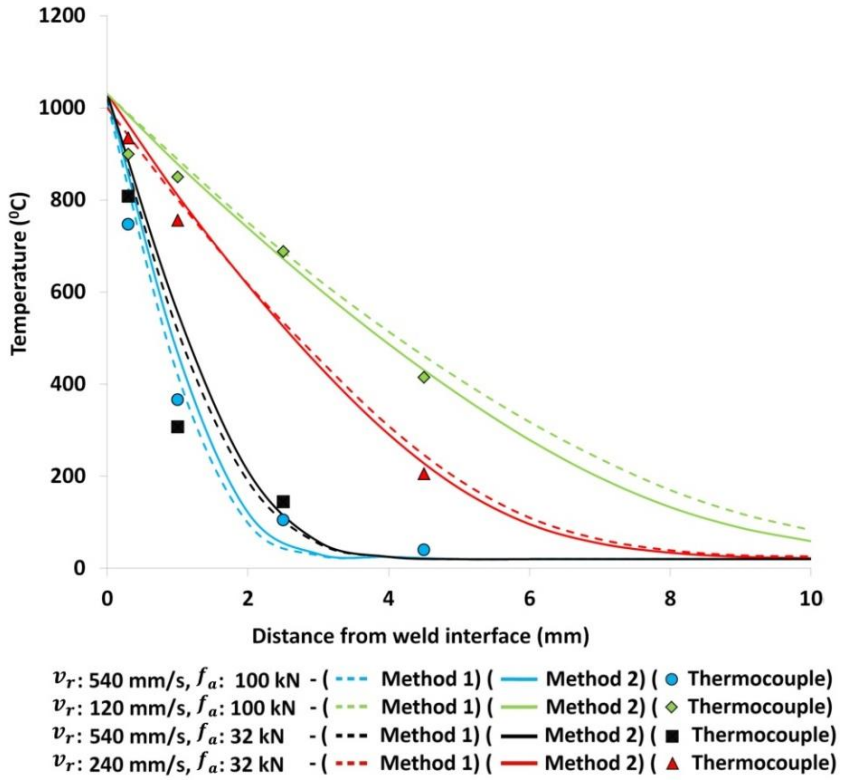

Figure 3.10: A comparison of the modelled thermal profiles and experimental measurements for different average rubbing velocities, v_r and applied forces, f_a, predicted at the end of phase 1. The modelled thermal profiles were estimated using: the heat flux calculated from the force and displacement history (Method 1), and the heat flux calculated from the statistical analysis (Method 2).

There was good agreement between the two methods for estimating the heat input and the experimental thermocouple recordings. An increase in the rubbing velocity and/or applied force increased the gradient of the thermal

profile, concentrating the heat close to the weld interface. As stated in the previous section, the high rubbing velocity welds generate more power and take a much shorter time. Therefore there was little time for the heat to conduct into the bulk material which is why the thickness of the highly heated region is reduced.

3.4 Conclusions

The following conclusions can be made from this chapter:

- The design of experiments technique allowed equations for describing the burn-off rate, duration, power input, interface shear force, friction coefficient and process energy to be determined for a range of process inputs and phases. These equations provide much of the input and validation data for the Ti-6Al-4V LFW process models presented in the subsequent chapters.

- The outputs were primarily dependent on the average rubbing velocity and applied force; adjusting the frequency and/or amplitude of oscillation while keeping the average rubbing velocity constant had little effect on the outputs.

- The weld interface consisted of either a Widmanstätten and/or Martensitic microstructure.

- Contaminants were present at the weld interface when low values of burn-off were used.

- The interface shear force increased with the applied force but was largely insensitive to the average rubbing velocity for all phases of the process.

- The coefficient of friction was not coulombic and varied between 0.3 and 1.3, being primarily dependent on the process phase and applied force.

- The energy required to produce a weld was reduced with higher rubbing velocities and applied forces due to the process taking less time.

- The thermal profiles predicted at the end of phase 1 indicated that irrespective of the process inputs the temperature at the interface was approximately 1000 °C, which corresponds to the beta-transus temperature for Ti-6Al-4V.

- An increase of the average rubbing velocity and/or applied force (pressure) increased the gradient of the thermal profile at the end of phase 1. The average rubbing velocity, however, had a much more noticeable effect.

The next chapter focuses on the development of 2D FEA models to better understand the effects of the process inputs on a Ti-6Al-4V linear friction weld. The following chapter also demonstrates how the data from this chapter can be used to validate the 2D FEA models.

Chapter 4: 2D Modelling of the Process Input Effects

This chapter is an edited version of the following articles:

McAndrew, A. R., Colegrove, P. A., Flipo, B. C. D. & Russell, M. J. Modelling of flash formation and defect removal in Ti-6Al-4V linear friction welds. in 1st international joint symposium on joining and welding, Osaka, Japan, 6-8 November 2013, (Fujii, H.) 291–298 (Woodhead publishing, 2013).

*McAndrew, A. R., Colegrove, P. A., Addison, A. C., Flipo, B. C. D. & Russell, M. J. Modelling the influence of the process inputs on the removal of surface contaminants from Ti-6Al-4V linear friction welds. Materials & Design **66**, 183–195 (2015).*

4.1 Introduction and Context

There have been many studies into the process input effects on Ti-6Al-4V welds[3,6–8,34,61,70] but there are still some fundamental areas that need addressing. For example, interface contaminant removal appears to be critically dependent on the combination of process inputs used[5,6], however, it is not understood why. Understanding the effects of the process inputs on the removal of contaminants from the weld interface into the flash is of particular industrial interest as they are known to affect the properties[5,6] and possibly the service life of a weld[7]. Moreover, there are some observations in the literature that need additional investigation and discussion. For example, the effects of the process inputs on the thermal fields and strain rates are inconclusive or even contradictory (see section 2.6.2 – modelling outputs). Many of the above responses are difficult to determine using experiments alone. Computational modelling offers a pragmatic method to addressing the stated issues.

The research reported in this chapter investigated how and why the process inputs affect the process behaviour. In particular, experimentally validated 2D models were used to investigate the process input effects on the material flow,

thermal fields and interface contaminant removal during the LFW of Ti-6Al-4V workpieces.

4.2 Methodology

4.2.1 Experimental

The previous chapter detailed how Design Expert V.7, a design of experiments (DOE) software package, was used to determine a range of experimental conditions. This experimental run was also used in the present chapter, i.e. welds 1 – 25 in Table 4.1. The Four thermocouple experiments also reported in the previous chapter were also used in the present one, i.e. welds 26 – 29 in Table 4.1.

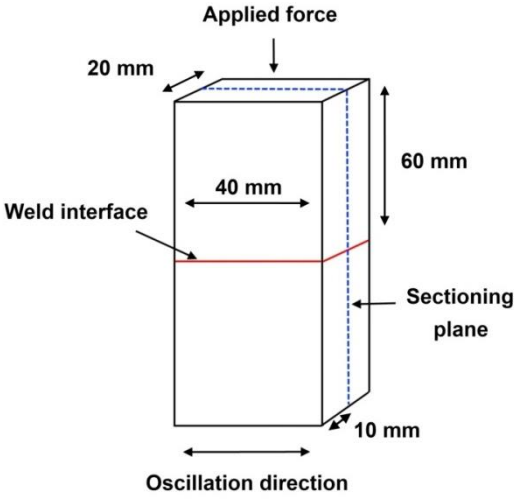

Figure 4.1: Experimental workpiece dimensions and location of the sectioning plane (Note that 60 mm represents the height of a single workpiece).

Finally, a few additional experiments were also completed to investigate how the burn-off affected interface contaminant removal for the geometry in Figure 4.1. Four different combinations of frequency, amplitude and applied force were used with burn-off values of 0.5 mm, 1 mm and 3 mm. These combinations are listed (welds 30 – 41) in Table 4.1. Unlike the previous welds (welds 1 – 25), the faying surfaces of these were not cleaned with acetone prior to welding to facilitate clearer observation of the interface contaminant removal in the post

weld analysis. All of the detailed experiments, which were completed using the FW34 LFW machine at TWI, Cambridge, were used to provide validation for the FEA models developed in this chapter.

Table 4.1: Experimental conditions.

Weld	*Oscillation frequency (Hz)*	*Oscillation amplitude (mm)*	*Average rubbing velocity ($mm \cdot s^{-1}$)*	*Applied force (kN)*	*Pressure (MPA)*	*Burn-off (mm)*	*Purpose*
1	*50*	*2.7*	*540*	*66*	*82.5*	*1*	*DOE*
2	*70*	*1*	*280*	*100*	*125*	*3*	*DOE*
3	*20*	*2.7*	*216*	*100*	*125*	*3*	*DOE*
4	*70*	*1*	*280*	*100*	*125*	*1*	*DOE*
5	*58.2*	*2*	*465.6*	*32*	*40*	*1*	*DOE*
6	*50*	*2.7*	*540*	*100*	*125*	*2*	*DOE*
7	*30*	*2.7*	*324*	*32*	*40*	*1*	*DOE*
8	*60*	*1.9*	*456*	*100*	*125*	*3*	*DOE*
9	*30*	*2*	*240*	*32*	*40*	*3*	*DOE*
10	*50*	*2.7*	*540*	*32*	*40*	*3*	*DOE*
11	*23.3*	*1.3*	*121.2*	*77.3*	*96.6*	*1*	*DOE*
12	*20*	*2.7*	*216*	*100*	*125*	*1*	*DOE*
13	*30*	*1*	*120*	*100*	*125*	*3*	*DOE*
14	*20*	*1.5*	*120*	*100*	*125*	*2*	*DOE*
15	*42.3*	*1.5*	*253.8*	*68.3*	*85.4*	*2*	*DOE*
16	*31.6*	*2.3*	*290.7*	*68.3*	*85.4*	*2.5*	*DOE*
17	*64.1*	*1.5*	*384.6*	*66*	*82.5*	*1*	*DOE*
18	*42.1*	*2.4*	*404.2*	*32*	*40*	*2*	*DOE*
19	*64.1*	*1.5*	*384.6*	*66*	*82.5*	*3*	*DOE*
20	*60*	*1.9*	*456*	*100*	*125*	*1*	*DOE*
21	*30*	*2*	*240*	*32*	*40*	*3*	*DOE*
22	*20*	*2.7*	*216*	*100*	*125*	*1*	*DOE*
23	*50*	*2.7*	*540*	*32*	*40*	*3*	*DOE*
24	*20*	*1.5*	*120*	*100*	*125*	*2*	*DOE*
25	*30*	*1*	*120*	*100*	*125*	*3*	*DOE*
26	*20*	*1.5*	*120*	*100*	*125*	*3*	*Thermocouple*
27	*50*	*2.7*	*540*	*100*	*125*	*3*	*Thermocouple*
28	*30*	*2*	*240*	*32*	*40*	*3*	*Thermocouple*
29	*50*	*2.7*	*540*	*32*	*40*	*3*	*Thermocouple*
30	*50*	*2.7*	*540*	*100*	*125*	*0.5*	*Burn-off investigation*
31	*50*	*2.7*	*540*	*100*	*125*	*1*	*Burn-off investigation*
32	*50*	*2.7*	*540*	*100*	*125*	*3*	*Burn-off investigation*
33	*50*	*2.7*	*540*	*32*	*40*	*0.5*	*Burn-off investigation*
34	*50*	*2.7*	*540*	*32*	*40*	*1*	*Burn-off investigation*
35	*50*	*2.7*	*540*	*32*	*40*	*3*	*Burn-off investigation*
36	*20*	*1.5*	*120*	*100*	*125*	*0.5*	*Burn-off investigation*
37	*20*	*1.5*	*120*	*100*	*125*	*1*	*Burn-off investigation*
38	*20*	*1.5*	*120*	*100*	*125*	*3*	*Burn-off investigation*
39	*30*	*2*	*240*	*32*	*40*	*0.5*	*Burn-off investigation*
40	*30*	*2*	*240*	*32*	*40*	*1*	*Burn-off investigation*
41	*30*	*2*	*240*	*32*	*40*	*3*	*Burn-off investigation*

In addition to the outputs obtained from the physical experiments in the previous chapter, metallographic specimens were produced from experiments 30 – 41 in Table 4.1 in accordance with the sectioning plane shown in Figure 4.1. The samples were sectioned and polished so that the centre of the weld may be viewed in the direction of oscillation. The sectioned samples were mounted and then ground using 240, 1200, 2500 and 4000 grit silicon carbide papers. After grinding, the sectioned samples were polished using colloidal silica on a micro-cloth and etched using a 3% hydrofluoric acid solution. The metallographic samples were viewed under a refractive microscope to determine the extent from one TMAZ/parent material boundary to the other (which will be referred to as the TMAZ thickness) and the thickness of the flash at the point of exit of the weld, as shown in Figure 4.2(a) and (b), respectively. Furthermore the samples were also inspected to see if interface contaminants could be observed.

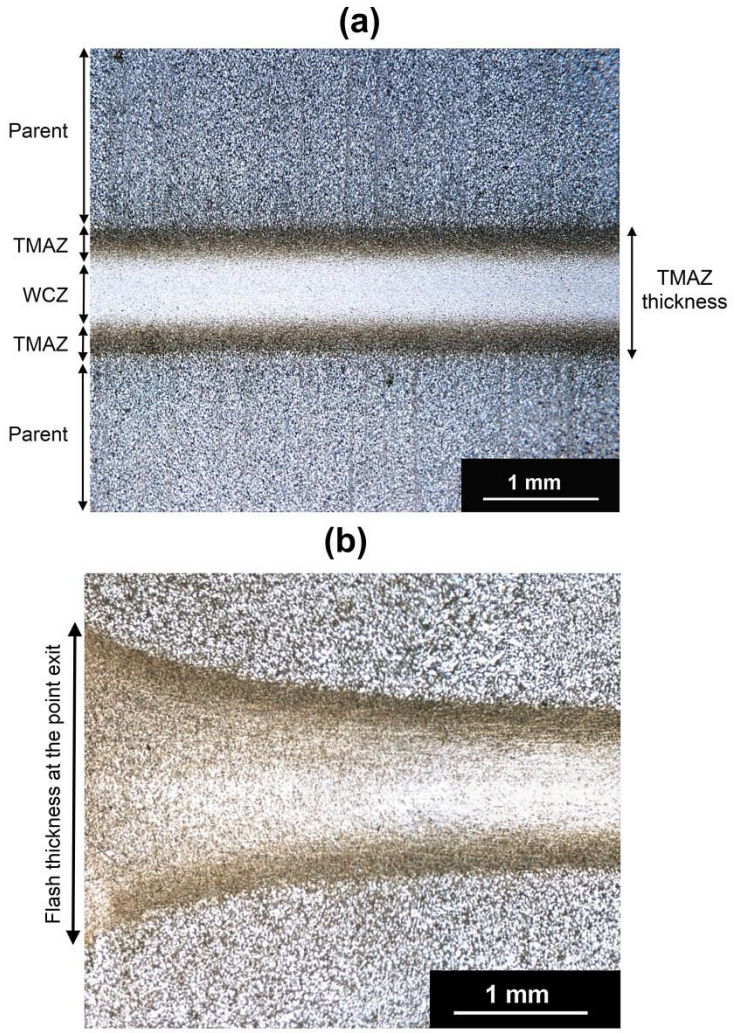

Figure 4.2: Experimental responses showing: (a) the weld centre zone (WCZ), thermo-mechanically affected zone (TMAZ), parent material (Parent) and TMAZ thickness; and (b) the flash thickness at the point of exit.

4.2.2 Development of a Numerical Model

The FEA modelling approach used in this chapter was the same as that reported by Turner et al. [7], i.e. modelling approach 3, as illustrated in Figure 2.30(c). This involved modelling the process as two distinct stages. The first stage used a purely thermal model to replicate the heating of the workpieces during phase 1. The second stage used a "single-body" plastic flow model to account for the material flow during phases 2 and 3.

The same design of experiments approach previously reported (welds 1 – 25 in Table 4.1) was used for the modelling work in this chapter, however, only 16 plastic flow models were required to cover the 25 design points since a single plastic flow model can describe multiple burn-off values for the same combination of frequency, amplitude and applied force. All of the plastic flow models were run to a burn-off of 3 mm and the process history was evaluated at the shorter burn-off values for the design points of interest. The development of the thermal models to account for the phase 1 heating was reported in Section 3.2.4 in the previous chapter (although the general concepts are reiterated below).

3D models require substantially more time to solve than their 2D counterparts. Therefore, to be pragmatic, a 2D modelling approach was used for the 16 conditions required for the DOE analysis. Consequently assumptions had to be made, like neglecting the material expulsion perpendicular to the direction of oscillation. To justify this approach the models were critically compared to their experimental counterparts, as will be discussed in section 4.3. The 2D models were developed with the finite element analysis (FEA) software DEFORM.

Thermal Model (Phase 1)

The thermal models developed in Section 3.2.4 in the previous chapter were used to account for the phase 1 heating for the conditions of interest in this chapter. The interface temperature at the end of phase 1, irrespective of the process inputs, was shown to reach approximately 1000 $^{\circ}$C. Therefore, the heat flux, which was determined by dividing the process input combination dependent phase 1 power input – see equation 3.12 – by the average in-contact interface area of the workpieces over a cycle of oscillation, was applied until the elements at the interface had achieved 1000 $^{\circ}$C. The generic appearance of the thermal profiles at the end of phase 1 is shown in Figure 4.3

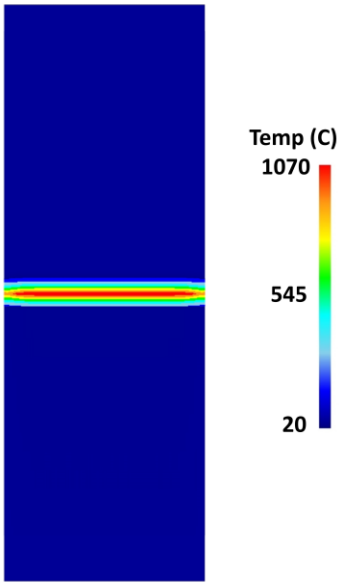

Figure 4.3: An illustration of the generic 2D thermal profile generated at the end of phase 1.

Plastic Flow Model (Phases 2 onward)

The 2D analysis assumed that no material flow occurred perpendicularly to the direction of oscillation. As such, a 2D plane strain condition was used so that the models represented a slice at the centre of the workpieces in Figure 4.1(a), with the direction of oscillation being in-plane. As shown in Figure 4.4(a), the 2D plastic flow models were specifically designed to focus on the weld interface of the workpieces displayed in Figure 4.1, i.e. 10 mm either side of the interface. This was to reduce the computational time. The oscillation movement and the applied force were provided by the lower and upper dies, respectively. The data from the phase 1 thermal model was mapped onto the “single-body” plastic model to provide the initial thermal condition, as illustrated in Figure 4.4(b).

A study on the effects of the mesh element size was performed. It was found that the plastic deformation results were independent of the mesh size for an average element size below 0.13 mm. Due to most of the plastic deformation and heat generation occurring at the interface, most of the mesh elements – with a width of 0.13 mm – were placed in a 4 mm band around the interface, as

shown in Figure 4.4(a). The element size was increased outside of the 4 mm band.

The responses obtained from the modelling will only be as accurate as the input data. As such, the material flow stress data used in this work was the same as that reported by Turner et al.[7]. In summary, the material flow stresses were obtained from stress and strain curves for temperatures, strains and strain rates between 20 °C and 1500 °C; 0 and 4; and 0.001 s^{-1} and 1000 s^{-1}, respectively (See appendix "C" for full details of the constitutive data used). The values for the thermal conductivity, specific heat capacity, emissivity, and heat transfer to the tooling and environment were identical to the values used for the thermal models.

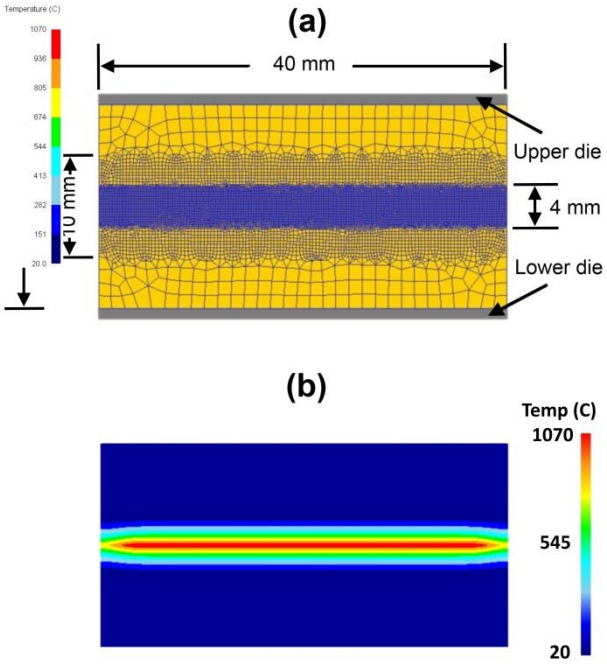

Figure 4.4: 2D modelling development showing: (a) plastic flow model setup and (b) plastic flow model with a thermal profile mapped on.

Each model was given a time-step so that the oscillation movement travelled approximately one third of the interface mesh element thickness per iteration. The thermal and mechanical aspects of the analysis were coupled and, in accordance with DEFORM's reccomendations[167], 90% of the mechanical

energy used to deform the material was estimated to be converted to heat. A re-mesh was initiated every 0.1 seconds for all cases.

Several responses were recorded from the models. To understand the expulsion of the interface contaminants point tracking was used at the interface, with a 1 mm gap between each tracked point, as shown in Figure 4.5(a). The models were then run to the desired burn-off and the amount of points that remained recorded. This allowed for an understanding of which combination of process inputs were required to ensure complete expulsion of the point tracking into the flash, as shown in Figure 4.5(b). Other responses investigated included: the steady-state burn-off rate, which was calculated by determining the gradient of the line when the burn-off rate is approximately constant; the peak interface temperature; strain rate; extent of the region being strained (FEA version of the TMAZ thickness); the average power input and interface shear force generated during phase 3; and the flash thickness at the point of exit.

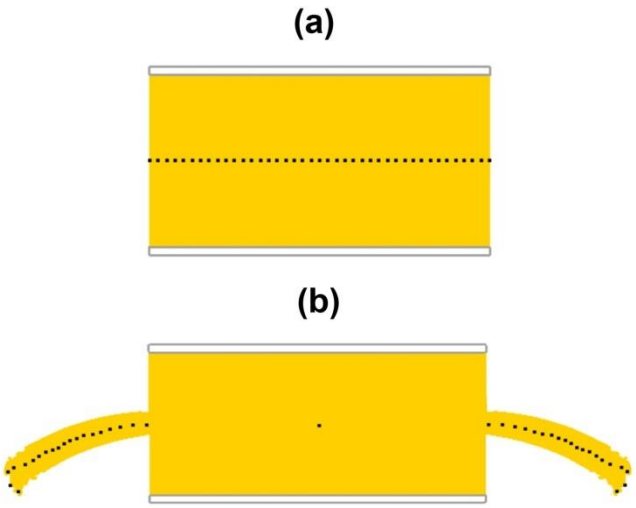

Figure 4.5: Recording the FEA responses: (a) interface point tracking and (b) point tracking removed from the interface into the flash (note that there is a "null flow" point at the centre).

4.2.3 Regression Analysis

An "analysis of variance" (ANOVA) was conducted using Design Expert V.7. This identified which inputs and input interactions were statistically important for

mathematically describing the process outputs. The statistically insignificant factors were then removed from the regression models. This approach took place for the FEA responses of interest, i.e. the interface temperature, burn-off rate, etc. Several statistical criteria were considered when reducing the factors, which were previously detailed in section 3.2.3 of this thesis.

4.3 Results and Discussions

4.3.1 Regression Analysis

The results from the statistical tests performed on the final regression models for the FEA results are displayed in Table 4.2. Note that *Av.* represents *average.* Much of the variability within the results is accounted for due to many of the values being close to 100 percent. The raw data obtained from the FEA models which were used for the statistical analysis are displayed in appendix "D". The relative error between the FEA design point values and the regression model values are shown in Table 4.3. Note that a positive relative error means that the experimental point value was lower than the predicted regression value. The relative error was calculated as using the same method as in the previous chapter.

Table 4.2: Statistical tests performed on the final regression analysis models.

Process output Equation	*Equation Units*	*R^2 (%)*	*Adj. R^2 (%)*	*Prd. R^2 (%)*	*Ad. Pr.*	*P-V*
Burn-off rate (FEA)	*[mm·s^{-1}]*	*99.8*	*99.7*	*99.6*	*125.9*	*<0.0001*
TMAZ thickness (FEA)	*[mm]*	*92.1*	*90.5*	*87.8*	*19.2*	*<0.0001*
Flash thickness (FEA)	*[mm]*	*94.8*	*93.8*	*91.9*	*24.1*	*<0.0001*
Interface temperature (FEA)	*[^{o}C]*	*99.8*	*99.6*	*99.3*	*88.1*	*<0.0001*
Interface strain rate (FEA)	*[s^{-1}]*	*99.7*	*99.6*	*99.3*	*90.3*	*<0.0001*
Remaining point tracking (FEA)	*[-]*	*99.1*	*98.4*	*97.0*	*36.8*	*<0.0001*
Av. phase 3 interface force (FEA)	*[kN]*	*96.0*	*95.0*	*93.8*	*30.8*	*<0.0001*
Av. phase 3 power input (FEA)	*[kW]*	*98.2*	*97.7*	*96.7*	*41.4*	*<0.0001*

The equations for the completed regression models are listed below:

$$\boldsymbol{Burn-off\ rate}\ (\boldsymbol{FEA}) = -1.36198 - 0.032022 * f + 1.30674 * A - 1.90035 * 10^{-3} * F_a + 0.028506 * f * A + 3.87983 * 10^{-4} * f * F_a + 2.69099 * 10^{-3} * A * F_a - 0.32656 * A^2 \quad \textbf{4.1}$$

$$\boldsymbol{TMAZ}\ \textbf{thickness}\ (\boldsymbol{FEA}) = 3.06495 + 1.17408 * A - 0.040652 * F_a - 0.29568 * A^2 + \quad \textbf{4.2}$$

$2.20636 * 10^{-4} * {F_a}^2$

$$\boldsymbol{Flash\ thickness}\ (\boldsymbol{FEA}) = 5.56032 - 3.84187 * 10^{-3} * f - 0.094892 * A - 0.049387 * F_a + 2.80758 * 10^{-4} * {F_a}^2 \quad \textbf{4.3}$$

$$\boldsymbol{Interface\ temperature}\ (\boldsymbol{FEA}) = 676.29677 + 6.21345 * f + 301.4961 * A - 0.40508 * F_a - 6.71761 * 10^{-3} * f * F_a - 0.57031 * A * F_a - 0.02614 * f^2 - 46.9745 * A^2 + 7.40249 * 10^{-3} * {F_a}^2 \quad \textbf{4.4}$$

$$\boldsymbol{Interface\ strain\ rate}\ (\boldsymbol{FEA}) = 53.01137 - 2.18777 * f - 56.11051 * A - 0.34278 * F_a + 5.55938 * f * A + 0.04545 * f * F_a + 0.99927 * A * F_a - 0.015 * {F_a}^2 \quad \textbf{4.5}$$

$$\boldsymbol{Remaining\ point\ tracking}\ (\boldsymbol{FEA}) = 31.54378 - 0.48038 * f + 0.088584 * A - 0.061352 * F_a - 13.51208 * b_o + 0.043083 * f * A + 6.99114 * 10^{-4} * f * F_a - 0.019211 * A * F_a + 0.022378 * F_a * b_o + 3.75413 * 10^{-3} * f^2 + 2.10029 * {B_o}^2 \quad \textbf{4.6}$$

$$\boldsymbol{Av.phase\ 3\ interface\ force}\ (\boldsymbol{FEA}) = 36.63998 - 0.12187 * f - 16.69319 * A + 0.29955 * F_a + 3.81874 * A^2 - 1.63274 * 10^{-3} * {F_a}^2 \quad \textbf{4.7}$$

$$\boldsymbol{Av.phase\ 3\ power}\ (\boldsymbol{FEA}) = -5.04395 - 3.26455 * 10^{-3} * f - 0.050195 * A + 0.16786 * F_a + 0.095837 * f * A - 9.8577 * 10^{-4} * {F_a}^2 \quad \textbf{4.8}$$

Where: A is the oscillation amplitude (mm), f the oscillation frequency (Hz), F_a the applied force (kN), and b_o the burn-off (mm).

Table 4.3: Relative error between the FEA values for the experimental design points and the regression model values for the FEA results.

FEA value corresponding to experimental design point	*Eq.* 4.1 *(%)*	*Eq.* 4.2 *(%)*	*Eq.* 4.3 *(%)*	*Eq.* 4.4 *(%)*	*Eq.* 4.5 *(%)*	*Eq.* 4.6 *(%)*	*Eq.* 4.7 *(%)*	*Eq.* 4.8 *(%)*
1	1.9	-1.8	6.0	-0.4	0.4	12.4	3.9	2.0
2	-1.5	-5.3	-1.1	-0.2	-0.7	33.4	1.6	1.4
3	-0.1	1.0	-0.1	-0.2	1.3	15.9	0.0	2.4
4	-1.5	-5.3	-1.1	-0.2	-0.7	1.1	1.6	1.4
5	1.6	8.8	-1.2	0.0	2.3	-1.0	0.8	1.9
6	-0.7	2.8	-0.6	0.7	-2.8	-0.9	-4.1	-6.9
7	4.9	-3.1	2.5	0.8	0.0	-3.7	1.6	-15.5
8	0.4	2.9	0.8	0.0	2.7	-23.3	-0.2	1.9
9	-1.7	-2.6	-0.9	-0.3	-3.4	26.6	-3.4	-2.6
10	-2.6	-1.8	-2.1	-0.2	-0.7	-2.4	-4.4	2.2
11	-3.8	-0.9	0.1	0.7	12.6	-3.4	-3.0	3.8
12	-0.1	1.0	-0.1	-0.2	1.3	-1.3	0.3	2.4
13	8.0	9.7	3.8	0.0	0.1	1.3	-0.2	-3.9
14	-2.9	-7.9	-6.2	0.1	-7.3	3.2	0.9	2.6
15	-4.6	-3.1	-0.1	-0.5	3.2	8.2	2.0	-3.1
16	1.5	0.7	-4.4	-0.4	-0.9	-7.7	1.7	5.6
17	1.5	2.5	-2.0	0.4	-2.3	7.5	-2.2	-3.0
18	2.0	3.9	4.9	0.2	4.0	-7.0	16.3	10.8
19	1.5	2.5	1.1	0.4	-2.3	-74.2	-2.2	-3.0
20	0.4	2.9	0.8	0.0	2.7	-6.9	-0.2	1.9
21	-1.7	-2.6	-0.9	-0.3	-3.4	26.6	-3.4	-2.6
22	-0.1	1.0	-0.1	-0.2	1.3	-1.3	0.3	2.4
23	-2.6	-1.8	-2.1	-0.2	-0.7	-2.4	-4.4	2.2
24	-2.9	-7.9	-6.2	0.1	-7.3	3.2	0.6	2.6
25	8.0	9.7	3.8	0.0	0.1	1.3	-0.2	-3.9

With the exception of the point tracking evolution described by equation 4.6, the burn-off, b_o, had no effect on any of the responses. This is in good agreement with other authors who have shown that once Ti-6Al-4V is in the steady-state phase (phase 3) the plastic deformations[3,7,149] and thermal profiles[7,24,156] are independent of the burn-off.

Where possible, the regression models (statistical equations [EXP]) from the previous chapter, which were generated for physical experimental results, are compared to the regression models in this chapter, which were generated for FEA results (statistical equations [FEA]). This allowed for a validation of the FEA results. All of the regression analysis plots from this point onward display

the results as a function of the statistical equations as this allowed for a better understanding of the process relationships. Where possible, the statistical equations (for the experimental and FEA work) are compared to the individual design points for the physical experiments and FEA. As will be shown in the regression graphs throughout this chapter and in Table 4.3, with several exceptions, the relative error between the statistical equations for the FEA work and the physical FEA design point values was typically less than 5%. This suggests that the statistical equations for the FEA work captured the process behaviour well. Please note that from this point onward, the term “model” refers to the FEA models, when referring to the regression models the term “regression model” is used.

4.3.2 Mechanisms Behind the Flash Formation

As with the previous chapter, the regression analysis demonstrated that it was acceptable to consider the frequency and amplitude of oscillation as a combined single input term called the average rubbing velocity, v_r. Varying the frequency or amplitude while keeping the average rubbing velocity constant had relatively little effect on the outputs. To illustrate this, the steady state burn-off rates determined from the models and experiments are plotted as a function of the frequency and average rubbing velocity in Figure 4.6(a). Therefore all subsequent regression analysis plots are displayed as a function of the average rubbing velocity.

The FEA demonstrated how the flash was generated in the direction of oscillation. When the amplitude was at maximum displacement the in-contact surface area was decreased. This caused a pressure increase, resulting in the cooler material being plunged further into the highly viscous material. As the workpieces were brought back together the cooler material extruded the viscous material from the interface generating the flash. Figure 4.6(b) shows how the burn-off rate (flash formation rate) was affected by the combination of rubbing velocity and applied force used – it increased with both. This phenomenon was due to the increased rubbing velocity causing a faster rate of extrusion; and the

increased force causing the cooler material to be plunged even further into the viscous material, resulting in a greater amount of material being extruded from the interface with each oscillatory cycle, thus increasing the burn-off rate.

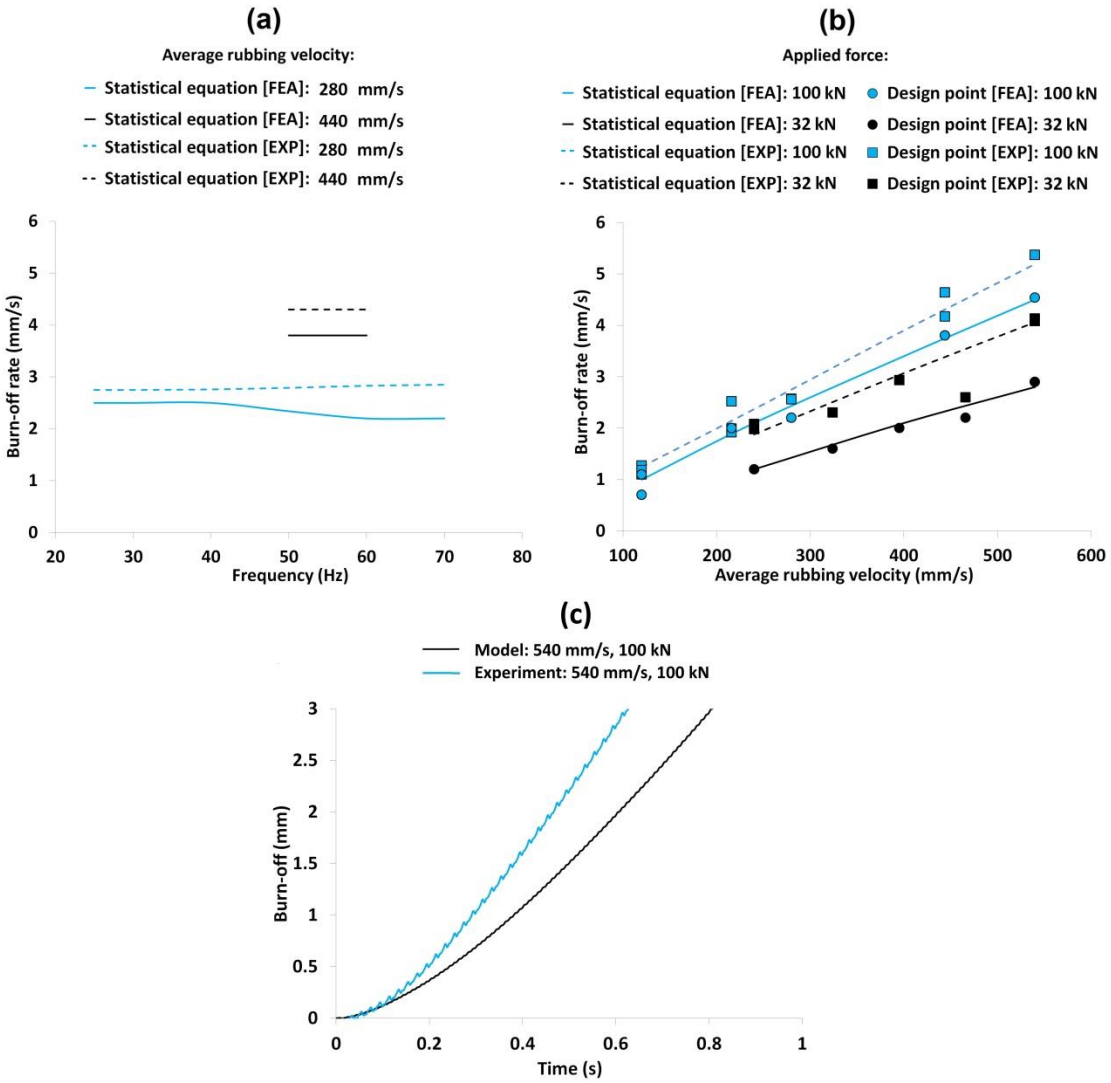

Figure 4.6: Regression analysis for the FEA and experimental steady-state burn-off rate: (a) as a function of the frequency and average rubbing velocity for an applied force of 100 kN, (b) as a function of the average rubbing velocity and applied force, and (c) a direct comparison of the burn-off history between an FEA model and an experiment (weld 32).

For all of the modelling conditions, the flash was “smooth” and did not display the “ripple” morphology observed by Turner et al.[7] and Schröder et al.[34,69]. Some of the experiments did, however, display a very fine rippling effect –

possibly too fine to be captured by the mesh used. The flash formation mechanisms are discussed in greater detail in the next chapter.

As shown in Figure 4.6, the FEA models captured the experimental trends but under-predicted the actual experimental burn-off rate values. This was observed for the regression models, see Figure 4.6(a) and (b), and the physical data, see Figure 4.6(c). Turner et al.[7] noticed that there are two mechanisms for expelling the viscous material. The first is the effect of the oscillatory motion pushing and dragging the material out of the weld in the direction of oscillation. The second is the applied force extruding the material in the direction perpendicular to oscillation. The mechanism that dominates depends on the process inputs used. 2D models cannot account for the material being expelled perpendicular to oscillation thus explaining the observed under-prediction. The difference between the experimental and modelled burn-off rates is greatest for low applied forces. This may indicate that under lower applied forces a greater percentage of the material is extruded perpendicular to the direction of oscillation.

As shown in Figure 4.6(c), the FEA burn-off histories did not exhibit such a defined stepwise shortening pattern when compared to a comparable experiment. This could have been due to the models not accounting for the out-of-plane material expulsion, a misalignment of the experimental workpieces, the difference between the flow stress values, or a combination of these factors.

4.3.3 Energy Usage, Thermal Fields and Microstructure

The results from the regression analysis for the peak interface temperature, peak interface strain rate, average interface force generated during phase 3 and the average power input generated during phase 3 are displayed in Figure 4.7(a), (b), (c) and (d), respectively.

The average interface force generated over a phase was relatively insensitive to the rubbing velocity (see Figure 4.7(c)). This can be explained by the effects of the temperature and strain rate on the flow stress. The weld line strain rate

increased with the average rubbing velocity (see Figure 4.7(b)), which increased the required flow stress[7,128]. However, the higher rubbing velocities also generated a greater heat input (see Figure 4.7(d)), which due to the relatively low thermal conductivity of titanium alloys[92] concentrated the heat close to the weld interface. The concentrated heat increased the interface temperature (see Figure 4.7(a)), reducing the required flow stress[7,105,128]. The net result appears to be a cancellation of the two effects.

As shown in Figure 4.7(a), the interface temperature increases as the applied force is *decreased*. This phenomenon in titanium alloy linear friction welds has also been made by Romero et al.[61], Attallah et al.[80] and Turner et al.[70]. This phenomenon can be explained by the relationship between the power input and the burn-off rate. For a comparable rubbing velocity, a reduction in the force resulted in the burn-off rate being reduced by a greater percentage than the power input, as can be seen by comparing Figure 4.6(b) and Figure 4.7(d). Although less heat went into the weld it was not expelled as fast. This increased the time the heat had to conduct back from the interface, increasing the size of the band of heated material - see the 540 mm/s profiles in Figure 4.8(a). Consequently, the material farther back from the interface was much hotter with lower applied forces. When this hotter material reached the interface its heat combined with the heat generated during the oscillatory motion producing a higher interface temperature.

The higher interface temperature would explain why the average interface force generated over a phase decreased as the applied force was reduced (see Figure 4.7(c)). The interface was hotter, reducing the flow stress[7,105,128], therefore requiring a lower force to maintain the oscillatory motion. The lower interface force would also explain why the peak strain rate and power input to maintain the steady-state condition were reduced with lower applied forces, as shown in Figure 4.7(b) and (d). Furthermore, the strain rates observed in this work are closer in agreement to those reported by Turner et al.[7] (500 s^{-1} to 2500 s^{-1}) and Chamanfar et al.[118] (1520 s^{-1}) than those reported by Vairis and Frost[3] (4.6 s^{-1}).

The models under-predicted the average interface forces and power inputs, as shown in Figure 4.7(c) and (d). This was probably due to two main factors. The first, the models didn't account for the heat that was expelled into the flash in the direction perpendicular to oscillation. This may have resulted in the modelled weld being comparably hotter than the experimental one. Consequently the models may have had a higher interface temperature, thus requiring a lower force to maintain oscillatory motion; the lower force would have also reduced the power input. The second factor was due to the difference between the flow stress values of the experimental weld and the modelled weld.

As shown in Figure 4.8(b), there is a good match between the purely thermal models and thermocouple recordings for the heating during the initial phase (phase 1) of the process. The reason there was disagreement between the thermocouple recordings and the plastic flow models (phases 2 and 3), particularly for the thermocouples initially closest to the interface, was probably due to the same problem encountered by Vairis and Frost[22]. The viscous plasticised material entered the thermocouple hole and pushed the thermocouple back from the interface causing it to record a lower value at an unknown distance farther back. This would explain why there was good initial agreement and then a drop off in the thermocouple recording. This problem was observed for all comparisons between the models and thermocouple trials. This would explain why the peak thermocouple recordings were lower than those of the models. Despite the differences between the models' temperature output and thermocouple recordings during phases 2 and 3, the modelling results are believed to be reasonably accurate. This is due to the weld line temperatures observed in this work (see Figure 4.7(a)) being in good agreement with other authors for Ti-6Al-4V, i.e. between 1000 $^{\circ}$C and 1300 $^{\circ}$C[7,45,69,70,157].

As shown in the previous chapter, the experimental Ti-6Al-4V workpiece material experienced significant microstructural changes around the interface region (see Figure 3.4). The models in this chapter can be used to provide a greater insight into processing effects at the WCZ. The temperature measurements from the models (see Figure 4.7(a)) indicated that the WCZ

exceeded the beta-transus temperature. The large strains and strain rates in the WCZ (see Figure 4.7(b)) induced dynamic recrystallisation of the beta-phase[106,131]. The body-centred-cubic (BCC) beta-phase microstructure[92,94] present at the WCZ during processing had more slip-systems than the hexagonal-close-packed (HCP) alpha-phase[86] and required a lower activation energy to initiate material flow[132,134]. This would explain why the commencement of material flow during the LFW of Ti-6Al-4V is associated with the beta-transus temperature, as reported in the previous chapter. Furthermore, the modelling work in this chapter showed that the boundary temperature between the flash formation and negligible material flow was 970 °C (±20 °C), also approximately corresponding to the beta-transus temperature, as shown in Figure 4.8(c).

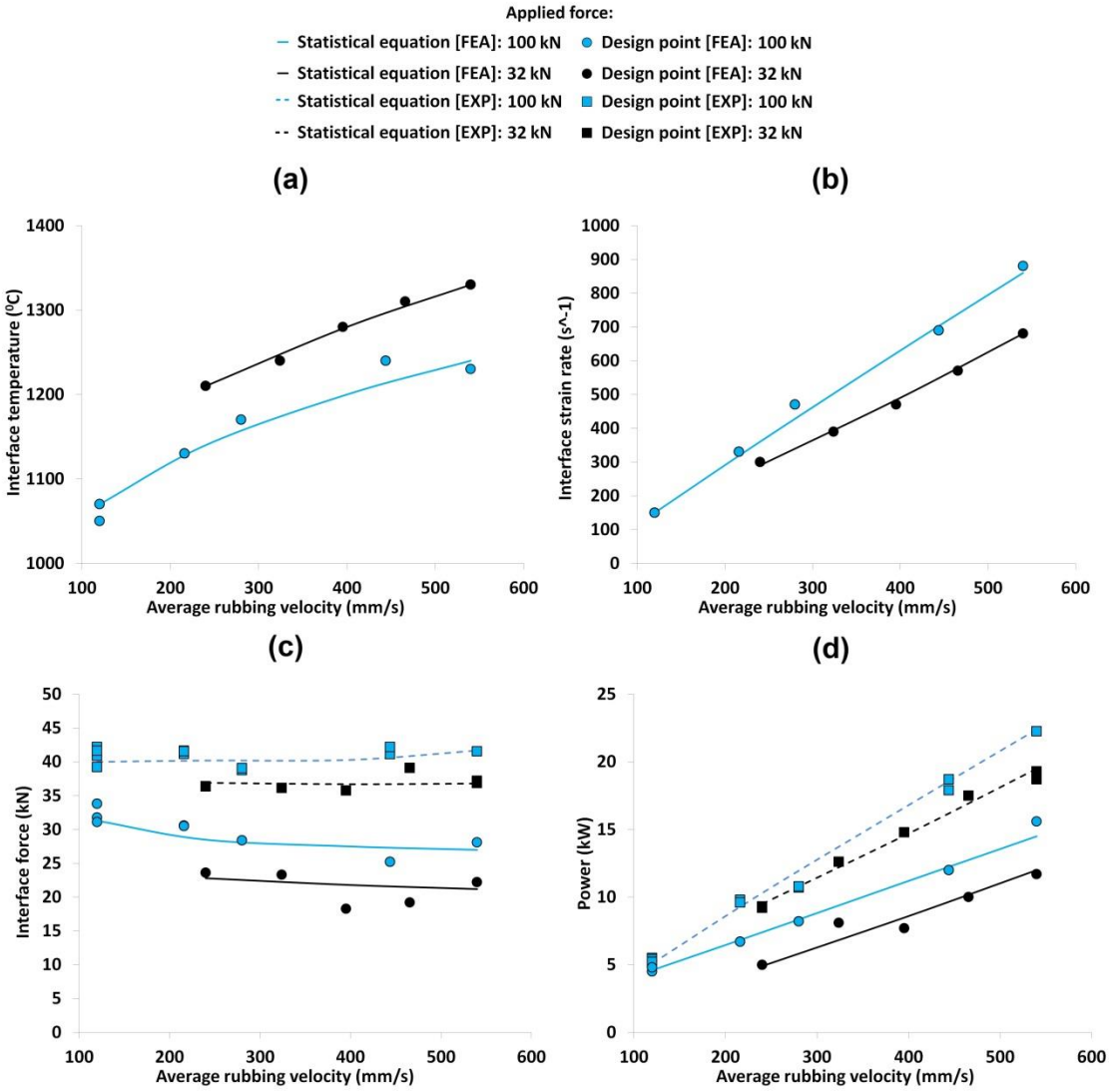

Figure 4.7: Regression analysis results for the FEA and experiments for the: (a) peak interface temperature, (b) peak interface strain rate, (c) average interface force during phase 3 and (d) average power input during phase 3.

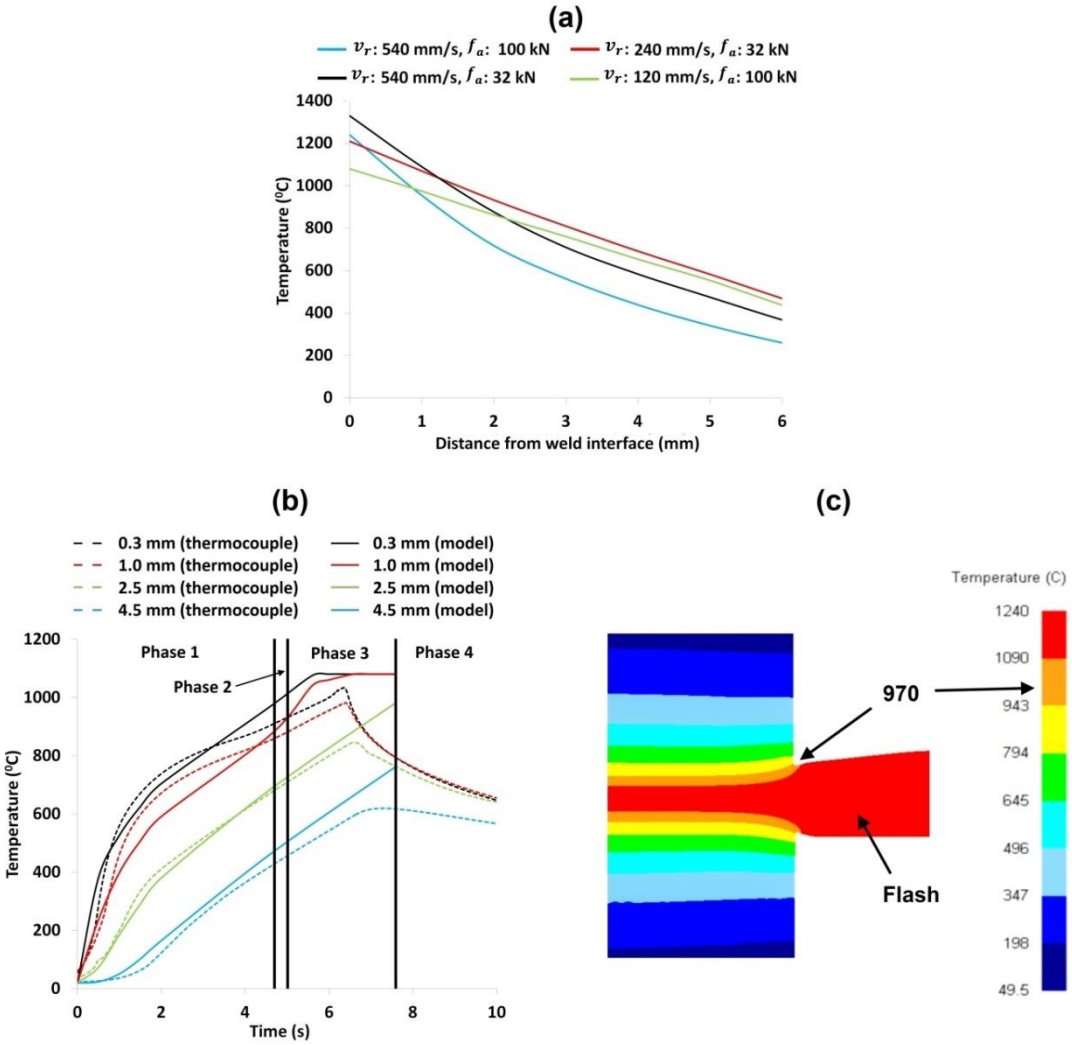

Figure 4.8: Thermal histories from the FEA and experiments showing: (a) the effects of different average rubbing velocities, v_r, and applied forces, f_a, on the generated FEA thermal profiles during phase 3; (b) a comparison of the thermal histories between a model and an experiment for the different phases for an oscillation frequency, oscillation amplitude, applied force and burn-off of 20 Hz, 1.5 mm, 100 kN and 3 mm, respectively. The phase times were determined from the experimental burn-off history in accordance with the descriptions given in section 2.4.2 (Note the distances in the key represent how far back from the interface the recorded points were at the beginning of the process); and (c) FEA boundary temperature between the flash formation and negligible material flow.

4.3.4 Interface Contaminant Removal

The results from the regression analysis for the combination of process inputs required to completely expel the point tracking into the flash, the TMAZ thickness and the flash thickness are displayed in Figure 4.9(a), (b) and (c), respectively. The burn-off values presented in Figure 4.9(a) are the minimum values – according to equation 4.6 – required to ensure fewer than two “tracked points” remained at the interface, i.e. the minimum burn-off required to ensure that only the null flow point remained. In addition, the experimental flash and TMAZ thicknesses were physical experimental recordings rather than values estimated by regression analysis equations.

As shown in Figure 4.9(a), when the applied force is increased the required burn-off to completely expel the point tracking into the flash decreases. This was due to the influence of the applied force on the generated thermal profiles. As discussed in section 4.3.3, for the rubbing velocity range investigated the higher forces generated a thinner band of highly heated viscous material (greater than 970 $^{\circ}$C). As the size of the band of highly heated material was reduced so was the amount of material required to be expelled along with the point tracking, thus reducing the required burn-off. Despite the large influence the rubbing velocity had on the gradient of the thermal profiles, for a comparable applied force a change in the rubbing velocity had relatively little effect on the extent of the band of material above 970 $^{\circ}$C, as shown in Figure 4.8(a). Consequently, the rubbing velocity had relatively little effect on the required burn-off to expel the point tracking for the conditions evaluated in this work.

As shown in Figure 4.10, there is good agreement between the expulsion of the interface contaminants (the dark clusters along the interface as shown in Figure 4.10(a), (b) and (d)) in the experimental welds and the point tracking results from the FEA. Both show that the contaminants and point tracking were increasingly expelled toward the edges of the workpieces as more burn-off occurred. For the experiments it became increasingly difficult to optically

observe the interface contaminants as the burn-off increased. This was to be expected as the contaminants would have been expelled into the flash and/or heavily strained, dispersing them thinly across the weld.

Although there was good agreement between the experiments and FEA for the contaminant evolution during phases 2 and 3, further justification of the assumption that point tracking can effectively represent the contaminants is required. Contaminants may affect the constitutive behaviour of the viscous interface layer, however due to their small size (see Figure 4.10(a)) relative to the extent of the flowing material (see Figure 4.9(b and c)) their effect is likely to be limited. To justify this view the LFW machine output data was interrogated for the DOE welds that had experienced 3 mm of burn-off (see Table 4.1). The average interface force between 0 mm and 1 mm of burn-off (where a heavy contaminant presence was expected, see Figure 4.10 and Figure 3.4(d)) was compared to the average interface force between 1.5 mm and 3 mm (where there was a negligible contaminant presence, see Figure 4.10(f)). The analyses showed that the average interface force between the two burn-off regimes typically varied by 3.8 percent – a minimal difference. The slightly larger forces at the lower burn-off values were more likely to be due to the inclusion of the transition phase (phase 2) than the contaminants. According to the models the interface temperature is slightly lower in this phase and typically requires a larger force to maintain oscillatory motion, as shown elsewhere[3,34,80] and in the previous chapter. Therefore the interface contaminants are likely to have had a negligible effect on the overall constitutive behaviour of the viscous interface layer. Consequently FEA used in conjunction with point tracking offers a pragmatic method for understanding the mechanisms behind interface contaminant removal during phases 2 and 3.

Furthermore, to investigate the effects of the contaminants during phase 1 on the experimental workpieces, the author compared the average force histories between pre-weld cleaned and non-pre-weld cleaned welds that were run at the same frequency, amplitude and applied force, i.e. weld 6 and weld 32; weld 10 and weld 35; weld 14 and weld 38; and weld 9 and 41 – as detailed in Table

4.1. The pre-weld cleaned workpieces should have had far less contaminants. The analyses showed no noticeable difference between the average force histories during phase 1, therefore the impact of contaminants during phase 1 also appeared to be small.

Due to a thinner band of highly heated material being generated in the welds produced with higher applied forces, the thickness of the flash and the overall TMAZ region are reduced under these conditions, as shown in Figure 4.9(b) and (c). An increase of the rubbing velocity had minimal effect on these values. The trends of the flash and TMAZ thickness were captured by the models, however the exact values did not match with the experimental welds. The extra heat in the models (as previously discussed) and the difference between the experimental and modelling material flow stress data may have contributed to the discrepancies. The experimental welds had also experienced extra material expulsion due to the forging force during phase 4, which may have reduced the values. In addition for the TMAZ thickness results, for the models, the distance between the points of negligible strain either side of the interface were recorded, while in the experimental welds the final observable TMAZ thickness was recorded, which may not have coincided with negligible strain.

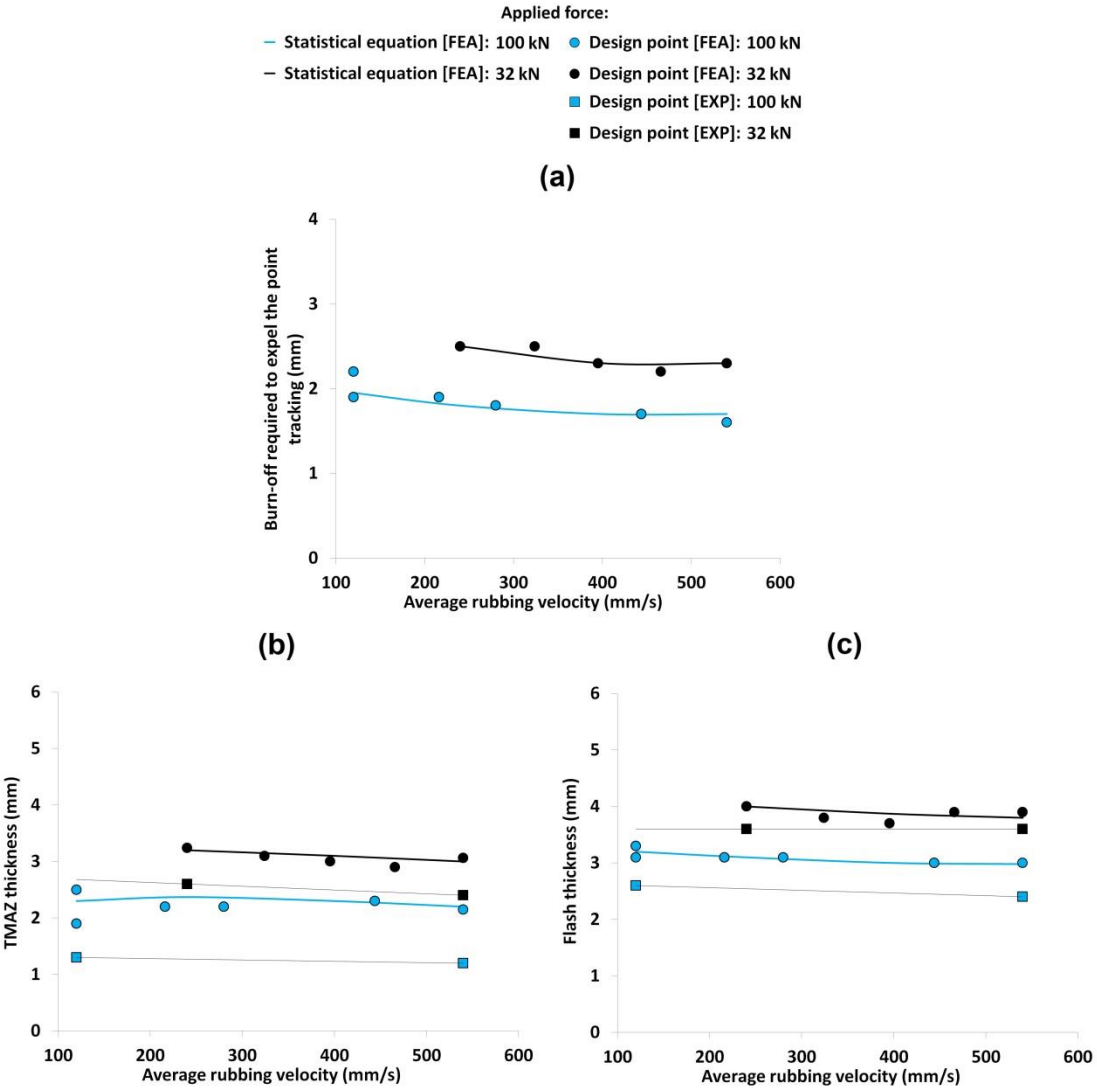

Figure 4.9: Regression analysis results for the FEA for the: (a) combination of process inputs required to completely expel the point tracking into the flash, (b) overall TMAZ thickness, and (c) flash thickness. The experimental flash and TMAZ thickness design points have had trend lines fitted to ease understanding of the results.

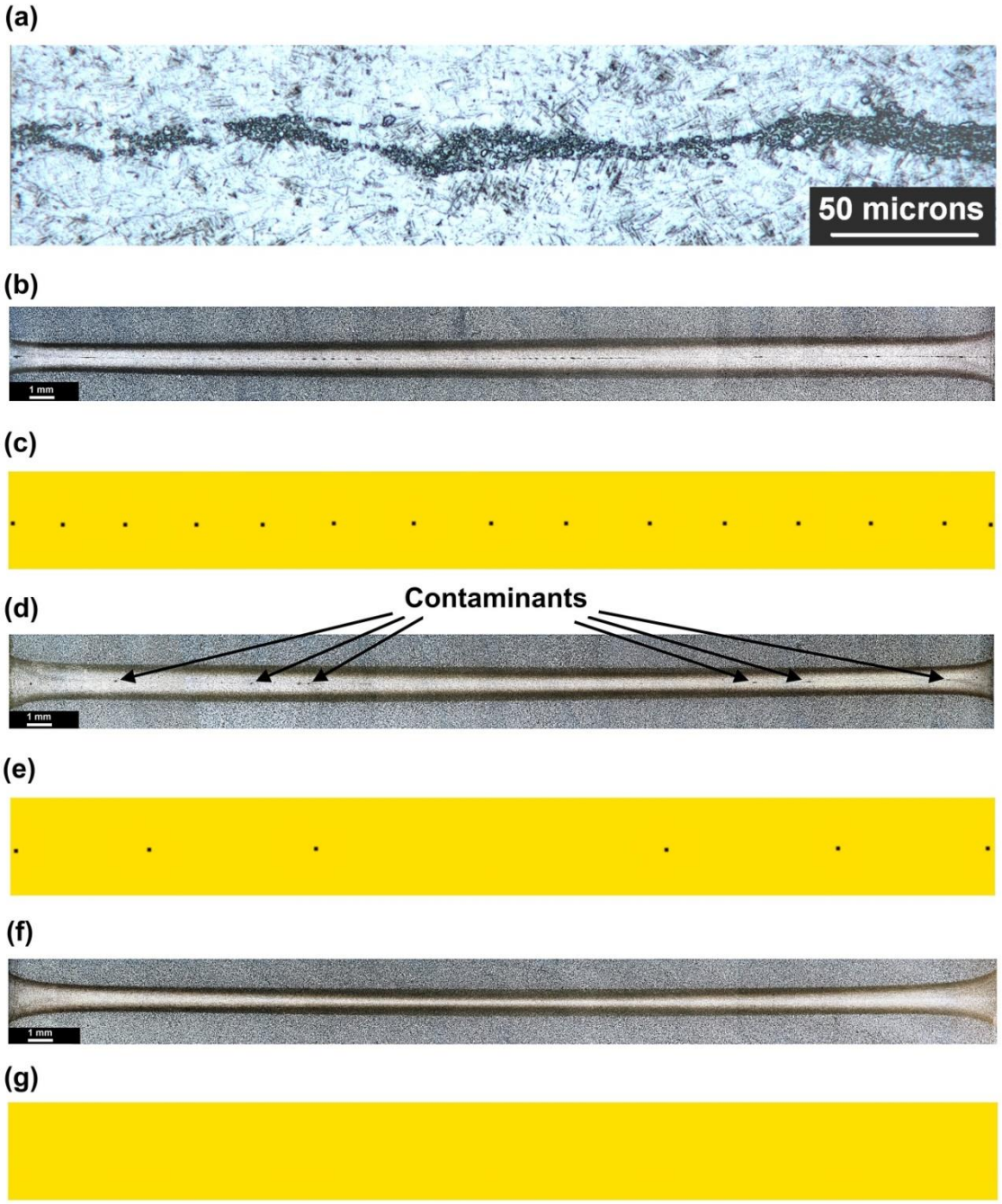

Figure 4.10: (a) High magnification of the contaminants present at the weld interface in weld number 11; and interface contaminant expulsion for an average rubbing velocity of 540 mm/s and an applied force of 100 kN for a burn-off of: (b) 0.5 mm (experiment) and (c) associated FEA, (d) 1 mm (experiment) and (e) associated FEA, (f) 3 mm (experiment) and (g) associated FEA. Note that the "null flow" point was removed for clarity from (e) and (g).

4.4 Conclusions

The following conclusions can be made from this chapter:

- Although the 2D models assumed no material expulsion perpendicularly to the direction of oscillation they still managed to capture the experimental trends, giving an insight into the process fundamentals for the LFW of Ti-6Al-4V workpieces.

- The measurements from the finite element analysis and the experimental microstructural observations suggest that the weld interface surpassed the beta-transus temperature and experienced dynamic recrystallisation.

- The finite element analysis demonstrated that the boundary temperature between the rapid flash formation and material with negligible flow was approximately 970 $^{\circ}$C. This corresponds to the beta-transus for Ti-6Al-4V.

- FEA used in conjunction with point tracking was an effective way to evaluate interface contaminant removal. The contaminants were increasingly expelled from the weld interface as the burn-off was increased.

- An increase of the applied force (pressure) increased the steady-state burn-off rate, interface strain rate, power input and interface shear force, whilst decreasing the interface temperature, flash thickness, TMAZ thickness, and the burn-off required to expel the point tracking/interface contaminants from the weld into the flash.

- An increase of the average rubbing velocity increased the interface temperature, strain rate, steady-state burn-off rate and power input, whilst having relatively little influence on the flash thickness, TMAZ thickness, interface shear force and the burn-off required to expel the point tracking/interface contaminants from the weld into the flash.

- For the process input combinations investigated it may be advantageous to produce Ti-6Al-4V linear friction welds using higher applied forces. This is because the material consumption to remove the interface contaminants will be reduced, increasing the safety factor for a set burn-off value.

The next chapter will present a similar investigation to the current chapter to show the impact of the workpiece geometry on Ti-6Al-4V linear friction welds.

Chapter 5: 2D Modelling of the Workpiece Geometry Effects

This chapter is an edited version of the following article:

*McAndrew, A. R., Colegrove, P. A., Addison, A. C., Flipo, B. C. D., Russell, M. J. & Lee, L. A. Modelling of the workpiece geometry effects on Ti-6Al-4V linear friction welds. Materials & Design **87**, 1087-1099 (2015).*

5.1 Introduction and Context

The majority of the investigations into the LFW process – modelling and experimental – have focused on characterising the "primary" process inputs, namely the amplitude, frequency, applied force/pressure and burn-off[3,7,48,64]. The effects of the workpiece geometry were often neglected. To the author's knowledge, only two journal publications specifically comment on the geometric effects; and both were concerned with titanium alloys. Karadge et al.[19], for an identical combination of process inputs, showed that the post-weld interface grain size and the thickness of the thermo-mechanically affected zone increased when larger workpieces were used. Sorina-Müller et al.[23] compared the interface temperatures between a "prismatic" and a "blade-like" geometry – the larger prismatic geometry had a higher peak temperature. The reasons why these phenomena occurred were not investigated in any significant detail. Furthermore, when 2D modelling Ti-6Al-4V linear friction welds, Turner et al.[7] and Schröder et al.[34,69] noticed "ripples" in the flash morphology, which was not observed in the previous chapter. The only major difference between the models was the size of the workpieces used, the in-plane width was larger in the previous chapter.

The research reported in this chapter investigated the reasons why the workpiece geometry affects the process behaviour. In particular, experimentally validated 2D models were used to investigate the workpiece geometry effects on the material flow, thermal fields and interface contaminant removal during the LFW of Ti-6Al-4V workpieces.

5.2 Methodology

5.2.1 Experimental

Several additional experiments were required to the data from chapter 3 to provide suitable model validation in this chapter. The experimental Ti-6Al-4V workpiece dimensions of interest for this study are displayed in Figure 5.1(a-d). The Ti-6Al-4V parent material had a bimodal alpha-beta microstructure, as shown in Figure 5.1(e).

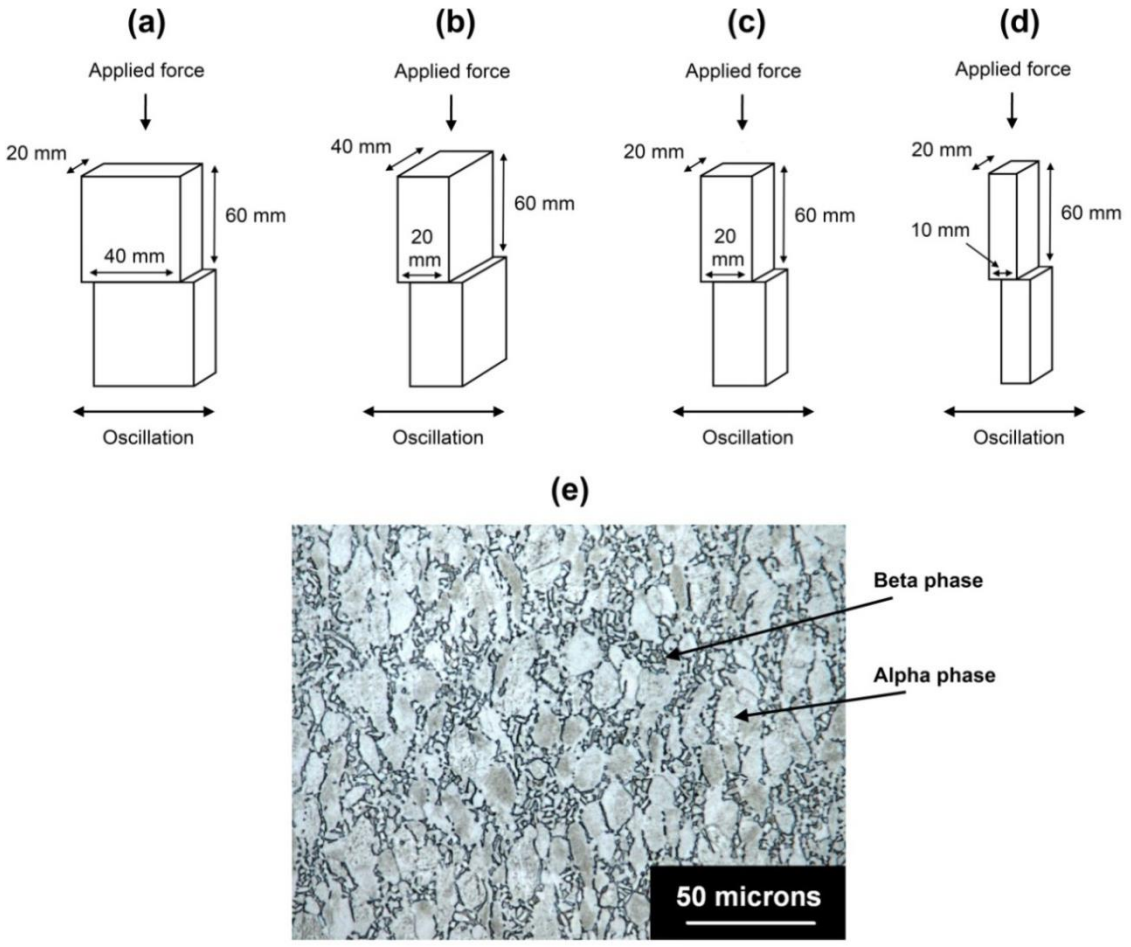

Figure 5.1: (a-d) An illustration of the workpiece dimensions and directions of motion and (e) Bi-modal alpha-beta microstructure of the material viewed under a microscope.

The experimental conditions investigated are displayed in Table 5.1. Note that the applied force was modified so that a constant normal pressure, p_n, of 125

MPa could be maintained between the different geometric conditions when the oscillatory displacement was at zero. For each experimental condition, the forging force applied during phase 4 was kept identical to the welding force applied in the earlier phases and was applied for 10 seconds. Also listed in table 1 is the average rubbing velocity. Worthy of note in Table 5.1, the in-plane width and out-of-plane dimension represent the in-plane width of the workpieces in the direction of oscillation and the dimension out-of-plane to oscillation, respectively. The welds were completed using the FW34 LFW machine at TWI, Cambridge. The faying surfaces were cleaned with acetone immediately prior to welding.

Table 5.1: Experiment conditions: (a) geometry and (b) process inputs

(a)

Weld	*Geometry*	*In-plane width (mm)*	*Out-of-plane dimension (mm)*	*Cross-sectional area (mm^2)*
32	*Fig.5.1 (a)*	*40*	*20*	*800*
42	*Fig.5.1 (b)*	*20*	*40*	*800*
43	*Fig.5.1 (c)*	*20*	*20*	*400*
44	*Fig.5.1 (d)*	*10*	*20*	*200*

(b)

Weld	*Oscillation frequency (Hz)*	*Oscillation amplitude (mm)*	*Average rubbing velocity ($mm \cdot s^{-1}$)*	*Applied force (kN)*	*Applied pressure (MPa)*	*Burn-off (mm)*
32	*50*	*2.7*	*540*	*100*	*125*	*3*
42	*50*	*2.7*	*540*	*100*	*125*	*3*
43	*50*	*2.7*	*540*	*50*	*125*	*3*
44	*50*	*2.7*	*540*	*25*	*125*	*3*

Metallographic specimens were produced from the experiments in Table 5.1, in accordance with the sectioning plane shown in Figure 5.2(a), i.e., they were sectioned and polished so that the centre of the weld may be viewed in-plane to the direction of oscillation. The sectioned samples were mounted and then ground using 240, 1200, 2500 and 4000 grit silicon carbide papers. After grinding, the sectioned samples were polished using colloidal silica on a micro-cloth and etched using a 3% hydrofluoric acid solution. The metallographic samples were viewed under a refractive microscope to determine the microstructure of the weld centre zone (WCZ) and the thermo-mechanically

affected zone (TMAZ), as shown in Figure 5.2(b). The distance from one TMAZ/parent material boundary to the other was also recorded and will be again be referred to as the TMAZ thickness in this chapter, as shown in Figure 5.2(b).

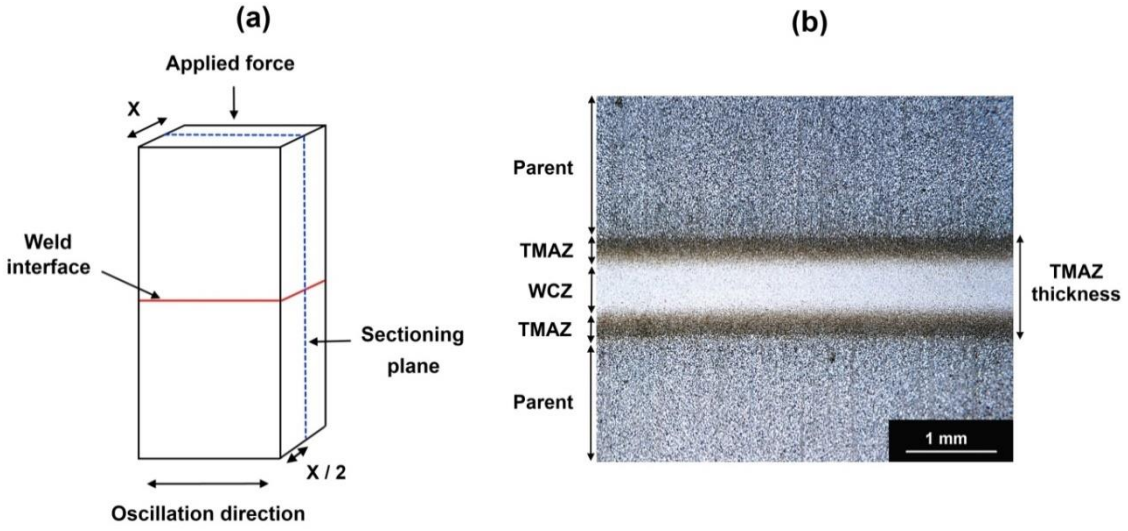

Figure 5.2: (a) Location of the sectioning plane where 'x' represents the out-of-plane dimension; and (b) a metallographic specimen showing the weld centre zone (WCZ), thermo-mechanically affected zone (TMAZ), parent material (Parent) and the TMAZ thickness.

Several other responses were recorded from the experimental welds. The steady-state burn-off rate was determined by calculating the gradient of the line when the burn-off occurred at a constant rate during phase 3. In addition, the total energy input to the weld interface for a phase, E_x, was estimated using the same methodology reported in Chapter 3 (see equation 3.4). To determine the *average* power input generated over a phase, the energy input for that phase was divided by the phase duration. The *average* interface shear force generated over a phase was also recorded.

5.2.2 Development of a Numerical Model

The 2D modelling approach used in this chapter is similar to the one reported in the previous. The only major difference was that the in-plane width of the

workpieces in the direction of oscillation was varied in this chapter. As such, only the key differences in the modelling are detailed.

The LFW process input combinations of interest for the modelling work are displayed in Table 5.2. Note that force per unit length is used to simulate the pressure in a 2D analysis. The purpose of the study was to model each process input combination detailed in Table 5.2 for each of the geometric conditions in Figure 5.1(a-d), therefore giving 16 conditions. However, the conditions in Figure 5.1(b) and (c) were suitably represented by the same 2D model – both having an in-plane width of 20 mm. This resulted in 24 models being required for the chapter investigation, 12 thermal and 12 plastic flow.

Table 5.2: Process inputs simulated by the models.

Input combination	*Oscillation amplitude (mm)*	*Oscillation frequency (Hz)*	*Average rubbing velocity (mm/s)*	*Simulated force per unit length (N/mm)*	*Simulated pressure (MPa)*	*Burn-off (mm)*
1	*2.7*	*50*	*540*	*125*	*125*	*3*
2	*1*	*30*	*120*	*125*	*125*	*3*
3	*2.7*	*50*	*540*	*40*	*40*	*3*
4	*2*	*30*	*240*	*40*	*40*	*3*

Thermal Model (Phase 1)

2D thermal models were developed in accordance with the dimensions shown in Figure 3.3, for in-plane widths of 40 mm, 20 mm and 10 mm. A uniform mesh size of 0.5 mm was used across the thermal models. The tooling extended to within 5 mm of the interface, as it did in the experiments.

Once again, a uniform heat flux (q') was applied across most of the workpiece interface which was linearly reduced to 50 percent of this value from the oscillation amplitude (*A*) away from the edge as shown in Figure 5.3. The heat flux was applied until the elements at the interface exceeded 1000 $^{\circ}$C (see Chapter 3). The heat flux was calculated by dividing the power input equation developed in Chapter 3 (see equation 3.12) by the average in-contact interface area of the workpieces over an oscillatory cycle. The heat flux was calculated for the 40 mm width case and was used for all width dimensions that used the

same combination of frequency, amplitude and force per unit length. The validity of this approach will be discussed later in this chapter.

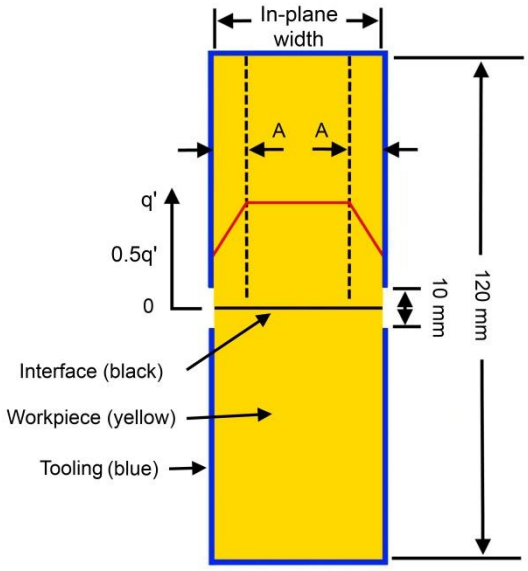

Figure 5.3: Schematic diagram of the 2D thermal model. (Note that the width and the 120 mm dimension are for the workpieces only – not the tooling).

Plastic Flow Model (Phase 2 onward)

Fully coupled thermo-mechanical 2D flow models were developed for the dimensions shown in Figure 5.4(a), for in-plane widths of 40 mm, 20 mm and 10 mm. The temperature profile generated from the thermal model at the end of phase 1 was mapped onto the single body to account for the phase 1 heating, as illustrated in Figure 5.4(b).

Once the desired burn-off had been reached, the oscillatory and forging motions, and plastic analysis were stopped to allow the models to cool down with a time step of 0.001 seconds.

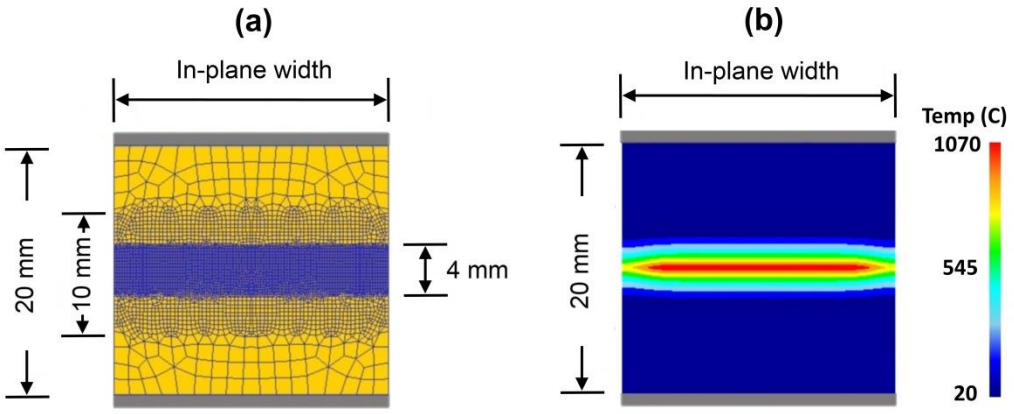

Figure 5.4: (a) Example of the mesh used for the plastic flow model and (b) an illustration of the assumed phase 1 thermal profile.

Several responses were recorded from the models. They included the steady-state burn-off rate, flash morphologies, thermal fields, strain rate, extent of the material being strained (FEA version of the TMAZ thickness), the average phase 3 power input and interface force, and the post oscillatory motion cooling rate. Finally, to understand the expulsion of the interface contaminants, the same approach used in the previous chapter was used. This involved placing tracked points across the interface, with a 1 mm gap between each tracked point, as shown in Figure 4.5(a). The evolution of the tracked points was monitored (see Figure 4.5(b)) and the amount of burn-off required to completely expel them into the flash was recorded, as shown in in Figure 4.5(c).

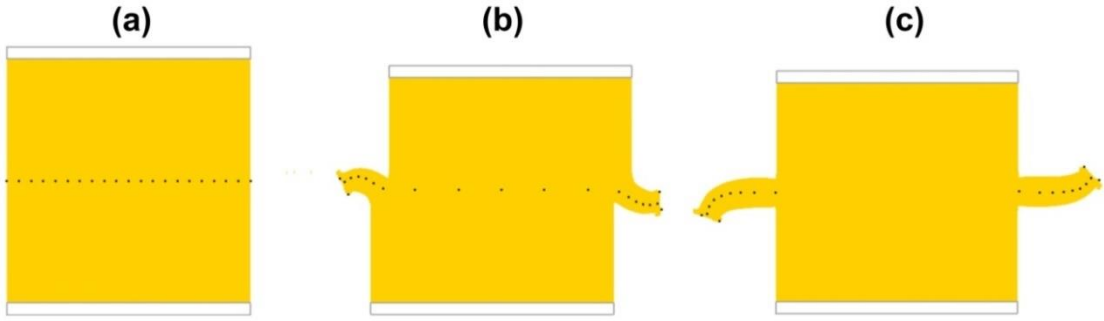

Figure 5.5: Point tracking evolution: (a) initial conditions, (b) flow during processing and (c) complete expulsion.

5.3 Results and Discussions

5.3.1 Experimental Phase One Phenomena

As shown in Table 5.3, the experimental phase 1 heat flux, shear stress and welding duration were dependent on the workpiece geometry. As the in-plane width was decreased the heat flux and the stress increased, whilst the duration decreased. These observations can be explained by the following theory. For a constant oscillation amplitude, a reduction of the in-plane width resulted in a greater percentage of the cross-sectional area not being in-contact over an oscillatory cycle. This resulted in a greater pressure variance and hence a larger *average* pressure. For example, the average pressure over a cycle of oscillation for weld 32 and weld 44 was approximately 131 MPa and 152 MPa, respectively. Larger pressures cause more of the interface asperities to be "squashed" onto each other – particularly whilst at the end of the displacement stroke when the in-contact surface area is decreased – and require a larger force to overcome the corresponding friction[28,32]. The increased force resulted in a greater energy input (see equation 3.4), which caused the interface material to heat and plasticise much more rapidly, thereby reducing the duration of phase 1.

Table 5.3: Experimental phase 1 responses for a rubbing velocity of 540 mm/s and a pressure of 125 MPa.

Weld	*Geometry*	*In-plane width (mm)*	*Cross-sectional area (mm^2)*	*Average phase 1 heat flux (W/mm^2)*	*Average phase 1 shear stress (N/mm^2)*	*Phase 1 duration (s)*
32	*Fig. 5.1 (a)*	*40*	*800*	*24.9*	*47.5*	*0.29*
42	*Fig. 5.1 (b)*	*20*	*800*	*27.9*	*53.4*	*0.25*
43	*Fig. 5.1 (c)*	*20*	*400*	*29.5*	*58.9*	*0.22*
44	*Fig. 5.1 (d)*	*10*	*200*	*52.1*	*104.6*	*0.15*

There are two further observations worth commenting on. First, the difference between the heat flux, shear stress and duration values in Table 5.3 for welds 42 and 43 was small. This suggests that the in-plane width had a larger influence on the weld output than the overall cross sectional area (weld 42 had

the same in-plane width but double the cross sectional area of weld 43). This phenomenon was also observed for a range of experimental outputs, as will be shown throughout this paper. Secondly, the values for the weld 44 heat flux and stress were almost twice as high as the other welds. This could have been a result of the greater pressure variance over a cycle of oscillation at these conditions or misaligned workpieces.

5.3.2 Material Flow, Thermal Fields and Contaminant Removal

Flash Formation and Morphology

The FEA demonstrated how the flash was generated in the direction of oscillation. When the oscillation amplitude was at maximum displacement the in-contact surface area was decreased. This caused a pressure increase, resulting in the cooler material being plunged farther into the highly viscous material. As the workpieces were brought back together, the cooler material forced the hotter viscous material from the interface. The mechanism by which the viscous material was forced from the weld was sensitive to the processing conditions simulated. Two primary flash formation mechanisms were identified, one that produced “ripples” in the flash and one that produced a “smooth” morphology, as shown in Figure 5.6. This finding is in agreement with the modelling work on flash formation reported by Turner et al.[7,70] and Schröder et al.[34,69].

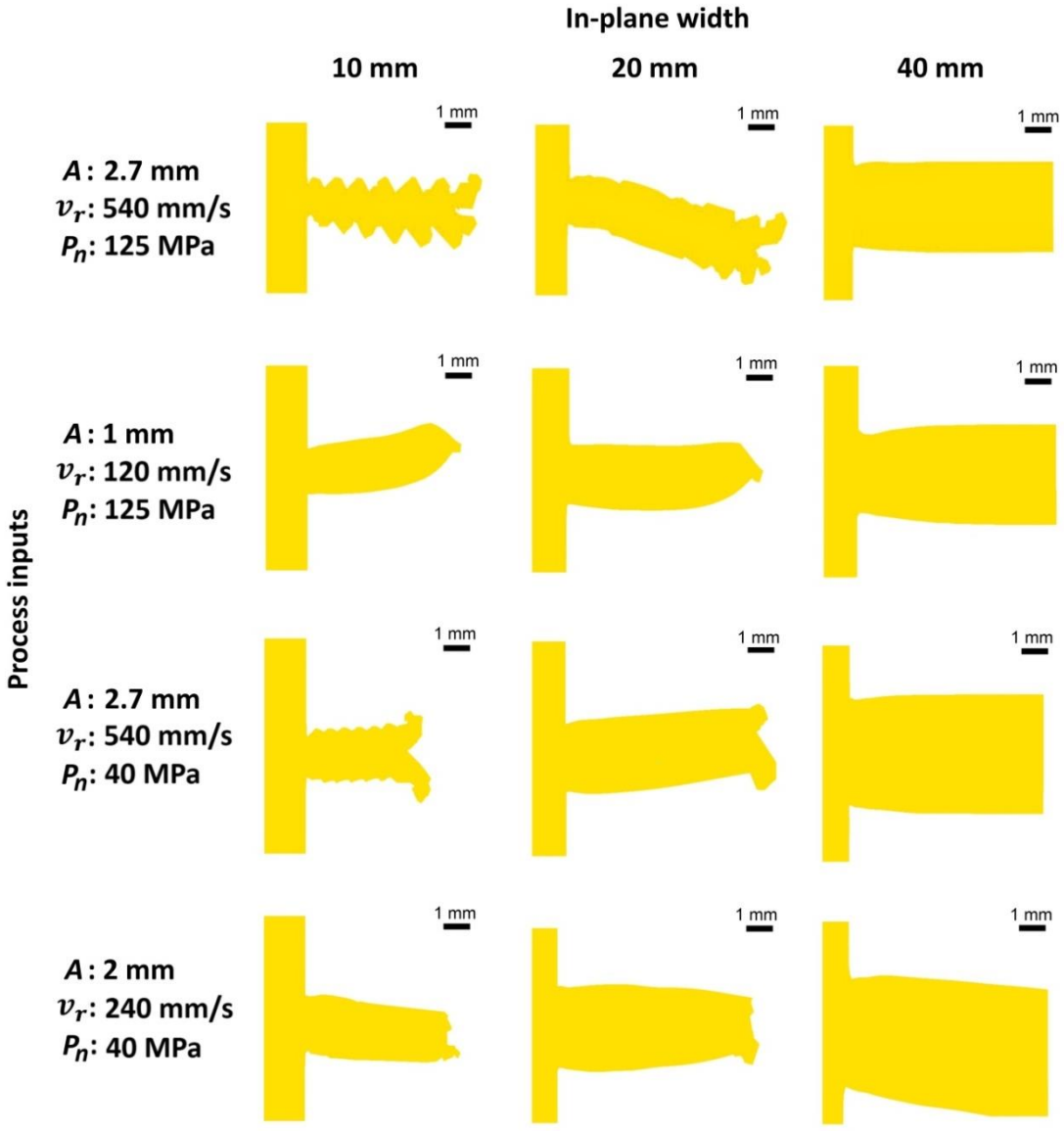

Figure 5.6: FEA flash morphologies as a function of the amplitude, A; average rubbing velocity, v_r; pressure, p_n; and in-plane width. Note that not all of the flash is shown for the 40 mm cases.

As originally reported by Schröder et al.[34] and supported by the present study, the ripple morphology occurred when the flash separated from the workpieces as the maximum amplitude displacement position was approached, as shown in Figure 5.7(a). According to the FEA, at the point of separation, very high strain rates (greater than 1500 s^{-1}) were produced, see Figure 5.7(d). The high strain rate regions corresponded to significant, local yielding. This phenomenon exposed a fresh layer of highly heated material which was then sheared from

the interface into the flash as the oscillatory motion was reversed. Each sheared layer corresponded to a ripple in the flash, see Figure 5.7(a). In agreement with Schröder et al.[34], the FEA demonstrated that the ripples were more noticeable when the ratio between the TMAZ thickness and the oscillation amplitude was reduced. For example, as shown in Figure 5.6, for a comparable amplitude, a reduction of the in-plane width or an increase of the pressure resulted in more noticeable ripples – the TMAZ thickness was reduced under these conditions. In addition, these conditions also decreased the flash thickness, see Figure 5.6. Possible reasons for why the TMAZ and flash thicknesses were reduced and the strain rate increased are discussed in greater detail in section 5.3.2 – *Energy, Force and Thermal Analysis*. The experimental work supported the modelling findings; ripples became more defined as the in-plane width was reduced as can be seen by comparing Figure 5.8(a) to Figure 5.8 (b). As shown in Figure 5.7(b), the "smooth" morphology was produced when the flash did not separate from the workpieces. This resulted in the interface material being extruded into the centre of the flash as the oscillatory motion was reversed.

Regardless of the flash morphology type, for all cases the modelling work demonstrated that the boundary temperature between the rapidly flowing viscous material and the workpiece material with negligible flow was approximately 970 $^{\circ}$C (±30 $^{\circ}$C), as shown in Figure 5.7(c). This is in good agreement with the previous chapters, which showed that significant material softening occurs at temperatures corresponding to the beta-transus, allowing for rapid material flow. Furthermore, although the extent of highly heated material was generally constant across the in-plane width of the workpieces it increased toward the extremities of the weld – see Figure 5.7(c) – possibly due to the heat from the flash conducting back into the periphery of the workpieces[157].

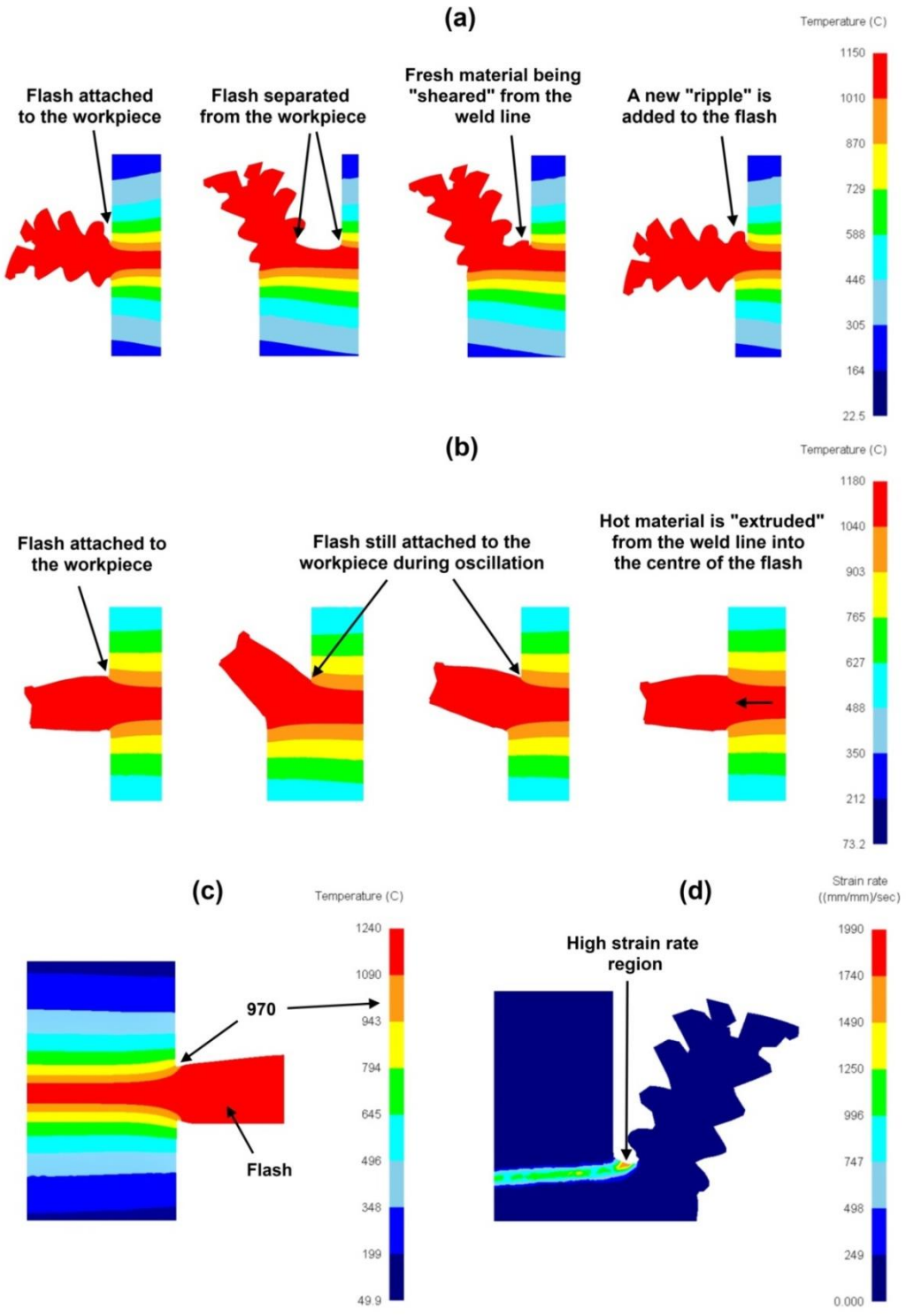

Figure 5.7: Flash formation and morphology determined from the FEA, showing: (a) the mechanisms behind the ripple morphology, (b) the mechanisms behind the smooth morphology, (c) the boundary temperature between the rapidly flowing viscous material and the workpiece material with negligible flow, and (d) region of high strain rate.

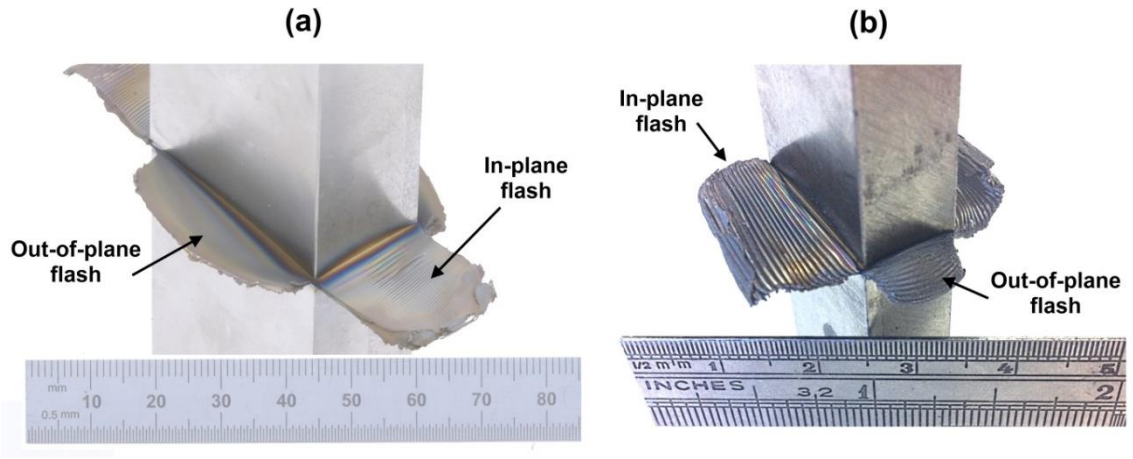

Figure 5.8: Flash morphology for: (a) 40 mm in-plane width and (b) 10 mm in-plane width.

Figure 5.9 shows the effects of the processing conditions on the rate of flash formation (burn-off rate). Note that the regression analysis graph in Figure 5.9(b) – along with all other regression graphs from this point onward – presents the results as a function of the average rubbing velocity. As stated previously, this was because the previous chapters showed that changing either the amplitude or frequency whilst keeping the rubbing velocity constant had a relatively weak effect on the results for the process input range of interest in this thesis.

The flash formation rate increased with an increase of the rubbing velocity or pressure, or a reduction of the in-plane width. This was due to the following: An increase of the rubbing velocity caused a faster rate of shearing/extruding; an increase of the pressure caused the cooler workpiece material to be plunged further into the viscous interface material, resulting in a greater amount of material being sheared/extruded from the interface with each oscillation; and, for a comparable set of process inputs, a reduction of the in-plane width removed a higher percentage of the total interface material with each oscillatory cycle, as shown in Figure 5.10.

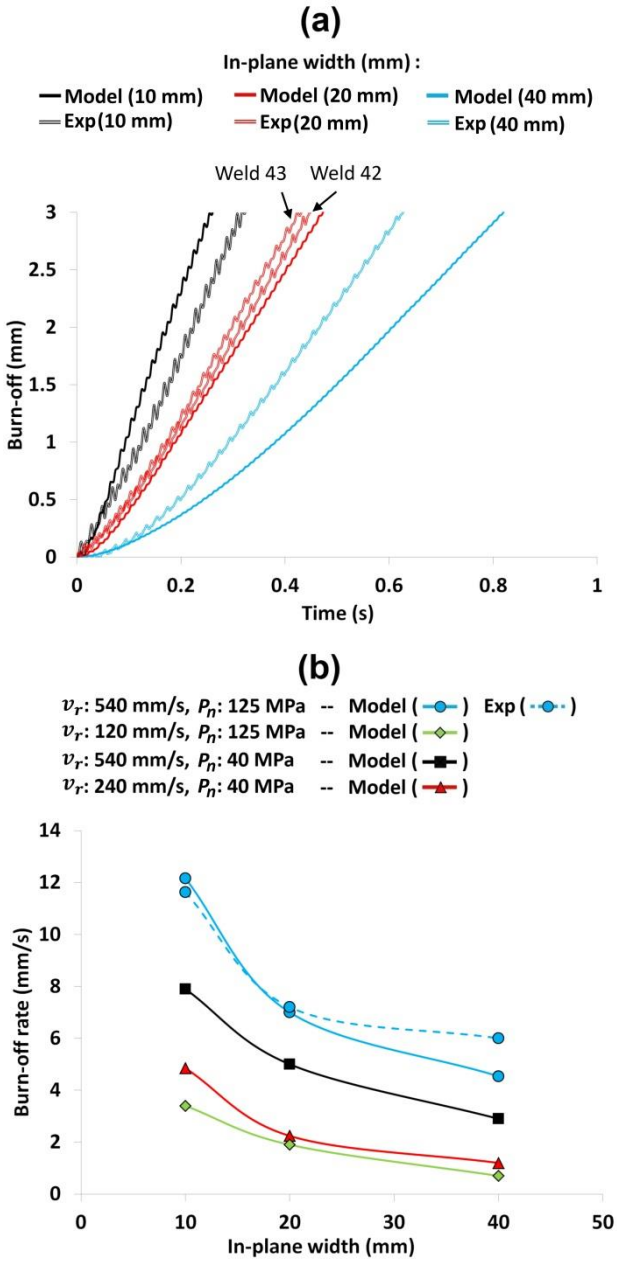

Figure 5.9: A comparison of the FEA (Model) and experimental (Exp) results for: (a) the burn-off during phases 2 and 3 vs. time as a function of the in-plane width for an average rubbing velocity of 540 mm/s and a pressure of 125 MPa; and (b) burn-off rate during phase 3 as a function of the in-plane width, average rubbing velocity, v_r, and the normal pressure, p_n.

The difference between the *experimental* 20 mm in-plane widths, i.e. experimental weld numbers 42 and 43 as illustrated in Figure 5.9(a), was minimal. This further illustrates that the in-plane width has a greater overall effect on the characteristics of a weld than the total cross-sectional surface

area. Consequently, an average of the burn-off rates for welds 42 and 43 was used for the 20 mm value presented in Figure 5.9(b). Unless otherwise stated this approach was used for all of the experimental 20 mm in-plane width values presented in the subsequent regression graphs, i.e., an average of the experimental weld 42 and 43 values was taken due to the difference between the two individual values being minimal.

According to the results in Table 5.3, the assumption of a constant heat flux during phase 1 for the models that had the same rubbing velocity and pressure (see the thermal modelling sub-section in section 5.2.2) was not fully justified. Despite the assumption, the burn-off history trends between the models and experiments were in good agreement, as shown in Figure 5.9(a). This was due to the models entering phase 3 prior to any significant burn-off occurring, i.e. less than 0.5 mm. Once in phase 3, the heat generation, and therefore the thermal profiles, were dependent on the material's constitutive data. Consequently, the thermal profile used to account for the heating during phase 1 had relatively little influence on the results – Turner et al.[7] also made similar conclusions in their modelling work of Ti-6Al-4V.

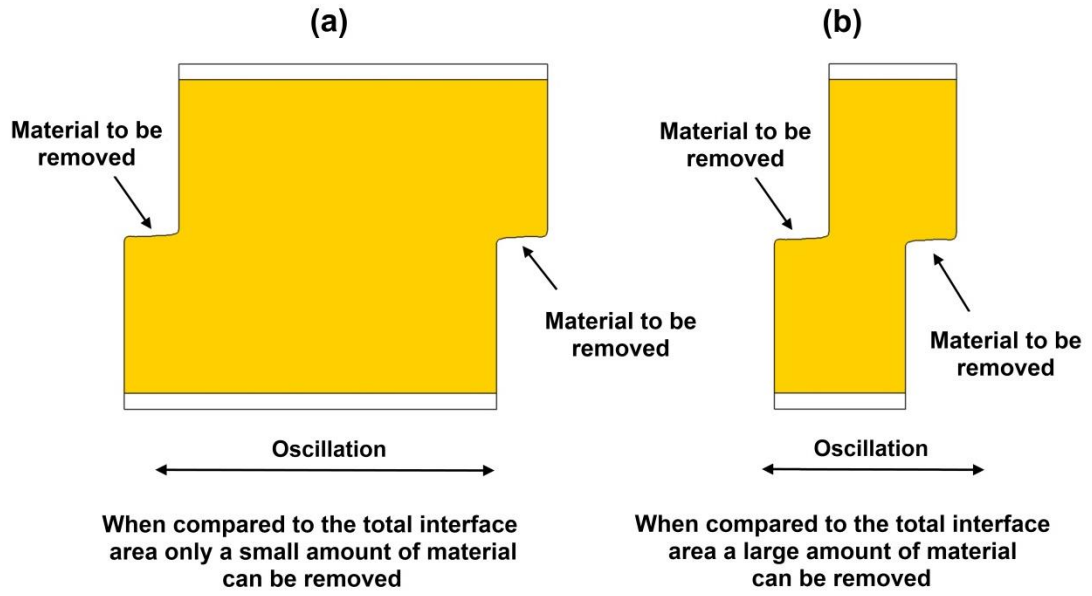

Figure 5.10: Workpiece in-plane width effects on the flash formation rate for: (a) large in-plane widths and (b) small in-plane widths.

In most cases, however, the 2D models under-predicted the experimental burn-off rate. This was primarily due to the 2D models not accounting for the experimental material expulsion out-of-plane to the direction of oscillation. The out-of-plane material expulsion decreased as the ratio of the in-plane width to the out-of-plane dimension was reduced, as shown in Figure 5.8. In addition, the weight of the flash was measured in the in and out-of-plane directions to oscillation for the experimental welds and the results are displayed in Table 5.4. Consequently, as the experimental out-of-plane material expulsion was reduced, so was the modelled under-prediction, as shown in Figure 5.9. Furthermore, Table 5.4 also shows that there is a strong correlation between the ratio of the in-plane to the out-of-plane dimension and the percent of directional material expulsion. The 10 mm width model slightly over predicted the burn-off rate, which was probably due to either variance in the experimental results or the difference between the flow stress values in the experimental weld and the simulated weld. As shown in Figure 5.9(a), the burn-off histories for all of the models did not exhibit such a defined stepwise shortening pattern when compared to a comparable experiment. This could have been due to the models not accounting for the out-of-plane material expulsion, a misalignment of the experimental workpieces, the difference between the flow stress values, or a combination of these factors.

Table 5.4: Experimental flash measurements.

Weld	*Geometry*	*In-plane width (mm)*	*Out-of-plane dimension (mm)*	*Ratio of in-plane to out-of-plane*	*% of flash expelled in-plane*	*% of flash expelled out-of-plane*
32	*Fig. 5.1 (a)*	*40*	*20*	*2*	*53.5*	*46.5*
42	*Fig. 5.1 (b)*	*20*	*40*	*0.5*	*85.4*	*14.6*
43	*Fig. 5.1 (c)*	*20*	*20*	*1*	*79.8*	*20.2*
44	*Fig. 5.1 (d)*	*10*	*20*	*0.5*	*87.6*	*12.4*

Energy, Force and Thermal Analysis

The results for the modelled and experimental peak interface temperature, average heat flux, TMAZ thickness, average interface stress and peak interface strain rate are displayed in Figure 5.11. The peak temperature and strain rate were recorded from the centre point of the interface. As shown in Figure 5.11,

regardless of the in-plane width, the process inputs (pressure and average rubbing velocity) had the same effect on these outputs as observed in previous chapters. Consequently, they are not discussed in significant detail in this chapter as the focus is on the geometry. The process input effects were as follows:

- An increase of the pressure increased the interface strain rate, interface shear stress and heat flux, whilst decreasing the interface temperature and TMAZ thickness.

- An increase of the average rubbing velocity increased the interface temperature, strain rate and heat flux, whilst having a minimal effect on the TMAZ thickness and interface shear stress.

As shown in Figure 5.11(a), the interface temperature decreased as the in-plane width was decreased. This phenomenon might be explained by the relationship between the heat flux and the burn-off rate. For a comparable rubbing velocity and pressure, a reduction of the in-plane width increased the burn-off rate by a greater percentage than it did the heat flux, as can be seen by comparing the FEA results in Figure 5.9(b) and Figure 5.11(b). Although more heat per unit area went into the weld, the heat was expelled at a much faster rate. This reduced the time the heat had to conduct back from the interface causing the extent of the band of highly heated material to be reduced, see Figure 5.12. Consequently, with the smaller in-plane widths, the material at a comparable point farther back from the interface was much cooler. When this cooler material reached the interface it effectively cooled the weld, producing a lower interface temperature. These findings suggest that it may be beneficial to oscillate the workpieces along the shorter of the two interface-contact dimensions. This is because the interface temperature is likely to be reduced, minimising the residual stresses formed during the post oscillatory motion cooling[61,70]. The relatively cooler thermal fields for the welds that were produced with smaller in-plane widths may also be beneficial from a microstructural perspective, as will be discussed in section 5.3.3.

The thinner band of highly heated material generated with the smaller in-plane widths was responsible for reducing the TMAZ thickness, as shown in Figure 5.11(c). Consequently, the extent of the band of highly heated material and the TMAZ thickness are directly related. The trends for the TMAZ thickness were captured by the models, but the exact values did not match. The difference between the experimental and modelling flow stress values may have contributed to the discrepancies. The experimental welds also experienced extra material expulsion due to the forging force during phase 4, which may have reduced the experimental TMAZ values. In addition, for the models, the distance between the points of negligible strain on either side of the interface was recorded, whereas, in the experiments, the final, observable TMAZ thickness was recorded, which may not have coincided with the points of negligible strain.

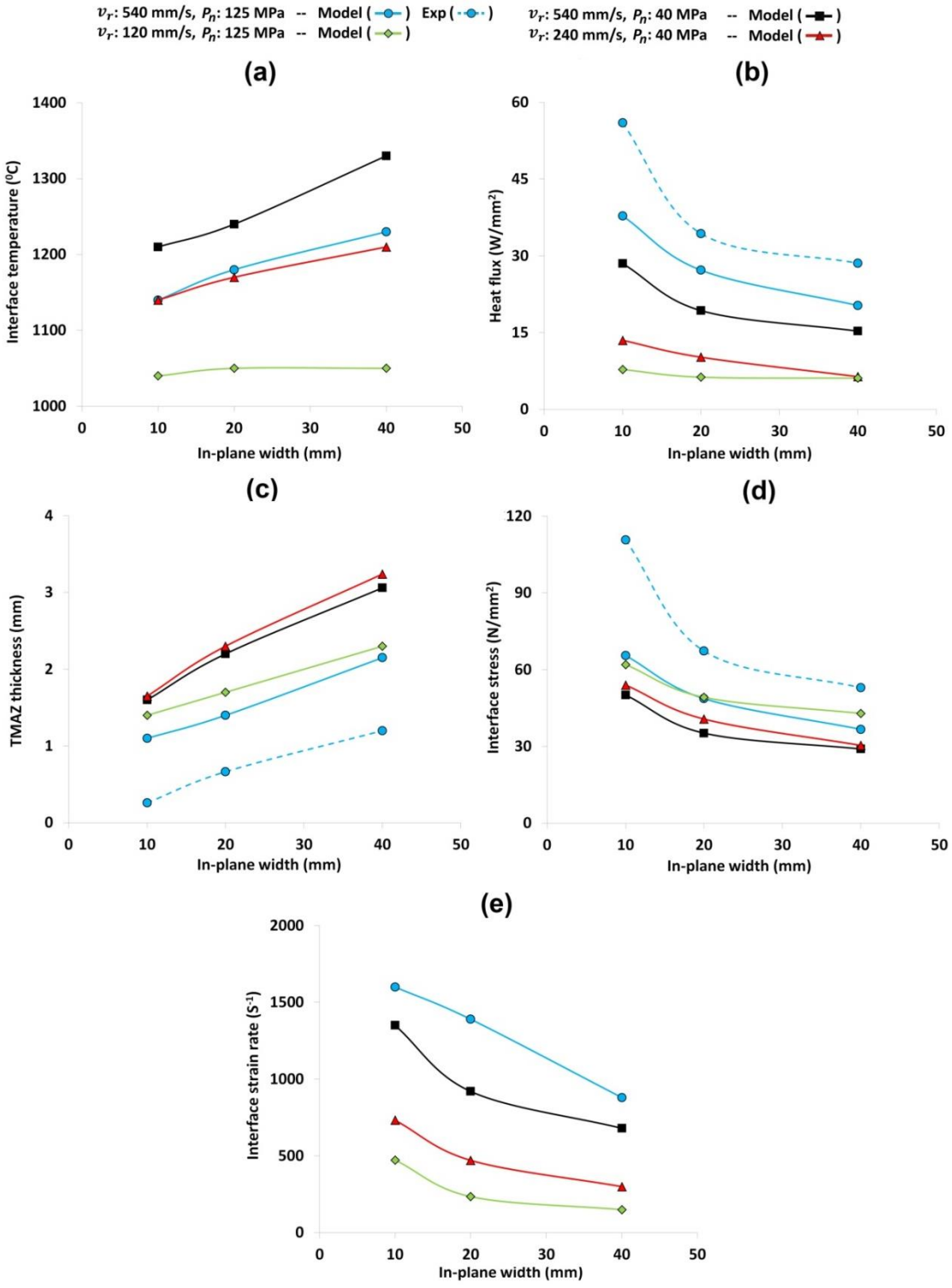

Figure 5.11: FEA (Model) and experimental (Exp) results as a function of average rubbing velocity, v_r, pressure, p_n, and in-plane width for the phase 3: (a) interface temperature, (b) average heat flux, (c) TMAZ thickness, (d) average interface stress, and (e) interface strain rate.

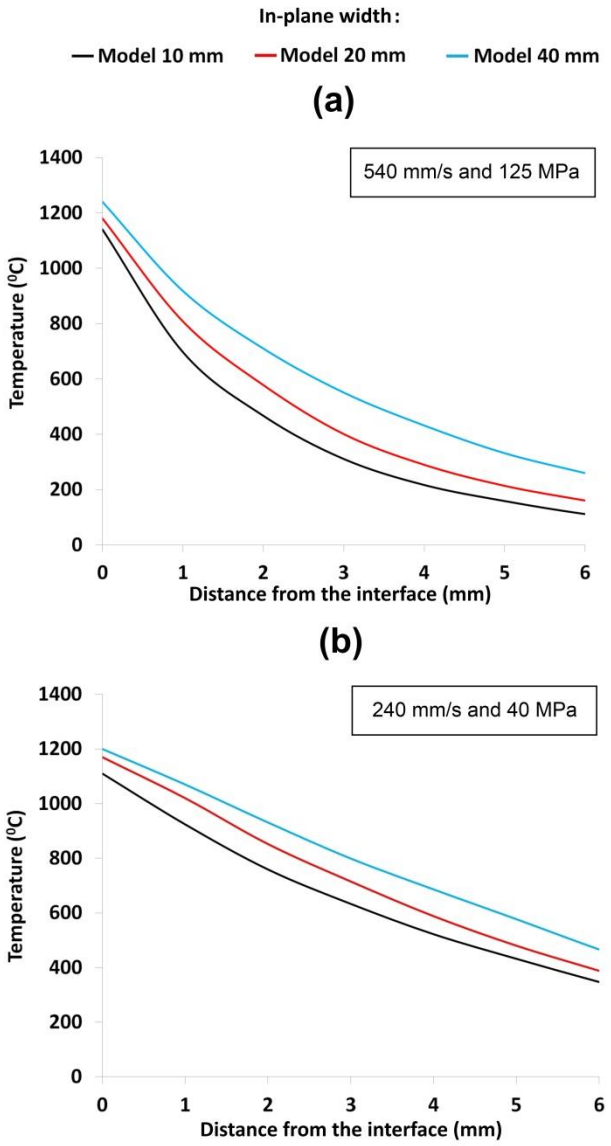

Figure 5.12: FEA results for the generated phase 3 thermal profiles as a function of the in-plane width for an average rubbing velocity, v_r, and pressure, p_n, of: (a) 540 mm/s and 125 MPa and (b) 240 mm/s and 40 MPa. The thermal profiles were symmetric around the interface.

The interface stress and heat flux increased with a reduction of the in-plane width, as shown in Figure 5.11(d) and (b), respectively. This was probably due to a reduction of the interface temperature at these conditions, see Figure 5.11(a). The lower interface temperature required a greater in-plane force per unit area to maintain oscillation, which increased the heat flux (see equation 3.4). As shown in Figure 5.11(b), the peak strain rate also increases with a reduction of the in-plane width, which was probably due to the greater force

being concentrated to a smaller area of flowing material (see Figure 5.11(c)). Once again, the strain rates recorded from the models in this chapter were in closer agreement to those reported by Turner et al.[7] (500 s^{-1} to 2500 s^{-1}) and Chamanfar et al.[118] (1520 s^{-1}) to those reported by Vairis and Frost[3] (4.6 s^{-1}).

For all conditions, the models under-predicted the average interface stress and, consequently, the heat flux, as shown in Figure 5.11(d) and Figure 5.11(b) respectively. This was probably due to two main factors. The first, the models did not account for the heat that was expelled into the flash in the direction out-of-plane to oscillation. This may have resulted in the modelled weld being comparably hotter than the experimental one. Consequently the models may have had a higher interface temperature, requiring a lower force to maintain oscillatory motion; the lower force would have also reduced the power input. The second factor was due to the difference between the flow stress values of the experimental weld and the modelled weld. As the flash expulsion perpendicular to the oscillation decreased it was expected that more of the expelled heat would be have been accounted for, therefore reducing the under-prediction. This was not observed and leads the author to conclude that the main cause for the discrepancy was a difference between the flow stress values in the experimental and the simulated welds.

Interface Contaminant Removal

Rich and Roberts[171] suggested that the removal of contaminants from the interface of a friction weld should not be considered as being dependent on the burn-off alone. Rather, the burn-off should be adjusted depending on the extent of flowing material / TMAZ thickness. The results from this chapter support this hypothesis for the linear friction welding of Ti-6Al-4V. For example, as shown in Figure 5.13, the burn-off required to remove the point tracking contaminants from the weld into the flash decreased with the in-plane width. This was due to the extent of flowing material (i.e. material above 970 $^{\circ}$C) being reduced with smaller in-plane widths, see Figure 5.12, meaning less material was required to be removed to expel the point tracking. These findings also suggest that that it may be beneficial to oscillate the workpieces along the shorter of the two

interface-contact dimensions. This is because the burn-off required to remove the contaminants from the weld into the flash is likely to be reduced. Hence for the same burn-off, the factor of safety on contaminant removal is greater.

As shown in Figure 5.13, the rubbing velocity had relatively little effect on the required burn-off, whilst an increase of the pressure reduced the value. This was for the same reasons reported in the previous chapter.

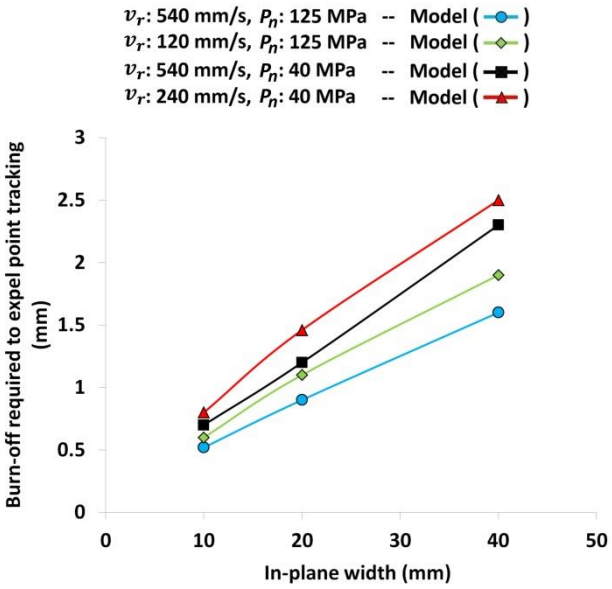

Figure 5.13: FEA results for the amount of burn-off required to expel the point-tracking as a function of the in-plane width, average rubbing velocity, v_r, and pressure, p_n.

5.3.3 Microstructural Observations

The interface region of the experimental Ti-6Al-4V workpieces experienced significant microstructural changes. The welds were similar in appearance in the fact that they had several distinct zones – a weld centre zone (WCZ), a thermo-mechanically affected zone (TMAZ) and the parent material. Due to the structural stability of Ti-6Al-4V below temperatures of 800 °C[76,128] it was often difficult to detect a purely heat affected zone. This is in good agreement with the literature[6,41,61,62].

According to the models the WCZ of the experiments exceeded the beta-transus temperature (see Figure 5.11(a)). The WCZ experienced large strains and strain rates (see Figure 5.11(e)) which would have resulted in significant, dynamic recrystallisation of the high-temperature beta-phase material[106],[131]. Upon cooling the recrystallised beta-phase material transformed into a Widmanstätten microstructure, as shown in Figure 5.14.

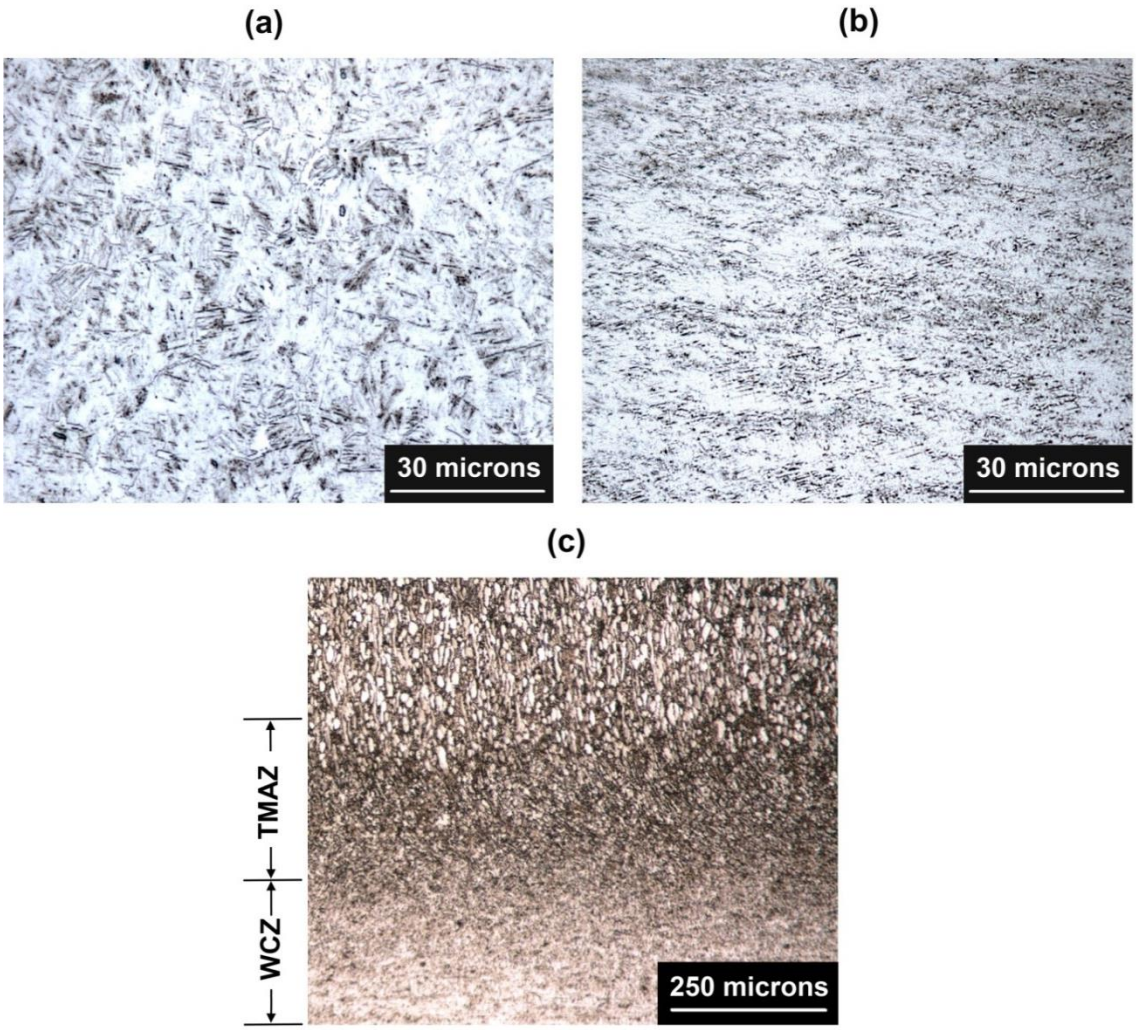

Figure 5.14: Ti-6Al-4V microstructure: (a) Widmanstätten at the WCZ for weld 43 (20 mm in-plane width), (b) Widmanstätten at the WCZ for weld 44 (10 mm in-plane width), and (c) deformed, elongated and re-orientated TMAZ grains for weld 32 (40 mm in-plane width). Note that the microstructure appears finer in (b) when compared to (a).

For the same combination of process inputs, the microstructure appeared much finer in the welds that were produced with smaller in-plane widths (compare Figure 5.14(a) and (b)). This finding is in good agreement with Karadge et al.[19].

The finer microstructure for the welds that were produced with the smaller in-plane widths could have been due to the higher strain rates experienced (see Figure 5.11(e)). This would have caused more recrystallisation during processing, refining the prior beta grains[128,131]. Furthermore, according to Gil et al.[172], the Widmanstätten morphology is finer with faster cooling rates. The modelling work showed that for an average rubbing velocity of 540 $mm \cdot s^{-1}$ and a pressure of 125 MPa the centre of the weld interface cooled from the beta transus temperature to 500 °C at a faster rate for the smaller in-plane widths. For example, for 40 mm, 20 mm and 10 mm in-plane widths the cooling rate was approximately 110 $°C \cdot s^{-1}$, 210 $°C \cdot s^{-1}$ and 320 $°C \cdot s^{-1}$, respectively. This phenomenon was due to the narrower band of highly heated material produced with smaller in-plane widths (see Figure 5.12(a)). The narrower band of heated material had less heat to be conducted from the interface region into the bulk material, allowing for a faster rate of cooling. The more refined WCZ microstructure for the welds produced with the smaller in-plane widths may, according to the literature, possess superior mechanical properties[45,173,174].

Due to the original alpha-grains of the parent material being present, the material in the TMAZ did not appear to have exceeded the beta-transus temperature or experienced any noticeable dynamic recrystallisation. However, many of the TMAZ grains were deformed, elongated and re-orientated toward the direction of oscillation, as shown in Figure 5.14(c), which is in agreement with the literature[6,20].

5.4 Conclusions

The primary conclusions from this chapter are as follows:

- The 2D models captured many of the experimental weld trends and gave good insight into the LFW process for the joining of Ti-6Al-4V workpieces with different sizes.

- For the LFW conditions evaluated, the in-plane width of the workpieces in the direction of oscillation (in-plane width) generally had a greater effect on the experimental welding process characteristics than the cross-sectional area.

- The flash morphology was sensitive to the processing conditions. The ripple morphology became more noticeable as the ratio between the TMAZ thickness and the amplitude was reduced.

- The experimental weld interface consisted of a Widmanstätten microstructure, which became finer when the in-plane width was reduced.

- A reduction of the in-plane width also increased the steady-state burn-off rate, strain rate and required heat flux, whilst decreasing the interface temperature, extent of highly heated material, TMAZ thickness and the burn-off required to remove the point tracking/interface contaminants from the weld into the flash.

- Regardless of the in-plane width used during processing, the process inputs had the same general effects on the weld as detailed in chapter 4.

- The burn-off required to remove the interface contaminants into the flash should not be considered as a stand-alone value, but rather as a function of the generated TMAZ thickness. As the TMAZ thickness is increased more burn-off is required to expel the interface contaminants. These findings suggest that it may be beneficial to oscillate the workpieces along the shorter of the two interface-contact dimensions. This is because the burn-off required to remove the interface contaminants into the flash is likely to be reduced. Hence, for the same burn-off, the factor of safety on contaminant removal is greater. Furthermore, these conditions are also likely to decrease the interface temperature, which may also offer additional process benefits.

The next chapter will investigate some select 3D models to see whether they address the shortcomings of the 2D models identified in this and the previous chapter. Furthermore, a 3D model is also presented to understand the material flow at the “triple point” in the keystone weld.

Chapter 6: 3D Modelling of Ti-6Al-4V Linear Friction Welds

This chapter is an edited version of the following article:

McAndrew, A. R., Colegrove, P. A., Addison, A. C., Flipo, B. C. D. & Russell, M. J. 3D modelling of Ti-6Al-4V linear friction welds. (*To be submitted*).

6.1 Introduction and Context

During the last five years considerable effort has been made to develop 3D LFW process models[23,45,78,84,101,111,121,155,156,158]. For example, Fratini et al.[78] modelled steel workpieces to investigate the effects of the process inputs on the temperature distribution. Li et al.[121,156] modelled steel and titanium workpieces to investigate the temperature distribution and axial shortening. Grujicic et al.[45,84] also investigated steel and titanium workpieces to show how the process can affect the microstructure. All of these works used either the first or second modelling approach, illustrated in Figure 2.30(a) and (b), respectively. As discussed in the literature review, an increasingly adopted approach for the 2D modelling of Ti-6Al-4V linear friction welds is the “single-body” approach[34,69,70]. This approach gives better insight into the material flow and thermal fields post phase 1 due to the adhesion being modelled. To date, with the exception of one very recent publication by Li et al.[111], the “single body” approach has not been applied to 3D geometries. Li et al.[111] used the 3D “single body” approach to investigate the effects of “micro-swinging” on Ti-6Al-4V welds, as detailed in the literature review. The 3D model by Li et al.[111] used the Johnson-Cook flow strength model, which assumes a linear reduction in strength up to the melting temperature, which does not occur in practice. This raises questions as to whether the true interface flow behaviour was captured by the model.

This chapter details the development of 3D single-body models for Ti-6Al-4V linear friction welds, using the flow stress data described in Turner et al.[7], to:

- Compare with the 2D models used in chapters 4 and 5. In particular to see if the 3D model, which includes the effects of the out-of-plane material expulsion, supports the 2D modelling results.

- Investigate the “triple point” material flow in the “keystone” weld, a weld where multiple surfaces must be joined concurrently.

6.2 Methodology

The methodology is discussed in two parts, the first deals with the 3D modelling of single-surface contacting workpieces (standard geometry) and the second deals with the keystone geometry.

6.2.1 Development of a 3D Model (Standard Geometry)

The process inputs and geometry of interest are shown in Table 6.1 and Figure 6.1, respectively. The only difference between the two conditions is the direction of oscillation. Throughout this chapter the 3D models that represent conditions 1 and 2, will be referred to as 3D modelling condition 1 and 2, respectively.

Table 6.1: Process inputs of interest.

Condition	*Oscillation frequency (Hz)*	*Oscillation amplitude (mm)*	*Average rubbing velocity ($mm \cdot s^{-1}$)*	*Applied force (kN)*	*Applied pressure (MPa)*	*Burn-off (mm)*	*Geometry*
1	*50*	*2.7*	*540*	*100*	*125*	*3*	*Figure 6.1 (a)*
2	*50*	*2.7*	*540*	*100*	*125*	*3*	*Figure 6.1 (b)*

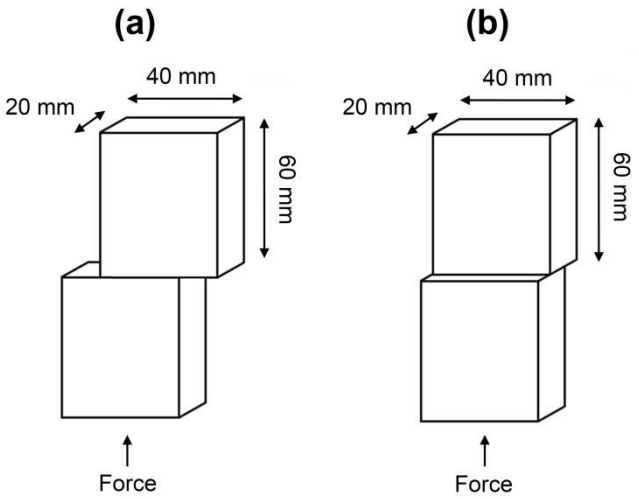

Figure 6.1: Geometric conditions of interest where the oscillations took place in the: (a) 40 mm dimension and (b) the 20 mm dimension.

The 3D models developed to describe the conditions in Table 6.1 used the same approach reported in the previous chapters, i.e. the single-body approach. The development of the phase 1 thermal model and the fully coupled thermo-mechanical plastic flow model are described below.

Thermal Model (Phase 1)

The thermal models were developed using the same methodology reported in the previous chapter (see section 5.2.2 – Thermal model (Phase 1)). Once the 2D models were complete the mesh was extruded into the third dimension to create a 3D model, as illustrated in Figure 6.2

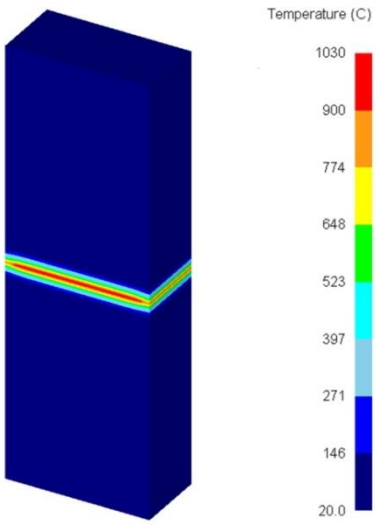

Figure 6.2: An illustration of the thermal model profile for 3D modelling condition 1.

Plastic Flow Model (Phase 2 onward)

The coupled thermo-mechanical models were developed using the same methodology in the previous chapter (see section 5.2.2 – Plastic Flow Model (Phase 2 onward)) to represent the conditions in Table 6.1. Once the 2D models were complete some modifications were made:

- The developed 2D models were extruded into the third dimension by 20 mm and 10 mm, as shown in Figure 6.3(a) and (b), respectively; i.e. only 50% of the weld was modelled. This was deemed acceptable because the plastic deformation is approximately symmetric around the XZ plane[24] (see Figure 6.3 for plane definition). This approach reduced the computational time.

- The hexahedral elements were replaced with tetrahedral elements to allow highly automated re-meshing. Re-meshing of 3D hexahedral elements requires user intervention and is labour intensive in DEFORM-3D[167].

- Mesh windows with the same dimensions defined in the previous chapters were initially implemented, however this resulted in the mesh at

the model centre coarsening when a re-mesh was initiated, as shown in Figure 5.4(c). This coarsening severely affected the modelling responses, so this approach was abandoned and a uniform mesh applied throughout the workpieces. In accordance with the literature (see section 2.6.2 – Reference Frames and Meshing) an element size of 0.5 mm was used for the uniform mesh.

- A “retrospective” analysis was used for the 3D models. This involved using the amplitude and burn-off displacement histories from an experiment for the model’s process inputs. The advantage of this approach is that the process inputs can be defined as “paths” instead of “forces” allowing for the conjugate gradient solver to be used. According to the DEFORM user’s manual the conjugate gradient solver reduces the computational time and memory storage size[167]. The oscillation and burn-off displacements were provided by the lower and upper dies, respectively. The displacement histories used to replicate the conditions in Table 6.1 were taken from experiments 32 and 42 (see Table 5.1) and are displayed in Figure 6.4. The displacement histories inputted to the models began at the point the experimental burn-off occurred. To justify this approach, the force histories obtained from the models will be compared to those obtained experimentally later in this chapter.

Once the 3D coupled thermo-mechanical models were complete the 3D thermal models from the previous section (Thermal Model (Phase 1)) were mapped on to them to provide the initial thermal conditions, as shown in Figure 6.3(a) and (b).

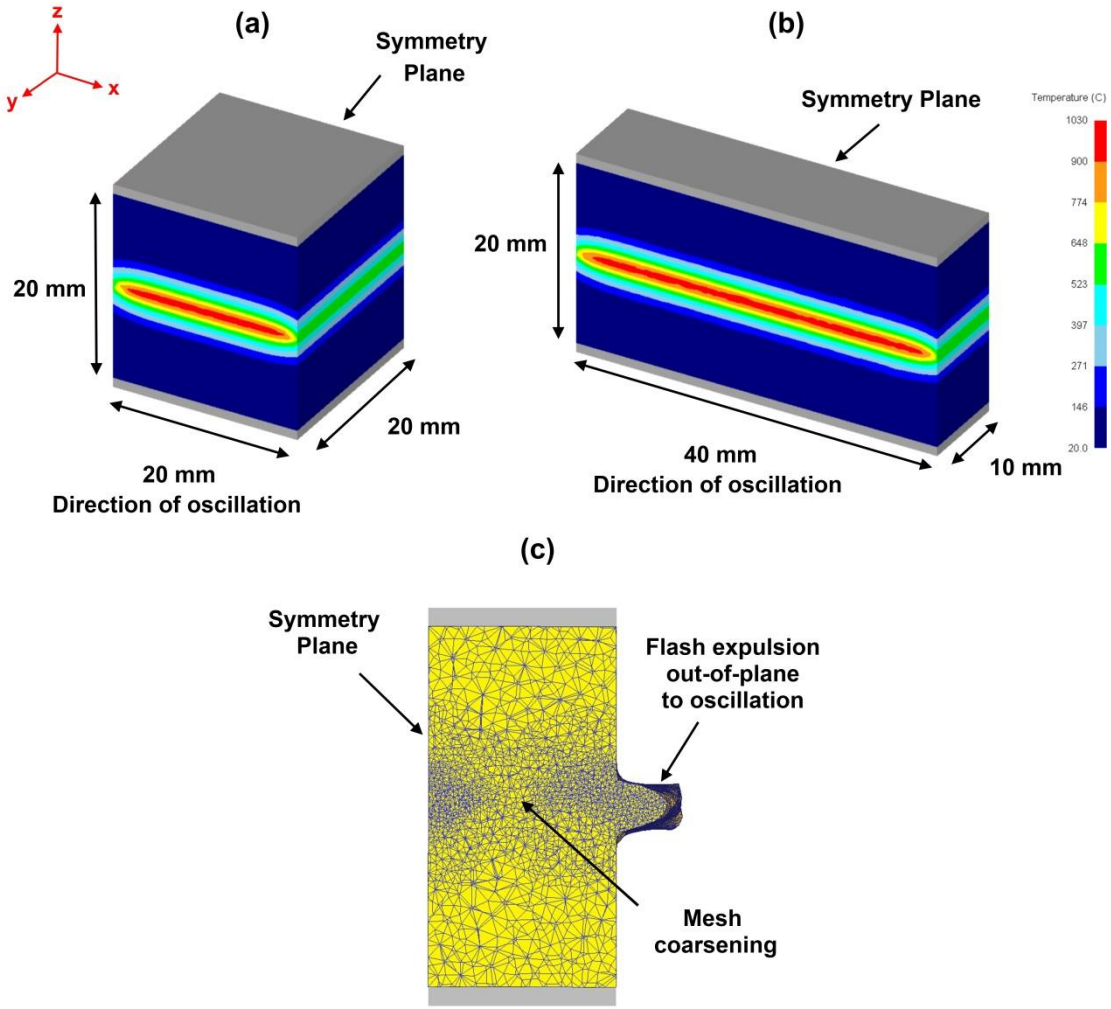

Figure 6.3: Plastic flow models showing the dimensions and symmetry plane for: (a) 3D modelling condition 2 and (b) 3D modelling condition 1; and (c) an illustration of the mesh coarsening. Note that the grey objects represent the displacement dies and are not included in the dimensions.

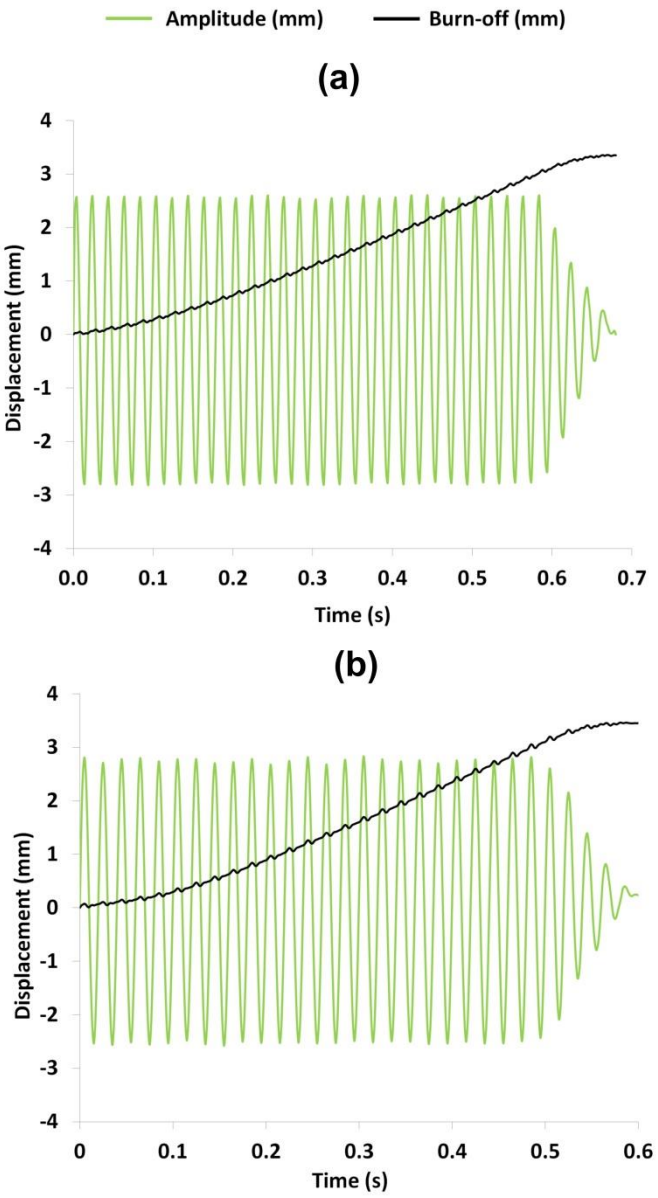

Figure 6.4: Experimental displacement histories for: (a) weld number 32 (inputs for 3D modelling condition 1) and (b) weld number 42 (inputs for 3D modelling condition 2).

To understand the mechanisms behind the multi-directional contaminant removal, point tracking was placed along the weld interface in accordance with the positions shown in Figure 6.5. Several other responses were recorded from the models, which included the thermal fields, strain fields, extent of flowing material, normal force and shear force.

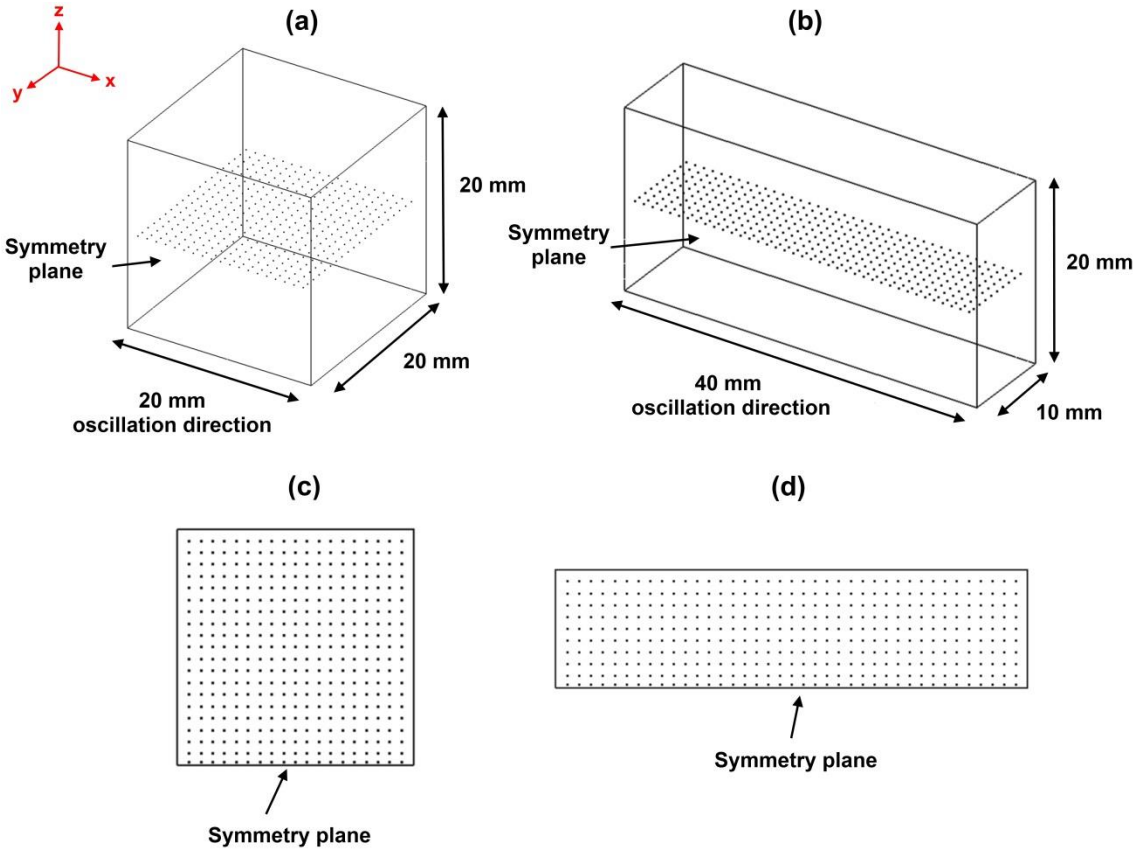

Figure 6.5: Placement of the point tracking along the interface for: (a) 3D modelling condition 2, (b) 3D modelling condition 1, (c) plan view of *(a)*, and (d) plan view of *(b)*.

6.2.2 Development of a 3D Model (Keystone Geometry)

As shown in the literature review (see section 2.4.9 and Figure 2.15) the "keystone" weld involves the joining of a trapezoid workpiece to two flanges and a base plate concurrently. The Boeing Company and TWI are specifically interested in understanding the mechanisms behind the material flow at the "triple point" region – the area where the keystone, flange and base plate interact during welding. The modelling work in this chapter is focused on welding of the keystone workpiece, not the initial joining of the flanges to the base plate.

The general modelling approach used throughout this thesis – the single-body approach – was used. In summary, the keystone weld was modelled as two

distinct stages. The first stage used a purely thermal model to replicate the heating of the workpieces during phase 1 and the second stage used a coupled thermo-mechanical plastic flow model to account for the material deformation during phase 2 and 3. The data from the phase 1 thermal model was mapped onto the plastic model to provide the initial thermal condition for the fully coupled model.

Due to the proprietary nature of the research, the processing conditions used for the experimental keystone weld (TWI's E20 weld number 2116) and the associated modelling cannot be disclosed.

Thermal Model (Phase 1)

Initially a 2D thermal model was developed to represent a slice at the centre of the workpieces to be joined, as shown in Figure 6.6. The thermal data and environmental conditions used were the same as that reported for the thermal models in the previous chapters. The heat flux for the experimental keystone weld was determined using the method 1 methodology reported in Chapter 3. The estimated heat flux was applied across the keystone contacting surfaces until the interface elements exceeded 1000 $^{\circ}$C, as shown in Figure 6.6. Once the 2D thermal model was complete the resulting thermal profile was extruded into the third dimension. Technically, this resulted in a 2½D thermal profile as the profile was constant throughout the third dimension and did not consider the lower heat input at the extremities of the workpieces to be joined, i.e. there was no 50% reduction in the heat flux at the edge. Turner et al.[7,70], showed that the initial thermal profile can be assumed to be constant across the contacting region as the results are minimally affected, justifying this approach.

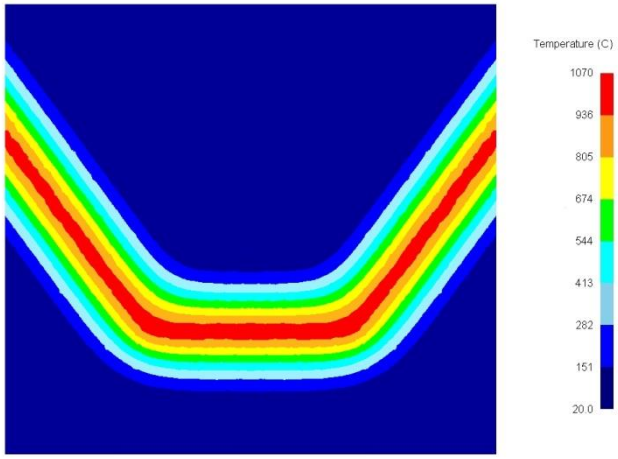

Figure 6.6: An illustration the 2D thermal model for the keystone geometry.

Plastic Flow Model (Phase 2 onward)

A fully coupled thermo-mechanical 3D model was developed for the keystone weld, and was based on the single-body approach. The model was designed to simulate the area around one of the “triple points” – not the full geometry – and is shown in Figure 6.7(a). This significantly reduced the element count and simulation time. The model was developed so that it could be mirrored around the centre of the keystone nose to give replication of both “triple points”, as illustrated in Figure 6.7(b). Moreover, an additional symmetry plane was applied to the opposite side of the model to prevent material expulsion out of this plane, this was to give better replication of the process. Due to the problems encountered using mesh windows, a uniform tetrahedral mesh was applied with an average element size of 0.35 mm – this value was chosen due to the findings in section 6.3.1. Values below 0.35 mm significantly slowed down the simulation. The temperature profile generated at the end of phase 1 from the thermal model was mapped onto the coupled model to account for the phase 1 heating, as illustrated in Figure 6.7(b).

To reduce the computational time further, a “retrospective” analysis was used, as was the case for the previous models in section 6.2.1. The oscillation and burn-off displacements histories were provided by TWI (E20 experiment weld

number 2116). The displacement histories inputted to the models began at the point the experimental burn-off occurred.

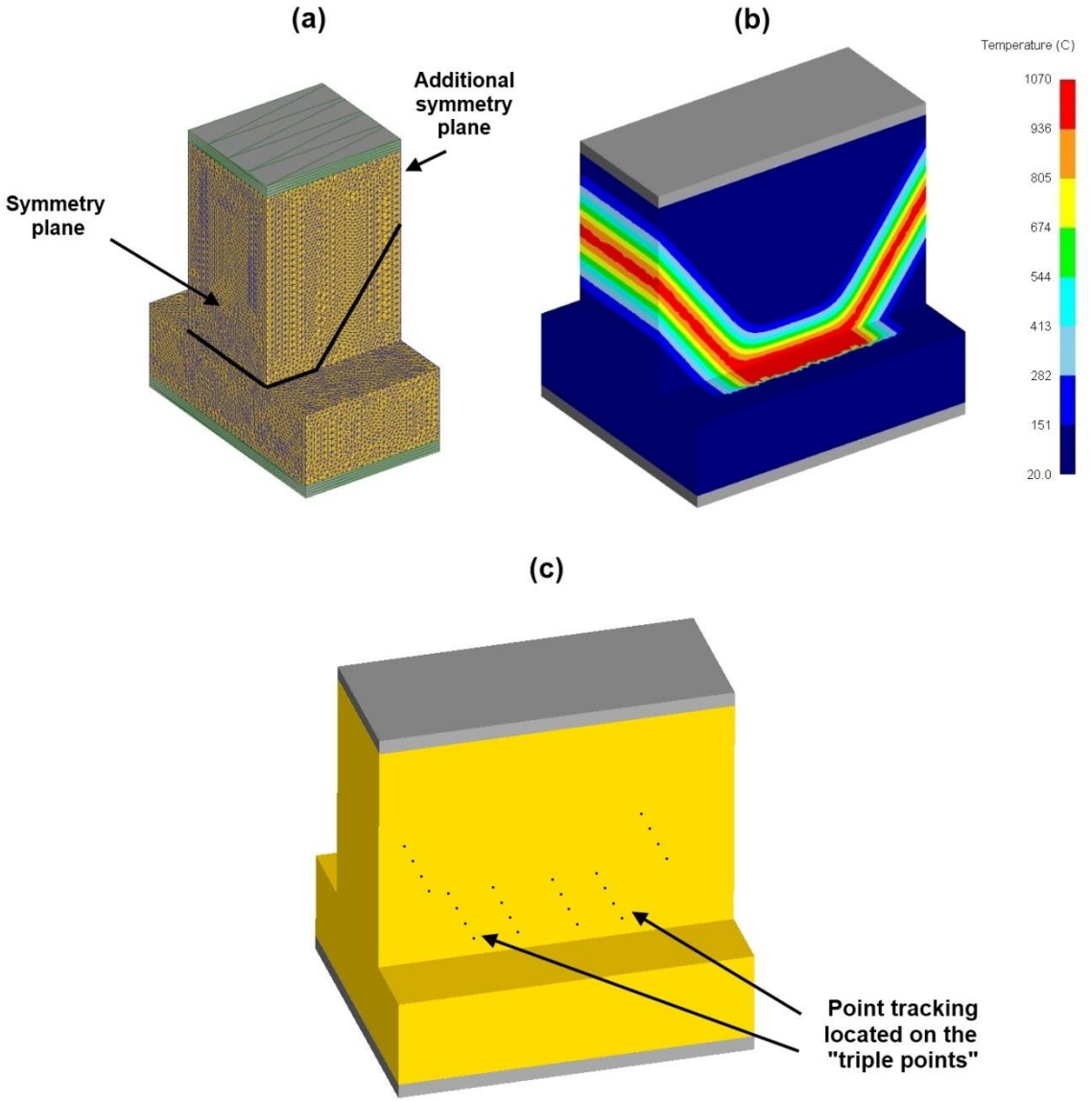

Figure 6.7: Keystone model showing (a) the initial set up with the weld line represented by a black line, (b) the model mirrored around the plane of symmetry with the mapped phase 1 thermal profile, and (c) location of the point tracking located internally on the weld interface. Note that the grey objects represent the displacement dies.

The constitutive material, thermal and environmental data used was the same as that reported for the fully coupled thermo-mechanical models in the previous chapters. The model was given a time-step so that the oscillation movement

travelled approximately one third of the interface mesh element thickness per iteration. A re-mesh was initiated every 0.1 seconds.

To understand the mechanisms behind the contaminant removal, point tracking was placed along the weld interface at the positions shown in Figure 6.7(c).

6.3 Results and Discussions

6.3.1 Standard Geometry

Figure 6.8 shows a comparison of the phase 3 thermal profiles generated from the 2D and 3D models. The 3D thermal profiles were generally constant throughout the workpieces. The only difference occurred close to the periphery, where the heat from the flash conducted back into the weld. This increased the extent of highly heated material, similar to the phenomenon observed for the 2D models in Figure 5.7(c).

For a comparable set of process inputs, the 3D models showed that the interface temperature was reduced if the workpieces were oscillated along the shorter of the two interface-contact dimensions. This is in agreement with the 2D analysis reported in chapter 5. However, the 3D models recorded a lower interface temperature by approximately 100 $^{\circ}$C when compared to the 2D models. One possible reason for the 2D models having a higher interface temperature was due to the limitations of the modelling approach. For example, in chapters 4 and 5 it was shown that the 2D models generally under-predict the burn-off rate due to exclusion of the out-of-plane material flow. The author proposed that this reduced the rate of heat expulsion, resulting in the modelled weld being comparably hotter than the experimental one. The 3D modelling work appears to support the hypothesis that the 2D models may have over predicted the interface temperature. For example, there is a noticeable amount of heated material expelled out-of-plane to the direction of oscillation when the true burn-off rate is modelled, as shown in Figure 6.9, possibly explaining why the interface temperature is reduced in the 3D model. Interestingly, however, the normal and shear forces required to generate the defined displacement

histories for the 3D models were *greater* than their experimental counterparts, as shown in Table 6.2. For example, the predicted mean normal forces for the 3D models were considerably larger than the 100 kN used in the experiments. This suggests that the 3D models may have *under-predicted* the true interface temperature – for a lower temperature a larger force is required to maintain the same rate of deformation[7,105,128]. Consequently, if the predicted 3D interface temperatures were correct, one would expect to see the modelled normal and shear forces being closer to their experimental counterparts. A reason for the 3D models possibly under-predicting the interface temperature could have been due to the size of the elements used at the interface. The elements may have been too large to capture the steep thermal gradients close to the interface, i.e. between 0 mm and 0.5 mm, and hence the true interface temperature. Furthermore, the peak strain rates recorded from the 3D models were between 440 s^{-1} to 500 s^{-1} – far lower than the comparable 2D predicted values of between 800 s^{-1} and 1500 s^{-1}. Modelled strain rates are known to be under-predicted when the element size is increased in LFW process models[7].

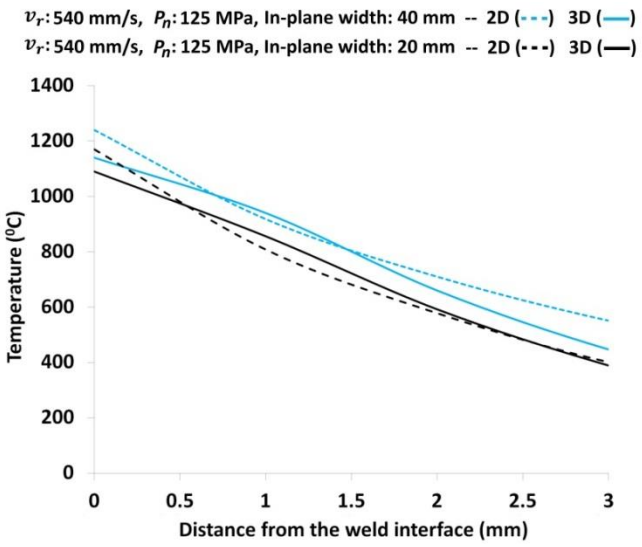

Figure 6.8: A comparison of the phase 3 thermal profiles generated from the 2D and 3D models as a function of the rubbing velocity, v_r, normal pressure, p_n, and in-plane width. The 40 mm and 20 mm in-plane widths represent the conditions in Figure 6.1(a) and (b), respectively. All profiles were symmetric around the interface.

Interestingly, however, at some locations father back from the interface the 3D models predicted a higher temperature than the 2D models. This was possibly due to the excessively large force required to maintain oscillation (see Table 6.2) straining some material farther from the interface. This would have generated extra heat, increasing the temperature.

Despite the simplifications made for the 2D models, they appeared to capture the general effects of the in-plane width on the thermal profiles. Each 2D model took approximately 12 hours whilst the 3D models took between 4 and 6 weeks. This observation would appear to justify the reason why many researchers opt for a 2D LFW process modelling analysis. Based on the 3D modelling observations, with currently available software and computer hardware (see appendix G) the 2D analysis used in the previous chapters was the most pragmatic approach for understanding the effect of a wide range of conditions in a reasonable timescale.

Table 6.2: A comparison of the force histories during phase 3 between the 3D models and their experimental counterparts.

Condition (see Table 6.1)	*3D modelled mean normal force (kN)*	*Experimental normal force (kN)*	*3D modelled mean shear force (kN)*	*Experimental mean shear force (kN)*
1	*139.1*	*100*	*47.5*	*41.6*
2	*126.3*	*100*	*58.1*	*44.9*

As shown in Figure 6.9, the boundary temperature between the rapid flash formation and material with negligible flow corresponded to the beta-transus (approximately 1000 $^{\circ}$C) for the 3D models. Consequently, as shown in Figure 6.8, the extent of material that was rapidly flowing was reduced when the workpieces were oscillated along the shorter of the two interface contacting dimensions. This is again in agreement with the findings in chapters 4 and 5.

The amount of point tracking that remained at interface after 3 mm of burn-off for each of the 3D models is shown in Figure 6.10. There is a significant amount remaining, which, for a comparable burn-off, is in disagreement to the 2D modelling results from the previous chapters. Once again, this discrepancy is

believed to be due to the interface element size used for the 3D analysis. The larger elements did not allow for the narrow region of rapidly flowing material close to the interface to be captured. Furthermore, for the model in Figure 6.10(a) there were many tracked points located in the centre of the weld close to the plane of symmetry. This is in contrast to experimental observations which, for a comparable burn-off, showed that this region was free from contaminants (see Figure 4.10(f)). This finding also indicates that the true interface flow behaviour was not captured by the 3D models.

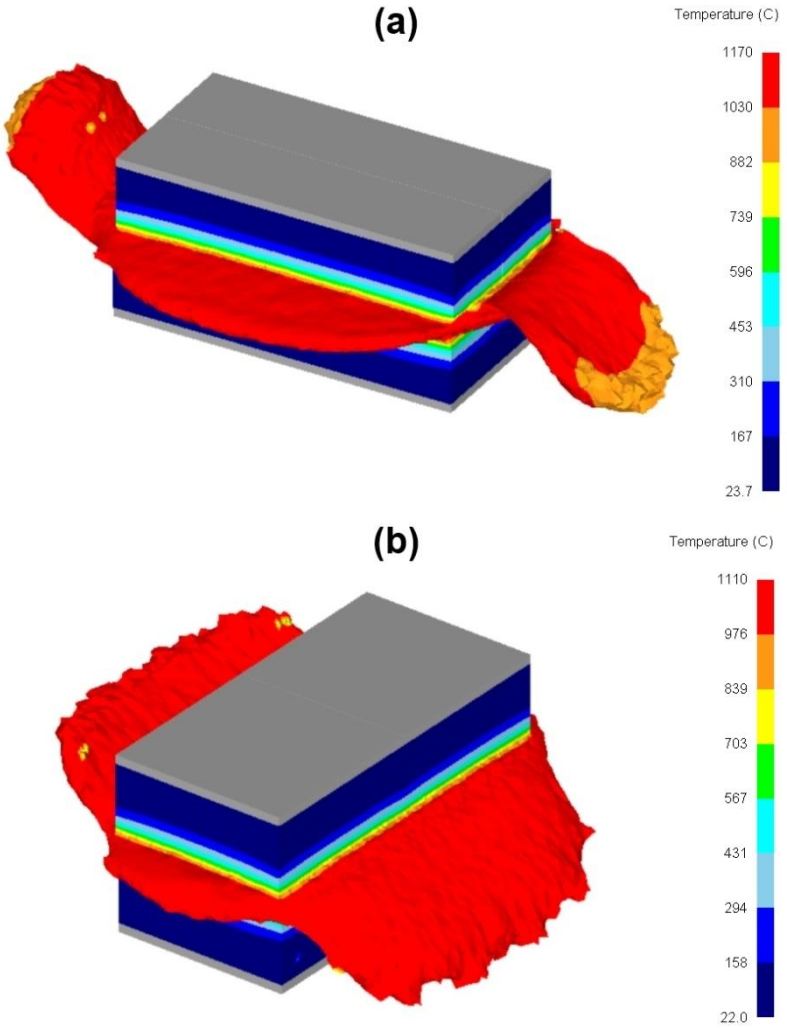

Figure 6.9: Appearance of the models for: (a) 3D modelling condition 1 and (b) 3D modelling condition 2.

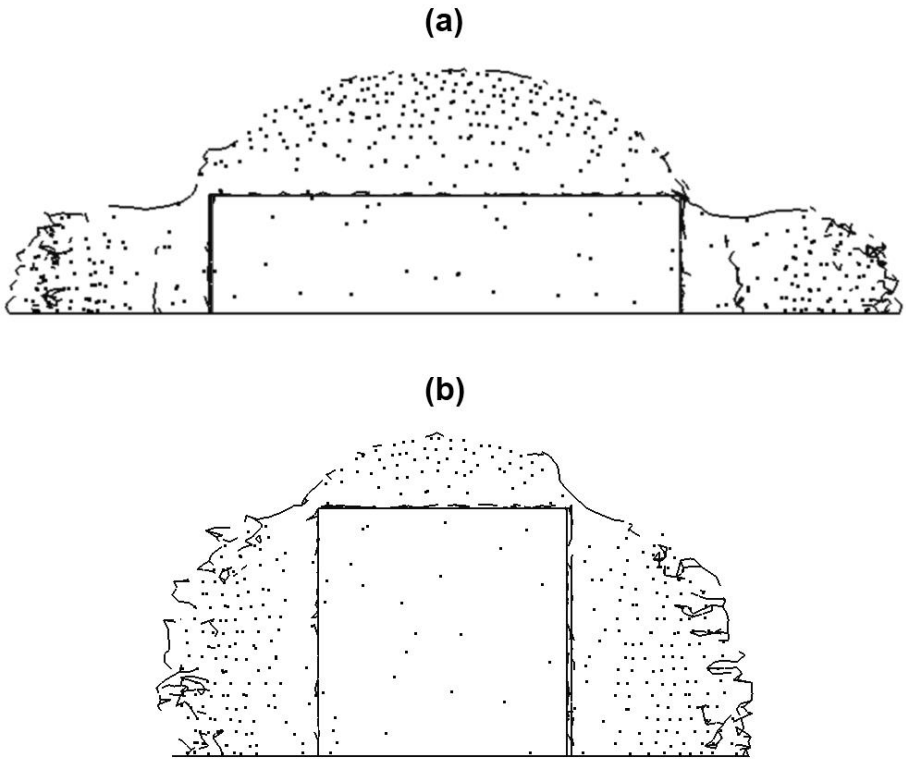

Figure 6.10: Plan view of the point tracking location for: (a) 3D modelling condition 1 at 3 mm of burn-off and (b) 3D modelling condition 2 at 3 mm of burn-off.

6.3.2 Keystone Geometry

Figure 6.11 shows some screen shots of the keystone model during processing. The FEA demonstrated that the peak interface temperature and strain rate during processing were approximately 1160 $^{\circ}$C and 500 s^{-1}, respectively. These values were relatively constant across the entire flowing region, i.e., the values were comparable along the flat contacting surface at the middle of the weld and the angled contacting surfaces. Once again, the temperature between the rapid and minimally flowing material approximately corresponded to the beta-transus. The profile of the rapidly flowing material during processing, however, did not match the initial dimensions of the keystone workpiece. A significant radius between the flat and angled surfaces was present. This was due to the thermal profiles generated during processing.

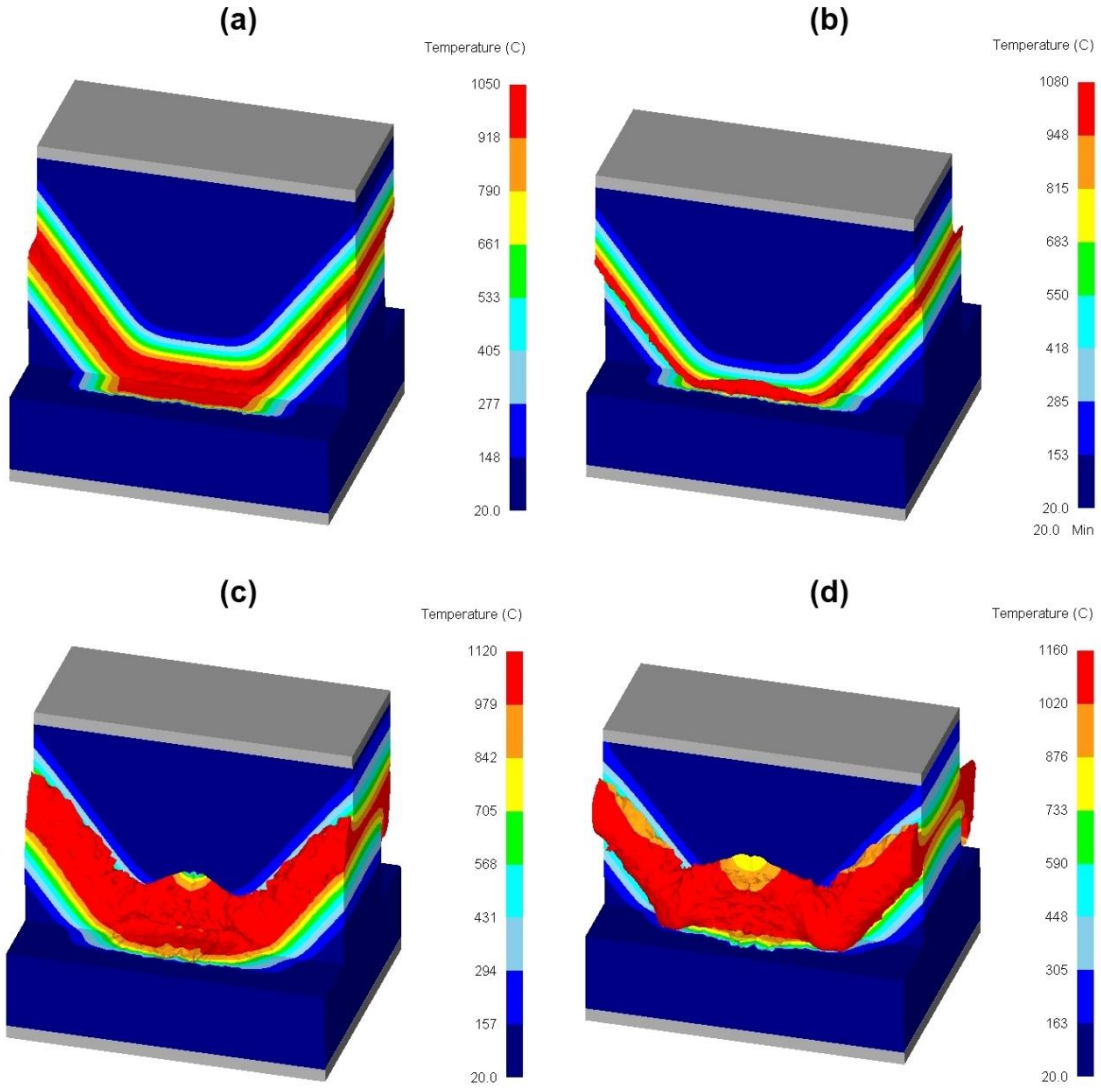

Figure 6.11: Material flow during processing for a time of: (a) 0.001 seconds, (b) 0.023 seconds, (c) 0.181 seconds and (d) 0.331 seconds.

During phase 1 of the process, as illustrated in Figure 6.12, the heat generated at the “triple point” region that conducted into the keystone workpiece was concentrated just above the “triple point”. This caused the material *above* the “triple point” to heat and soften. Whereas the heat inputted into the flange and base plate was free to conduct into the bulk material in a relatively uniform manner. This resulted in the “triple point” being comparably cooler than the rest of the contacting surfaces. This is further illustrated in Figure 6.13(a), notice that the point tracking initially located on the “triple point” is closer to the orange colour bar when compared to the other tracked points. The hot material above

the “triple point” connected with the hot material at the flat and angled surfaces, generating a radius in the profile of the lower flow strength material.

The radius feature in the profile of the lower flow strength material was increased when the process entered phases 2 and 3, as shown in Figure 6.13(b). This forced the “triple point” region to remain cooler than the rest of the initial contacting surfaces. The radius in the profile of the low strength flowing material predicted by the model is in good agreement with experimental observations[97].

The comparatively cooler material at the “triple point” had an effect on the expulsion of the point tracking. As shown in Figure 6.14, the tracked points initially located on the flat and angled surfaces flowed freely into the flash; two points did remain but this was due to insufficient simulated burn-off. The point tracking initially located on the “triple point” did not flow as easily as the other tracked points due to the material in this region being cooler. This result suggests, when compared to the rest of the contacting surfaces, the contaminants at the “triple point” require more burn-off to ensure they are expelled into the flash.

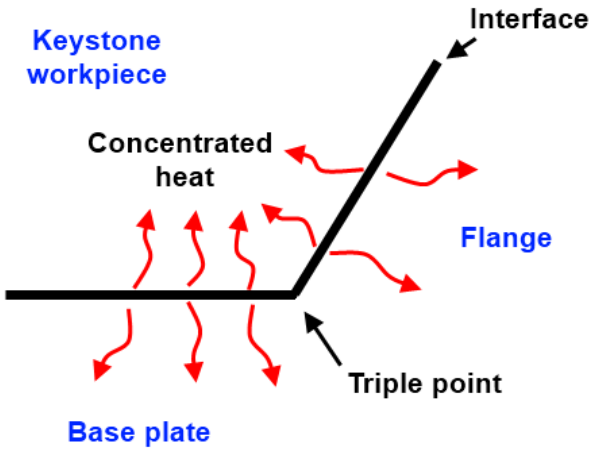

Figure 6.12: An illustration of the heat dissipation at the "triple point "region during phase 1.

The model captured the general appearance of the experimental flash morphology[97], i.e., the flash protruded more at the regions where the radius occurred (see Figure 6.11(d)).

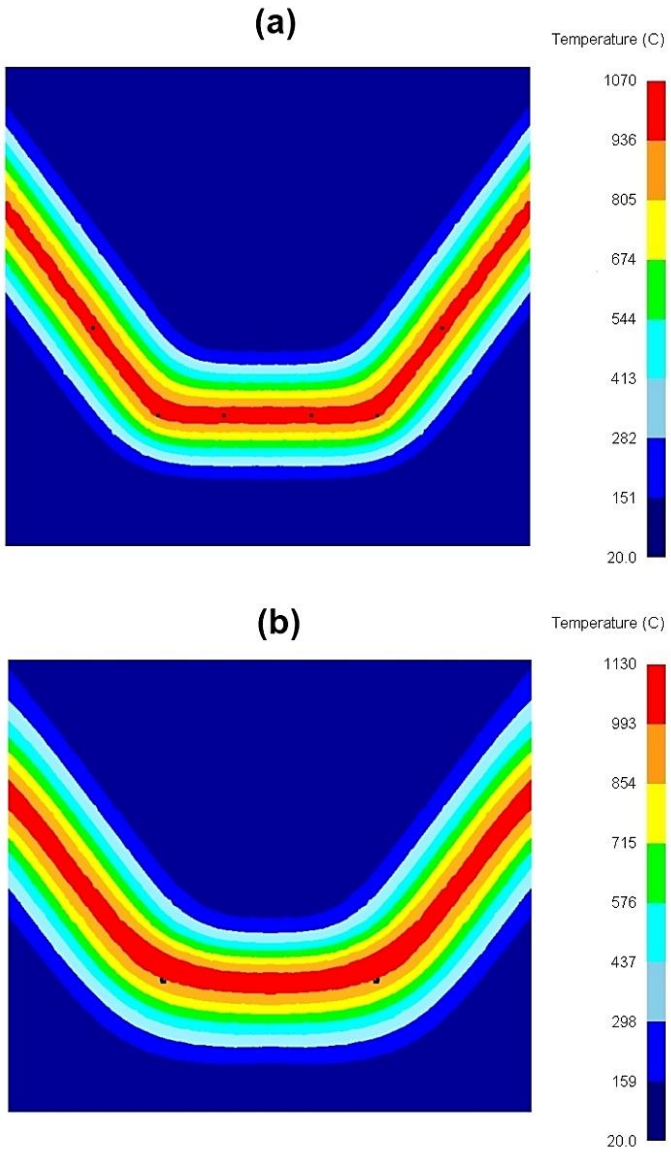

Figure 6.13: A 2D cross-section of the thermal profiles at the centre of the keystone weld showing: (a) thermal profile generated at the end of phase 1 and the initial location of the point tracking, and (b) thermal profile generated during phase 3 and the location of the "triple point" point tracking only. Note that the point tracking for each of the images was super-imposed onto the 2D cross-section. In reality the tracked points were in the dimension perpendicular to the cross-section plane.

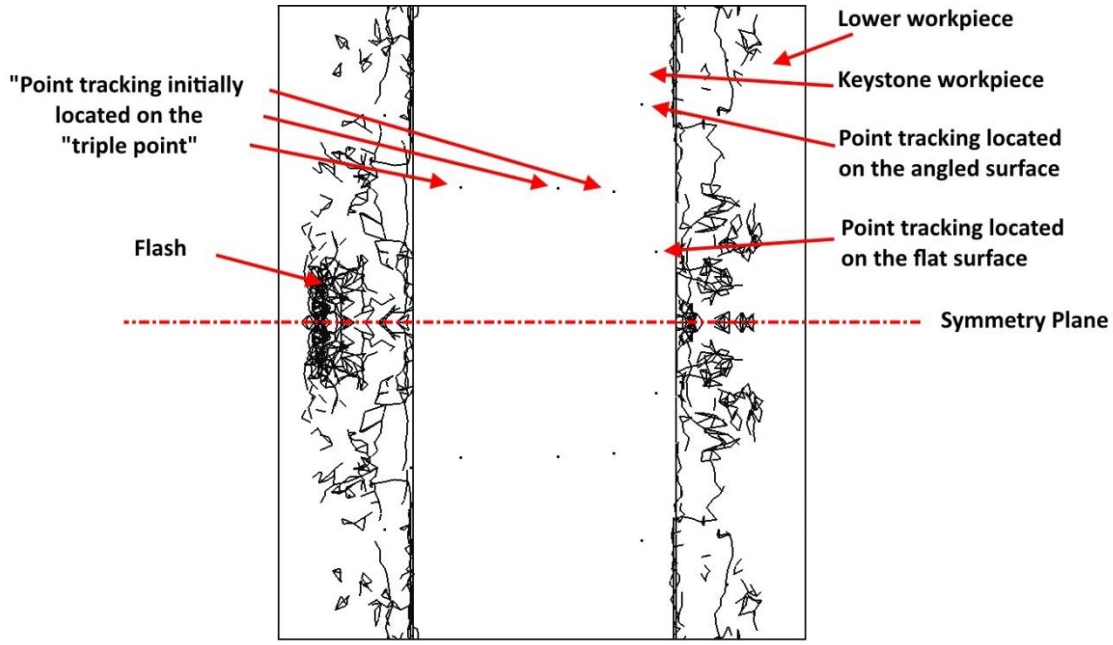

Figure 6.14: Plan view of Figure 6.11(d) showing the point tracking location within the keystone weld (2.37 mm of burn-off).

6.4 Conclusions

The primary conclusions from this chapter are as follows:

- A novel LFW process modelling technique, the “retrospective” analysis, was presented. The advantage of this technique is that the process inputs can be defined as “paths” instead of “forces” allowing for the conjugate gradient solver to be used. This approach decreases the required computational time and memory storage. The “retrospective” analysis offers significant practical benefits for future 3D modelling work – particularly if computational time and memory storage size is of concern.

- The 3D models overcame the primary limitation of the 2D modelling approach, namely the 3D models included the effects of the out-of-plane material expulsion. Despite this, the work highlighted the difficulty in using 3D models to capture the LFW process phenomena. For example, comparisons of the normal forces, shear forces, and contaminant

expulsion with the experiments, and the strain rates with the 2D models indicated that the mesh size used for this study was too large. Any reduction in the mesh size would have significantly increased the computational time, making the length of time required to complete a simulation unreasonable.

- Despite the simplifications made for the 2D models in the previous chapters, they predicted the in-plane width to have the same generic effect on the thermal profiles and extent of flowing material as the more complex 3D models. This observation further justifies their use in chapters 4 and 5.

- The 3D “keystone” weld model captured many of the experimental trends, which was probably due to the finer mesh used, providing an insight into the process. The model showed that the profile of the rapidly flowing material was different to the initial dimensions of the keystone workpiece. This resulted in the “triple point” being cooler than the rest of the contacting surfaces, reducing its ability to flow. This result suggests that, when compared to the rest of the contacting surfaces, the contaminants at the “triple point” require more burn-off to ensure they are expelled into the flash.

Chapter 7: General Discussions

7.1 Introduction and Context

This chapter presents a general discussion of the thesis research outcomes. The thesis research outcomes are discussed in a “global” context and are then compared to the LFW literature. Finally, practical implications of the research outcomes are presented.

7.2 Research Outcomes

The focus of this thesis was on the development and validation of numerical models to increase the fundamental scientific understanding of the LFW process for the joining of Ti-6Al-4V. Although the literature on computational modelling of Ti-6Al-4V linear friction welds is not scarce[7,24,34,45,69,70], up to now most studies investigated only a few select conditions and neglected the geometric effects of the workpieces to be joined. The aim of the present study was to provide an in-depth, detailed understanding of the process input and workpiece geometry effects on the weld outputs. The outputs of particular interest included the: thermal fields, material flow, flash morphology and interface contaminant removal.

Like many researchers[7,24,34,45,69,70], computational modelling was chosen as the primary method to understand the LFW process behaviour because it is pragmatic. It is difficult to understand the process behaviour using experiments alone due to the rapidness of the process and the fact that the interface of the workpieces cannot be observed. Despite this observation, the thesis methodology still included a wide range of physical experiments. This was to provide input and validation data for the computational modelling work.

At this point it is important to integrate the primary research outcomes from the work reported in chapters 3, 4, 5 and 6 to give a “global” perspective of the thesis contributions.

Through the numerical and experimental investigations it was shown that adjusting the frequency and/or amplitude of oscillation while keeping the average rubbing velocity constant had relatively little effect on the outputs. However, an increase of the average rubbing velocity:

- increased the interface temperature, interface strain rate, steady-state burn-off rate and power input.
- decreased the weld duration and total energy required to produce a weld.
- had little influence on the flash thickness, TMAZ thickness, shear force and the burn-off required to expel the interface contaminants from the weld into the flash.

The other process input that strongly affected the results was the applied pressure. An increase of the applied pressure:

- increased the steady-state burn-off rate, interface strain rate, power input and shear force.
- decreased the interface temperature, flash thickness, TMAZ thickness, weld duration, total energy required to produce a weld, and the burn-off required to expel the interface contaminants from the weld into the flash.

The final process input that was studied was the burn-off. The main impact of this input was on the contaminant expulsion and energy usage. An increase of the burn-off expelled more of the interface contaminants from the weld into the flash and increased the total energy required to make a weld. The burn-off had no effect on any of the other responses.

The numerical and experimental investigations also showed that the workpiece geometry affects the process outputs. In particular, a decrease of the workpiece width in the direction of oscillation (in-plane width):

- increased the steady-state burn-off rate, interface strain rate and required heat flux to maintain oscillation.

- decreased the interface temperature, TMAZ thickness, flash thickness, weld grain size and the burn-off required to remove the interface contaminants from the weld into the flash.

Workpieces with multiple surfaces of contact were modelled for the first time, namely the keystone weld. The modelling work demonstrated that the region corresponding to the “triple point” in the keystone welds, where several weld planes meet, required more burn-off than the rest of the contacting surfaces to expel the interface contaminants. This is an important finding as this “triple point” location is likely to be the primary location for defects in production components.

In addition to the parametric and geometric results there are some other contributions to knowledge worth commenting on, which are discussed in the following paragraphs.

The weld interface of a Ti-6AL-4V linear friction weld has to achieve the beta-transus temperature (~1000 $^{\circ}$C) in order for the weld to progress from phase 1 to phase 2. This temperature allows for sufficient flow softening and adhesion of the separate workpieces to occur. This is an interesting finding as it suggests that it is impossible to make a Ti-6Al-4V linear friction weld whilst the interface temperature is below the beta-transus.

The flash morphology was sensitive to the processing conditions. The ripple morphology was more noticeable when the ratio between the TMAZ thickness and the amplitude of oscillation was reduced. Moreover, the temperature between the rapidly forming flash and the material with negligible flow also corresponded to the beta-transus.

In the author’s opinion, integration of computational modelling and physical experiments was paramount to obtain the results presented in the above paragraphs. Many of the relationships would have been difficult to characterise using experiments alone; therefore highlighting the importance of numerical modelling to characterise the LFW process. Moreover, the experimental work

validated many of the modelling results. Successful validation for a range of outputs that are measurable in both the models and experiments allows for the data predicted by the models that are non-measurable in the experiments to be trusted.

Interestingly, the modelling work showed that although the 3D models captured the full multi-directional flow behaviour of the LFW process, 2D models were better suited to parametric and geometric studies. This was due to the significantly reduced computational time requirements. In the author's opinion, the LFW community will have to wait several more years for desktop computational power to advance before a systematic investigation can take place using 3D models that yield reliable results. Alternatively, software developers could make applications on supercomputer facilities more straight-forward which would facilitate these complex calculations.

7.2.1 Comparisons with the Literature

The research outcomes from this thesis also allows the author to "add his weight" to certain "schools of thought" within the LFW community. For example, there is a debate as to what effects the process inputs have on the interface temperature of a weld (phase 2 onward), in this work it was shown that an increase of the amplitude of oscillation and oscillation frequency increased the interface temperature. This is in agreement with Turner et al.[7] and Fratini et al.[78], and in contrast to others[24,121]. Moreover, it is often stated that an increase of the applied force (pressure) decreases the interface temperature of a titanium alloy linear friction weld[61,80]. The results from this thesis support this observation, as shown in Figure 4.7(a), Figure 5.11(a) and Figure 6.8.

There is also a debate among researchers about the strain rates that are achieved at the interface of a linear friction weld. The thesis work showed that the values can range between 100 s^{-1} to 2000 s^{-1}, which is in agreement to the values reported by Turner et al.[7] (500 s^{-1} to 2500 s^{-1}) and Chamanfar et al.[118] (1520 s^{-1}). These values are in contrast to those reported by Vairis and Frost[3] (4.6 s^{-1}). The possible reason for the large difference may be that the simple

strain rate model developed by Vairis and Frost[3] had incorrect assumptions made; in fact the assumption and concepts behind the model were not presented in the original article.

Ofem et al.[50] hypothesised that the overall energy required to make a linear friction weld could be reduced if it is produced with high rubbing velocities. The results from this thesis support this hypothesis. This is a consequence of the higher power input of the higher rubbing velocities, which cause the interface material to heat and plasticise more rapidly during phase 1, then shorten much more rapidly during phases 2 and 3. This reduces the overall welding duration and hence energy wasted due to conduction, convection and radiation.

Finally, the thesis work showed that a Ti-6Al-4V linear friction weld can be free from interface contaminants if a sufficient burn-off is applied, the amount of which is dependent on the combination of frequency, amplitude, pressure and in-plane width used. This finding is in contrast to Wanjara and Jahazi[6], who suggested that a weld made with a low power input will have contaminants present at the interface. The low power inputs in their work were produced by using lower values of frequency, amplitude and pressure[6]. The possible reason for the difference in thought is that Wanjara and Jahazi[6] did not apply enough burn-off for the combination of amplitude, frequency and pressure investigated.

7.2.2 Practical Implications

The burn-off required to remove the interface contaminants from the weld line into the flash should not be considered as a stand-alone value but rather as a function of the generated TMAZ thickness; the greater the TMAZ thickness the more burn-off. Consequently, there may be a benefit to using larger pressures and oscillating the workpieces along the shorter of the two interface-contact dimensions when producing Ti-6Al-4V welds, as shown in Figure 7.1. This is because the burn-off required to remove the interface contaminants is reduced. Hence for the same burn-off, the factor of safety on contaminant removal is greater. Furthermore, these conditions can also reduce the interface temperature and refine the weld microstructure, which may offer additional

benefits, such as reduced residual stresses[61] and improved mechanical properties[45,173,174].

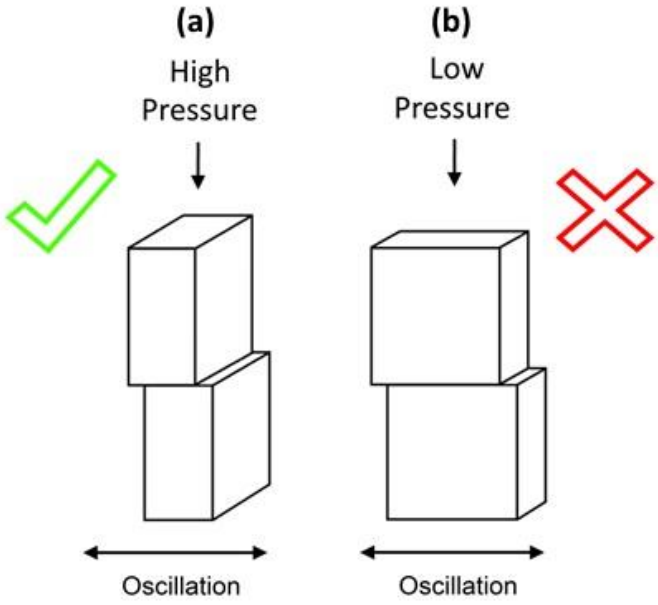

Figure 7.1: An illustration of the (a) best approach and (b) worst approach to minimise the burn-off to expel the interface contaminants from the weld line into the flash for Ti-6Al-4V linear friction welds.

The “triple point” appears to require more burn-off than the rest of the keystone contacting surfaces to expel the interface contaminants. This is an important finding as this location is likely to be a primary source for defects in production components.

A novel LFW process modelling technique for 3D geometries, the “retrospective” analysis, was presented in Chapter 6. The advantage of this technique is that the process inputs can be defined as “paths” instead of “forces” allowing for the conjugate gradient solver to be used. This approach decreased the required computational time and memory storage. This approach may also offer significant, practical benefits for future 3D modelling work if simulation time and memory storage size are limiting factors. The limitation of this approach is that prior knowledge of the displacement histories must be known.

Chapter 8: Thesis Conclusions

8.1 Introduction and Context

This chapter presents a summary of the thesis and recommendations for further research.

8.2 Thesis Summary

The aim of this thesis was to use computational modelling to increase the fundamental scientific understanding of the LFW process for the joining of Ti-6Al-4V.

The primary objectives were as follows:

- Conduct a systematic series of experimental welds to provide input and validation data for the computational modelling work.
- Use the finite element analysis (FEA) software DEFORM to develop 2D models that predict the effects of the process inputs and workpiece geometry on the thermal fields, material flow and interface contaminant removal.
- Use DEFORM to develop 3D models to compare with the 2D modelling approach; and to investigate the “keystone” weld, which has multiple surfaces that must be joined concurrently.

Chapter 1 introduced the project background. Chapter 2 presented a comprehensive literature review, emphasis was placed on the LFW process, the titanium alloy Ti-6Al-4V and computational modelling techniques. The conclusions from the literature review allowed for the above aim and objectives to be identified. Chapters 3 to 6 demonstrated how the thesis objectives were achieved.

The first objective point was primarily addressed in chapter 3. To do this, a design of experiments approach was used to investigate the process input

effects on various experimental Ti-6Al-4V weld outputs. The data obtained from these welds provided a valuable source of input and validation data for the computational modelling work reported in this thesis. In addition to the experiments in chapter 3, several experiments were conducted in chapters 4 and 5 to provide data for validating the interface contaminant removal and workpiece geometry effects, respectively.

The second objective point was addressed in chapters 3, 4 and 5. In chapter 3 a novel 2D thermal modelling approach was presented to understand the reason for the transition from phase 1 to phase 2. The 2D thermal modelling results were supported by thermocouple recordings. Chapters 4 and 5 focused on the development and validation of 2D thermo-mechanical "single-body" models to characterise the effects of the process inputs and workpiece geometry, respectively, on the weld outputs. The outputs of particular interest included the thermal fields, material flow, flash formation and interface contaminant removal. The 2D thermo-mechanical models were limited in that they did not account for the material expulsion out-of-plane to the oscillation direction. Despite this, the 2D thermo-mechanical modelling work captured the experimental trends, providing an insight into the process fundamentals for the LFW of Ti-6Al-4V. The 2D modelling parametric and geometric studies reported in chapters 4 and 5, respectively, addressed many of the LFW knowledge shortfalls in the literature.

The final objective point was addressed in chapter 6. A novel LFW process modelling technique was presented, the "retrospective" analysis, which has the advantage of reducing computational time and memory storage size. The limitation of this approach is that prior knowledge of the displacement histories must be known. The 3D models overcame the primary limitation of the 2D models in chapters 4 and 5 in that they included the effects of the out-of-plane material expulsion. Despite this, the work highlighted the difficulty in using 3D models to capture the LFW process phenomena – further justifying the use of 2D models in chapters 4 and 5. Furthermore, for the first time ever, a model was developed to investigate the "keystone" weld. The 3D "keystone" model,

which had a finer mesh than the earlier 3D models, captured many of the experimental trends providing a good insight into the “triple point” material flow.

Chapter 7 presented a general discussion of the thesis research outcomes. The thesis research outcomes were discussed in a “global” context and were then compared to the LFW literature. Finally, practical implications of the research outcomes were presented.

In conclusion, the thesis aim was successfully addressed; the fundamental scientific understanding of the LFW process for the joining of Ti-6Al-4V has been increased. The results obtained have significant, practical implications and will possibly aid further industrial development, optimisation and implementation of LFW. The remainder of the thesis identifies possible areas for further research.

8.3 Recommendations for Further Research

This thesis addressed many of the “gaps” in the knowledge of LFW process understanding to provide a platform that further process development, optimisation and implementation may be based upon. Despite the advancement in knowledge reported in this thesis, there are still many more knowledge “gaps” that need addressing to aid further industrial facilitation of LFW.

Some recommended areas for further work are:

- **Microstructure modelling**. Models could be used to investigate the impact of the processing conditions on the microstructure and alpha/beta phase evolution. This would allow for the effects of the processing conditions on the allotropic phase, average grain size, grain microstructure and grain spatial distribution to be characterised.

- **Residual stress modelling**. Models could be used to investigate the impact of the processing conditions on the formation and magnitude of residual stresses in linear friction welds. The effectiveness of post-weld

heat-treatment on the reduction of the residual stresses could also be considered.

- **Extension to other materials**. The general methodology detailed in this thesis could be used to investigate the effects of the LFW process on the joining of aluminium and aluminium-lithium alloys, nickel-based superalloys and steels – all materials that are finding increasing industrial interest. Dissimilar material combinations could also be considered to understand how the different material properties affect the process and to identify conditions that mitigate intermetallic formation.

- **Process input characterisation and "triple point" removal**. In comparison to research by other authors, the process input range in this study was fairly narrow. For example, the amplitudes investigated ranged between 1 mm to 2.7 mm, whereas the literature[7,34] reports values as high as 5 mm. Future work could consider values outside of this range to see if the trends reported in this thesis are still valid. Future work could also consider investigating the effects of the process inputs on the keystone weld thermal profiles. Ideally, conditions that encapsulate the "triple point" region into the rapidly flowing material would be identified. This would allow for it to be expelled at the same rate as the rest of the interface material, reducing the burn-off required to remove the interface contaminants.

- **Geometry characterisation**. With the exception of the work on the keystone geometry, this thesis investigated the joining of workpieces with symmetrical dimensions. Future work could consider the joining of non-symmetrical workpieces, such as coupons to plate.

- **3D modelling**. Chapter 6 presented a general methodology for developing a 3D "single body" model, however many problems were encountered. Future research could consider modelling the process with a finer mesh, allowing for greater insight into multi-directional material flow and contaminant removal.

References

1. Addison, A. C. *Linear friction welding information for production engineering. TWI industrial members report - 961/2010*. (2010).

2. Addison, A. C. *Linear friction welding of engineering metals. TWI industrial members report - 894/2008*. (2008).

3. Vairis, A. & Frost, M. High frequency linear friction welding of a titanium alloy. *Wear* **217,** 117–131 (1998).

4. García, A. M. M. BLISK fabrication by linear friction welding. *Adv. Gas Turbine Technol.* 411–434 (2011).

5. Chamanfar, A., Jahazi, M., Gholipour, J., Wanjara, P. & Yue, S. Maximizing the integrity of linear friction welded waspaloy. *Mater. Sci. Eng. A* **555,** 117–130 (2012).

6. Wanjara, P. & Jahazi, M. Linear friction welding of Ti-6Al-4V: Processing, microstructure, and mechanical-property inter-relationships. *Metall. Mater. Trans. A* **36,** 2149–2164 (2005).

7. Turner, R., Gebelin, J.-C., Ward, R. M. & Reed, R. C. Linear friction welding of Ti-6Al-4V: Modelling and validation. *Acta Mater.* **59,** 3792–3803 (2011).

8. Bhamji, I., Preuss, M., Threadgill, P. L. & Addison, A. C. Solid state joining of metals by linear friction welding: a literature review. *Mater. Sci. Technol.* **27,** 2–12 (2011).

9. Baeslack III, W. A., Broderick, T. F., Juhas, M. & Fraser, H. L. Characterization of solid-phase welds between Ti-6A1-2Sn-4Zr-2Mo-0.1Si and Ti-13.5A1-21.5Nb titanium aluminide. *Mater. Charact.* **33,** 357–367 (1994).

10. Maalekian, M. Friction welding - critical assessment of literature. *Inst. Mater. Miner. Min.* **12,** 738 – 758 (2007).

11. Uday, M. B., Ahmad Fauzi, M. N., Zuhailawati, H. & Ismail, a. B. Advances in friction welding process: a review. *Sci. Technol. Weld. Join.* **15,** 534–558 (2010).

12. Chamanfar, A., Jahazi, M. & Cormier, J. A Review on Inertia and Linear Friction Welding of Ni-Based Superalloys. *Metall. Mater. Trans. A* **46,** 1639–1669 (2015).

13. Bhamji, I., Moat, R. J., Preuss, M., Threadgill, P. L., Addison, A. C. & Peel, M. J. Linear friction welding of aluminium to copper. *Sci. Technol. Weld. Join.* **17,** 314–320 (2012).

14. Wanjara, P., Dalgaard, E., Trigo, G., Mandache, C., Comeau, G. & Jonas, J. J. Linear friction welding of Al-Cu: Part 1 - Process evaluation. *Can. Metall. Q.* **50,** Pages 350–359 (2011).

15. Dalgaard, E., Wanjara, P., Trigo, G., Jahazi, M., Comeau, G. & Jonas, J. J. Linear friction welding of Al-Cu part 2 - Interfacial characteristics. *Can. Metall. Q.* **50,** Pages 360–370 (2011).

16. Bhandari, V. Linear friction welding of titanium to stainless steel. M.Sc. thesis, Cranfield University (2010).

17. Bhamji, I., Preuss, M., Moat, R. J., Threadgill, P. L. & Addison, A. C. Linear friction welding of aluminium to magnesium. *Sci. Technol. Weld. Join.* **17,** 368–374 (2012).

18. Guo, Y., Jung, T., Lung, Y., Li, H., Bray, S. & Bowen, P. Microstructure and microhardness of Ti6246 linear friction weld. *Mater. Sci. Eng. A* **562,** 17–24 (2013).

19. Karadge, M., Preuss, M., Lovell, C., Withers, P. J. & Bray, S. Texture development in Ti–6Al–4V linear friction welds. *Mater. Sci. Eng. A* **459,** 182–191 (2007).

20. Guo, Y., Chiu, Y., Attallah, M. & Li, H. Characterization of dissimilar linear friction welds of alpha + beta titanium alloys. *J. Mater. Eng. Perform.* **21,** 770–776 (2012).

21. Li, W., Suo, J., Ma, T., Feng, Y. & Kim, K. Abnormal microstructure in the weld zone of linear friction welded Ti-6.5Al-3.5Mo-1.5Zr-0.3Si titanium alloy joint and its influence on joint properties. *Mater. Sci. Eng. A* **599,** 38–45 (2014).

22. Vairis, A. & Frost, M. Modelling the linear friction welding of titanium blocks. *Mater. Sci. Eng. A* **292,** 8–17 (2000).

23. Sorina-Müller, J., Rettenmayr, M., Schneefeld, D., Roder, O. & Fried, W. FEM simulation of the linear friction welding of titanium alloys. *Comput. Mater. Sci.* **48,** 749–758 (2010).

24. Li, W., Ma, T. & Li, J. Numerical simulation of linear friction welding of titanium alloy: Effects of processing parameters. *Mater. Des.* **31,** 1497–1507 (2010).

25. Blau, P. The significance and use of the friction coefficient. *Tribol. Int.* **34,** 585–591 (2001).

26. Desmond F. Moore. *Principles and Application of Tribology*. (Pergamon Press Ltd, 1975).

27. Vairis, A. & Christakis, N. The development of a continuum framework for friction welding processes with the aid of micro-mechanical parameterisations. *Int. J. Model. Identif. Control* **2,** 347–355 (2007).

28. Bowden, F. P. & Tabor, D. *The friction and lubrication of solids*. (Oxford University Press, 1950).

29. Gohar, R. & Rahnejat, H. *Fundamentals of tribology*. (Imperial College Press, 2008).

30. Stachowiak, G. W. & Batchelor, A. W. *Engineering Tribology*. (Butterworth-Heinemann, 2000).

31. Gao, J., Luedtke, W. D., Gourdon, D. Ruths, M., Israelachvili, J. N. & Landman, U. Frictional Forces and Amontons ' Law : From the Molecular to the Macroscopic Scale. *J. Phys. Chem. B* **108,** 3410–3425 (2004).

32. Bhushan, B. *Introduction to Tribology*. (John Wiley and Sons, inc, 2002).

33. Maalekian, M., Kozeschnik, E., Brantner, H. . & Cerjak, H. Comparative analysis of heat generation in friction welding of steel bars. *Acta Mater.* **56,** 2843–2855 (2008).

34. Schröder, F., Ward, R. M., Walpole, A. R., Turner, R. P., Attallah, M. M., Gebelin, J.-C. & Reed, R. C. Linear friction welding of Ti6Al4V: experiments and modelling. *Mater. Sci. Technol.* **31,** 372–384 (2015).

35. Yang, L. Modelling of the inertia welding of inconel 718. (2010).

36. Koo, H. H. & Baeslack III, W. A. 1. Characterization of inertia-friction welds in a high-temperature RS/PM Al-8.5Fe-1.3V-1.7Si alloy (AA-8009). *Mater. Charact.* **28,** Pages 157–164 (1992).

37. Koo, H. H. & Baeslack III, W. A. Structure, properties , and fracture of linear friction welded Al-Fe-V-Si alloy 8009. *Mater. Charact.* **28,** 157–164 (1992).

38. Daymond, M. R. & Bonner, N. W. Measurement of strain in a titanium linear friction weld by neutron diffraction. *Phys. B* **325,** 130–137 (2003).

39. Ma, T. J., Zhong, B., Li, W.-Y., Zhang, Y., Yang, S. & Yang, C. On microstructure and mechanical properties of linear friction welded

dissimilar Ti-6Al-4V and Ti-6·5Al-3·5Mo-1·5Zr-0·3Si joint. *Sci. Technol. Weld. Join.* **17,** 9–12 (2012).

40. Ceretti, E., Fratini, L., Giardini, C. & Spisa, D. Numerical modelling of the linear friction welding process. *Int. J. Mater. Form.* **3,** 1015–1018 (2010).

41. Li, W., Ma, T., Zhang, Y., Xu, Q., Li, J., Yang, S. & Liao, H. Microstructure characterization and mechanical properties of linear friction welded Ti-6Al-4V alloy. *Adv. Eng. Mater.* **10,** 89–92 (2008).

42. Ma, T. J., Li, W. Y., Zhong, B., Zhang, Y. & Li, J. L. Effect of post-weld heat treatment on microstructure and property of linear friction welded Ti17 titanium alloy joint. *Sci. Technol. Weld. Join.* **17,** 180–185 (2012).

43. Corzo, V., Casals, O., Alcalá, J., Mateo, A. & Anglada, M. Mechanical evaluation of linear friction welds in titanium alloys through indentation experiments. *Weld. Int.* **21,** 125–129 (2007).

44. Rotundo, F., Marconi, A., Morri, A. & Ceschini, A. Dissimilar linear friction welding between a SiC particle reinforced aluminum composite and a monolithic aluminum alloy: Microstructural, tensile and fatigue properties. *Mater. Sci. Eng. A* **559,** 852–860 (2013).

45. Grujicic, M., Arakere, G., Pandurangan, B., Yen, C. F. & Cheeseman, B. A. Process modeling of Ti-6Al-4V linear friction welding (LFW). *J. Mater. Eng. Perform.* **21,** 2011–2023 (2011).

46. Bhamji, I., Preuss, M., Threadgill, P. L., Moat, R. J., Addison, A. C. & Peel, M. J. Linear friction welding of AISI 316L stainless steel. *Mater. Sci. Eng. A* **528,** 680–690 (2010).

47. Xie, M. Y., Jun, T. S., Korsunsky, A. M. & Drakopoulos, M. Analysis of preferred orientations in linear friction welded (LFW) aluminium alloy specimens using ‘one-shot’ multi-element energy dispersive synchrotron X-ray diffraction. *Powder Diffr.* **28,** 327–332 (2013).

48. Chamanfar, A., Jahazi, M., Gholipour, J., Wanjara, P. & Yue, S. Mechanical Property and Microstructure of Linear Friction Welded WASPALOY. *Metall. Mater. Trans. A* **42,** 729–744 (2010).

49. Bergmann, J. P., Petzoldt, F., Schürer, R. & Schneider, S. Solid-state welding of aluminum to copper—case studies. *Weld. World* **57,** 541–550 (2013).

50. Ofem, U. U., Colegrove, P. A., Addison, A. & Russell, M. J. Energy and force analysis of linear friction welds in medium carbon steel. *Sci. Technol. Weld. Join.* **15,** 479–485 (2010).

51. TWI. *The Boeing linear friction welding programme: Comprehensive report volume 1 - Introduction*. **1,** (2009).

52. Mendez, P. F. & Eagar, T. W. Welding processes for aeronautics. *Adv. Mater. Process.* **159,** 39–43 (2001).

53. Pashazadeh, H., Masoumi, a. & Teimournezhad, J. A study on material flow pattern in friction stir welding using finite element method. *Proc. Inst. Mech. Eng. Part B J. Eng. Manuf.* **227,** 1453–1466 (2013).

54. Pashazadeh, H., Teimournezhad, J. & Masoumi, A. Numerical investigation on the mechanical, thermal, metallurgical and material flow characteristics in friction stir welding of copper sheets with experimental verification. *Mater. Des.* **55,** 619–632 (2014).

55. Mendez, P. F. & Eagar, T. W. New trends in welding in the aeronautic industry. in *2nd Conf. New Manuf. Trends* 1–10 (2002).

56. Mitlin, D., Radmilovic, V., Pan, T., Chen, J., Feng, Z. & Santella, M. L. Structure–properties relations in spot friction welded (also known as friction stir spot welded) 6111 aluminum. *Mater. Sci. Eng. A* **441,** 79–96 (2006).

57. Gao, Z., Niu, J. T., Krumphals, F., Enzinger, N., Mitsche, S. & Sommitsch, C. FE modelling of microstructure evolution during friction stir spot welding in AA6082-T6. *Weld. World* **57,** 895–902 (2013).

58. Vill, V. I. *Friction Welding of Metals*. (American Welding Society, 1962).

59. Boeing. Structural assemblies and preforms therefor formed by linear friction welding. (2007).

60. Vairis, A. & Frost, M. On the extrusion stage of linear friction welding of Ti-6Al-4V. *Mater. Sci. Eng. A* **271,** 477–484 (1999).

61. Romero, J., Attallah, M. M., Preuss, M., Karadge, M. & Bray, S. E. Effect of the forging pressure on the microstructure and residual stress development in Ti–6Al–4V linear friction welds. *Acta Mater.* **57,** 5582–5592 (2009).

62. Ma, T. J., Li, W.-Y. & Yang, S. Y. Impact toughness and fracture analysis of linear friction welded Ti–6Al–4V alloy joints. *Mater. Des.* **30,** 2128–2132 (2009).

63. Mary, C. & Jahazi, M. Multi-scale analysis of IN-718 microstructure evolution during linear friction welding. *Adv. Eng. Mater.* **10,** 573–578 (2008).

64. Jun, T.-S., Rotundo, F., Song, X., Ceschini, L. & Korsunsky, A. M. Residual strains in AA2024/AlSiCp composite linear friction welds. *Mater. Des.* **31,** S117–S120 (2010).

65. Rotundo, F., Ceschini, L., Morri, A., Jun, T.-S. & Korsunsky, A. M. Mechanical and microstructural characterization of 2124Al/25vol.%SiCp joints obtained by linear friction welding (LFW). *Compos. Part A Appl. Sci. Manuf.* **41,** 1028–1037 (2010).

66. Lang, B., Zhang, T. C., Li, X. H. & Guo, D. L. Microstructural evolution of a TC11 titanium alloy during linear friction welding. *J. Mater. Sci.* **45,** 6218–6224 (2010).

67. Ma, T., Chen, T., Li, W.-Y., Wang, S. & Yang, S. Formation mechanism of linear friction welded Ti–6Al–4V alloy joint based on microstructure observation. *Mater. Charact.* **62,** 130–135 (2011).

68. Li, W., Wu, H., Ma, T., Yang, C. & Chen, Z. Influence of parent metal microstructure and post-weld heat treatment on microstructure and mechanical properties of linear friction welded Ti-6Al-4V joint. *Adv. Eng. Mater.* **14,** 312–318 (2012).

69. Schroeder, F., Ward, R. M., Turner, R. P., Attallah, M. M., Gebelin, J. & Reed, R. C. Linear friction welding of titanium alloys for aeroengine applications: modelling and validation. in *9th Int. Conf. Trends Weld. Res.* 886 – 892 (2012).

70. Turner, R., Ward, R. M., March, R. & Reed, R. C. The magnitude and origin of residual stress in Ti-6Al-4V linear friction welds: An investigation by validated numerical modeling. *Metall. Mater. Trans. B* **43,** 186–197 (2012).

71. Corzo, M., Torres, Y., Anglada, M. & Mateo, A. Fracture behaviour of linear friction welds in titanium alloys. *An. la Mecánica Fract.* **1,** 75–80 (2007).

72. Dalgaard, E., Wanjara, P., Gholipour, J., Cao, X. & Jonas, J. J. Linear friction welding of a near-beta titanium alloy. *Acta Mater.* **60,** Pages 770–780 (2011).

73. Li, W., Ma, T. & Yang, S. Microstructure evolution and mechanical properties of linear friction welded Ti-5Al-2Sn-2Zr-4Mo-4Cr (Ti17) titanium alloy joints. *Adv. Eng. Mater.* **12,** 35–43 (2010).

74. Frankel, P., Preuss, M., Steuwer, A., Withers, P. J. & Bray, S. Comparison of residual stresses in Ti–6Al–4V and Ti–6Al–2Sn–4Zr–2Mo linear friction welds. *Mater. Sci. Technol.* **25,** 640–650 (2009).

75. Ola, O. T., Ojo, O. a., Wanjara, P. & Chaturvedi, M. C. A study of linear friction weld microstructure in single crystal CMSX-486 superalloy. *Metall. Mater. Trans. A* **43,** 921–933 (2011).

76. Ma, T. J., Li, W.-Y., Xu, Q. Z., Zhang, Y., Li, J. L., Yang, S. Q. & Liao, H. L. Microstructure evolution and mechanical properties of linear friction welded 45 steel joint. *Adv. Eng. Mater.* **9,** 703–707 (2007).

77. Li, W., Ma, T. J., Yang, S. Q., Xu, Q. Z., Zhang, Y., Li, J. L. & Liao, H. L. Effect of friction time on flash shape and axial shortening of linear friction welded 45 steel. *Mater. Lett.* **62,** 293–296 (2008).

78. Fratini, L., Buffa, G., Campanella, D. & La Spisa, D. Investigations on the linear friction welding process through numerical simulations and experiments. *Mater. Des.* **40,** 285–291 (2012).

79. Ola, O. T., Ojo, O. a., Wanjara, P. & Chaturvedi, M. C. Enhanced resistance to weld cracking by strain-induced rapid solidification during linear friction welding. *Philos. Mag. Lett.* **91,** 140–149 (2011).

80. Attallah, M. M., Preuss, M. & Bray, S. Microstructural development during Linear friction welding of titanium alloys. in *8th Int. Conf. Trends Weld. Res.* 486–491 (2009).

81. Dalgaard, E. C. Evolution of Microstructure , Microtexture and Mechanical Properties in Linear Friction Welded Titanium Alloys. (2011).

82. Turner, R., Schroeder, F., Ward, R. M. & Brooks, J. W. The importance of materials data and modelling parameters in an FE simulation of linear friction welding. *Adv. Mater. Sci. Eng.* **2014,** 1–8 (2014).

83. Amegadzie, M. Y., Ola, O. T., Ojo, O. A., Wanjara, P. & Chaturvedi, M. C. On liquidation and liquid phase oxidation during linear friction welding of nickel-base IN 738and CMSX 486 superalloys. in *Superalloys 2012 12"' Int. Symp. Superalloys* (eds. Huron, E. S., Reed, R. C., Hardy, M. C., Mills, M. J., Montero, R. E., Portella, P. D. & Telesman, J.) 587–594 (The Minerals, Metals & Materials Society, 2012).

84. Grujicic, M., Yavari, R., Snipes, J. S., Ramaswami, S., Yen, C.-F. & Cheeseman, B. A. Linear friction welding process model for carpenter custom 465 precipitation-hardened martensitic stainless steel. *J. Mater. Eng. Perform.* **23,** 2182–2198 (2014).

85. Dewald, A. T., Legzdina, D., Clausen, B., Brown, D. W., Sisneros, T. A. & Hill, M. R. A comparison of residual stress measurements on a linear friction weld using the contour method and neutron diffraction. *Conf. Proc. Soc. Exp. Mech. Ser.* **4,** 183–189 (2013).

86. Askeland, D. & Phule, P. *The Science and Engineering of Materials*. (Thomson, 2006).

87. Song, X., Xie, M., Hofmann, F., Jun, T. S., Connolley, T., Reinhard, C., Atwood, R. C., Connor, L., Drakopoulos, M., Harding, S. & Korsunsky, A. M. Residual stresses in linear friction welding of aluminium alloys. *Mater. Des.* **50,** 360–369 (2013).

88. Vishwakarma, K. R., Ojo, O. A., Wanjara, P. & Chaturvedi, M. C. Microstructural analysis of linear friction-welded 718 plus superalloy. *J. Miner. Met. Mater. Soc.* **66,** 2525–2534 (2014).

89. Wanjara, P., Dalgaard, E., Gholipour, J., Cao, X., Cuddy, J. & Jonas, J. J. Effect of pre- and post-weld heat treatments on linear friction welded Ti-5553. *Metall. Mater. Trans. A* **45,** 5138–5157 (2014).

90. Bhamji, I. M. Development of the linear friction welding process. Eng.D. thesis, University of Manchester (2012).

91. www.howstuffworks.com. (2000).

92. Leyens, C. & Peters, M. *Titanium and Titanium Alloys: Fundamentals and Applications*. (Wiley-VCH, 2003).

93. Kallee, S. W., Nicholas, E. D. & Russell, M. J. Friction welding of aero engine components. in *10th world Conf. Titan. TI-2003* (eds. Lutjering, G. & Albrecht, J.) 2867–2874 (Wiley-VCH, 2003).

94. Lütjering, G. & Williams, J. C. *Titanium*. *Engineering* (Springer, 2007).

95. Ji, Y., Chai, Z., Zhao, D. & Wu, S. Linear friction welding of Ti–5Al–2Sn–2Zr–4Mo–4Cr alloy with dissimilar microstructure. *J. Mater. Process. Technol.* **214,** 979–987 (2014).

96. TWI. *Boeing linear friction welding programme: Comprehensive report volume 4*. **4,** (2011).

97. TWI. *Boeing linear friction welding programme: Keystone flaw elimination*. (2012).

98. Moody, S. M. & Atkinson, J. R. Linear friction welding of polypropylene and polycarbonate. Part II. The microstructures and mechanical properties of PP welds made using optimum conditions. *Plast. Rubber Compos. Process. Appl.* **17,** Pages 211–217 (1992).

99. Moody, S. M. & Atkinson, J. R. Linear friction welding of polypropylene and polycarbonate. Part I. Effects of welding conditions on strength of welds. *Plast. Rubber Compos. Process. Appl.* **17,** pp. 203–209 (1992).

100. Vaziri, M., Lindgren, O. & Pizzi, A. Influence of machine setting and wood parameters on crack formation in scots pine joints produced by linear friction welding. *J. Adhes. Sci. Technol.* **26,** 37–41 (2012).

101. Vaziri, M., Berg, S., Sandberg, D. & Gheinani, I. T. Three-dimensional finite element modelling of heat transfer for linear friction welding of scots pine. *Wood Mater. Sci. Eng.* 1–8 (2014).

102. Ma, T.-J., Shi, D.-G., Zhang, Y. & Yang, S.-Q. Mechanical properties and microstructure of linear friction welded TC4 + TC17 joint. *Hangkong Cailiao Xuebao/Journal Aeronaut. Mater.* **29,** Pages 33–37 (2009).

103. Mateo, A. A., Corzo, M. A., Anglada, M. A., Mendez, J. B., Villechaise, P. B., Ferte, J.-P. C. & , Roder, O. Welding repair by linear friction in titanium alloys. *Mater. Sci. Technol.* **25,** Pages 905–913 (2009).

104. Tan, L.-J., Yao, Z.-K., Zhou, W., Guo, H.-Z., Yang, S.-Q. & Zhang, J.-W. Linear friction welding of dissimilar titanium alloys Ti-22Al-25Nb and TC11. *Suxing Gongcheng Xuebao/Journal Plast. Eng.* **16,** Pages 135–138 (2009).

105. Lee, W. & Lin, C. High-temperature deformation behaviour of Ti6Al4V alloy evaluated by high strain-rate compression tests. *J. Mater. Process. Technol.* **75,** 127–136 (1998).

106. Ding, R., Guo, Z. X. & Wilson, A. Microstructural evolution of a Ti–6Al–4V alloy during thermomechanical processing. *Mater. Sci. Eng. A* **327,** 233–245 (2002).

107. Wen, G. D., Ma, T. J., Li, W. Y., Li, J. L., Guo, H. Z. & Chen, D. L. Cyclic deformation behavior of linear friction welded Ti6Al4V joints. *Mater. Sci. Eng. A* **597,** 408–414 (2014).

108. Wen, G. D., Li, W. Y., Wang, S. Q., Guo, H. Z. & Chen, D. L. Strain-controlled fatigue properties of linear friction welded dissimilar joints between Ti-6Al-4V and Ti-6.5Al-3.5Mo-1.5Zr-0.3Si alloys. *Mater. Sci. Eng. A* **612,** 80–88 (2014).

109. Medvedev, A. Y., Bychkov, V. M., Selivanov, A. S., Pavlinich, S. P., Dautov, S. K. & Supov, A. V. Linear friction welding of two-phase titanium alloys VT6 and VT8-1. *Weld. Int.* 1–4 (2014).

110. Zhao, P., Fu, L. & Zhong, D. Numerical simulation of transient temperature and axial deformation during linear friction welding between TC11 and TC17 titanium alloys. *Comput. Mater. Sci.* **92,** 325–333 (2014).

111. Li, W., Guo, J., Yang, X. & Vairis, A. The effect of micro-swinging on joint formation in linear friction welding. *J. Eng. Sci. Technol. Rev.* **7,** 55–58 (2014).

112. Bikmeyev, A. T., Gazizov, R. K., Vairis, A. & Yamileva, A. M. Modelling the temperature distribution in the contact area of a moving object in the case of linear friction welding. in *Proc. ASME 2013 Int. Mech. Eng. Congr. Expo. IMECE2013* 1–8 (ASME, 2013).

113. Zhao, P. & Fu, L. Strain hardening behavior of linear friction welded joints between TC11 and TC17 dissimilar titanium alloys. *Mater. Sci. Eng. A* **621,** 149–156 (2015).

114. Stinville, J. C., Bridier, F., Ponsen, D., Wanjara, P. & Bocher, P. High and low cycle fatigue behavior of linear friction welded Ti–6Al–4V. *Int. J. Fatigue* **70,** 278–288 (2015).

115. Jing, L., Fu, R., Li, Y., Shi, Y., Wang, J. & Du, D. Physical simulation of microstructural evolution in linear friction welded joints of Ti–6Al–4V alloy. *Sci. Technol. Weld. Join.* **20,** 286 – 290 (2015).

116. Chamanfar, A., Sarrat, L., Jahazi, M., Asadi, M., Weck, A. & Koul, A. K. Microstructural characteristics of forged and heat treated Inconel-718 disks. *Mater. Des.* **52,** 791–800 (2013).

117. Karadge, M., Preuss, M., Withers, P. J. & Bray, S. Importance of crystal orientation in linear friction joining of single crystal to polycrystalline nickel-based superalloys. *Mater. Sci. Eng. A* **491,** 446–453 (2008).

118. Chamanfar, A., Jahazi, M., Gholipour, J., Wanjara, P. & Yue, S. Modeling grain size and strain rate in linear friction welded waspaloy. *Metall. Mater. Trans. A* **44,** 4230–4238 (2013).

119. Chamanfar, A., Jahazi, M., Gholipour, J., Wanjara, P. & Yue, S. Suppressed liquation and microcracking in linear friction welded WASPALOY. *Mater. Des.* **36,** 113–122 (2012).

120. Fratini, L., Buffa, G., Cammalleri, M. & Campanella, D. On the linear friction welding process of aluminum alloys : Experimental insights through process monitoring. *CIRP Ann. - Manuf. Technol.* **62,** 295–298 (2013).

121. Li, W., Wang, F., Shi, S., Ma, T., Li, J. & Vairis, A. 3D finite element analysis of the effect of process parameters on linear friction welding of mild steel. *J. Mater. Eng. Perform.* **23,** 4010–4018 (2014).

122. Shtrikman, M. M. Linear friction welding. *Weld. Int.* **24,** 563–569 (2010).

123. www.astarmathsandphysics.com. (2015).

124. Pederson, R. Microstructure and phase transformation of Ti-6Al-4V. (2002).

125. Charles, C. Modelling microstructure evolution of weld deposited Ti-6Al-4V. (2008).

126. Henry, S. D. & Reidenbach, F. *Fatigue Data Book - Light Structural Alloys*. *Fatigue Data B. - Light Struct. Alloy.* (ASM International, 1994).

127. Chen, H.-C., Pinkerton, A. J. & Li, L. Fibre laser welding of dissimilar alloys of Ti-6Al-4V and Inconel 718 for aerospace applications. *Int. J. Adv. Manuf. Technol.* **52,** 977–987 (2010).

128. Seshacharyulu, T., Medeiros, S. C., Frazier, W. G. & Prasad, Y. V. R. K. Hot working of commercial Ti-6Al-4V with an equiaxed alpha-beta microstructure: Materials modeling considerations. *Mater. Sci. Eng. A* **284,** 184–194 (2000).

129. Boivineau, M., Cagran, C., Doytier, D., Eyraud, V., Nadal, M.-H., Wilthan, B. & Pottlacher, G. Thermophysical properties of solid and liquid Ti-6Al-4V (TA6V) alloy. *Int. J. Thermophys.* **27,** 507–529 (2006).

130. Ahmed, T. & Rack, H, J. Phase transformations during cooling in α+β titanium alloys. *Mater. Sci. Eng. A* **243,** 206–211 (1998).

131. Seshacharyulu, T., Medeiros, S. C., Frazier, W. G. & Prasad, Y. V. R. K. Microstructural mechanisms during hot working of commercial grade Ti – 6Al – 4V with lamellar starting structure. *Mater. Sci. Eng. A* **325,** 112–125 (2002).

132. Fan, X. G. & Yang, H. Internal-state-variable based self-consistent constitutive modeling for hot working of two-phase titanium alloys coupling microstructure evolution. *Int. J. Plast.* **27,** 1833–1852 (2011).

133. Schulze, V. & Zanger, F. Numerical Analysis of the Influence of Johnson-Cook-Material Parameters on the Surface Integrity of Ti-6Al-4V. *Procedia Eng.* **19,** 306–311 (2011).

134. Sheppard, T. & Norley, J. Deformation characteristics of Ti-6Al-4V. *Mater. Sci. Technol.* **4,** 903–908 (1988).

135. Johnson, G. R. & Cook, W. . A constitutive model and data for metals subjected to large strains, high strain rates and high temperatures. in *Seventh Int. Symp. Ballist.* 541–547 (1983).

136. Hubert, W., Meyer, J. R. & Kleponis, David, S. Modeling the high strain rate behaviour of titanium undergoing ballistic impact and penetration. *Int. J. Impact Eng.* **26,** 509–521 (2001).

137. JMatPro Software. Thermotech Sente Sofware. Guildford, Surrey, U.K.

138. Zhang, M., Zhang, J. & McDowell, D. L. Microstructure-based crystal plasticity modeling of cyclic deformation of Ti–6Al–4V. *Int. J. Plast.* **23,** 1328–1348 (2007).

139. Roush, E. D., Kobryn, P. A. & Semiatin, S. L. Anisotropy of plastic flow and microstructure evolution during hot working of laser-deposited Ti-6Al-4V. *Scr. Mater.* **45,** 717–724 (2001).

140. Vo, P., Jahazi, M. & Yue, S. Recrystallization during thermomechanical processing of IMI834. *Metall. Mater. Trans. A* **39,** 2965–2980 (2008).

141. Zhao, J., Ding, H., Zhao, W., Cao, F., Hou, H. & Li, Z. Modeling of dynamic recrystallization of Ti6Al4V alloy using a cellular automaton approach. *Acta Metall. Sin. (English Lett.* **21,** 260–268 (2008).

142. Luo, J., Li, M., Yu, W. & Li, H. The variation of strain rate sensitivity exponent and strain hardening exponent in isothermal compression of Ti–6Al–4V alloy. *Mater. Des.* **31,** 741–748 (2010).

143. Sargent, G. A., Zane, A. P., Fagin, P. N., Ghosh, A. K. & Semiatin, S. L. Low-temperature coarsening and plastic flow behavior of an alpha/beta titanium billet material with an ultrafine microstructure. *Metall. Mater. Trans. A* **39,** 2949–2964 (2008).

144. Grong, Ø. *Metallurgical Modelling of Welding*. (Maney publishing, 1997).

145. Mills, K. C. *Recommended values of thermophysical properties for selected commercial alloys*. (Woodhead publishing, 2002).

146. Yang, J., Sun, S., Brandt, M. & Yan, W. Experimental investigation and 3D finite element prediction of the heat affected zone during laser assisted machining of Ti6Al4V alloy. *J. Mater. Process. Technol.* **210,** 2215–2222 (2010).

147. Reilly, A. Modelling of friction stir spot welding. (2013).

148. Cozzolino, L. D. Finite element analysis of localised rolling to reduce residual stress and distortion. (2014).

149. Vairis, A. Mathematical modelling of the linear friction welding process. *J. Eng. Sci. Technol. Rev.* **5,** 25–31 (2012).

150. Medvedev, A., Vairis, A., Nikiforov, R. & Supov, A. Energy balance of the linear friction welding process. *J. Eng. Sci. Technol. Rev.* **5,** 20–24 (2012).

151. Lacey, A. A. & Voong, C. Transient thermal behaviour in a model of linear friction welding. *J. Eng. Math.* (2013).

152. Carslaw, H. S. & Jaeger, J. C. *Conduction of Heat in Solids*. (Oxford University Press, 1959).

153. Lindgren, L.-E. Numerical modelling of welding. *Comput. Methods Appl. Mech. Eng.* **195,** 6710–6736 (2006).

154. Jiao, Z., Song, C., Lin, T. & He, P. Molecular dynamics simulation of the effect of surface roughness and pore on linear friction welding between Ni and Al. *Comput. Mater. Sci.* **50,** 3385–3389 (2011).

155. Liu, Z. M., Guo, Z. U., Zhao, G. Y., Zhang, S. & Pan, J. L. 3D numerical simulation of linear friction welding of 45# carbon steel. *Adv. Mater. Res.* **538-541,** 1443–1446 (2012).

156. Li, W., Wang, F., Shi, S. & Ma, T. Numerical simulation of linear friction welding based on ABAQUS environment: Challenges and perspectives. *J. Mater. Eng. Perform.* **23,** 384–390 (2014).

157. Li, W., Shi, S. X., Wang, F. F., Ma, T. J., Li, J. L., Gao, D. L. & Vairis, A. Heat reflux in flash and its effect on joint temperature history during linear friction welding of steel. *Int. J. Therm. Sci.* **67,** 192–199 (2013).

158. Wu, X. Finite element simulation of linear friction welding. *Adv. Mater. Res.* **411,** 126–129 (2012).

159. Tao, J., Zhang, T., Liu, P., Li, J. & Mang, Y. Numerical computation of a linear friction welding process. *Mater. Sci. Forum* **575 -578,** 811–815 (2008).

160. Kobayashi, S., Oh, S.-I. & Altan, T. *Metal forming and finite element method*. (Oxford University Press, 1989).

161. Shimoda, Y., Tsubaki, M., Yasui, T. & Fukumoto, M. Experimental and numerical studies of material flow during welding by friction stirring. *Yosetsu Gakkai Ronbunshu/Quarterly J. Japan Weld. Soc.* **29,** 114–118 (2010).

162. Jain, R., Pal, S. K. & Singh, S. B. Finite Element Simulation of Temperature and Strain Distribution in Al2024 Aluminum Alloy by Friction Stir Welding. in *5th Int. 26th All India Manuf. Technol. Des. Res. Conf. (AIMTDR 2014)* 3–7 (2014).

163. WildeAnalysis. www.WildeAnalysis.co.uk. (2012). at <http://wildeanalysis.co.uk/fea/software/deform>

164. Wang, E., Nelson, T. & Rauch, R. Back to elements - tetrahedra vs. hexahedra. in *Int. ANSYS Conf. Proc.* (2004).

165. Benzley, S. E., Perry, E., Merkley, K., Clark, B. & Sjaardema, G. A comparison of all hexagonal and all tetrahedral finite element meshes for elastic and elastic-plastic analysis. in *Conf. Proceedings, 4th Int. Meshing Roundtable* 179–191 (Sandia National Laboratories, 1995).

166. Tadepalli, S. C., Erdemir, A. & Cavanagh, P. R. Comparison of hexahedral and tetrahedral elements in finite element analysis of the foot and footwear. *J. Biomech.* **44,** 2337–43 (2011).

167. Scientific Forming Technologies Corporation (SFTC). *DEFORM User's Manual V.11*. (2014).

168. Martina, F., Mehnen, J., Williams, S. W., Colegrove, P. & Wang, F. Investigation of the benefits of plasma deposition for the additive layer manufacture of Ti–6Al–4V. *J. Mater. Process. Technol.* **212,** 1377–1386 (2012).

169. Montgomery, D. C. & Runger, G. C. *Applied Statistics and Probability for Engineers*. (John Wiley and Sons, inc, 2010).

170. Montgomery, D. C. *Design and Analysis of Experiments*. (John Wiley and Sons, inc, 2000).

171. Rich, T. & Robert, R. The Forge Phase of Friction Welding. *Weld. J.* **53,** 137–146 (1971).

172. Gil, F. J., Ginebra, M. P., Manero, J. M. & Planell, J. A. Formation of alpha-Widmanstatten structure: effects of grain size and cooling rate on the Widmanstatten morphologies and on the mechanical properties in Ti6Al4V alloy. *J. Alloys Compd.* **329,** 142–152 (2001).

173. Zhang, Y., Sato, Y. S., Kokawa, H., Park, S. H. C. & Hirano, S. Microstructural characteristics and mechanical properties of Ti–6Al–4V friction stir welds. *Mater. Sci. Eng. A* **485,** 448–455 (2008).

174. Lütjering, G. Influence of processing on microstructure and mechanical properties of (alpha + beta) titanium alloys. *J. Alloys Compd.* **243,** 32–45 (1998).

Appendix A : Workpiece Material Properties and Technical Drawing Details

Material Property details for the workpieces used in this thesis:

Approved Certificate No 80531035

Original
Customer P.O. Number / Date
P717258 / 10 Sep, 2012
TIMET Sales Order Number / Date
354952 / 10 Sep, 2012
TIMET Delivery Number / Date
80531035 / 12 Sep, 2012

TIMET UK Limited
TIMET Service Centre
PO Box 57
Off Ystrad Road
Wsunarlwydd
Swansea
SA1 1XD
Tel: 01792 873471 Fax: 01792 879930

Ship-to Address
The Welding Institute (TWI)
Granta Park
Great Abington
Cambridge
CB1 6AL

Sold-to Address
The Welding Institute (TWI)
Granta Park
Great Abington
Cambridge
CB1 6AL

B. FLIPO

Incoming Approved Certificate No. H16972-12

BS EN ISO 9001 : 2008 Approval Certificate No. 851813

TIMET Item / Cust. Item	Material No / Customer Material Number	Description	Quantity	Weight
000010	110365	TIMETAL® 6-4 Titanium Aero Plate	1.000 PC	30.000 KG

Heat Treatment	: Mill Annealed
Specifications	: ASTM B 265-10 GRADE 5
Tolerances	: LENGTH +3MM/-0
	: WIDTH +3MM/-0
Batch Number	: H16972-R04
Batch Dimensions	: 20.000mm X 405.000mm X 800.000mm
Batch Number of Pieces	: 1.000
Country of Origin	: USA
Heat Number	: H16972-12
Metal ID	: 1-2-7
Method of Manufacturing Type	: Hot Rolled
Test Number	: J11438

Certified that the whole of the supplies detailed hereon, unless otherwise stated are covered by the source's certificate of conformity or test certificate reference hereon and has been subject to Quality System Requirements, in accordance with the conditions of our ISO Registration No. ISO 9001.

These materials are in the same condition as when received and unless stated otherwise conform to the specification required by your order.

SC UK 013

Signed M. Foster
Approved Signatory for and on behalf of TIMET UK Limited

Date 11/9/12

PAGE 1 / 1

TIMET

Titanium Metals Corporation

100 Titanium Way, Toronto, OH 43964
Telephone (740) 537-5694, Fax (740) 537-5653

Approved Certificate

CERT ID
H16972-12
09-JAN-2012 19:14:17 GMT

PURCHASE ORDER
20077004

SOLD TO CUSTOMER
TIMET Service Center St. Louis
109 Interstate Drive, Wentzville, MO 63385

HEAT NUMBER
H16972

GRADE
TIMETAL®6-4

SHIP TO ADDRESS
TIMET Service Center St. Louis
109 Interstate Drive, Wentzville, MO 63385

TEST NUMBER
J11438

PRODUCT DESCRIPTION
.787" (20mm) SQ Plate

DELIVERY CONDITION
Annealed

Specifications
This material complies with the following specifications:

AMS 4911 L	
AMS-T-9046 A	AB-1 CONDITION A
ASTM B 265 -10	GRADE 5
BS 2TA56 2009	
BS EN 3464 2009	
MIL-T-9046 J AM 2	AB-1 CONDITION A

Melt Method	*Melt/Process Location*
3-VAR	TIMET - Henderson, NV, USA / TIMET - Toronto, OH, USA

Compliance Statements

1. Surface free from alpha case and product conforms to the other technical requirements of the referenced specification(s).
2. Microstructure examined and acceptable to the order specifications.
3. Immersion ultrasonic tested per prEN 4050-4 Ed P1 Class S and acceptable.
4. Immersion ultrasonic tested per AMS 2631 C Class A1 and acceptable.
5. Dimensional tolerances (except where overriden by Purchase Order) and testing requirements per BS3TA100.
6. Flatness requirements in accordance with LN 9297 Revision A1.
7. Material certificate in compliance with EN 10204:2004 Type 3.1.
8. Quality system per MIL-I-45208A Am. 1, calibration system per MIL-STD-45662A.
9. Airbus SAS approval number 100390 applies. We certify that the whole of the supplies detailed hereon have been manufactured, inspected, tested and, unless other wise stated, conform in all respects to the relevant specifications, drawings, and contract/order.
10. TIMET-Toronto is on the BAE Systems Register of Evaluated Suppliers by virtue of AS/EN9100 series approval (reference S. Pollard letter dated 01-Nov-06, letter reference ACO/T/LT/AG/1457).
11. Material has been processed in accordance with the quality system per RR9000: SABRe Approval #10727.
12. TIMET-Toronto has a Quality Management System that is in compliance with ISO 9001:2008, ANSI/ISO/ASQ Q9001-2008 and AS 9100:2001 Revision B, Certificate No. UQA 0113328, through Lloyd's Register Quality Assurance, effective 24-Jul-03.

Accredited Nadcap — Materials Testing Laboratory, Mechanical Testing, Heat Treating
REGISTERED ISO 9001/AS9100 FACILITY

First in Titanium Worldwide

Titanium Metals Corporation
100 Titanium Way, Toronto, OH 43964
Telephone (740) 537-5694, Fax (740) 537-5653

Approved Certificate

CERT ID
H16972-12
09-JAN-2012 19:14:17 GMT

PURCHASE ORDER
20077004

SOLD TO CUSTOMER
TIMET Service Center St. Louis
109 Interstate Drive, Wentzville, MO 63385

Ingot Chemical Analysis
(Weight percent)

Unless otherwise noted, Ingot Chemical Analysis performed at Henderson Process Lab, 181 N. Water Street, Henderson, NV, 89015, USA

Sample ID	Fe	V	Al	C	O	N	Y
TOP	0.16	4.08	6.36	0.017	0.18	0.006	<0.0004
BOTTOM	0.15	4.04	6.36	0.014	0.18	0.005	<0.0004

Product Analysis
(Weight percent)

Unless otherwise noted, Product Analysis performed at Toronto Laboratory, 100 Titanium Way, Toronto, OH, 43964, USA

Sample ID	H
1UR1	47

Chemistry Statements

1. Hydrogen values reported in PPM. Hydrogen determined by inert gas fusion per ASTM E1447. Carbon determined by combustion per ASTM E1941. Oxygen and Nitrogen determined by inert gas fusion per ASTM E1409. Henderson Melt: Metallics determined by Inductively Coupled Plasma-Atomic Emission Spectrometry (ICP-AES) per ASTM E2371. Morgantown Melt: Copper and Boron by atomic spectrometry (ingot only) and all other elements by x-ray fluorescence spectrometry.
2. Residual elements each less than 0.10% maximum, 0.40% maximum total.
3. Balance titanium.

Mechanical Properties

Unless otherwise noted, testing performed at Toronto Laboratory, 100 Titanium Way, Toronto, OH, 43964, USA

RTT - Longitudinal (ASTM E 8)
Test Condition: Mill Annealed 1 Hour @ 1400°F (760°C) AC

Sample ID	0.2YS	U.T.S	2inEL	EL 5.65A %	R.A.
	MPa	MPa	%	%	%
1U	863	944	16	14	31

RTT - Transverse (ASTM E 8)
Test Condition: Mill Annealed 1 Hour @ 1400°F (760°C) AC

Sample ID	0.2YS	U.T.S	2inEL	EL 5.65A %	R.A.
	MPa	MPa	%	%	%
1U	965	1040	16	14	31

Accredited Nadcap — Materials Testing Laboratory ISO/IEC 17025; Nondestructive Testing; Heat Treating

REGISTERED ISO 9001/AS9100 FACILITY

First in Titanium Worldwide

Titanium Metals Corporation
100 Titanium Way, Toronto, OH 43964
Telephone (740) 537-5694, Fax (740) 537-5653

Approved Certificate

CERT ID
H16972-12
09-JAN-2012 19:14:17 GMT

PURCHASE ORDER
20077004

SOLD TO CUSTOMER
TIMET Service Center St. Louis
109 Interstate Drive, Wentzville, MO 63385

Metallurgical Properties

Unless otherwise noted, testing performed at Toronto Laboratory, 100 Titanium Way, Toronto, OH, 43964, USA

Grain Size (ASTM E 112)
Test Condition: Mill Annealed 1 Hour @ 1400°F (760°C) AC

Sample ID	GRAIN SIZE
	Grn
1U	9.0

Micro Exam - Transverse
ETTC 4,KROLLS,100X
Test Condition: Mill Annealed 1 Hour @ 1400°F (760°C) AC

Sample ID	MT-PRE	OVERALL
	Micr	P/F
1U	P6	PASS

Tests on Other Material

Unless otherwise noted, testing performed at Toronto Laboratory, 100 Titanium Way, Toronto, OH, 43964, USA

Batch: 08137DD-11 (J11473)
RTT - Longitudinal (ASTM E 8)
Test Condition: Periodic Test: Mill Annealed 60 Minutes 1400°F AC + Lab Annealed 20 Minutes @ 1325°F AC

Sample ID	0.2YS	U.T.S.	4DEL	R.A.
	ksi	ksi	%	%
1	124	137	13	23

Results are from TIMET Quality Control Records on file
Sales Order # 323760 Item # 10
v.1

Bill Williamson - Certification Specialist

Accredited Nadcap Materials Testing Laboratory ISO/IEC 17025 Nondestructive Testing Heat Treating

REGISTERED ISO 9001/AS9100 FACILITY

First in Titanium Worldwide

Technical drawings for the 40 · 20 · 60 mm^3 workpieces used in this thesis:

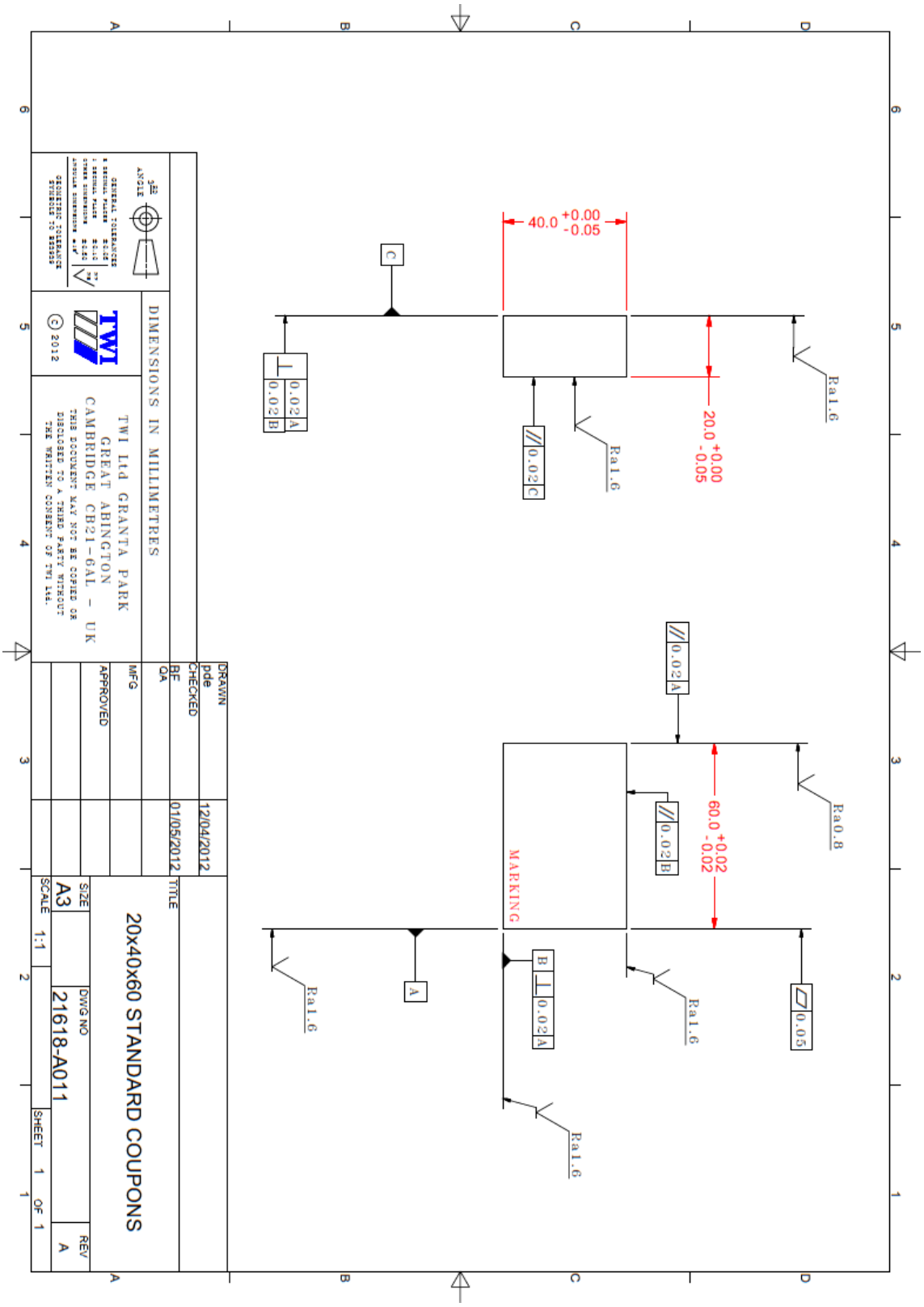

Note that the smaller workpieces detailed in chapter five (weld numbers 43 and 44) were machined from the workpieces detailed above.

The technical drawing for the $40 \cdot 20 \cdot 60$ mm^3 workpieces that were modified to have thermocouples fitted is shown in the following:

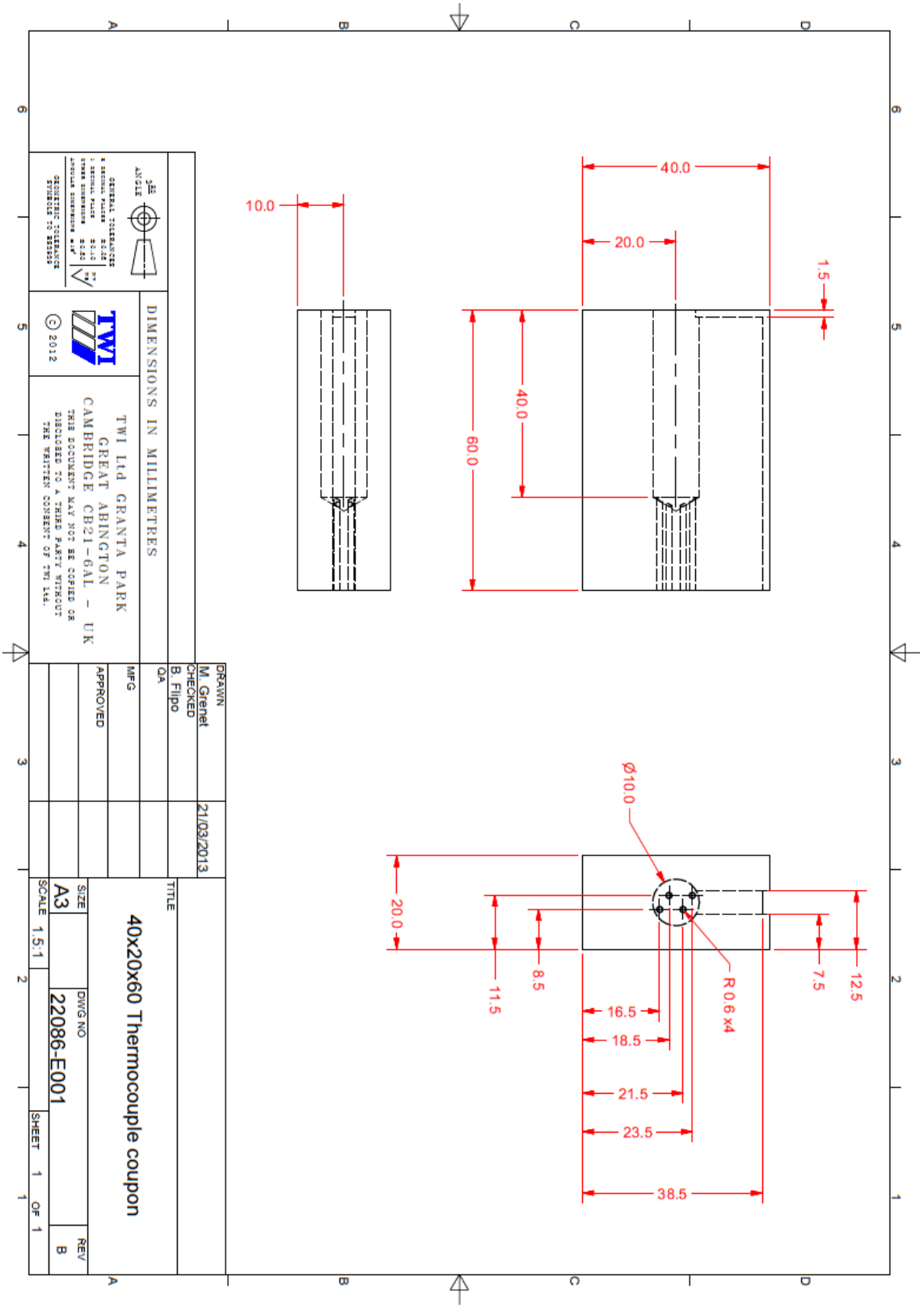
10.0
40.0
20.0
1.5
40.0
60.0
Ø10.0
20.0
11.5
8.5
7.5
12.5
R 0.6 x4
16.5
18.5
21.5
23.5
38.5
DIMENSIONS IN MILLIMETRES
TWI Ltd GRANTA PARK
GREAT ABINGTON
CAMBRIDGE CB21-6AL - UK
THIS DOCUMENT MAY NOT BE COPIED OR
DISCLOSED TO A THIRD PARTY WITHOUT
THE WRITTEN CONSENT OF TWI Ltd.
© 2012
DRAWN
M. Grenet
21/03/2013
CHECKED
B. Filipo
QA
MFG
APPROVED
TITLE
40x20x60 Thermocouple coupon
SIZE
A3
DWG NO
22086-E001
REV
B
SCALE
1.5:1
SHEET 1 OF 1

Appendix B : Experimental Conditions

The experimental and geometric conditions used in this thesis are displayed in the table and figure, respectively, below.

Experimental Input Conditions

TC = thermocouple

Experiments used in thesis

Thesis weld number	FW34 (E20) Number	Frequency (Hz)	Amplitude (mm)	Applied force (kN)	Burn-off (mm)	Average rubbing velocity (mm/s)	Pressure (MPa)	Workpiece geometry	Used in Chapter(s)
1	2762	50	2.7	66	1	540	82.5	(a)	3, 4
2	2763	70	1	100	3	280	125	(a)	3, 4
3	2764	20	2.7	100	3	216	125	(a)	3, 4
4	2765	70	1	100	1	280	125	(a)	3, 4
5	2766	58.2	2	32	1	465.6	40	(a)	3, 4
6	2767	50	2.7	100	2	540	125	(a)	3, 4
7	2768	30	2.7	32	1	324	40	(a)	3, 4
8	2769	60	1.9	100	3	456	125	(a)	3, 4
9	2770	30	2	32	3	240	40	(a)	3, 4
10	2771	50	2.7	32	3	540	40	(a)	3, 4
11	2772	23.3	1.3	77.3	1	121.16	96.625	(a)	3, 4
12	2773	20	2.7	100	1	216	125	(a)	3, 4
13	2774	30	1	100	3	120	125	(a)	3, 4
14	2775	20	1.5	100	2	120	125	(a)	3, 4
15	2776	42.3	1.5	68.3	2	253.8	85.375	(a)	3, 4
16	2777	31.6	2.3	68.3	2.5	290.72	85.375	(a)	3, 4
17	2778	64.1	1.5	66	1	384.6	82.5	(a)	3, 4
18	2779	42.1	2.4	32	2	404.16	40	(a)	3, 4
19	2780	64.1	1.5	66	3	384.6	82.5	(a)	3, 4
20	2781	60	1.9	100	1	456	125	(a)	3, 4
21	2782	30	2	32	3	240	40	(a)	3, 4
22	2783	20	2.7	100	1	216	125	(a)	3, 4
23	2784	50	2.7	32	3	540	40	(a)	3, 4
24	2785	20	1.5	100	2	120	125	(a)	3, 4
25	2786	30	1	100	3	120	125	(a)	3, 4
26	3140	20	1.5	100	3	120	125	(a)	3, 4 (TC)
27	3143	50	2.7	100	3	540	125	(a)	3, 4 (TC)
28	3145	30	2	32	3	240	40	(a)	3, 4 (TC)
29	3147	50	2.7	32	3	540	40	(a)	3, 4 (TC)
30	3044	50	2.7	100	0.5	540	125	(a)	4
31	3045	50	2.7	100	1	540	125	(a)	4
32	3046	50	2.7	100	3	540	125	(a)	4, 5, 6
33	3047	50	2.7	32	0.5	540	40	(a)	4
34	3048	50	2.7	32	1	540	40	(a)	4
35	3050	50	2.7	32	3	540	40	(a)	4
36	3051	20	1.5	100	0.5	120	125	(a)	4
37	3052	20	1.5	100	1	120	125	(a)	4
38	3053	20	1.5	100	3	120	125	(a)	4
39	3054	30	2	32	0.5	240	40	(a)	4
40	3055	30	2	32	1	240	40	(a)	4
41	3056	30	2	32	3	240	40	(a)	4,6
42	3543	50	2.7	100	3	540	125	(b)	5,6
43	3545	50	2.7	50	3	540	125	(c)	5
44	3548	50	2.7	25	3	540	125	(d)	5
45	2116	-	-	-	-	-	-	Keystone	6

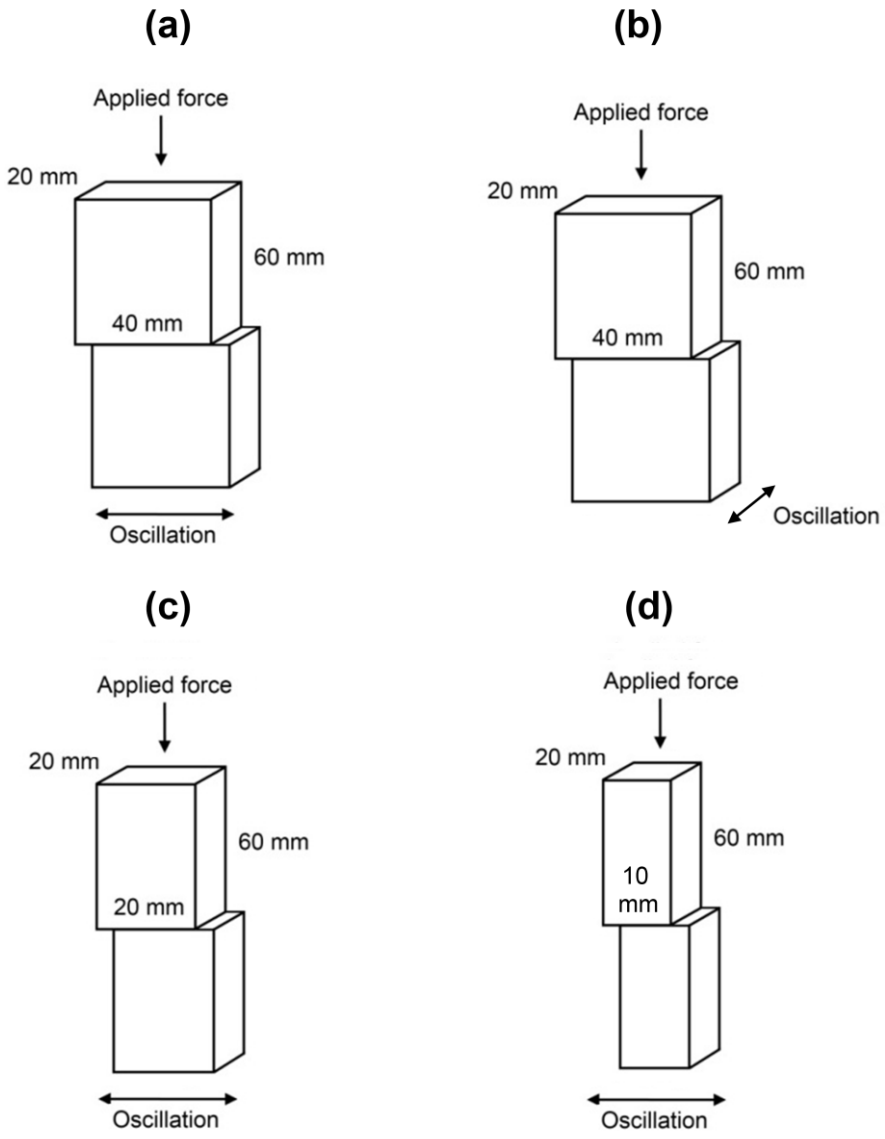

Workpiece dimensions used in this thesis (not to scale).

The experimental results are displayed in the tables below.

Experimental Results (a)

	Responses							
Thesis weld number	*Burn-off rate (mm/s)*	*Welding time [phase 1-4 Oscillations only] (s)*	*Welding time [phase 1] (s)*	*Welding time [phase 2] (s)*	*Welding time [phase 3] (s)*	*Average power input [phase 1] (kW)*	*Average power input [phase 2] (kW)*	*Average power input [phase 3] (kW)*
1	4.12	0.89	0.42	0.22	0.16	17.4	**21.3**	21.1
2	2.57	2.39	1.01	0.33	1.05	9.66	11.4	10.7
3	2.52	3.11	1.41	0.41	1.29	8.4	10	9.6
4	2.56	1.66	1.15	0.23	0.27	9.9	11.2	10.8
5	2.6	1.35	0.49	0.37	0.26	15.43	18.8	17.5
6	5.37	1.02	0.29	0.2	0.32	19.1	23.55	22.25
7	2.313	1.99	0.89	0.66	0.31	9.14	13.2	12.6
8	4.64	1.39	0.47	0.14	0.58	16.9	19	17.9
9	2.08	4.28	2.23	0.54	1.31	7	10.1	9.3
10	4.138	1.62	0.64	0.21	0.66	15.9	20.1	18.7
11	0.92	7.27	5.49	0.87	0.75	4.1	5.7	5.4
12	1.99	2.25	1.35	0.42	0.36	8.4	10.3	9.8
13	1.1	7.9	4.11	1.13	2.46	4.46	5.8	5.4
14	1.18	6.8	4.5	0.72	1.44	4.6	5.8	5.5
15	2.57	2.61	1.55	0.29	0.67	8.9	10.7	10.1
16	3.13	2.19	1.16	0.23	0.69	10.63	12.4	12
17	3.29	1.36	0.84	0.18	0.22	12.94	15.1	14.7
18	2.93	1.75	0.66	0.4	0.59	12.6	16.3	14.8
19	3.62	1.73	0.64	0.23	0.75	13.6	15.8	14.7
20	4.17	0.88	0.4	0.2	0.16	17	20	18.7
21	1.98	3.88	1.57	0.84	1.35	7	9.9	9.2
22	1.92	2.25	1.31	0.45	0.36	8.3	10.3	9.6
23	4.08	1.56	0.58	0.21	0.66	16.5	19.9	19.3
24	1.27	6.85	4.8	0.6	1.33	4.55	5.7	5.4
25	1.18	8.15	5.05	0.67	2.25	4.38	5.6	5.2
26	-	-	-	-	-	-	-	-
27	-	-	-	-	-	-	-	-
28	-	-	-	-	-	-	-	-
29	-	-	-	-	-	-	-	-
30	-	-	-	-	-	-	-	-
31	-	-	-	-	-	-	-	-
32	6	-	0.32	-	-	-	-	-
33	-	-	-	-	-	-	-	-
34	-	-	-	-	-	-	-	-
35	-	-	-	-	-	-	-	-
36	-	-	-	-	-	-	-	-
37	-	-	-	-	-	-	-	-
38	-	-	-	-	-	-	-	-
39	-	-	-	-	-	-	-	-
40	-	-	-	-	-	-	-	-
41	-	-	-	-	-	-	-	-
42	7.1	-	0.25	-	-	20.45	-	23.21
43	7.3	-	0.22	-	-	10.79	-	13.56
44	11.63	-	0.15	-	-	8.65	-	9.3
45	-	-	-	-	-	-	-	-

Experimental Results (b)

	Responses						
Thesis weld number	*Average interface force [phase 1] (kN)*	*Average interface force [phase 2] (kN)*	*Average interface force [phase 3] (kN)*	*Total process energy [phases 0 - 4] (kJ)*	*Total weld energy [phases 1 - 4] (kJ)*	*TMAZ thickness (mm)*	*Flash thickness (mm)*
1	32.74	40.25	37.43	35.35	16.45	1.6	-
2	35.38	41.6	38.75	30.81	25.72	1.1	-
3	36.6	43.36	41.16	31.55	29.57	1.3	-
4	36.09	39.63	39.08	22.39	17.45	1.3	-
5	34.2	41.88	39.1	37.62	19.89	2.2	-
6	36.4	45.1	41.57	33.44	18.31	1.2	-
7	26.61	37.95	36.12	27.25	21.547	2.3	-
8	38.25	44.65	41.12	34	21.72	1.3	-
9	27.67	39.45	36.4	36.875	33.59	2.6	-
10	30.83	39.73	37.2	49.7	27.51	2.4	-
11	32.2	43.9	41.2	32.9	32	1.8	-
12	36.73	44.5	41.63	21.9	19.7	1.6	-
13	35.05	44.18	40.89	39.14	38.65	1.5	-
14	35.8	45.6	42.2	33.91	32.97	1.3	-
15	33.43	40.43	37.75	27.63	24.07	1.9	-
16	33.98	40.35	38.5	28.32	24.23	1.9	-
17	34.98	41.6	39.38	26.93	17.56	1.7	-
18	30.44	38.76	35.74	34.78	24.17	2.5	-
19	36.62	43	38.476	33.51	24.1	1.7	-
20	37.9	45	42.2	27.41	14.8	1.5	-
21	28.11	38.92	36.34	35.55	32.37	2.9	-
22	36.33	44.37	41.54	21.7	19.58	1.5	-
23	31.11	38.1	36.84	48.96	27.37	2.3	-
24	35.66	44.55	41.66	33.56	32.72	1.5	-
25	34.34	43.07	39.25	38.57	38.11	1.3	-
26	-	-	-	-	-	-	-
27	-	-	-	-	-	-	-
28	-	-	-	-	-	-	-
29	-	-	-	-	-	-	-
30	-	-	-	-	-	-	-
31	-	-	-	-	-	-	-
32	-	-	-	-	-	1.2	2.4
33	-	-	-	-	-	-	-
34	-	-	-	-	-	-	-
35	-	-	-	-	-	2.4	3.2
36	-	-	-	-	-	-	-
37	-	-	-	-	-	-	-
38	-	-	-	-	-	1.3	2.6
39	-	-	-	-	-	-	-
40	-	-	-	-	-	-	-
41	-	-	-	-	-	2.6	3.2
42	39.13	-	44.94	-	-	0.67	-
43	21.59	-	26.83	-	-	0.66	-
44	17.37	-	18.39	-	-	0.26	-
45	-	-	-	-	-	-	-

Experimental Results (c)

	Responses			
Thesis weld number	*Average interface force between 0 mm and 1 mm of burn-off (kN)*	*Average interface force between 1.5 mm and 3 mm of burn-off (kN)*	*Average in-plane force during phase 1 (kN) (for contaminant comparison)*	*Average theoretical interface area in-contact (mm^2)*
1	-	-	-	766.7
2	37.3	38.5	-	788.1
3	42.5	40.8	-	766.5
4	-	-	-	788.1
5	-	-	-	775.3
6	-	-	39.9	766.7
7	-	-	-	766.4
8	43.3	40.9	-	776.6
9	38.4	36.3	25.6	775.3
10	38.1	37.6	38.4	766.7
11	-	-	-	784.2
12	-	-	-	766.5
13	43	40.7	-	788.1
14	-	-	34.8	781.7
15	-	-	-	781.7
16	-	-	-	771.6
17	-	-	-	781.7
18	-	-	-	770.3
19	41.9	39.3	-	781.7
20	-	-	-	776.6
21	38	36.3	-	775.3
22	-	-	-	766.5
23	37.7	37.3	-	766.7
24	-	-	-	781.7
25	41.6	39.2	-	788.1
26	-	-	-	781.7
27	-	-	-	766.7
28	-	-	-	775.3
29	-	-	-	766.7
30	-	-	-	766.7
31	-	-	-	766.7
32	-	-	38.6	766.7
33	-	-	-	766.7
34	-	-	-	766.7
35	-	-	37.9	766.7
36	-	-	-	781.7
37	-	-	-	781.7
38	-	-	33.3	781.7
39	-	-	-	775.3
40	-	-	-	775.3
41	-	-	25.5	775.3
42	-	-	-	732.6
43	-	-	-	366.3
44	-	-	-	166.1
45	-	-	-	-

Appendix C : Ti-6Al-4V Material Constitutive Data Used in the Modelling Work

This appendix details the material constitutive data used in the 2D and 3D FEA work. The flow stress values and the thermal properties used are shown in the figures below. The emissivity was assumed to be 0.7 for all conditions evaluated in this thesis[167].

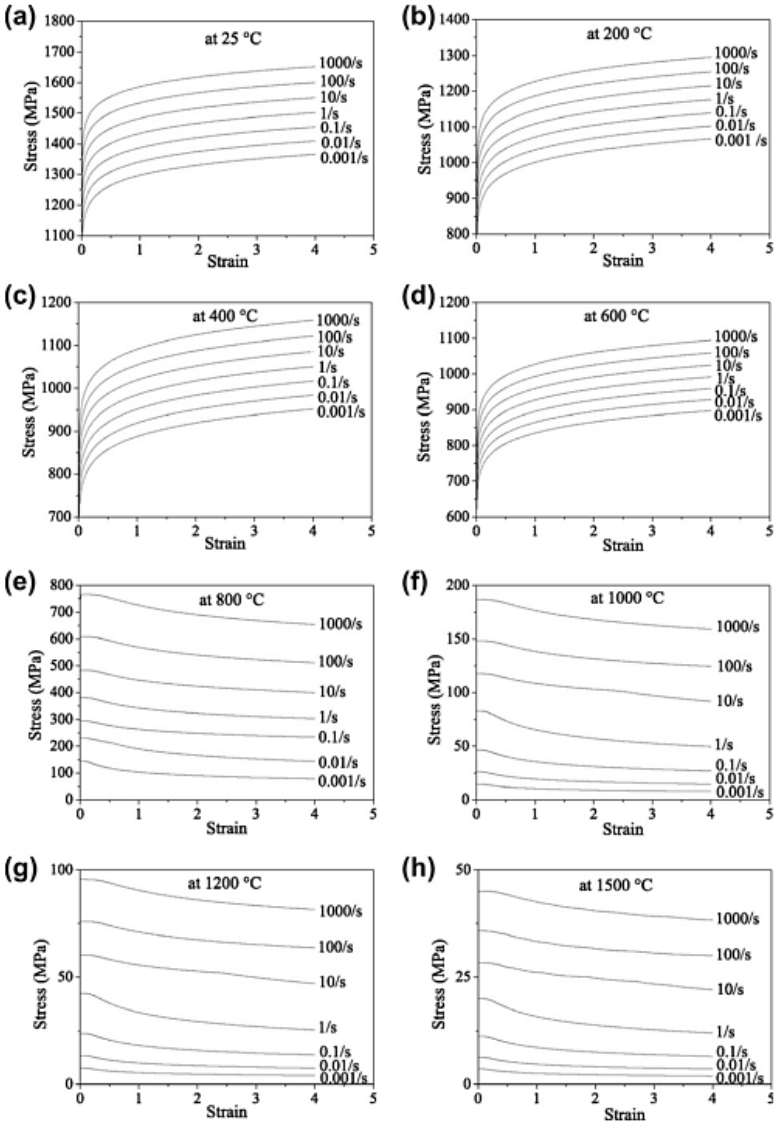

Ti–6Al–4V stress–strain curves assumed for the modelling, for differing strain rates at fixed temperatures of (a) 25 °C, (b) 200 °C, (c) 400 °C, (d) 600 °C, (e) 800 °C, (f) 1000 °C, (g) 1200 °C and (h) 1500 °C. Note that the values begin from the material yield point[7].

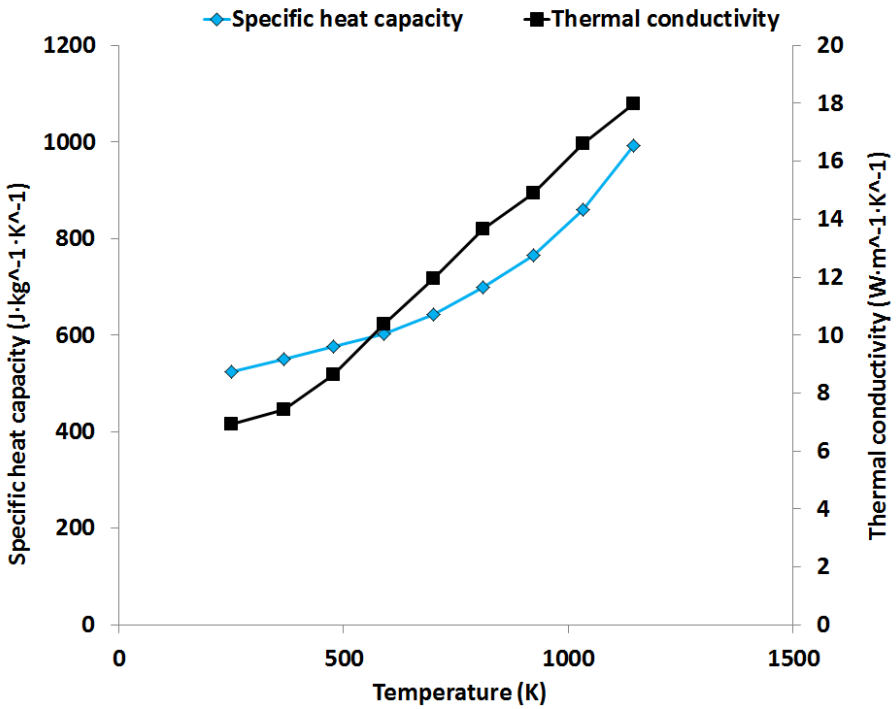

Thermal properties used in the modelling work. The values were taken from the DEFORM software's standard library.

Appendix D : Modelling Conditions

The tables below shows the different conditions used for the fully coupled thermo-mechanical models, along with the obtained results.

Modelling Conditions

Model number	Model dimension	Simulated Frequency (Hz)	Simulated Amplitude (mm)	Average rubbing velocity (mm/s)	Simulated Force (kN) / Pressure (MPa)	Simulated Burn-off (mm)	In-plane width (mm)	Corresponding thesis experiment number	Used in Chapter(s)
1	2d	50	2.7	540	66 / 82.5	3	40	1	4
2	2d	70	1	280	100 / 125	3	40	2 and 4	4
3	2d	20	2.7	216	100 / 125	3	40	3, 12 and 22	4
4	2d	58.2	2	465.6	32 / 40	3	40	5	4
5	2d	50	2.7	540	100 / 125	3	40	6	4,5
6	2d	30	2.7	324	32 / 40	3	40	7	4
7	2d	60	1.9	456	100 / 125	3	40	8 and 20	4
8	2d	30	2	240	32 / 40	3	40	9 and 21	4,5
9	2d	50	2.7	540	32 / 40	3	40	10 and 23	4,5
10	2d	23.3	1.3	121.16	77.3 / 96.6	3	40	11	4
11	2d	30	1	120	100 / 125	3	40	13 and 25	4,5
12	2d	20	1.5	120	100 / 125	3	40	14 and 24	4
13	2d	42.3	1.5	253.8	68.3 / 85.4	3	40	15	4
14	2d	31.6	2.3	290.72	68.3 / 85.4	3	40	16	4
15	2d	64.1	1.5	384.6	66 / 82.5	3	40	17 and 19	4
16	2d	42.1	2.4	404.16	32 / 40	3	40	18	4
17	2d	50	2.7	540	50 / 125	3	20	42 and 43	5
18	2d	30	1	120	50 / 125	3	20	-	5
19	2d	50	2.7	540	16 / 40	3	20	-	5
20	2d	30	2	240	16 / 40	3	20	-	5
21	2d	50	2.7	540	25 / 125	3	10	44	5
22	2d	30	1	120	25 / 125	3	10	-	5
23	2d	50	2.7	540	8 / 40.	3	10	-	5
24	2d	30	2	240	8 / 40.	3	10	-	5
25	3d	50	2.7	540	100 / 125	3	40	32	6
26	3d	50	2.7	540	100 / 125	3	20	42	6
27	3d	-	-	-	-	-	-	Keystone weld	6

Modelling Results (a)

	Responses					
Model number	*Burn-off rate (mm/s)*	*TMAZ thickness (mm)*	*Flash thickness (mm)*	*Peak interface temperature [phase 3] (c)*	*Peak interface strain rate [phase 3] (s^-1)*	*Remaining point tracking at design point burn-off*
1	3.6	2.4	2.9	1280	780	7
2	2.2	2.2	3.1	1170	470	1 and 7
3	2	2.2	3.1	1130	330	1, 7 and 7
4	2.2	2.9	3.9	1310	570	9
5	4.54	2.15	3	1230	880	1
6	1.6	3.1	3.8	1240	390	11
7	3.8	2.3	3	1240	690	1 and 7
8	1.2	3.24	4	1210	300	1 and 1
9	2.9	3.06	3.9	1330	680	1 and 1
10	0.8	2.3	3.2	1060	150	9
11	0.7	1.9	3.1	1050	150	1 and 1
12	1.1	2.5	3.3	1070	160	3 and 3
13	1.6	2.48	3.2	1170	350	1
14	2.1	2.43	3.3	1200	430	1
15	2.3	2.38	3.2	1230	580	7 and 1
16	2	3	3.7	1280	470	3
17	7	1.4	1.8	1180	1390	-
18	1.9	1.7	2.2	1050	235	-
19	5	2.2	2.5	1240	920	-
20	2.24	2.3	3.1	1170	471	-
21	12.16	1.1	1.2	1140	1600	-
22	3.4	1.4	1.7	1040	473	-
23	7.9	1.6	1.6	1210	1350	-
24	4.85	1.65	2.1	1140	732	-
25	-	-	-	??	440	-
26	-	-	-	??	500	-
27	-	-	-	1160	500	-

Modelling Results (b)

	Responses			
Model number	*Average phase 3 interface force (kN)*	*Average phase 3 interface stress (N/mm^2)*	*Average phase 3 power input (kW)*	*Average phase 3 power input density (W/mm^2)*
1	25	32.6	14.1	18.4
2	28.4	36.0	8.2	10.4
3	30.6	39.9	6.7	8.7
4	19.2	24.8	10	12.9
5	28.1	36.7	15.6	20.3
6	23.3	30.4	8.1	10.6
7	25.2	32.4	12	15.5
8	23.6	30.4	5	6.4
9	22.2	29.0	11.7	15.3
10	32.7	41.7	4.7	6.0
11	33.8	42.9	4.8	6.1
12	31.1	39.8	4.5	5.8
13	27.5	35.2	7.8	10.0
14	27	35.0	8.2	10.6
15	25.6	32.7	11	14.1
16	18.3	23.8	7.7	10.0
17	35.6 / 17.8	48.6 / 48.6	20 / 10.0	27.3 / 27.3
18	19.1	49.3	2.43	6.3
19	12.9	35.2	7.05	19.2
20	15.24	40.7	3.82	10.2
21	10.88	65.5	6.27	37.7
22	11.62	62.0	1.45	7.7
23	8.32	50.1	4.73	28.5
24	9.44	54.0	2.36	13.5
25	47.5	62.0	-	-
26	58.1	79.3	-	-
27	-	-	-	-

Modelling Results (c)

	Responses		
Model number	*Burn-off to remove point tracking (mm)*	*Beta transus to 500 C cooling rate (C/s)*	*Average theoretical interface area in-contact assuming the inclusion of the out-of-plane dimension (mm^2)*
1	1.8	-	766.7
2	1.8	-	788.1
3	1.9	-	766.5
4	2.2	-	775.3
5	1.6	110	766.7
6	2.5	-	766.4
7	1.7	-	776.6
8	2.5	66	775.3
9	2.3	70	766.7
10	2.2	-	784.2
11	1.9	80	788.1
12	2.2	-	781.7
13	2	-	781.7
14	1.9	-	771.6
15	1.9	-	781.7
16	2.3	-	770.3
17	0.9	210	732.6 / 366.3
18	1.1	70	387.7
19	1.2	90	366.3
20	1.46	70	374.9
21	0.52	320	166.1
22	0.6	70	187.5
23	0.7	130	166.1
24	0.8	66	174.7
25	Did not expel	-	766.7
26	Did not expel	-	732.6
27	Did not expel	-	-

Appendix E : Mathematical Justification for the Sinusoidal Motion Power Input Assumption

Power input Calculation

power = Force x Velocity.

displacement = $x = A \sin \omega t$

* differentiate displacement to get Velocity.

Velocity = $v = A\omega \cos(\omega t)$

Energy input per cycle =

$$\int_0^T \text{Force} \times A\omega \cos(\omega t)$$

$$= \left[\int_0^T \text{Force} \times A \sin(\omega t) \right]$$

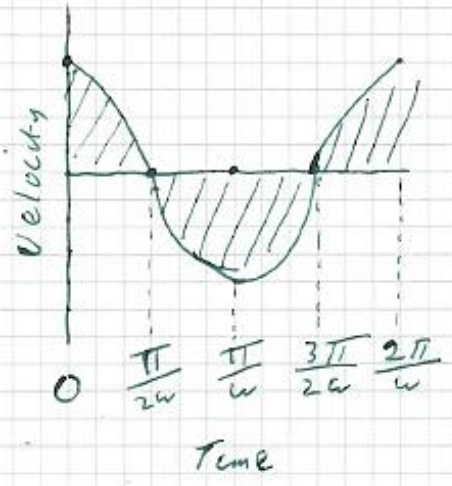

$\omega = 2\pi f$

f = frequency

A = Amplitude

F = Normal force.

Force = interface force

μ = coefficient of friction.

∴ Energy input per cycle =

$$\int_0^{\frac{\pi}{2w}} [\text{Force} \times A\sin(wt)]$$

$$- \int_{\frac{\pi}{2w}}^{\frac{3\pi}{2w}} [\text{Force} \times A\sin(wt)]$$

$$+ \int_{\frac{3\pi}{2w}}^{\frac{2\pi}{w}} [\text{Force} \times A\sin(wt)]$$

$$= [\text{Force} \times A] - [-2 \times \text{Force} \times A] + [\text{Force} \times A]$$

$$= 4 \times \text{Force} \times A.$$

* If we consider the Force as a product of the normal force and coefficient of friction, μ, we have:

$$4 \times F \times \mu \times A.$$

* To convert to power per cycle we divide by $\frac{2\pi}{w}$

$$= \frac{4F\mu \times A}{\frac{2\pi}{w}} = 4F\mu A f$$

(Same as the literature)

For positions near the edge there will be incomplete contact over a cycle. Consider a position, x_1, which is less than the amplitude A from the edge.

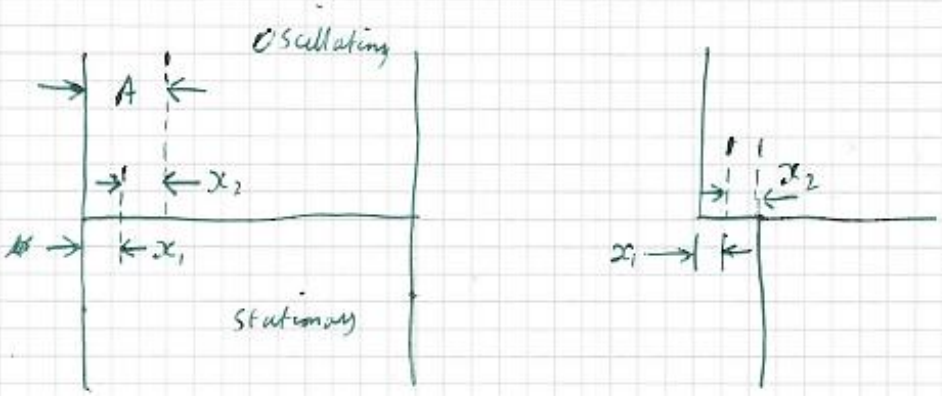

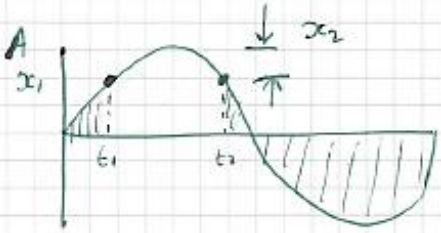

Hence the energy input will be less than that previously calculated.
We will need to modify the integral.

First identify the times when contact is lost.

i.e $x = x_1 = A \sin \omega t_1$

$\therefore \quad \frac{x_1}{A} = \sin \omega t_1$

$$\omega t_1 = \sin^{-1}\left(\frac{x_1}{A}\right)$$

$$t_1 = \frac{\sin^{-1}\left(\frac{x_1}{A}\right)}{\omega}$$

$$t_2 = \frac{\pi}{\omega} - \frac{\sin^{-1}\left(\frac{x_1}{A_1}\right)}{\omega} = \frac{\pi - \sin^{-1}\left(\frac{x_1}{A}\right)}{\omega}$$

* Re-evaluating the energy input:

Energy input per cycle =

$$\int_0^{\frac{\sin^{-1}\left(\frac{x_1}{A}\right)}{\omega}} \left[\text{Force} \times A\sin(\omega t)\right]$$

$$- \int_{\frac{\sin^{-1}\left(\frac{x_1}{A}\right)}{\omega}}^{\frac{3\pi}{2\omega}} \left[\text{Force} \times A\sin(\omega t)\right]$$

$$+ \int_{\frac{3\pi}{2\omega}}^{\frac{2\pi}{\omega}} \left[\text{Force} \times A\sin(\omega t)\right]$$

$$= \left[\text{Force} \times A \times \left(\frac{x_1}{A}\right) \right]$$

$$- \left[- \text{Force} \times A \quad - \text{Force} \times A \times \left(\frac{x_1}{A}\right) \right]$$

$$+ \left[\text{Force} \times A \right]$$

$$= 2\,\text{Force} \times A \quad + 2 \times \text{Force} \times A \times \left(\frac{x_1}{A}\right)$$

$$= 2\,\text{Force} \times A \times \left(1 + \left(\frac{x_1}{A}\right)\right)$$

* Convert to $F \times \mu$

$$= 2\mu F A \times \left(1 + \left(\frac{x_1}{A}\right)\right)$$

* divide by $\frac{2\pi}{\omega}$ to get power:

$$\frac{2\mu F A \times \left(1 + \left(\frac{x_1}{A}\right)\right)}{\frac{2\pi}{\omega}} = 2\mu F A f \left(1 + \frac{x_1}{A}\right)$$

Appendix F : Preliminary and Miscellaneous Modelling

Meshing investigation

Calculations were carried out to investigate the mesh size effects on the responses. This allowed for a suitable element size to be selected. 2D models were built in accordance with the methodology in chapter 5 and run for 10 oscillation cycles for a 10 mm in-plane width, 2.7 mm amplitude, 50 Hz frequency, and 125 MPa simulated pressure for the element sizes displayed in the table below.

Meshing Results

Mesh Element Length (mm)	Temp (◦C)	Burn-off (mm)
0.2	1050	1.13
0.15	1120	1.1
0.13	1140	1.06
0.11	1140	1.06

DOE justification model

To test the validity of the DOE equations in chapter 4, a model was produced at the following conditions:

- 40 mm in-plane width, 2 mm amplitude, 40 Hz frequency, 80 kN simulated applied force, burn-off to steady-state.

The predicted (95% PI) results from the equations are compared to the actual results from the model in the table below.

Comparison of Results

Equation	Units	95% Predicted Interval	Actual FEA
Burn-off rate	mm/s	2.35 - 2.58	2.54
TMAZ thickness	mm	2.11 - 2.67	2.35
Flash thickness	mm	2.86 - 3.27	3.16
Peak Temp	celcius	1187 - 1213	1180
Peak Strain rate	s^-1	448 - 511	502
Phase 3 interface force	kN	24.99 - 29.35	29.7
Phase 3 power input	Kw	8.42 - 10.6	9.8

In general the DOE equations gave a good predictive insight. The interface temperature and phase 3 power input were slightly out of the 95% predicted interval range. A possibly reason for this could be due to a newer version of DEFORM being used to calculate these values (V.11); the DOE equations were developed using data from DEFORM V.10.2.

Mechanical energy to heat energy conversion efficiency during plastic deformation

The figure below shows a comparison of the phase 3 thermal profiles generated for an amplitude, frequency, applied force and in-plane width of 2.7 mm, 50 Hz, 100 kN and 40 mm, respectively, for a heating conversion efficiency of 90 % (blue line) and 100 % (black line). The 100 % efficiency produced a slightly hotter interface temperature.

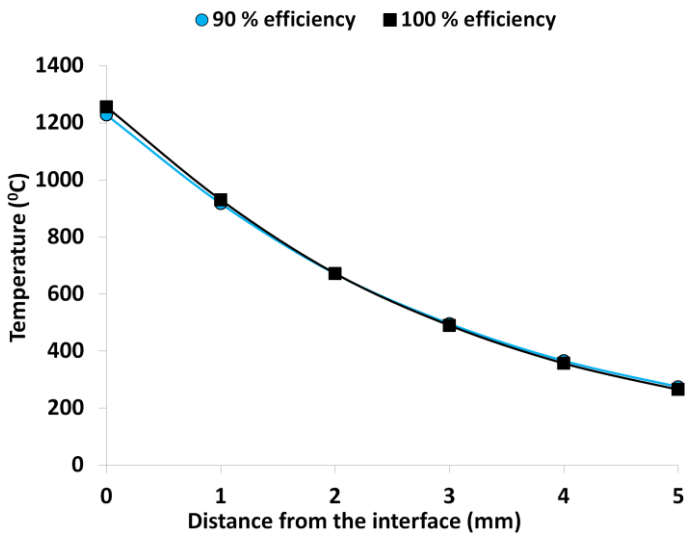

A comparison of the phase 3 thermal profiles generated for an amplitude, frequency, applied force and in-plane width of 2.7 mm, 50 Hz, 100 kN and 40 mm, respectively, for a heating conversion efficiency of 90 % (blue line) and 100 % (black line).

Appendix G : Computer Specification, DEFORM versions, Boundary Conditions, and Simulation Times

Computer Specification

The specification of the computer used for the modelling work in this thesis was as follows:

- *PC processor:* Intel Core i7 Processor i7-2600 (3.40GHz, 8MB L2, LGA1155) VT.
- *Graphics card:* PNY (Nvidia) Quadro 2000D 1GB Dual DVI.
- *Solid-state-drive (SSD):* OCZ RevoDrive 3 X2 PCI-Express SSD solid state drive 480GB.

DEFORM Version

Two versions of DEFORM were used for the modelling work in this thesis: Version 10.2 and Version 11. Version 10.2 was used for the modelling work in chapters 3 and 4. Version 11 was used for the modelling work in chapters 5 and 6.

Boundary Conditions

In addition to the modelling assumptions discussed in the preceding chapters the following boundary conditions were implemented:

- Gravity was excluded from the analysis.
- A limiting strain rate of $1*10^{-6}$ was applied. This meant that no deformation was assumed to occur at strain rates below this value.
- The tooling was assumed to be non-deformable and did not experience any moments, i.e. no rotation of the tooling occurred.
- The tooling interacted with the workpieces via the “sticking condition”, i.e. the two individual objects never separated.

Simulation Times

The table below shows the typical processing times required to complete a simulation using the computer specification detailed above.

Simulation times

Analysis	*Used in Chapters*	*Duration*
2D models (thermal only)	*3,6*	*2 minutes*
2D models (visco-plastic)	*3,4,5*	*12 hours*
3D models (visco-plastic)	*6*	*4 – 6 weeks*
3D keystone model (visco-plastic)	*6*	*4 weeks*

Appendix H : Experimental weld photos

This appendix displays photographs of the weld geometry and TMAZ micrographs for welds 1 to 25, 42, 43 and 44. Other than the several images previously presented in chapters 4 (Figure 4.10), no images were recorded for welds 26 to 41 due to them replicating the frequency, amplitude and force combinations used in welds 1 to 25.

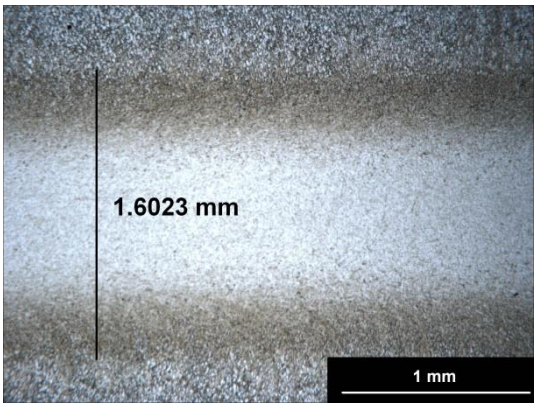

Weld 1

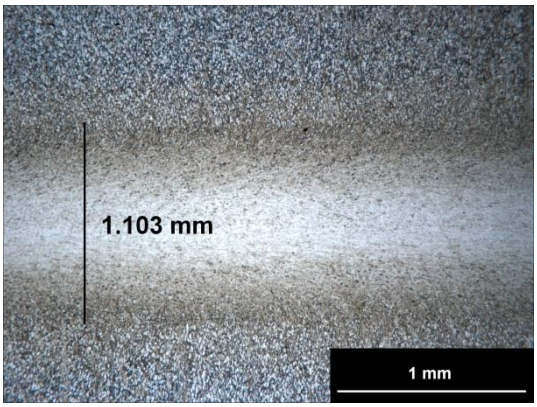

Weld 2

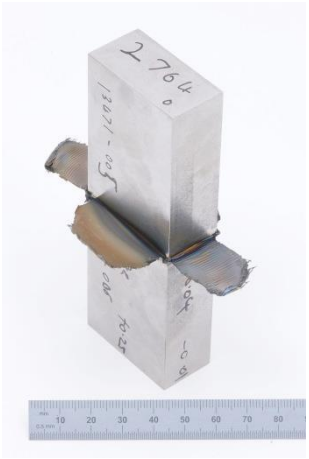

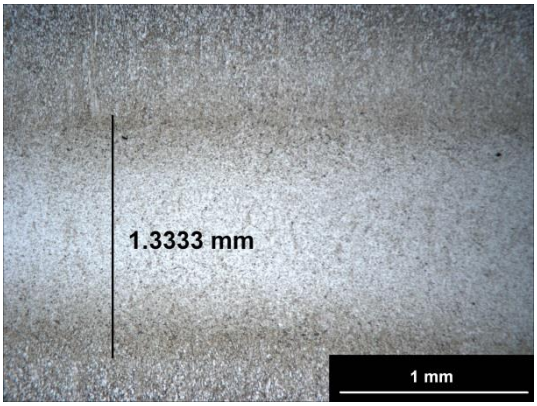

Weld 3

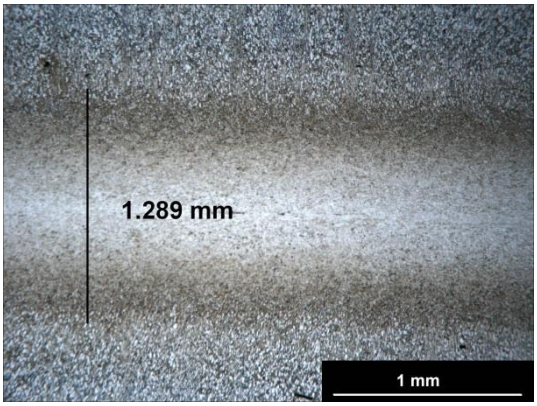

Weld 4

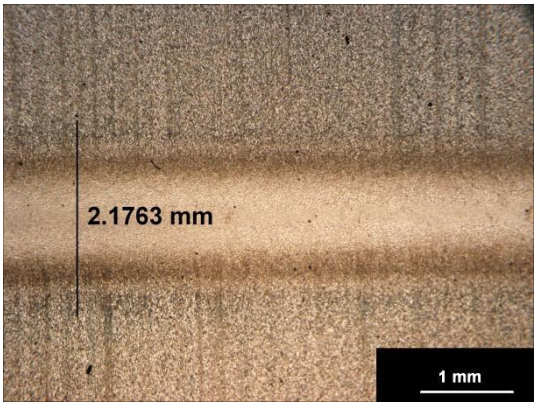

Weld 5

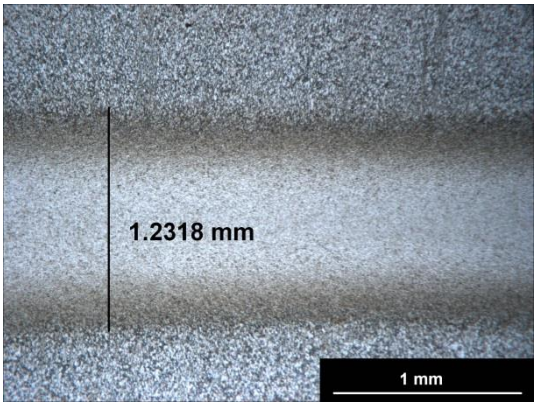

Weld 6

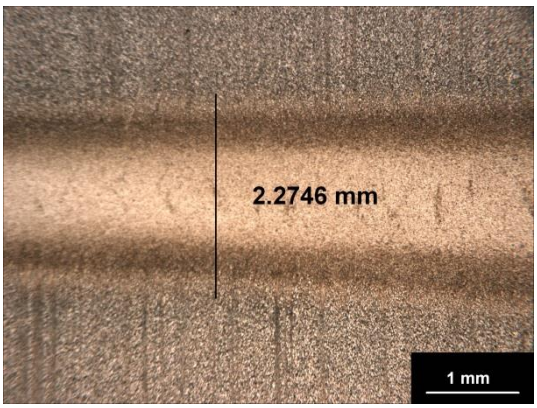

Weld 7

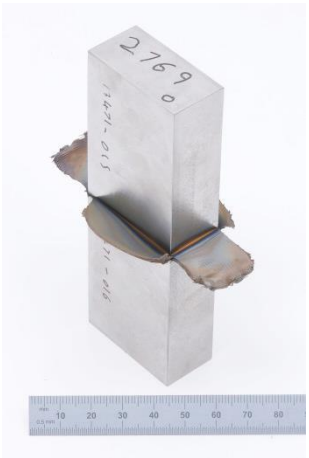

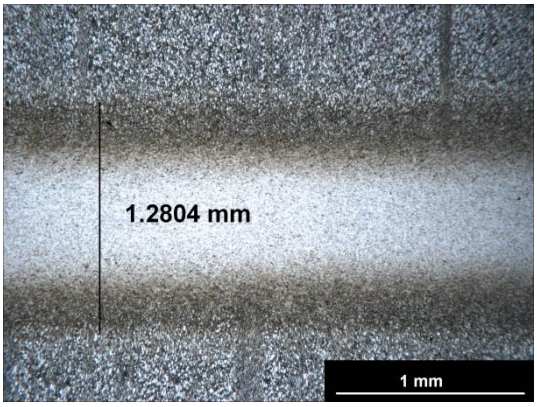

Weld 8

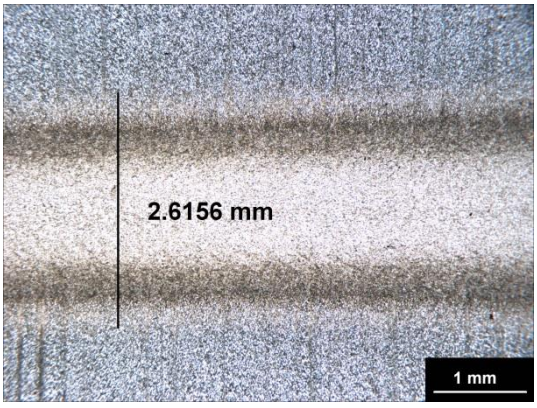

Weld 9

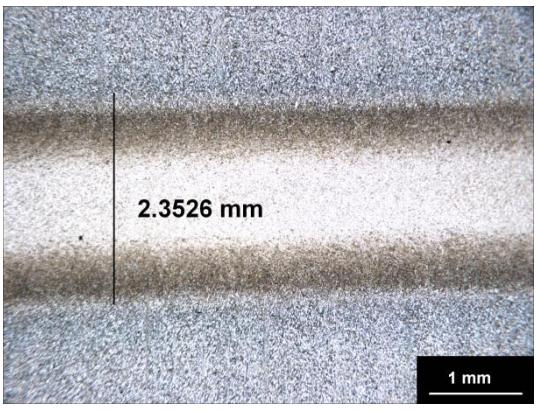

Weld 10

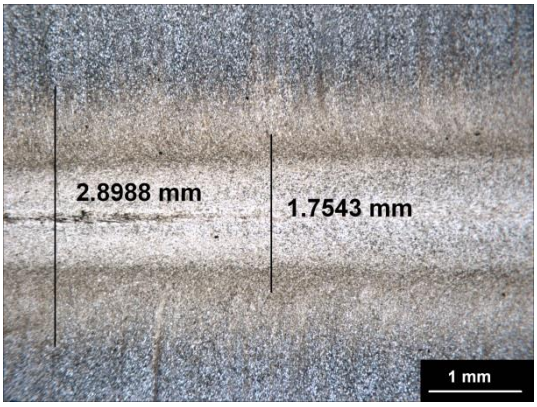

Weld 11 (note that there is also a noticeable HAZ – 2.9 mm)

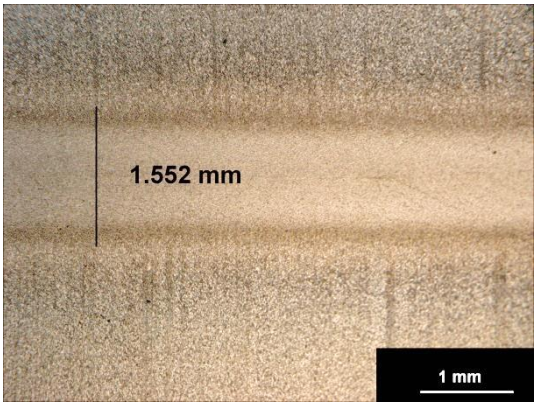

Weld 12

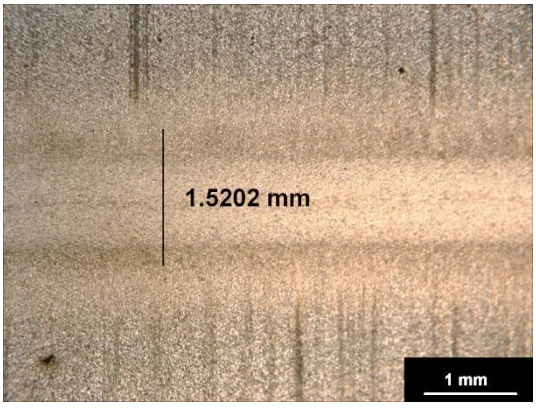

Weld 13 (note that there is also a noticeable HAZ)

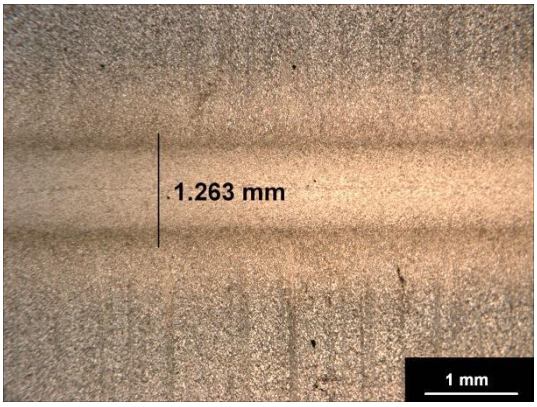

Weld 14 (note that there is also a noticeable HAZ)

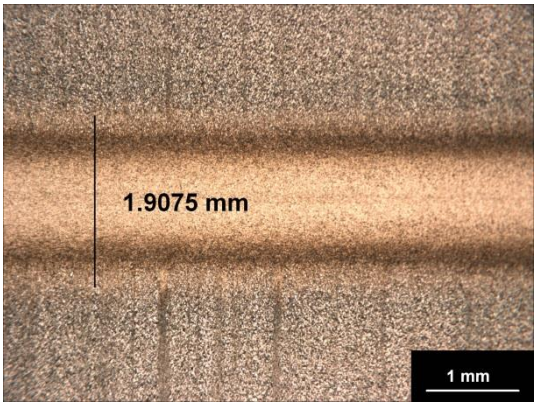

Weld 15

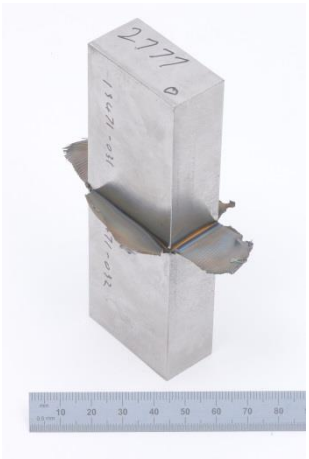

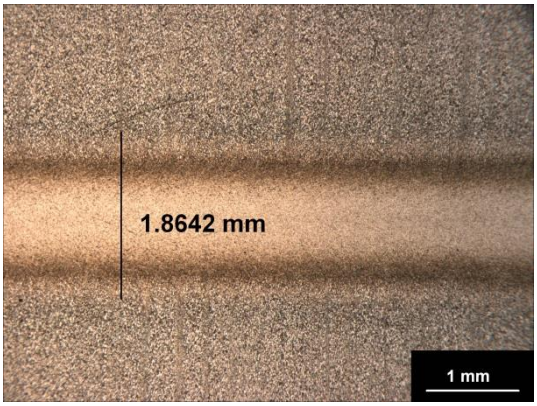

Weld 16

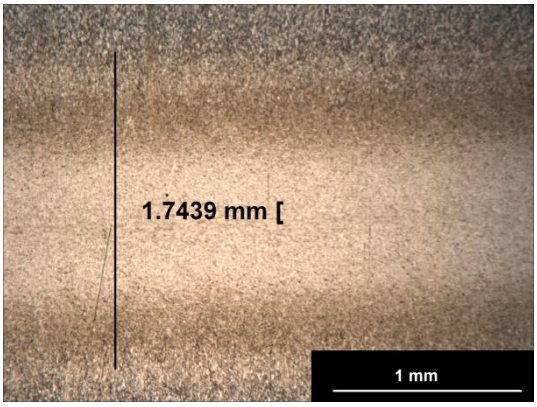

Weld 17

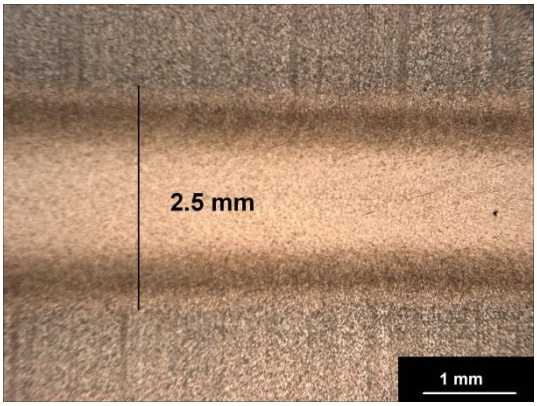

Weld 18

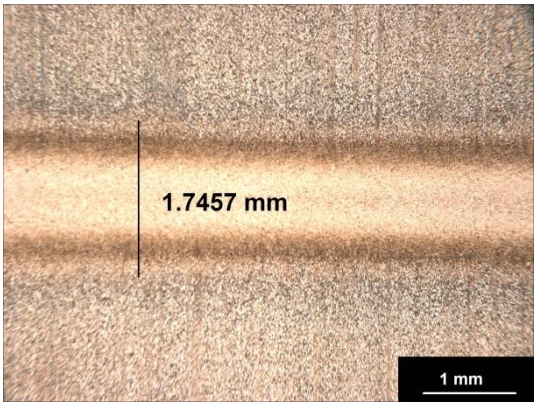

Weld 19

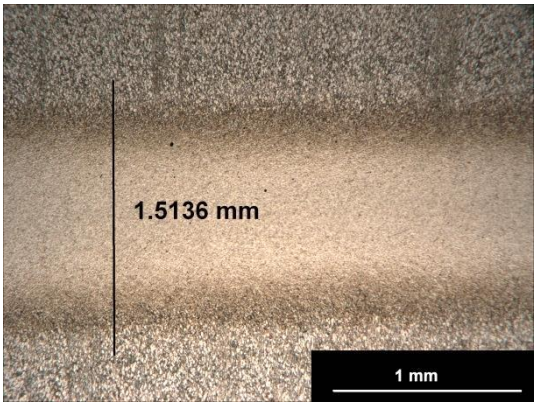

Weld 20

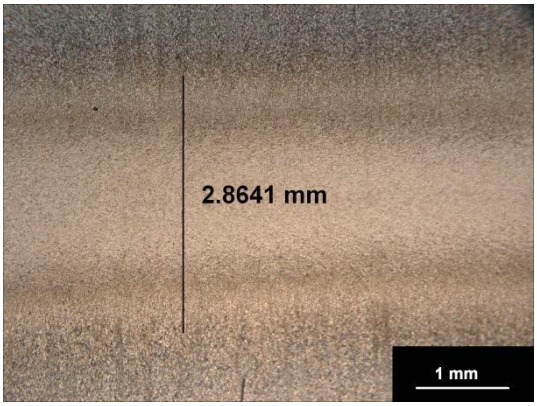

Weld 21

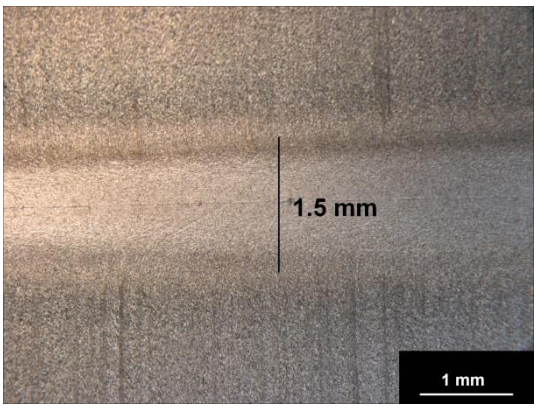

Weld 22

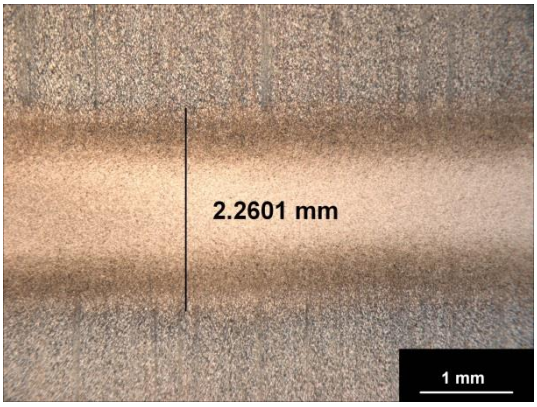

Weld 23

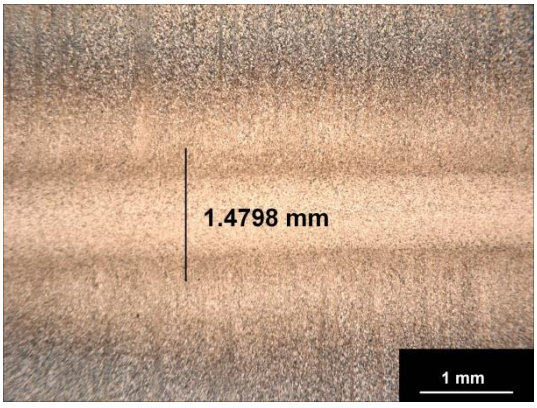

Weld 24 (note that there is also a noticeable HAZ)

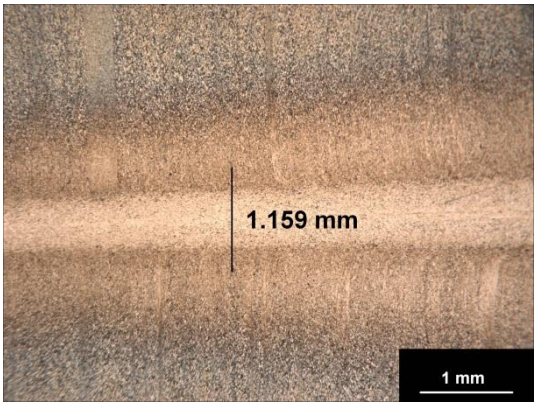

Weld 25 (note that there is also a noticeable HAZ)

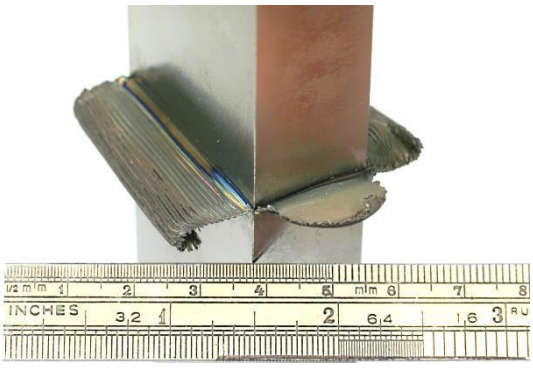

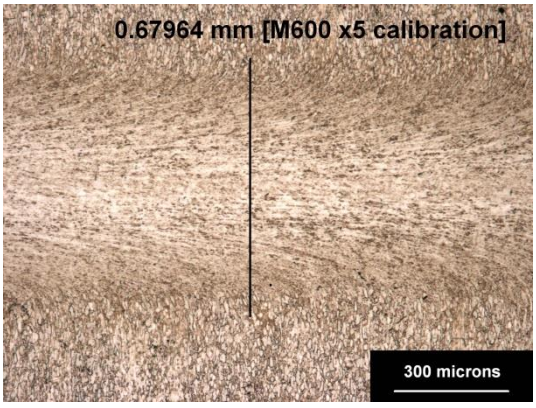

Weld 42

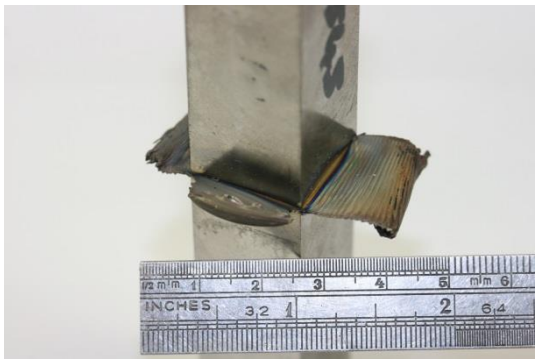

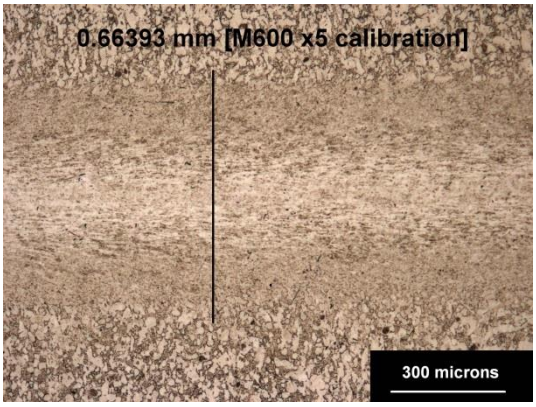

Weld 43

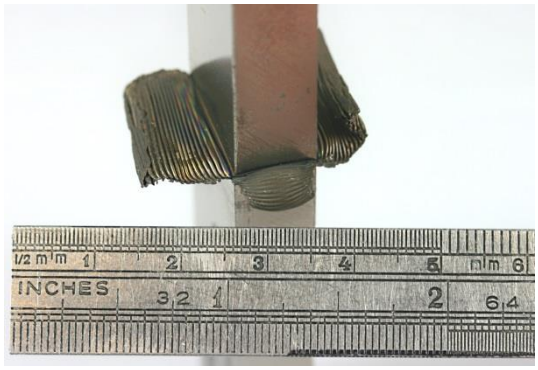

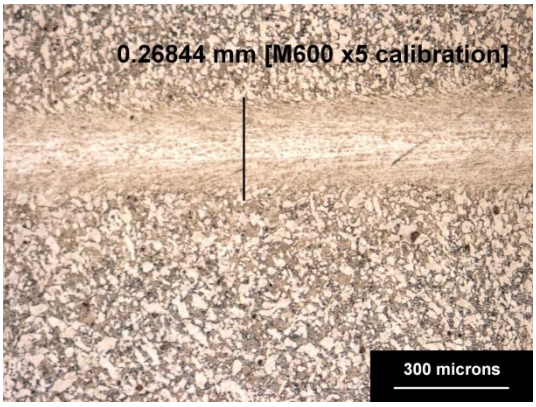

Weld 44